Università degli Studi di Napoli *Federico II*

DOTTORATO DI RICERCA IN FISICA

Ciclo XXXVI

Coordinatore: prof. Vincenzo Canale

Anisotropic Nanoparticles for Enhanced Plasmonic Effects

Settore Scientifico Disciplinare FIS/07

Dottorando
Adriano ACUNZO

Tutor
Prof. Raffaele VELOTTA

Anni 2021/2024

Contents

Introduction

Chapters

References

Introduction

Single–molecule detection is a current challenge in biosensing, posed by the great concern for ultra–sensitivity in biomedical analyses, especially in the wake of the COVID–19 pandemic. Many pathogenic and non–pathogenic diseases present chemical and biological markers in clinical samples at trace concentrations as low as attomolar (*a*M) levels. Early diagnostics often requires detecting such low analyte concentrations. Additionally, single–molecule detection is also needed when only a minimum volume of sample (few µL) is available, or when multiplexed analysis of many target analytes is demanded simultaneously.

Research in single–molecule bioanalytical technologies has primarily focused on optical detection techniques. These techniques generally exploits high–quality photodetection methods or optical enhancement mechanisms, or both, in order to increase the sensitivity and selectivity towards target analytes. For instance, waveguide interferometric biosensors, which employ bimodal nanowaveguide interferometers, are a relevant example of the former technology. Instead, the latter employs enhancement mechanisms provided by plasmonic structures and nanostructures upon optical excitation of surface plasmons (SP) and localized surface plasmons (LSP), respectively. SPs and LSPs lead to the enhancement of the external optical perturbation within a subwavelength volume surrounding the plasmonic structure/nanostructure, reaching a maximum at the SP resonance (SPR) or LSP resonance (LSPR) wavelength. In this thesis, we will deal with the plasmon–enhanced effects offered by simple plasmonic nanostructures made by arrays of both isotropic and anisotropic gold nanoparticles (AuNPs).

A large class of optical nanoplasmonic biosensors directly exploits the aforementioned inherent plasmon–enhanced phenomena and, hence, are often termed “LSPR–based” biosensors. Typical sensing parameters are related to the extinction spectrum of the nanostructured transducers, such as shifts of the LSPR wavelength or variations of the LSPR peak intensity, both due to variations of the local refractive index contingent to analyte detection. Therefore, LSPR–based biosensors offer label–free detection and can also provide real–time responses to the variations of the local refractive index. However, this class of biosensors typically reaches limits of detections (LODs) in the range nM–pM, which are sufficient in many cases, but still far from the *aM* level (typically assumed as synonymous with single–molecule level).

Among the plasmon–enhanced optical techniques capable of single–molecule detection, those relying on the amplification of an *external* signal (not inherent to the transducer), such as surface–enhanced Raman spectroscopy (SERS), surface–enhanced infrared absorption (SEIRA), and surface–enhanced fluorescence are the most studied. The latter is usually referred to as plasmon–enhanced fluorescence (PEF) or metal–enhanced fluorescence (MEF) depending on which aspect, the physical principle, or the material, is given priority. We will treat them as synonymous and use the MEF acronym.

We will thoroughly investigate the MEF technique, covering all the main steps involved in developing and testing simple nanostructures which could be employed in the future as transducers for MEF-based biosensors. These steps include formulating basic concepts, designing

the experiment, simulating the devices, fabricating them, conducting experimental measurements, and finally, comparing the results with computational outputs. Our primary focus will be thus on methodology. Indeed, despite MEF has a long scientific history, its applications are still in its infancy because of complex underlying physicochemical phenomena which are not yet fully understood. As a consequence, there are no general practical instructions on the choice of proper fluorophores, spectral matchings, excitation wavelengths, etc. We will provide our guidelines based on our understanding, or interpretation, of MEF. We believe that our holistic and meticulous approach to this subject can be of practical utility in developing MEF–based biosensors or, at least, in increasing awareness of the challenges involved and how to address them.

We will apply our methodology for determining the extent to which the MEF performance of simple nanostructures, such as random arrays of AuNPs, can be improved by the adoption of anisotropic AuNPs instead of isotropic ones (nanospheres). With state–of–the–art seed–mediated growth methods, various types of high–quality anisotropic NPs can now be synthesized with exceptional yield and monodispersion. MEF mechanisms benefit from the enhanced electromagnetic field offered by sharp features, enabling enhancements of photoluminescence by sharp anisotropic polyhedral NPs alone, while leaving the rest unmodified. Even relatively small improvements in fluorescence intensity, such as a factor of 1–10, can substantially lower the LODs by orders of magnitude, possibly reaching fM–*a*M levels, i.e., single–molecule detection.

The thesis has been organised to gradually introduce the reader to plasmonics, AuNPs synthesis, AuNPs array fabrication, and finally, our MEF study. Chapter 1 includes a selection of topics from Plasmonics. The concept of volume plasmons as excited collective oscillations of an interacting electron gas (due to the long–range part of the Coulomb potential) is first introduced in a classical hamiltonian formalism, and then discussed in both the first and second quantization formalisms. The possibility to excite plasmons in metal nanoparticles by optical radiation marks the transition to the classical Mie theory. The two main predictions of the quasi–static approximation of Mie theory are then pragmatically discussed by using nanophotonic simulations. The simulation software and the simulation workspaces used throughout this work are presented and discussed in detail. Finally, a selection of simulations from our recent works are presented to highlight the essential role played by simulations in plasmonics.

Chapter 2 is devoted to nanofabrication. Both isotropic (spherical) and anisotropic (cubic) gold nanoparticles were synthesized combining seed–mediated methods with Liz-Marzán's dissolution reaction, embracing Mirkin's renewed attention to seeds quality. Meticulous morphological characterizations and analysis of the nanoparticles products are presented, particularly for nanocubes. All interesting experimental results are corroborated by FDTD simulations run by Ansys Lumerical software. In this case, they were paramount for the modelling of nanocubes as "rounded" nanocubes. Finally, electrostatic self–assembly technique was used for the fabrication of random arrays of nanospheres and nanocubes on glass substrate. Collective plasmon phenomena were observed and then deeply investigated by FDTD simulations.

Chapter 3 starts with the analytical treatment of the metal–enhanced fluorescence (MEF) developed by Khurgin and Sun (et al.). Both absorption and emission of molecules placed close to a metal nanosphere are described as two–step processes in the presence of the plasmon modes supported by the sphere. A clear understanding of what is and what is not possible to achieve by

MEF is provided. In particular, the role played by the total absorption cross section of the molecules in limiting the absorption enhancement is unveiled. The negative impact of the higher–order modes of a sphere on the emission enhancement is highlighted. Then, the special case of fluorophores with high original quantum yield is presented through the classical works of Anger, Bharadwaj, and Novotny. Especially for these fluorophores, whose quantum yield can only diminish during MEF processes, the breaking of the spherical symmetry is advised as a route to limit the quenching. Anisotropic nanoparticles are thus introduced as a natural way to address the issue, as well as to further increase the absorption enhancement thanks to higher electric fields produced by their sharp features.

Chapter 4 presents our comparative study of the distance-dependent MEF performance on two of the fabricated nanostructures: an array of nanospheres serving as a reference and an array of nanocubes. We provide and thoroughly discuss our guidelines for a MEF experiment (see above). In particular, we consider the choice of a high-quality fluorophore over a low-quality one as the most suitable for future biosensing applications, as the fluorescence intensity is the actual sensing parameter to be maximized rather than its enhancement. Additionally, double-strand DNAs (dsDNAs) were employed as nanometric spacers, which are highly appealing from a biosensing perspective. We analyse and discuss the experimental results one by one with the help of simulated electromagnetic field profiles of target nanoparticles from the arrays. Few results could not be fully explained by MEF mechanisms and may be attributed to the complexity of dsDNA. In particular, we speculate about a novel effect.

After a brief conclusion, the last part of the manuscript includes supplementary, but relevant, material such as: nanofabrication protocols and procedures (Appendix A and B); technical details about the morphological analysis of electron micrographs by ImageJ software (Appendix C); dsDNA sequences (Appendix D); MEF experiments procedures (Appendix E); and supplementary data, analysis, and simulations (Appendix F). The list of references finally closes this manuscript.

Chapter 1. Selected Topics on Plasmonics

1.1 What is a Plasmon

Plasmons are the quanta quasi–particles (bosons) describing the excited collective oscillations of the valence electrons of a metal.[1,2] These collective oscillations can be excited either by inelastic scattering of fast electrons, acting as longitudinal probes, or by scattering of high–energy electromagnetic (EM) radiations, acting as transverse probes. The former method results in electron energy loss spectra (EELS), and is more suitable for the excitation of plasmons in the high–energy region ($\gtrsim 15$ eV), whereas optical experiments excite plasmons in the low–energy region.[1,2] Plasmons can be excited in the interior volume of bulk metals (volume plasmons, VP), at the metal/dielectric interface of bulk metals or metal films (surface plasmons, SP), or at the metal/dielectric interface of metal nanoparticles (NPs) or nanostructures (localized surface plasmons, LSP). [1–3] It is easy to understand that the energy required to excite VPs, SPs, and LSPs are generally ordered as $\mathrm{E[VPs]} > \mathrm{E[SPs]} > \mathrm{E[LSPs]}$ since the number of electrons moving together in a coherent fashion decreases with dimensionality. This is the fundamental reason why VPs are more easily excited by fast electrons (keV). Instead, SPs and LSPs can be easily excited even by optical frequencies (1.5 – 3 eV) (SPs need momentum matching by gratings and prisms; LSPs can be excited in NPs even in vacuum thanks to the small size).[3]

1.1.1 The Collective Description of the Interacting Electron Gas

In this section, we will follow the works by Pines[1] and Madelung[2] to illustrate how plasmons emerge in an attempt to circumvent the divergences which affects any perturbative treatment of the Coulomb interaction. The Coulomb interaction (equation (1.0)) cannot be rigorously treated by perturbation techniques beyond the first order, as the contributions of second and higher orders diverge. These divergences arise from the long–range part of the Coulomb interaction. Various many–body approximations have been developed to circumvent this difficulty, e.g., Hartree and Hartree-Fock approximations. The method we illustrate here circumvents the divergences by splitting the Coulomb interaction into two parts, a short-range and a long-range interaction. The long–range part, which is firstly neglected, is reintroduced in the description in the form of additional collective oscillations of the electron gas, termed (volume) plasmons.

Let us consider an electron gas with a uniformly distributed charge density. If we now introduce an additional negative charge at a point **r** (roughly resembling an EELS experiment), the uniform negative charge distribution is broken, and electrons are driven away from **r** (where the probe charge is placed) by Coulomb repulsions. On account of the long–range part of the Coulomb potential, the rearrangement will initially extend too far, and the electrons will possibly start to flow back and forward seeking a new equilibrium: collective longitudinal oscillations/waves in the electron gas charge density (plasma oscillations or plasmons) possibly appear. At the end of this dynamical process, the system reaches a final equilibrium state. On account of the short–range part of the Coulomb potential, the electrons rearrangement entails a positive charge–cloud around

the probe electron in **r** compared to the average charge density of the electron gas. This in turn means a screening of the charge of the probe electron in **r**.

According to the above–mentioned picture, screening of the Coulomb interaction of individual charges and collective oscillations result from the short–range and long–range parts of the Coulomb potential, respectively. Therefore, this treatment starts with the Coulomb potential U and its rewriting as a Fourier series, indexed by **k**. A specific $\mathbf{k}_c$ (to be determined) realizes the division into the short–range $(k > k_c)$ and long–range $(0 < k < k_c)$ parts, see Figure 1.1.

In formulae:

$$U = \frac{1}{2}\frac{e^2}{4\pi\varepsilon_0}\sum_{i\neq j}\frac{1}{|\mathbf{r}_i - \mathbf{r}_j|} = \frac{e^2}{2V_g\varepsilon_0}\sum_{i\neq j}\sum_{\mathbf{k}\neq\mathbf{0}}\frac{e^{i\mathbf{k}\cdot(\mathbf{r}_i-\mathbf{r}_j)}}{k^2} =$$

$$= \frac{e^2}{2V_g\varepsilon_0}\sum_{i\neq j}\left[\left(\sum_{\substack{\mathbf{k}\\ k>k_c}} + \sum_{\substack{\mathbf{k}\\ 0<k<k_c}}\right)\frac{e^{i\mathbf{k}\cdot(\mathbf{r}_i-\mathbf{r}_j)}}{k^2}\right] \tag{1.0}$$

where V_g is the volume of the electron gas and ε_0 the dielectric constant of the vacuum. The term associated with $\mathbf{k} = \mathbf{0}$ was neglected as it yields the mean value of the Coulomb potential, i.e., a finite constant value which can be set to zero.

It is also worth to write down the usual Hamiltonian for the interacting electron gas:

$$H = \sum_i \frac{|\mathbf{p}_i|^2}{2m} + U \tag{1.1}$$

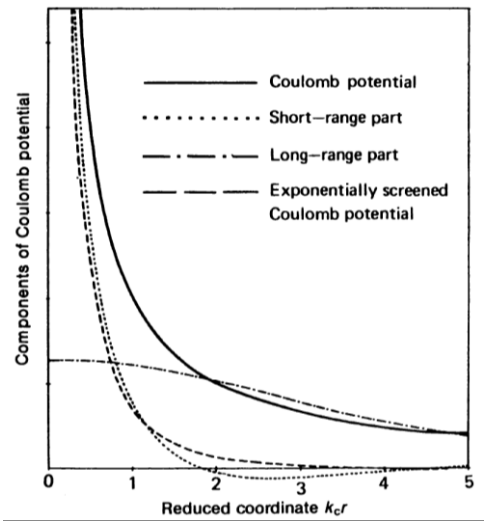

Figure 1.1 The Coulomb potential (solid line) and its division into a short–range component $(k > k_c)$ (dotted line) and a long–range component $(0 < k < k_c)$ (dash dotted line). (From Madelung[2]).

An interacting electron gas is a gas of electrons interacting with the (electrostatic) Coulomb field which they themselves produce. Generally, the Hamiltonian for electrons in interaction with an electromagnetic field can be written as:

$$\mathrm{H} = \left[\sum_{\mathrm{i}} \frac{\left(\mathbf{p}_{\mathrm{i}} + \mathrm{e}\mathbf{A}(\mathbf{r}_{\mathrm{i}})\right)^2}{2\mathrm{m}} - \sum_{\mathbf{i}} \mathrm{e}\Phi(\mathbf{r}_{\mathrm{i}})\right] + \mathrm{H}_{\text{e.m. free}} \tag{1.2}$$

where we recall that $\mathcal{A} \equiv (\Phi, \mathbf{A})$, $\mathbf{B} \equiv \boldsymbol{\nabla} \times \mathbf{A}$, $\mathbf{E} \equiv -\boldsymbol{\nabla}\Phi - \frac{\partial \mathbf{A}}{\partial \mathrm{t}}$ being Φ the scalar potential, $\mathbf{A}$ the vector potential, $\mathbf{B}$ the magnetic field and $\mathbf{E}$ the electric field. Instead, $\mathrm{H}_{\text{e.m. free}}$ is the Hamiltonian of the "free" electromagnetic field.

In our case:

$$\begin{cases} \mathbf{B} = \mathbf{0} \\ \mathbf{B} \equiv \boldsymbol{\nabla} \times \mathbf{A} \end{cases} \quad \Rightarrow \quad \boldsymbol{\nabla} \times \mathbf{A} = \mathbf{0} \quad \Rightarrow \quad \mathbf{A}(\mathbf{r}_{\mathbf{i}}) = \frac{1}{\sqrt{\mathrm{V_g}\varepsilon_0}} \sum_{\mathbf{k}\neq\mathbf{0}} \frac{\mathbf{k}}{\mathrm{k}} \mathrm{Q}_{\mathbf{k}} \mathrm{e}^{\mathrm{i}\mathbf{k}\cdot\mathbf{r}_{\mathrm{i}}} \tag{1.3}$$

where the last implication results from a straightforward calculation, i.e., writing $\mathbf{A}(\mathbf{r})$ as the Fourier series $\mathbf{A}(\mathbf{r}) \equiv \sum_{\mathbf{k}\neq\mathbf{0}} \mathbf{Q}_{\mathbf{k}} \mathrm{e}^{\mathrm{i}\mathbf{k}\cdot\mathbf{r}}$ and requiring $\boldsymbol{\nabla} \times \mathbf{A} = \mathbf{0}$. In particular, it results $\mathbf{Q}_{\mathbf{k}} /\!/ \mathbf{k}$. The factor $1/\sqrt{V_g \varepsilon_0}$ is chosen for convenience. For the properties of Fourier series, $\boldsymbol{k} = \left(2\pi/\sqrt[3]{V_g}\right)\boldsymbol{n}$ with $\boldsymbol{n} \in \mathbb{Z}^3 - \{\mathbf{0}\}$. Since $\mathbf{A}$ is real, the Fourier coefficients are such that $Q_{\boldsymbol{k}}^* = -Q_{-\boldsymbol{k}}$.

Let us now choose the Weyl gauge (also known as temporal gauge). It follows:

$$\begin{matrix} \text{gauge Weyl:} \\ \Phi = 0 \end{matrix} \quad \Rightarrow \quad \mathbf{E} = -\frac{\partial \mathbf{A}}{\partial \mathrm{t}} = -\frac{1}{\sqrt{\mathrm{V_g}\varepsilon_0}} \sum_{\mathbf{k}\neq\mathbf{0}} \frac{\mathbf{k}}{\mathrm{k}} \dot{\mathrm{Q}}_{\mathbf{k}} \mathrm{e}^{\mathrm{i}\mathbf{k}\cdot\mathbf{r}_{\mathrm{i}}} = -\frac{1}{\sqrt{\mathrm{V_g}\varepsilon_0}} \sum_{\mathbf{k}\neq\mathbf{0}} \frac{\mathbf{k}}{\mathrm{k}} \mathrm{P}_{\mathbf{k}}^* \, \mathrm{e}^{\mathrm{i}\mathbf{k}\cdot\mathbf{r}_{\mathrm{i}}} , \tag{1.4}$$

where we set $\dot{Q}_{\boldsymbol{k}} \equiv P_{\boldsymbol{k}}^*$. In fact, it can be shown that $(\mathrm{Q}_{\mathbf{k}}, \mathrm{P}_{\mathbf{k}})$ are canonical conjugates variables. Since $\mathbf{E}$ is real, it must be $\mathrm{P}_{\mathbf{k}}^* = -\mathrm{P}_{-\mathbf{k}}$.

Formula (1.4) allows to calculate $\mathrm{H}_{\text{e.m. free}}$ in our case:

$$\mathrm{H}_{\text{e.m. free}} = \frac{\varepsilon_0}{2} \int |\mathbf{E}|^2 \mathrm{dV} = \frac{1}{2\mathrm{V_g}} \sum_{\mathbf{k},\mathbf{k}'\neq\mathbf{0}} \frac{\mathbf{k}\cdot\mathbf{k}'}{\mathrm{k}\mathrm{k}'} \mathrm{P}_{\mathbf{k}}^* \mathrm{P}_{\mathbf{k}'}^* \int \mathbf{e}^{\mathbf{i}(\mathbf{k}+\mathbf{k}')\cdot\mathbf{r}_{\mathrm{i}}} \, \mathrm{dV}_{\mathrm{i}} = \frac{1}{2} \sum_{\mathbf{k}\neq\mathbf{0}} \mathrm{P}_{\mathbf{k}}^* \mathrm{P}_{\mathbf{k}} , \tag{1.5}$$

where we used the relations $\int \mathbf{e}^{\mathbf{i}(\mathbf{k}+\mathbf{k}')\cdot\mathbf{r}} \, \mathrm{dV} = \mathrm{V_g} \boldsymbol{\delta}_{\mathbf{k},-\mathbf{k}'}$ and $\mathrm{P}_{\mathbf{k}}^* = -\mathrm{P}_{-\mathbf{k}}$.

Therefore, the Hamiltonian (1.2) can be formally rewritten as:

$$\mathrm{H} = \frac{1}{2\mathrm{m}} \sum_{\mathrm{i}} \left(\mathbf{p}_{\mathrm{i}} + \frac{\mathrm{e}}{\sqrt{\mathrm{V_g}\varepsilon_0}} \sum_{\mathbf{k}\neq\mathbf{0}} \frac{\mathbf{k}}{\mathrm{k}} \mathrm{Q}_{\mathbf{k}} \mathrm{e}^{\mathrm{i}\mathbf{k}\cdot\mathbf{r}_{\mathrm{i}}} \right)^2 + \frac{1}{2} \sum_{\mathbf{k}\neq\mathbf{0}} \mathrm{P}_{\mathbf{k}}^* \mathrm{P}_{\mathbf{k}} . \tag{1.6}$$

The fundamental idea by Pines[1] (and Bohm) was to write down a "hybrid" Hamiltonian of the kind shown in (1.6), i.e., including both the old $(\mathbf{p}_{\mathrm{i}}, \mathbf{r}_{\mathrm{i}})$ and the new collective $(\mathrm{Q}_{\mathbf{k}}, \mathrm{P}_{\mathbf{k}})$ variables rather than only $(\mathrm{Q}_{\mathbf{k}}, \mathrm{P}_{\mathbf{k}})$. In fact, the only well–defined collective modes are the long–wavelength plasmons associated to $0 < k < k_c$, which are $N' = k_c^3 V_g / 6\pi^2$ in number (ratio between a sphere of radius k_c, i.e., $\frac{4}{3}\pi {k_c}^3$, and the elementary volume associated to each $\mathbf{k}$, i.e., $(2\pi)^3/V_g$). Since only these N' coordinates describe longitudinal collective modes, and since $N' << N$ for electrons in metals, it is not fruitful to attempt a complete redescription of the single–particle motion by collective coordinates only.

The additional N' collective variables would raise the degrees of freedom of the system without N' constraints connecting the two sets of coordinates. Maxwell's equation $\boldsymbol{\nabla}\cdot\mathbf{E}-\rho/\varepsilon_0=0$ provides the necessary constraints. After expanding $\rho(\mathbf{r})=\mathrm{e}\sum_j \boldsymbol{\delta}(\mathbf{r}-\mathbf{r}_\mathrm{j})$ as a Fourier series, we will have for each Fourier component:

$$\text{constraints:}\quad \boldsymbol{\nabla}\cdot\mathbf{E}-\frac{\rho}{\varepsilon_0}=0 \quad\Rightarrow\quad \mathrm{P}_\mathbf{k}-\mathrm{i}\sqrt{\frac{\mathrm{e}^2}{\mathrm{V_g}\varepsilon_0\,\mathrm{k}^2}}\sum_\mathrm{j}\mathrm{e}^{\mathrm{i}\mathbf{k}\cdot\mathbf{r}_\mathrm{j}}=0\,. \tag{1.7}$$

There is a constraint for each new pair $(\mathrm{Q}_\mathbf{k}\,,\mathrm{P}_\mathbf{k})$. The number of degrees of freedom is preserved.

It is also worthwhile to note that the constraints (1.7) allows the following rewriting of the expression (1.5) previously found for $\mathrm{H}_{\mathrm{e.m.\,free}}$:

$$\begin{aligned}\mathrm{H}_{\mathrm{e.m.\,free}}=\frac{1}{2}\sum_{\mathbf{k}\neq\mathbf{0}}\mathrm{P}^*_\mathbf{k}\mathrm{P}_\mathbf{k}=\frac{e^2}{2V_g\varepsilon_0}\sum_{\mathbf{k}\neq\mathbf{0}}\sum_{i,j}\frac{e^{i\boldsymbol{k}\cdot(\boldsymbol{r}_i-\boldsymbol{r}_j)}}{k^2}=\\ =U+\frac{\mathrm{Ne}^2}{2\mathrm{V_g}\varepsilon_0}\sum_{\mathbf{k}\neq\mathbf{0}}\frac{1}{\mathrm{k}^2},\end{aligned} \tag{1.8}$$

in other words, $\mathrm{H}_{\mathrm{e.m.\,free}}$ is the Coulomb potential plus the self–energy contributions, which we need to subtract "by hand" from equation (1.6) for physical consistency.

Considering eq. (1.8), we can rewrite the Hamiltonian (1.6) in a specific "hybrid" manner, with the long–range terms $(0<k<k_c)$ expressed as functions of (only) the new collective coordinates $(\mathrm{Q}_\mathbf{k}\,,\mathrm{P}_\mathbf{k})$ and the short–range terms $(k>k_c)$ as functions of (only) the old coordinates $(\mathbf{p}_\mathrm{i},\mathbf{r}_\mathrm{i})$: [2]

$$\begin{aligned}\mathrm{H}\;=&\frac{1}{2\mathrm{m}}\sum_\mathrm{i}\left(\mathbf{p}_\mathrm{i}+\frac{\mathrm{e}}{\sqrt{\mathrm{V_g}\varepsilon_0}}\sum_{\substack{\mathbf{k}\\0<\mathrm{k}<\mathrm{k_c}}}\frac{\mathbf{k}}{\mathrm{k}}\mathrm{Q}_\mathbf{k}\mathrm{e}^{\mathrm{i}\mathbf{k}\cdot\mathbf{r}_\mathrm{i}}\right)^2+\\ &+\frac{1}{2}\sum_{\substack{\mathbf{k}\\0<\mathrm{k}<\mathrm{k_c}}}\mathrm{P}^*_\mathbf{k}\mathrm{P}_\mathbf{k}-\frac{\mathrm{Ne}^2}{2\mathrm{V_g}\varepsilon_0}\sum_{\substack{\mathbf{k}\\0<\mathrm{k}<\mathrm{k_c}}}\frac{1}{\mathrm{k}^2}+\\ &+\frac{\mathrm{e}^2}{2\mathrm{V_g}\varepsilon_0}\sum_{\mathrm{i,j}}\sum_{\substack{\mathbf{k}\\\mathrm{k}>\mathrm{k_c}}}\frac{\mathrm{e}^{\mathrm{i}\mathbf{k}\cdot(\mathbf{r}_\mathrm{i}-\mathbf{r}_\mathrm{j})}}{\mathrm{k}^2}-\frac{\mathrm{Ne}^2}{2\mathrm{V_g}\varepsilon_0}\sum_{\substack{\mathbf{k}\\\mathrm{k}>\mathrm{k_c}}}\frac{1}{\mathrm{k}^2}\,.\end{aligned} \tag{1.9}$$

The first line accounts for the kinetic contributions from all the individual electrons as well as for "mixed" terms (to be better interpreted), i.e., terms exhibiting products of old and new variables. Since there are only N' collective variables $\mathrm{Q}_\mathbf{k}$, associated to $0<k<k_c$, the original sum over all $\mathbf{k}\neq\mathbf{0}$ reported in equation (1.6) reduces to the sum over the $\mathbf{k}$ such that $0<k<k_c$.
The second line accounts for the long–range part of the Coulomb potential, entirely expressed in terms of the new collective variables. The third line accounts for the short–range parts of the Coulomb potential, entirely expressed in terms of the old variables. Note that the self-energy contribution can be re-absorbed into the main sum over i, j as soon as one further imposes $\mathrm{i}\neq\mathrm{j}$.

The Hamiltonian (1.9) is equivalent to the (1.6), which is equivalent to the (1.1), once the constraints (1.7) are fulfilled. We are just describing the same system differently.

Computing the square and reorganizing the addenda, we obtain:

$$\begin{aligned} H = & \sum_{\mathbf{i}} \frac{|\mathbf{p}_\mathrm{i}|^2}{2m} + \frac{e^2}{2V_g\varepsilon_0} \sum_{\substack{\mathrm{i,j} \\ \mathrm{i}\neq\mathrm{j}}} \sum_{\substack{\mathbf{k} \\ \mathrm{k}>\mathrm{k_c}}} \frac{e^{i\mathbf{k}\cdot(\mathbf{r}_\mathrm{i}-\mathbf{r}_\mathrm{j})}}{k^2} + \\ & + \frac{1}{2} \sum_{\substack{\mathbf{k} \\ 0<\mathrm{k}<\mathrm{k_c}}} \left(P_{\mathbf{k}}^* P_{\mathbf{k}} + \omega_p^2 Q_{\mathbf{k}}^* Q_{\mathbf{k}} - \frac{m\omega_p^2}{k^2} \right) + \\ & + \frac{e}{m\sqrt{V_g\varepsilon_0}} \sum_{\mathbf{i}} \sum_{\substack{\mathbf{k} \\ 0<\mathrm{k}<\mathrm{k_c}}} \frac{\mathbf{p}_\mathrm{i}\cdot\mathbf{k}}{k} Q_{\mathbf{k}} e^{i\mathbf{k}\cdot\mathbf{r}_\mathrm{i}} + \frac{e^2}{2V_g\varepsilon_0 m} \sum_{\substack{\mathbf{k},\mathbf{k}' \\ \mathbf{k}'\neq-\mathbf{k} \\ \mathrm{k},\mathrm{k}'<\mathrm{k_c}}} \frac{\mathbf{k}\cdot\mathbf{k}'}{kk'} Q_{\mathbf{k}} Q_{\mathbf{k}'} \sum_{\mathbf{i}} e^{i(\mathbf{k}+\mathbf{k}')\cdot\mathbf{r}_\mathrm{i}} \end{aligned} \tag{1.10}$$

where $n \equiv N/V_g$ and $\omega_p \equiv \sqrt{\frac{ne^2}{m\varepsilon_0}}$ is called "plasma frequency".

The first line is the Hamiltonian of an *electron gas with screened Coulomb interaction* ($k > k_c$).
The second line is a sum over Hamiltonians of independent harmonic oscillators of frequency ω_p (less the self–energy), and describes the well–defined, long–range ($0 < k < k_c$) collective oscillations of the electron gas *(plasma oscillations).*
The third line is the interaction Hamiltonian between screened electrons and plasmons. The interactions follow from the products between the new collective coordinates $Q_{\mathbf{k}}$ and the old individual coordinates $\mathbf{p}_\mathrm{i}$ and $\mathbf{r}_\mathrm{i}$.

The above treatment was entirely classical. Let us now move to the quantum description.
Assuming the usual commutation relations between canonical variables, we have:

$$\begin{cases} \left[r_{i\alpha} , p_{j\beta} \right] = i\hbar\delta_{ij}\delta_{\alpha\beta} \\ \left[Q_{\mathbf{k}}, P_{\mathbf{k}'} \right] = i\hbar\delta_{\mathbf{k}\mathbf{k}'} \end{cases} \qquad \Rightarrow \qquad \left[\mathbf{p_i}, e^{i\mathbf{k}\cdot\mathbf{r}_\mathrm{i}} \right] = (2\mathbf{p_i} - \hbar\mathbf{k})\, e^{i\mathbf{k}\cdot\mathbf{r}_\mathrm{i}} \ . \tag{1.11}$$

The quantum Hamiltonian is:

$$\begin{aligned} H = & \sum_{\mathbf{i}} \frac{|\mathbf{p}_\mathrm{i}|^2}{2m} + \frac{e^2}{2V_g\varepsilon_0} \sum_{\substack{\mathrm{i,j} \\ \mathrm{i}\neq\mathrm{j}}} \sum_{\substack{\mathbf{k} \\ \mathrm{k}>\mathrm{k_c}}} \frac{e^{i\mathbf{k}\cdot(\mathbf{r}_\mathrm{i}-\mathbf{r}_\mathrm{j})}}{k^2} + \\ & + \frac{1}{2} \sum_{\substack{\mathbf{k} \\ 0<\mathrm{k}<\mathrm{k_c}}} \left(P_{\mathbf{k}}^* P_{\mathbf{k}} + \omega_p^2 Q_{\mathbf{k}}^* Q_{\mathbf{k}} - \frac{m\omega_p^2}{k^2} \right) + \\ & + \frac{e}{m\sqrt{V_g\varepsilon_0}} \sum_{\substack{\mathbf{k} \\ 0<\mathrm{k}<\mathrm{k_c}}} Q_{\mathbf{k}} \frac{\mathbf{k}}{k} \cdot \sum_{\mathbf{i}} \left(\mathbf{p_i} - \frac{\hbar\mathbf{k}}{2} \right) e^{i\mathbf{k}\cdot\mathbf{r}_\mathrm{i}} + \\ & + \frac{e^2}{2V_g\varepsilon_0 m} \sum_{\substack{\mathbf{k}'\neq-\mathbf{k} \\ k,k'<k_c}} \frac{\mathbf{k}\cdot\mathbf{k}'}{kk'} Q_{\mathbf{k}} Q_{\mathbf{k}'} \sum_{\mathbf{i}} e^{i(\mathbf{k}+\mathbf{k}')\cdot\mathbf{r}_\mathrm{i}} \end{aligned} \tag{1.12}$$

The interpretation for the various terms is the same for the classical case. Let us just stress that the second line is the Hamiltonian (less the self-energy) of non–interacting quantum harmonic oscillators. These are the quanta of the collective oscillations of the electron gas.

To better interpret the interaction terms and to gain a deeper insight, we can eventually rewrite the Hamiltonian (1.12) according to the second quantization formalism. Let us then consider the creation and annihilation operators for bosons and fermions, denoted by $a_{\boldsymbol{k}}^{\dagger}, a_{\boldsymbol{k}}$ and $c_{\boldsymbol{k}}^{\dagger}, c_{\boldsymbol{k}}$ respectively, satisfying the algebras $\left[a_{\boldsymbol{k}}, a_{\boldsymbol{k}}^{\dagger}\right] = \delta_{\boldsymbol{k}\boldsymbol{k}'}$ and $\left\{c_{\boldsymbol{k}}, c_{\boldsymbol{k}}^{\dagger}\right\} = \delta_{\boldsymbol{k}\boldsymbol{k}'}$. Electrons are fermions while plasmons are bosons (as they are described by harmonic oscillators). It easily follows that $Q_{\boldsymbol{k}} = \sqrt{\hbar/2\omega_{\boldsymbol{p}}}\left(a_{\boldsymbol{k}} + a_{-\boldsymbol{k}}^{\dagger}\right)$. Considering a basis of plane waves labelled by $\boldsymbol{k}_{\lambda}$, each of the addenda of the Hamiltonian (1.12) can be manipulated, obtaining the representation in Fock space:[2]

$$
\begin{aligned}
H &= H_{el,1} + H_{el,2} + H_{pl} + H_{el-pl,1} + H_{el-pl,2} = \\
&= \sum_{\boldsymbol{k}} \frac{\hbar k^2}{2m} c_{\boldsymbol{k}}^{\dagger} c_{\boldsymbol{k}} + \\
&+ \frac{e^2}{2V_g \varepsilon_0} \sum_{k>k_c} \frac{1}{k^2} \sum_{\boldsymbol{k}_{\lambda},\, \boldsymbol{k}_{\mu}} c_{\boldsymbol{k}_{\lambda}+\boldsymbol{k}}^{\dagger} c_{\boldsymbol{k}_{\mu}-\boldsymbol{k}}^{\dagger} c_{\boldsymbol{k}_{\mu}} c_{\boldsymbol{k}_{\lambda}} + \\
&+ \sum_{\substack{\boldsymbol{k} \\ 0<k<k_c}} \hbar\omega_p \left(a_{\boldsymbol{k}}^{\dagger} a_{\boldsymbol{k}} + \frac{1}{2}\right) - \frac{m\omega_p^2}{k^2} + \\
&+ \sum_{\substack{\boldsymbol{k} \\ 0<k<k_c}} \sqrt{\frac{e^2\hbar^3}{8\, V_g \varepsilon_0 m^2 k^2}} \sum_{\boldsymbol{k}_{\lambda}} (2\boldsymbol{k}\cdot\boldsymbol{k}_{\lambda} + k^2)\left(a_{\boldsymbol{k}} c_{\boldsymbol{k}_{\lambda}+\boldsymbol{k}}^{\dagger} c_{\boldsymbol{k}_{\lambda}} + a_{-\boldsymbol{k}}^{\dagger} c_{\boldsymbol{k}_{\lambda}+\boldsymbol{k}}^{\dagger} c_{\boldsymbol{k}_{\lambda}}\right) + \\
&+ \frac{e^2}{2V_g \varepsilon_0 m} \sum_{\substack{\boldsymbol{k},\boldsymbol{k}' \\ k,k'<k_c \\ \boldsymbol{k}'\neq -\boldsymbol{k}}} \frac{\boldsymbol{k}\cdot\boldsymbol{k}'}{kk'} \left(a_{\boldsymbol{k}} a_{\boldsymbol{k}'} + a_{-\boldsymbol{k}}^{\dagger} a_{-\boldsymbol{k}'}^{\dagger} + a_{-\boldsymbol{k}}^{\dagger} a_{\boldsymbol{k}'} + a_{\boldsymbol{k}} a_{-\boldsymbol{k}'}^{\dagger}\right) c_{\boldsymbol{k}+\boldsymbol{k}'+\boldsymbol{k}_{\lambda}}^{\dagger} c_{\boldsymbol{k}_{\lambda}}
\end{aligned}
\tag{1.13}
$$

The first line in Equation (1.13), $\mathrm{H_{el,1}}$, is the Hamiltonian of the non–interacting electron gas.
The second line, $\mathrm{H_{el,2}}$, represents the screened Coulomb interaction, which is described by individual interaction processes in which the momentum **k** is transferred from the μ–th electron to the λ–th electron (annihilation of two electrons with momenta $\boldsymbol{k}_{\mu}$, $\boldsymbol{k}_{\lambda}$ and creation of two electrons with momenta $\boldsymbol{k}_{\lambda} + \boldsymbol{k}$ and $\boldsymbol{k}_{\mu} - \boldsymbol{k}$).
The third line, $\mathrm{H_{pl}}$, is the Hamiltonian (less self–energy) of a gas of non–interacting bosons: these are the *volume plasmons*, i.e., quanta of collective oscillations of the electron gas volume.
The fourth line, $\mathrm{H_{el-pl,1}}$, represents an electron–plasmon interaction, described by processes in which a momentum $\mathbf{k}$ is transferred to an electron either because it absorbs a plasmon $\mathbf{k}$ (first term) or it emits a plasmon $-\mathbf{k}$ (second term).
The fifth line, $\mathrm{H_{el-pl,1}}$, represents an electron–plasmon interaction of the second–order, i.e., in which two plasmons are involved simultaneously. This term describes processes in which a momentum $(\mathbf{k} + \mathbf{k}')$ is transferred to the λ-th electron through the simultaneous absorption of

two plasmons $\mathbf{k}$, $\mathbf{k}'$, or simultaneous emission of two plasmons $-\mathbf{k}, -\mathbf{k}'$, or simultaneous absorption and emission of plasmons $\pm\mathbf{k}$.

Two final technical notes. In equation (1.13), $\mathbf{k}$ defines a state with spin, hence the sums over $\mathbf{k}$ imply sums over spin as well. Moreover, in our case, $\mathcal{A} \equiv (\Phi, \mathbf{A}) = (0, \mathrm{A}_1(\mathbf{r}), \mathrm{A}_2(\mathbf{r}), \mathrm{f}(\mathrm{A}_1, \mathrm{A}_2))$, since we used the Weyl gauge $\Phi = 0$, and $\mathbf{0} = \mathbf{B} \equiv \boldsymbol{\nabla} \times \mathbf{A}$ is a constraint on $\mathbf{A}$ which allows one of its components to be expressed in terms of the other two. Therefore, $\mathcal{A}$ has only two independent components, which warrants a proper quantization of the electromagnetic field (electrostatic, in our case), in particular, with no longitudinal states nor ghost states

We conclude this section with the estimation of k_c.[2]

k_c is often estimated by comparing the energy E_{pl} of a plasmon with the maximum energy E_{pair}^{MAX} for an electron-hole pair of a non–interacting electron gas. If one sees an excited state of a non–interacting electron gas as an electron-hole pair, then, for a given κ,

$$\mathrm{E}_{\mathrm{pair}}^{\mathrm{MAX}} = \frac{\hbar^2}{2\mathrm{m}}[(\kappa + \mathrm{k_F})^2 - k_F^2] = \frac{\hbar^2\kappa^2}{2\mathrm{m}} + \hbar\kappa\mathrm{v_F}$$

where $v_F = \hbar k_F/m$ is the velocity of an electron on the Fermi sphere (the electron to be excited).

Instead, the energy of the first excited plasmon state of a non–interacting plasmon gas is simply $\mathrm{E_{pl}} = \hbar\omega_\mathrm{p}$. An electron can thus excite (or decay into) a plasmon whenever $\mathrm{E_{pl}} \leq \mathrm{E}_{\mathrm{pair}}^{\mathrm{MAX}}$:

$$\text{plasmon excited if } \mathrm{E_{pl}} \leq \mathrm{E}_{\mathrm{pair}}^{\mathrm{MAX}} \;\Leftrightarrow\; \hbar\omega_\mathrm{p} \leq \frac{\hbar^2\kappa^2}{2\mathrm{m}} + \hbar\kappa\mathrm{v_F}\,.$$

Let us call κ_p the value of κ such that $\mathrm{E_{pl}} = \mathrm{E}_{\mathrm{pair}}^{\mathrm{MAX}}$. It follows that:

$$\kappa = \kappa_p \;\overset{\text{def}}{\Leftrightarrow}\; \mathrm{E_{pl}} = \hbar\omega_\mathrm{p} = \frac{\hbar^2\kappa_p^2}{2\mathrm{m}} + \hbar\kappa_p\,\mathrm{v_F} = \mathrm{E}_{\mathrm{pair}}^{\mathrm{MAX}}$$

$$\kappa < \kappa_p \;\Rightarrow\; E_{pl} > E_{pair}^{MAX} \quad \text{(no plasmons excited)}$$

$$\kappa > \kappa_p \;\Rightarrow\; E_{pl} < E_{pair}^{MAX} \quad \text{(plasmons excited)}$$

Therefore, κ_p serves as a natural threshold for plasmon excitations, and one usually sets $k_c = \kappa_p$. From the definition of κ_p and the assumption $k_c = \kappa_p$, it follows

$$k_c \approx \frac{\omega_{\boldsymbol{p}}}{v_F} \quad (for\ small\ \kappa)$$

Note that k_c depends through $\omega_{\boldsymbol{p}}$ and v_F on the density n of the electron gas.

For our interesting case of $\kappa < k_c$, plasmons can neither be excited by individual pair excitations of the electron gas, nor can they decay into them, since $E_{pl} > E_{pair}^{MAX}$. The fact that it is impossible to excite plasmons by particle excitations of the gas itself in the stable region $\kappa < k_c$ means that plasmon effects can mostly be ignored in an unperturbed system. Pictorially, we could say that

plasmons cannot be excited “from inside”. Plasmon effects do become important when sufficient energy is supplied from outside, e.g., by the transit of fast electrons (keV) through a solid. Fast electrons suffer characteristic energy losses in solids due to plasmon excitation, see Figure 1.2.

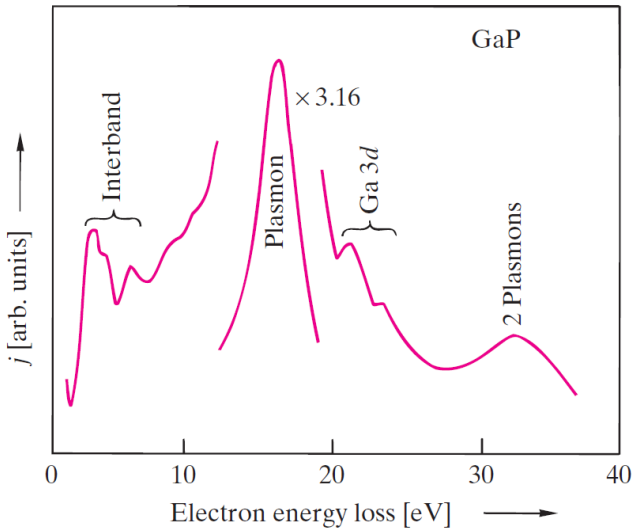

Figure 1.2. EELS spectrum of GaP (a semiconductor) showing characteristic features due to interband transitions, core levels transitions, and the typical resonances due to the excitation of individual plasmons as well as the simultaneous excitation of two plasmons.

We conclude this section by stressing that (volume) plasmons can be excited by electromagnetic radiation, too. A fundamental question arises: how can a longitudinal mode (plasma oscillations) be excited by a transverse mode (electromagnetic waves)? This question is ambiguous, as electromagnetic waves are exclusively transverse in vacuum, but can have longitudinal components when traveling through a material medium.
Indeed, Maxwell’s Equations

$$\nabla \cdot \mathbf{D} = \rho_{ext} \ , \qquad \nabla \cdot \mathbf{B} = 0 \ , \qquad \nabla \times \mathbf{E} = -\partial_t \mathbf{B} \ , \qquad \nabla \times \mathbf{H} = \mathbf{J}_{ext} + \partial_t \mathbf{D} \ ,$$

can be combined (the curl equations) to obtain the wave equations for the propagation of electromagnetic field inside a linear, isotropic, and nonmagnetic medium ($\mathbf{D} = \varepsilon_0 \varepsilon \mathbf{E}$, $\boldsymbol{B} = \mu_0 \mathbf{H}$). In absence of external charges and currents sources, ($\rho_{ext} = 0$ and $\mathbf{J}_{ext} = \mathbf{0}$):

$$\nabla \times \nabla \times \mathbf{E} = -\mu_0 \frac{\partial^2 \mathbf{D}}{\partial t^2} \quad \overset{\text{Fourier}}{\Longleftrightarrow} \quad \mathbf{k}\,(\mathbf{k} \cdot \mathbf{E}) - k^2 \mathbf{E} = -\varepsilon(\mathbf{k}, \omega) \frac{\omega^2}{c^2} \mathbf{E} \, .$$

Whenever $\varepsilon(\mathbf{k}, \omega) = 0$, entirely longitudinal electromagnetic waves ($\mathbf{E} \propto \mathbf{k}$), which have the potential to excite and sustain plasmon modes, are permitted. Specifically, longitudinal electromagnetic waves can excite (volume) plasmons at frequencies ω such that $\varepsilon(\omega) = 0$.

Therefore, (volume) plasmons in a metal can be excited by electromagnetic radiation through a suitable metal/dielectric interface. However, since the required energies are usually very high (tens of eV, see Figure 1.2), the excitation by fast electrons (keV) is much easier and convenient.

1.2 Localized Surface Plasmons (LSPs) in Classical Optics

Plasmons can also occur within a narrow surface layer of a solid. According to the electron gas model, we could just think to these plasmons as electron collective oscillations *localized* at the surface of the gas rather than involving the entire volume gas.[1,2] In the case of an extended (flat) surface, e.g., a (flat) metal or semiconductor film, such plasmons are *localized* in the direction normal to the surface but *extended* parallel to the surface (*surface plasmons*, SP). In the case of a non–extended surface, i.e., a small, closed, and curved (3D) surface of a metal NP, such plasmons are essentially localized in all directions (*localized surface plasmons*, LSP). Since the number of electrons (coherently moving) decreases with dimensionality, SPs and LSPs generally requires less energy than volume plasmons to be excited (few eV). Remarkably, this energy can often be provided by optical radiation $(1.5 - 3\ \mathrm{eV})$, eliminating the need for fast electrons (keV).

The excitation of SPs by electromagnetic radiation is contingent to a metal/dielectric interface for reasons analogous to those discussed at the end of the previous section (the need for longitudinal electromagnetic modes). In particular, specific configurations, e.g., Otto and Kretschmann configurations are employed for the momentum matching.[3] Instead, LSPs in metal NPs do not suffer the "momentum matching" issue and can be excited by direct illumination, even in vacuum. This inherent feature of NPs is due to their small sizes or, equivalently, to their small, closed, and curved 3D surface. This point will be clearer later. Therefore, the optical features of LSPs arise from the scattering problem of a (metal) NP with an external electromagnetic field (Mie scattering problem).[4] We will limit ourselves to the *quasi–static (or dipolar) approximation* of Mie problem.

1.2.1 Quasi–static Approximation of Mie Theory

In order to understand the colours of colloidal gold nanoparticles (AuNPs) in solution, Mie in 1908 developed a complete theory of the scattering and absorption of electromagnetic radiation by a sphere.[4] We are going to illustrate its quasi–static approximation. This approximation assumes that the phase of the oscillating external field is constant over the entire volume of the sphere. Therefore, it is strictly valid only for vanishingly small spheres, i.e., with radius $a \ll \lambda$, with λ the wavelength of the external radiation. For instance, spherical AuNPs with diameters of 10–100 nm have LSPs resonances in the range 500–600 nm in water, hence the quasi–static approximation is valid for diameters up to 50 nm. In practice, the quasi–static approximation provides reliable results for metal nanospheres up to 100 nm.[3,5] For larger nanospheres, the phase of the electric field significantly varies over the sphere volume, and the full electrodynamic approach is required.

It is worth noting that the quasi–static approximation consists in considering an electric field with no spatial dependence, of the type $\boldsymbol{E}(t) = \boldsymbol{E}_0 e^{-i\omega t}$ with $\boldsymbol{E}_0$ the electrostatic part. This field has no momentum (it does not travel through space), hence $\varepsilon(\mathbf{k}, \omega) = 0$, which implies that the field is longitudinal and can always excite and sustain plasmons. Therefore, we readily see that in the quasi–static approximation plasmons can always be excited by direct illumination, even in vacuum. Since the approximation holds when $a \ll \lambda$, we conclude that nanoparticles LSPs can be excited by direct illumination as their nanoscale size intrinsically facilitates the momentum matching.

The quasi–static approximation provides analytical solutions for many interesting quantities when considering a homogeneous and isotropic metal nanosphere of radius $a \ll \lambda$ (described by a

complex dielectric function $\varepsilon_1(\omega)$) embedded in a homogeneous, isotropic, and non–absorbing medium (real dielectric constant ε_2), interacting with an external time–harmonic electromagnetic field. The phase of the harmonically oscillating electromagnetic field is nearly constant over the particle volume, so that one can calculate the spatial field distribution by assuming the simplified problem of a sphere in an electrostatic field $\boldsymbol{E} = E_0\,\hat{\boldsymbol{z}}$. The harmonic time dependence can then be added to the solutions once the spatial field distributions are known. Figure 1.3 sketches the problem in spherical coordinates. We will follow the work by Maier[3] in the following.

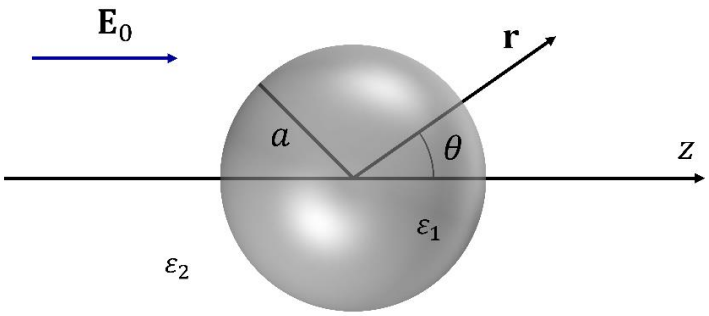

Figure 1.3. Homogeneous and isotropic metal nanosphere placed into an electrostatic field.

Given the azimuthal symmetry of the system, the general solution of the Laplace equation $\Delta\Phi = 0$ for the electrostatic potential Φ is[3,5]

$$\Phi(r,\theta) = \sum_{l=0}^{\infty}\left[A_l r^l + B_l r^{-(l+1)}\right]P_l(\cos\theta) \tag{1.14}$$

where $P_l(cos\theta)$ are the Legendre polynomials of order l and θ the angle between **r** and the *z*-axis.

After imposing that Φ remains finite at the origin, the solution (1.14) can be separated into the contributions inside Φ_{in} and outside Φ_{out} the nanosphere:

$$\Phi_{\text{in}}(r,\theta) = \sum_{l=0}^{\infty} A_l r^l P_l(\cos\theta) \tag{1.15a}$$

$$\Phi_{\text{out}}(r,\theta) = \sum_{l=0}^{\infty}\left[B_l r^l + C_l r^{-(l+1)}\right]P_l(\cos\theta) \tag{1.15b}$$

Note that the coefficient relative to $r^{-(l+1)}$ in the (1.15a) is lacking as it must be zero to keep finite Φ_{in} at the origin (centre of the sphere).

The coefficients A_l, B_l and C_l are determined from the boundary conditions at infinite ($r \to \infty$) and at the sphere surface ($r = a$). At $r \to \infty$, it must be $\Phi_{\text{out}} \to -E_0 z = -E_0 r\cos\theta$, which demands $B_1 = -E_0$ and $B_l = 0$ for $l \neq 1$. At the metal/dielectric interface $r = a$, the continuity of the tangential components of $\boldsymbol{E}$ and of the normal components of $\boldsymbol{D} = \varepsilon_0\varepsilon\boldsymbol{E}$ demand that

$$-\frac{1}{a}\frac{\partial\Phi_{\text{in}}}{\partial\theta}\bigg|_{r=a} = -\frac{1}{a}\frac{\partial\Phi_{\text{out}}}{\partial\theta}\bigg|_{r=a} \tag{1.16a}$$

$$-\varepsilon_0\varepsilon_1\frac{\partial\Phi_{\text{in}}}{\partial r}\bigg|_{r=a} = -\varepsilon_0\varepsilon_2\frac{\partial\Phi_{\text{out}}}{\partial r}\bigg|_{r=a} \tag{1.16b}$$

By inserting the expressions of the potential (1.15) into the previous conditions (1.16), it follows $A_l = C_l = 0$ for $l \neq 1$, and the only nonzero coefficients are

$$A_1 = -\frac{3\varepsilon_2}{\varepsilon_1 + 2\varepsilon_2} E_0 \qquad \text{(1.17a)} \qquad\qquad C_1 = \frac{\varepsilon_1 - \varepsilon_2}{\varepsilon_1 + 2\varepsilon_2} a^3 E_0 \qquad \text{(1.17b)}$$

Therefore, the solutions inside Φ_{in} and outside Φ_{out} the nanosphere are:

$$\Phi_{\text{in}}(r, \theta) = -\frac{3\varepsilon_2}{\varepsilon_1 + 2\varepsilon_2} E_0 r \cos\theta \qquad \text{(1.18a)}$$

$$\Phi_{\text{out}}(r, \theta) = -E_0 r \cos\theta + \frac{\varepsilon_1 - \varepsilon_2}{\varepsilon_1 + 2\varepsilon_2} E_0 a^3 \frac{\cos\theta}{r^2} \qquad \text{(1.18b)}$$

The solution (1.18b) for Φ_{out} has a simple physical interpretation: it is the superposition of the external electrostatic field and the field produced by an electric dipole located at the origin of the reference system (at the sphere centre). Φ_{out} can be rewritten in terms of the dipole moment $\mathbf{p}$:

$$\Phi_{\text{out}} = -E_0 r \cos\theta + \frac{\mathbf{p} \cdot \mathbf{r}}{4\pi\varepsilon_0\varepsilon_2 r^3} \qquad \text{(1.19a)}$$

$$\mathbf{p} = 4\pi\varepsilon_0\varepsilon_2 a^3 \frac{\varepsilon_1 - \varepsilon_2}{\varepsilon_1 + 2\varepsilon_2} \mathbf{E}_0 \qquad \text{(1.19b)}$$

Therefore, the applied external (electrostatic) field induces a dipole moment $\mathbf{p} \propto \mathbf{E}_0$ inside the sphere. The nanosphere can be then modelled as a *single* electric dipole in the quasi–static approximation, which is also called dipolar approximation. If we imagine for a moment (as it will be done explicitly later) to introduce the time–harmonic dependency, the nanosphere will behave as a *single* oscillating electric dipole of moment $\mathbf{p}(\mathrm{t}) \propto \boldsymbol{E}(t)$. From this perspective, we do not have a gas of electrons but just *two point charges* (located at the origin) *coherently* oscillating at the frequency ω of the external radiation along the direction of the external electrostatic field itself *(longitudinal oscillation),* by definition of oscillating dipole. There is no need for momentum matching since the quasi–static electric field is already longitudinal. According to the quasi–static approximation (quasi–static electric field, or vanishingly small sphere), LSPs can be excited by direct illumination, even in vacuum (where electromagnetic radiation is strictly transverse)

The dipole moment (1.19b) can be rewritten as $\mathbf{p} = \varepsilon_0\varepsilon_2\alpha\mathbf{E}_0$ with α the polarizability of the sphere

$$\alpha = 4\pi a^3 \frac{\varepsilon_1(\omega) - \varepsilon_2}{\varepsilon_1(\omega) + 2\varepsilon_2} \qquad \text{(1.20)}$$

Equation (1.20) is the central result of this section, the (complex) polarizability of a small sphere of sub-wavelength diameter in the electrostatic approximation. It is complex because the dielectric function $\varepsilon_1(\omega)$ describing the metal NP is complex.

The polarizability (1.20) experiences a resonant enhancement at the minimum of $|\varepsilon_1(\omega) + 2\varepsilon_2|$. In the case of a small or slowly–varying $\mathrm{Im}\{\varepsilon_1(\omega)\}$ around the resonance frequency , the minimum of $|\varepsilon_1(\omega) + 2\varepsilon_2|$, hence the maximum of α, is provided by the condition

Fröhlich condition: $\mathrm{Re}\{\varepsilon_1(\omega)\} = -2\varepsilon_2 \implies \alpha \; is \; maximum$ (1.21)

The relation is called Fröhlich condition, and the associated resonant mode (in an oscillating field) is called the *dipole localized surface plasmon resonance (dipole LSPR)* mode of the metal nanoparticle.[3,5] Fröhlich condition further expresses the strong dependence of the resonance on the local dielectric environment: the LSPR wavelength red-shifts as the dielectric constant ε_2 is increased. Metal NPs are ideal platforms for optical sensing of changes in (local) refractive index.[6,7]

It is also worth to notice that the magnitude of the polarizability α at resonance frequency ω is limited by the incomplete vanishing of its denominator, due to $\mathrm{Im}\{\varepsilon_1(\omega)\} \neq 0$. [3,5]

The distribution of the electric field inside and outside the sphere follows from $\mathbf{E} \equiv -\boldsymbol{\nabla}\Phi$:

$$\mathbf{E}_{\mathrm{in}} = \frac{3\varepsilon_2}{\varepsilon_1(\omega) + 2\varepsilon_2}\mathbf{E}_0 \tag{1.22a}$$

$$\mathbf{E}_{\mathrm{out}} = \mathbf{E}_0 + \frac{3\mathbf{n}(\mathbf{n}\cdot\mathbf{p}) - \mathbf{p}}{4\pi\varepsilon_0\varepsilon_2}\frac{1}{r^3} \tag{1.22b}$$

where $\mathbf{n} \equiv \hat{\boldsymbol{r}}$, i.e., the unit vector in the direction of a point P in space. Note that a resonance in polarizability α (when ω is such that $\mathrm{Re}\{\varepsilon_1(\omega)\} = -2\varepsilon_2$) entails a resonant enhancement of both the internal $\mathbf{E}_{\mathrm{in}}$ and dipolar $\mathbf{E}_{\mathrm{out}}$ fields ($\mathbf{p}$ is resonantly enhanced). This field enhancement at the plasmon resonance is one the most relevant features exhibited by NPs. Note that not only $\mathbf{E}_{\mathrm{out}}$ is enhanced, but it is also highly confined in the NP surroundings ($\propto 1/r^3$). In fact, the characteristic decay length l_{d} of the LSP near–field is much shorter (approximately 5–10 nm)[8,9] when compared to SPs (typically 0.1-1 μm).[10] Many of the prominent applications of metal nanoparticles in optical devices and sensors rely on such effects of field enhancement and confined. [6,7]

Let us now "switch on" the time–harmonic dependence of the external electromagnetic electric field, i.e., a plane wave $\mathbf{E}(\boldsymbol{r},t) = \mathbf{E}_0(\boldsymbol{r})\mathrm{e}^{-i\omega t}$. This external perturbation now excites the nanosphere inducing a coherent oscillating electric dipole $\mathbf{p}(\mathrm{t}) = \varepsilon_0\varepsilon_2\alpha\mathbf{E}_0\mathrm{e}^{-i\omega t}$, with negligible spatial retardation effects over the NP volume thanks to the quasi–static regime ($a \ll \lambda$).
The excited oscillating electric dipole (modelling the optical response of the NP) radiates an electromagnetic field that leads to the scattering of the external plane wave by the NP.
The total electric and magnetic fields emitted by the oscillating dipole are[3,11]

$$\mathbf{H}(\boldsymbol{r},t) = \frac{ck^2}{4\pi}(\mathbf{n}\times\mathbf{p})\frac{\mathrm{e}^{ikr}}{r}\left(1 - \frac{1}{ikr}\right)\mathrm{e}^{-i\omega t} \tag{1.23a}$$

$$\mathbf{E}(\boldsymbol{r},t) = \frac{1}{4\pi\varepsilon_0\varepsilon_2}\left\{k^2(\mathbf{n}\times\mathbf{p})\times\mathbf{n}\frac{\mathrm{e}^{ikr}}{r} + [3\mathbf{n}(\mathbf{n}\cdot\mathbf{p}) - \mathbf{p}]\left(\frac{1}{r^3} - \frac{ik}{r^2}\right)\mathrm{e}^{ikr}\right\}\mathrm{e}^{-i\omega t} \tag{1.23b}$$

where $k = 2\pi/\lambda$ and $\mathbf{n} \equiv \hat{\boldsymbol{r}}$ is the unit vector in the direction of the point P of interest.

In the near–field region ($kr \ll 1$), Equations (1.23) become[3,11]

$$\mathbf{H}(\boldsymbol{r},t) = \frac{i\omega}{4\pi}(\mathbf{n}\times\mathbf{p})\frac{1}{r^2}\mathrm{e}^{-i\omega t} \tag{1.24a}$$

$$\mathbf{E}(\boldsymbol{r},t) = \frac{3\mathbf{n}(\mathbf{n}\cdot\mathbf{p}) - \mathbf{p}}{4\pi\varepsilon_0\varepsilon_2}\frac{1}{r^3}\mathrm{e}^{-i\omega t} \tag{1.24b}$$

i.e., in the near–field region, the electrostatic result (1.22b) is recovered for the electric field, apart from the time–harmonic dependency. In this zone, the electric field dominates over the magnetic field. In particular, for static fields ($kr \to 0$), the magnetic field vanishes.

In the radiation zone ($kr \gg 1$), the dipole fields propagate as spherical-waves[3,11]

$$\mathbf{H}(\boldsymbol{r},t) = \frac{ck^2}{4\pi}(\mathbf{n}\times\mathbf{p})\frac{\mathrm{e}^{ikr}}{r}\mathrm{e}^{-i\omega t} \ , \tag{1.25a}$$

$$\mathbf{E}(\boldsymbol{r},t) = \sqrt{\frac{\mu_0}{\varepsilon_0\varepsilon_2}}\mathbf{H}\times\mathbf{n}\,\mathrm{e}^{-i\omega t} \ . \tag{1.25b}$$

From the viewpoint of optics, it is much more interesting to note that another consequence of the resonantly enhanced polarization α is a concomitant enhancement in the efficiency with which a metal nanoparticle scatters and absorbs light. In fact, in the quasi-static approximation, the scattering and absorption cross sections result:[3,5]

$$\sigma_{\mathrm{sca}} = \frac{k^4}{6\pi}|\alpha|^2 = \frac{8\pi}{3}k^4a^6\left|\frac{\varepsilon_1(\omega)-\varepsilon_2}{\varepsilon_1(\omega)+2\varepsilon_2}\right|^2 , \tag{1.26a}$$

$$\sigma_{\mathrm{abs}} = k\ \mathrm{Im}[\alpha] = 4\pi k a^3\ \mathrm{Im}\left[\frac{\varepsilon_1(\omega)-\varepsilon_2}{\varepsilon_1(\omega)+2\varepsilon_2}\right]. \tag{1.26b}$$

For small particles with $a \ll \lambda$, the absorption, proportional to a^3, dominates over the scattering, which scales with a^6. However, the rapid scaling of scattering makes it the dominant contribution for larger particles. It is worth to recall that the colours of NPs colloids (including AuNPs) are determined by their ability to absorb and scatter light, measured by σ_{sca} and σ_{abs}.

The extinction cross section, defined as $\sigma_{\mathrm{ext}} \equiv \sigma_{\mathrm{abs}} + \sigma_{\mathrm{sca}}$, is:[3,5]

$$\sigma_{\mathrm{ext}} = 9\,V\frac{\omega}{c}\frac{\mathrm{Im}[\varepsilon_1(\omega)]\ \varepsilon_2^{3/2}}{\{\mathrm{Re}[\varepsilon_1(\omega)]+2\varepsilon_2\}^2+\{\mathrm{Im}[\varepsilon_1(\omega)]\}^2} \ , \tag{1.27}$$

with V denoting the volume of the sphere.

Eqs. (1.26) and (1.27) are valid for both metals and dielectric media. *In the case of metal NPs, in the quasi–static approximation, both absorption and scattering – and thus extinction – are resonantly enhanced at the dipole LSPR frequency ω_{LSPR} entailed by the Fröhlich condition (1.21)*.

For a metal nanosphere of given radius modelled as a *free* electron gas (Drude model), at optical frequencies the Fröhlich condition is fulfilled by:[3,12]

$$\omega_{\mathrm{LSPR}} = \frac{\omega_{\mathrm{p}}}{\sqrt{2\varepsilon_2+1}} \tag{1.28a}$$

$$\lambda_{\mathrm{LSPR}} = \lambda_{\mathrm{p}}\sqrt{2n_2^2+1} \tag{1.28b}$$

where $n_2 = \sqrt{\varepsilon_2}$ is the refractive index of the surrounding medium and $\lambda_{\mathrm{p}} = 2\pi c/\omega_{\mathrm{p}}$ is the wavelength corresponding to the plasma frequency ω_{p} of the bulk metal. Equations (1.28) shows that the dipole LSPR strongly depends on the local dielectric environment, in particular the λ_{LSPR}

red–shifts as the dielectric constant of the medium increases.[3,12] Such a dependence turns out to be approximately linear over small variations of the refractive index at optical frequencies.[12]

1.2.2 Elements of the Full (Electrodynamic) Mie Theory

It is understood that the full (electrodynamic) Mie theory includes all multipolar terms. A brief treatment of the complete theory can be found in the book by Trügler[13], from which Figure 1.4 was also taken. It shows the σ_{ext} spectra of a gold (Figure 1.4a) and a silver (Figure 1.4b) nanosphere of diameter 150 nm calculated by the full Mie theory, and decomposed into contributions from absorption A_n and scattering S_n electric modes with $n = 1, 2, 3, 4$ (dipole, quadrupole, hexapole, and octupole modes). For simplicity, magnetic modes were omitted but also give important contributions.[13] Johnson and Christy[14] datasets for the dielectric functions of gold and silver were used for these calculations.

The diameter of 150 nm is beyond the practical limit of validity of the quasi–static approximation (100 nm) and, in fact, the higher–order modes are essential to accurately describe the σ_{ext} spectra of Figure 1.4. For instance, features like the secondary resonances in the σ_{ext} spectra at shorter wavelengths are entirely due to the higher–order (non–dipolar) modes.

Let us limit our attention to the dipole modes A_1 and S_1, which obviously provide the main contributions to the σ_{ext} spectra. We note that the S_1 mode is greatly redshifted compared to the A_1 mode. As a trivial consequence, the dipole absorption λ_{LSPR} and the dipole scattering λ_{LSPR} of such big NPs do not coincide but are (very) different. This feature is in sharp contrast with the results of the quasi–static approximation, according to which σ_{abs} and σ_{sca} have local maxima at the same λ_{LSPR}. Therefore, the quasi–static approximation of Mie theory cannot be strictly considered as the first–order (dipolar) approximation of the full theory, as it is even weaker than that (due to the hypothesis $a \ll \lambda$).

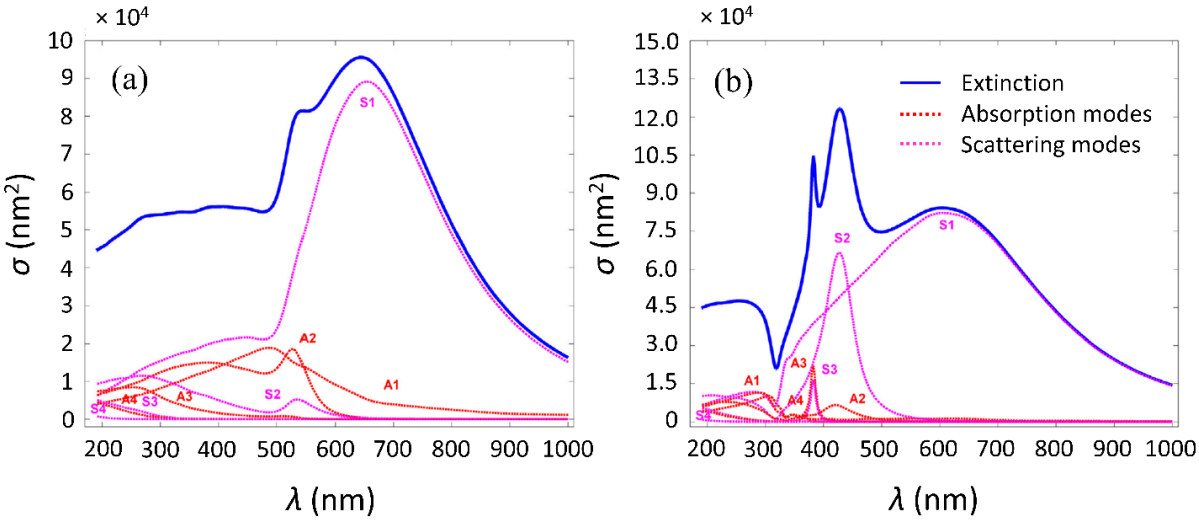

Figure 1.41. Extinction (solid blue line), absorption (solid red line), and scattering (solid pink line) cross sections calculated for (a) gold and (b) silver sphere of 150 nm diameter. The spectra are decomposed into contributions from absorption and scattering electric modes for dipole (A_1 and S_1), quadrupole (A_2 and S_2), hexapole (A_3 and S_3), and octupole (A_4 and S_4) electric mode, respectively. (From Ref. [13]).

1.3 Nanophotonic Simulations

The previous sections highlighted two main features of the optical response of metal NPs: the enhancement (and confinement) of an external radiation in their near–field zone; and the enhancement of the efficiency with which they absorb and scatter light. Both these properties are due to the excitation of LSPs. For small NPs ($a \ll \lambda$), all quantities are maxima at a specific frequency, ω_{LSPR} (or, λ_{LSPR}), which depends on the refractive index of the surrounding dielectric medium. In the general case, there are various frequencies maximizing the various quantities.

1.3.1 Simulations of $\mathrm{EF_{e.m.}}$

The former property can be "visualized" by simulations of the electromagnetic near–field intensity of metal NPs. Figure 1.5 shows two such examples for AuNPs with diameter $D = 50$ nm, run by the finite–difference time–domain (FDTD) solver toolbox of Ansys Lumerical software (which solves the full Maxwell equations). Figure 1.5a displays the case of a single AuNP in vacuum while Figure 1.5b displays the case of three AuNPs aligned on a glass substrate (in vacuum) with interparticle gap of 20 nm. In the former case, we are visualizing the near–field intensity in the quasi–static approximation (we consider $D = 50$ nm as small). Instead, the latter case provides an example of plasmon coupling among AuNPs (on a substrate). For both simulations, the external incident radiation is a x–polarized plane wave and the xz–monitors intersect the AuNPs through the centre. Johnson and Christy[14] experimental dataset was chosen for the dielectric function of gold. According to this specific dataset, the extinction λ_{LSPR} (the wavelength at which σ_{ext} is maximum) was found to be 515 nm for a 50 nm AuNP in vacuum, and the intensity profile of Figure 1.5a refers to this specific wavelength. Instead, for the simulation of Figure 1.5b, we considered the wavelength (560 nm) at which the intensity was found to be maximum.

In both cases, we clearly see the strong enhancement (and confinement) of the electromagnetic field, contingent to the excitation of LSPs. Since the result are plotted in term of $|\boldsymbol{E}/\boldsymbol{E}_0|^2$, with $|\boldsymbol{E}_0|^2$ the intensity of the external incident radiation, we are already visualizing the electromagnetic enhancement factor $\mathrm{EF_{e.m.}} \equiv |\boldsymbol{E}/\boldsymbol{E}_0|^2$. In the case of the single AuNP, we can note the typical shape of the near–field of an oscillating dipole (Figure 1.5a). Here, the max $\mathrm{EF_{e.m.}} = 17$ onto the NP surface (x=25, z=0) rapidly decays and reduces to $\mathrm{EF_{e.m.}} = 5$ at 10 nm far from the NP surface (along z=0). Instead, the three aligned AuNPs (Figure 1.5b) are close enough to allow their LSPs to couple. As a result, the $\mathrm{EF_{e.m.}}$ are even higher, with a max $\mathrm{EF_{e.m.}} = 45$ onto the

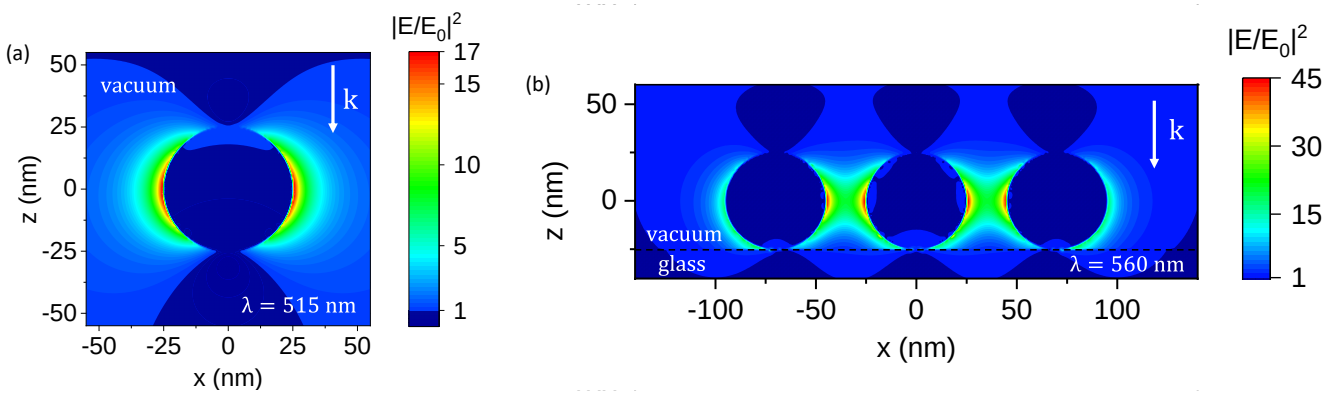

Figure 1.5 FDTD simulations of the near–field $\mathrm{EF_{e.m.}}$ (a) a single spherical AuNP with $D = 50$ nm in vacuum and (b) three spherical AuNPs with $D = 50$ nm aligned on a glass substrate, in vacuum. The incident radiation is x–polarized.

surface of the central AuNP (x=25, z=0) and $\mathrm{EF}_{\mathrm{e.m.}} = 20$ in the middle of the gap (x=35, z=0), i.e., 10 nm far from both NPs. Note that it is 4 times higher than the single particle case ("hot spot")

It is worth noting that regions with $\mathrm{EF}_{\mathrm{e.m.}} < 1$ are also present, due to energy conservation. They are localized inside the NPs, above and below the NPs, and also at the sides (beyond the frame shown). These regions are stressed by a dark blue pattern in Figure 1.5. Therefore, this type of simulations let us to visualize the interplay between the NP and the external radiation. In particular, how a NP absorbs energy from the external radiation, and how it "stores" a fraction of this energy in its near–field (before it is finally absorbed/lost inside the NP, or flow to the far field). The excitation of LSPs underlies these processes, as a fraction of the energy provided by the external radiation is absorbed by LSPs (excite the LSPs) and "stored" in the various LSPs modes.

1.3.2 Simulations of $\sigma_{abs}, \sigma_{sca}, \sigma_{ext}$

The properties of absorption and scattering of light directly determine the colour of colloidal solutions of NPs. As mentioned above, Mie actually developed his theory to explain the changes in colours exhibited by colloidal solution of AuNPs of different sizes (Figure 1.6).

Figure 1.6 Colloidal solutions of spheroidal AuNPs with diameters in the range 10–100 nm, at increments of 10 nm.

Simulations are a powerful tool for calculating the spectra of σ_{abs}, σ_{sca}, and σ_{ext}. For instance, in a recent work (Shafiqa et al., 2018),[15] the authors investigated for the first time how both σ_{abs} and σ_{sca} of single spherical AuNPs (in water) with diameters in the range 20–100 nm are affected by the excitation of LSPs. The authors utilized a MATLAB Toolbox called MNPBEM (metal nanoparticle boundary element method), available online. Full BEM simulation solver (BEMret) was chosen as it solves the simulations based on the full Maxwell equations, which works perfectly for all AuNPs dimensions. The dielectric function of gold was taken from the experimental datasets of Johnson and Christy.[14] The results are shown in Figure 1.7.

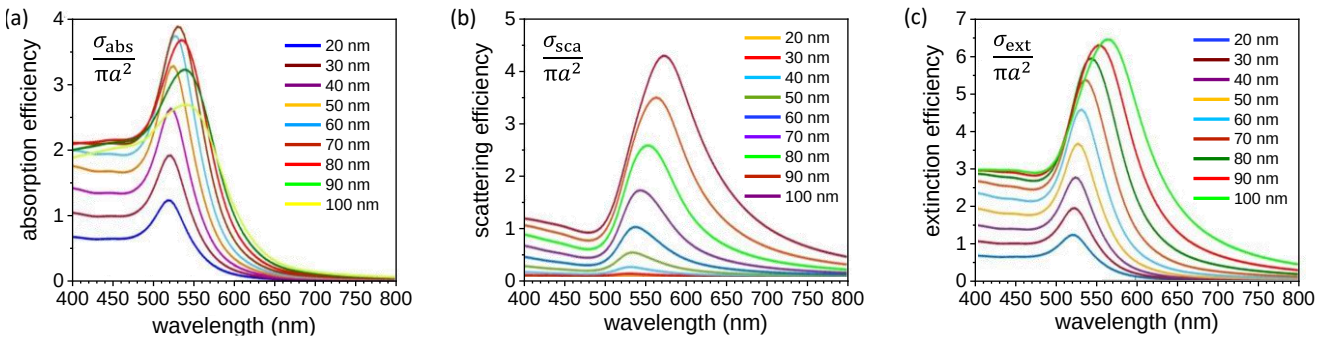

Figure 1.7. (a) Absorption, (b) scattering, and (c) extinction efficiencies of spherical AuNPs in water. (From Ref.[15])

The graphs are highly informative. Let us start with two general observations.

Experimentally, spectrophotometers are routinely employed to measure NPs transmittance spectrum T, connected to the extinction spectrum E through the Beer–Lambert law $E = -\ln(T)$. E and σ_{ext} are proportional: $E = \varepsilon_{ext} l c_{\text{M}}$, where $\varepsilon_{ext} \equiv \frac{N_{\text{A}}}{\ln(10)} \sigma_{\text{ext}}$ is the molar extinction coefficient, l is the optical path, c_{M} the sample molarity, and N_{A} Avogadro's number. Analogous relations hold for the absorption A and the scattering S. Therefore, for the "transmitted colours" of spherical AuNPs one must consider the η_{ext} spectra showed in Figure 1.7c. Instead, for the "scattered colours" (at some angle other than 0°) one must refer to the spectra η_{sca} showed in Figure 1.7b. All spectra of all AuNPs exhibit a "resonant zone" (LSPR) at optical frequencies, due to the excitation of LSPs. All LSPRs monotonically redshift for increasing NP size, explaining the changes in colours exhibited by colloidal solution of AuNPs of increasing sizes (Figure 1.5)

Secondly, we note (again) that the maxima of η_{abs} and η_{sca} spectra for a given AuNP size are associated to two *different* values of λ_{LSPR}, except for the smallest AuNPs with diameters of 20 and 30 nm (whose scattering is, however, negligible). The discrepancies between the absorption λ_{LSPR} and the scattering λ_{LSPR} can be considered small up to 50 nm, which can be assumed as the threshold above which the quasi–static approximation does not work anymore for AuNPs.

It is now worth mentioning that all results in Figure 1.6 are presented in terms of efficiencies, instead of cross sectional area. The absorption, scattering, and extinction efficiencies are:

$$\eta_{abs} \equiv \frac{\sigma_{abs}}{\pi a^2} \qquad \eta_{\text{sca}} \equiv \frac{\sigma_{\text{sca}}}{\pi a^2} \qquad \eta_{\text{ext}} \equiv \frac{\sigma_{\text{ext}}}{\pi a^2}$$

i.e., pure numbers describing the ratios between optical and geometric cross sections of a spherical NP. η_{abs}, η_{sca}, and η_{ext} allow to quantify the enhancements of σ_{abs}, σ_{sca}, and σ_{ext} due to plasmon effects. In a loose sense, $\eta_{abs} = 1$ means that the sphere is absorbing light "as expected" by a sphere of that specific geometric cross section; instead, for $\eta_{abs} < 1$ and $\eta_{abs} > 1$, it is absorbing less and more than expected, respectively. Similar considerations apply to η_{sca} and η_{ext}. The above interpretation has to be meant in a loose sense. For instance, AuNPs with diameters $\leq 40-50$ nm exhibit a negligible η_{sca}, and mainly absorb light. We could say they scatter less than expected, but actually there is not a general reference. Even for these sizes with low scattering, we can note a resonance due to LSPs. Obviously, for a non–absorbing dielectric material there is no sense to introduce η_{abs} and η_{ext} since, by definition, its σ_{abs} is always zero.

In terms of η_{abs}, η_{sca}, and η_{ext}, we can better formalize the optical consequences of LSPs excitation on the optical cross sections of NPs. The excitation of LSPs entail significant enhancements of the absorption and scattering efficiencies of the AuNPs, allowing them to absorb/scatter light significantly more than what "expected" from their geometric cross section.

Finally, the main result of the presented paper.[15] Considering the absolute maxima of η_{abs}, η_{sca}, and η_{ext} for each AuNP size, it can be noted that the maxima of η_{ext} and η_{sca} monotonically increase with the size of the AuNPs. Instead, the maxima of η_{abs} first monotonically increases with the size, then reaches a maximum for the AuNP of 70 nm, and then monotonically decrease. In other words, the AuNP of 70 nm has the highest absorption efficiency.

1.3.3 Lumerical: High-performance Simulation Software

The next chapters of this thesis include several simulations of both $\mathrm{EF}_{\mathrm{e.m.}}$ profiles and σ_{abs}, σ_{sca}, σ_{ext} of single AuNPs and AuNPs arrays. These simulations served multiple purposes. Firstly, they theoretically corroborated the experimental characterizations, such as extinction spectra and electron micrographs. For anisotropic (cubic) AuNPs colloids, they were essential for developing optical models of the "true" NPs. Secondly, simulations were useful for investigating and explaining unusual plasmonic properties exhibited by the fabricated AuNPs arrays. Lastly, simulations helped in designing a metal–enhanced fluorescence (MEF) experiment, and analyse and discuss its results.

All our simulations, like those shown in Figure 1.5, were run by the FDTD solver toolbox implemented in the Ansys Lumerical software. Depending on the specific kind of simulation, we utilized two different workspaces, schematized in Figure 1.8.

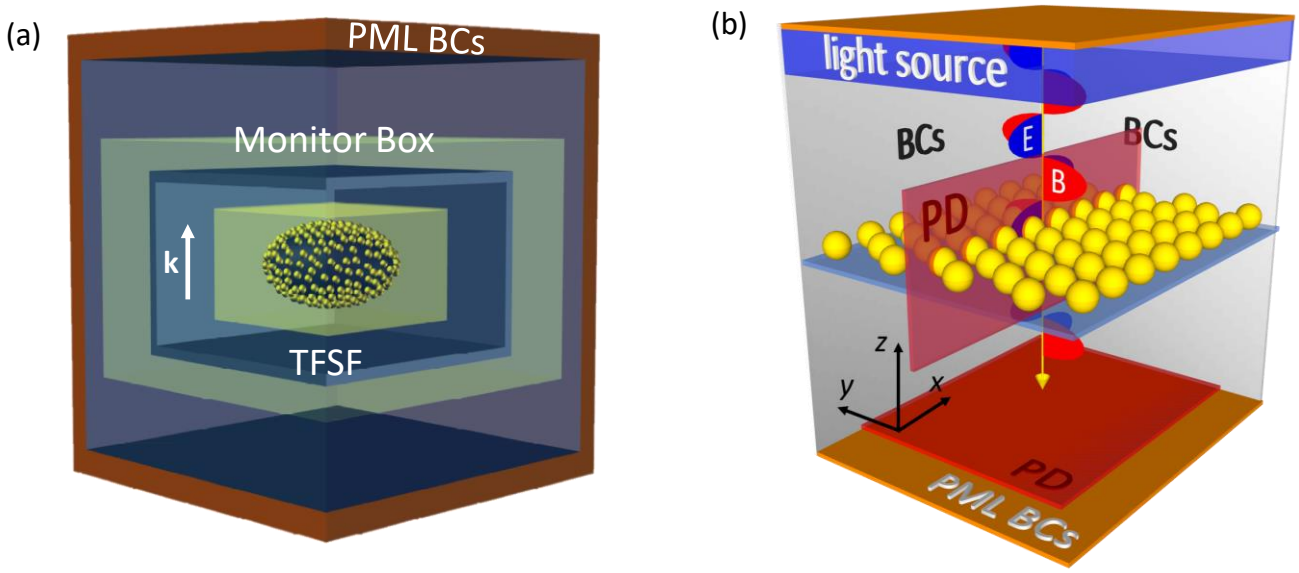

Figure 1.8. Schematic representations of the workspaces utilized for the simulation of the optical responses of (a) non extended targets (single or few NPs) and (b) extended NPs arrays (nanostructures). (From Ref.[16] and Ref.[17])

Figure 1.8a represents the so–called "Mie scattering workspace" recommended for nanophotonic simulations of non–extended scatterers (in this case, a model for a Fe_3O_4@Au core@satellite NP,[16] see next section). Instead, Figure 1.8b represents the setup we utilized for extended structures, like "infinite" NPs arrays. The Mie scattering setup was used, e.g., for the simulations of the extinction spectra of the AuNPs synthesized in Chapter 2. Instead, the extended setup was used, e.g., for the extinction spectra of the AuNPs arrays fabricated in Chapter 2. Simulations of the $\mathrm{EF}_{\mathrm{e.m.}}$ profile of single scatterers or few scatterers (like those of Figure 1.5, or Appendix F.7.1) were run by the Mie scattering workspace, while the $\mathrm{EF}_{\mathrm{e.m.}}$ profiles of AuNPs arrays (like those in Chapter 3 or Appendix F.7.2) were run by the extended object workspace.

Both workspaces are delimited (at least in one direction) by perfect matched layer (PML) boundary conditions (BCs). PML BCs serve two purposes: they act as walls delimiting the discretized region of space within which the full Maxwell equations are solved; and they act as absorbers for the radiation hitting them, thereby simulating radiation flowing outward the workspace. In practice, PML BCs are not perfect absorbers but cause back–reflections. Therefore, it is important to place

both sources and monitors at a suitable distance from PML BCs to avoid artifacts. In the Mie scattering workspace (Figure 1.8a), PML BCs are imposed in all directions. Instead, in the extended structures workspace, they are imposed only in the z–direction (parallel to the incident radiation and normal to the NP array), while periodic BCs are imposed along the other two directions to simulate an infinite array. Since the latter setup is used for nanophotonic simulations of infinite objects, at least the plane wave source (located at the top of Figure 1.8b) must also be an infinite object. In practice, this is achieved by extending the source (as well as a transmittance PD monitor of interest) beyond the walls onto which periodic BCs are imposed.

The fundamental difference between the two setups of Figure 1.8 is the source. The extended structures workspace of Figure 1.8b employs an infinite plane–wave source; instead, the Mie scattering setup of Figure 1.8a employs the so–called total–field scattered–field (TFSF) source. TFSF source is also referred to as "TFSF region" because it is, in fact, a closed box within which the non–extended scatterer must be placed. One of the facets of the TFSF region (the bottom one in the case of Figure 1.8a) serves as source of a non–extended plane wave (having the dimensions of that facet). All TFSF facets, including the one serving as source, act as electromagnetic filters and allows only the radiation scattered by the non–extended object to flow outward. For this reason, a set of monitors realizing a closed box enclosing the TFSF region will record (only) the scattered power and can be used to calculate σ_{sca}. Instead, a closed monitor box placed inside the TFSF region and enclosing the scatterer allows for the calculation of σ_{abs}. It follows $\sigma_{\mathrm{ext}} = \sigma_{abs} + \sigma_{sca}$. It is also worth mentioning that the scatterer must be placed at a suitable distance from the walls of the TFSF region to avoid that it absorbs energy from outside the TFSF, which leads to artifacts and wrong values for σ_{abs}, σ_{sca}, σ_{ext}.

The two workspaces shown in Figure 1.8 are not rigid; in particular, the monitor boxes used in the former workspace can be used (and were) also in the latter; vice versa, photodetector (PD) monitors used in the latter can be used (and were) in the former. For example, the absorbance A, the scattering *S*, and the extinction *E* can be indirectly retrieved even for extended objects by using a slight modification of the basic workspace shown in Figure 1.8b. In fact, one can enclose the extended object into a monitor box (like the one in Figure 1.8a) and then move the side monitors to infinity, extending the top and bottom monitors of the monitor box beyond the side walls with periodic BCs. Doing so, the monitor box degenerates into just two infinite monitors, one below and one above the extended object. The difference between the powers recorded by these two monitors is equal to the absorbance A of the extended object. On the other hand, the transmittance PD monitor (at the bottom of Figure 1.8b) allows to record the transmittance T and, hence, to calculate the extinction $E = -\ln(T)$. The scattering S can be obtained as $S = E - A$. This modified workspace helped us in designing the MEF experiment presented in Chapter 3.

1.3.4 Modelling of a Fe_3O_4@Au CSMP

In this section we show how nanophotonic simulations (by Ansys Lumerical) are a powerful tool both for modelling even complex NPs and for providing theoretical basis to experimentally observed phenomena. The presented material was selected from previous works by our group, Campanile et al.[16], and Marra et al. (submitted). Both works deal with biosensors benefiting from the multiple properties offered by Fe_3O_4@Au core@satellite (para)magnetic nanoparticles (CSMP),

in particular: the surface chemistry of gold, immuno–functionalized by the well–established photochemical immobilization technique (PIT) developed by our group;[18] the paramagnetic properties of Fe_3O_4 composite particles (MCPs); the plasmonic properties of AuNPs.

In both works, we employed Fe_3O_4@Au CSMPs made by PEGylated Fe_3O_4 paramagnetic MCPs (core) housing spheroidal AuNPs onto its surface (satellites). Each MCP is a cluster of small individual Fe_3O_4 crystals (diameters: 5 to 15 nm) embedded in a dextran matrix, further modified by PEG 300. Such PEGylated Fe_3O_4 MCPs were purchased from Micromod (product name: nanomag–D; product code: 09-54-252; hydrodynamic diameter: 250 nm) while spheroidal AuNPs were grafted onto the MCPs surfaces via modifications of the protocol by M. Silva et al.[19] Figure 1.9a shows TEM micrographs of the as–purchased MCPs (top panel), and CSMPs (bottom panel) synthesized according to our (first) modified protocol.[16] We can note large MCPs (measured hydrodynamic diameter of ≈ 250 nm) having highly irregular shapes, a feature quite common for this kind of composite particles.[20,21] The CSMPs exhibit small AuNPs with diameters of 15–20 nm (determined by an analysis of the micrograph). The presence of Au crystalline phase was ultimately demonstrated by X-ray diffraction (XRD) spectra of the CSMPs. However, it is also manifest in the extinction spectrum, displayed in Figure 1.9b: while the spectrum of the MCPs (solid black line) does not exhibit any peak, the CSMPs spectrum (solid red line) has a resonance at 567 nm ascribable to the excitation of LSPs of the AuNPs.

In order to corroborate the experimental results, we simulated the optical response of CSMPs in water employing the Mie scattering (Lumerical) workspace shown in Figure 1.8a. It is understood that these simulations were contingent to the modelling of both MCPs and CSMPs. The irregular shape of MCPs was modelled as a prolate spheroid with axes of 250 nm × 130 nm × 130 nm, and was optimized by simulations themselves against the MCP experimental extinction spectrum. Specifically, we kept the major axis fixed at 250 nm (the nominal value of the seller company, confirmed by DLS measurements) and varied the lengths of the other axes. The full optimization procedure and the dependence of the extinction spectra on the spheroid dimensions are discussed in the Supporting Information of our work.[16] It is worth noticing that the extinction spectrum of the model MCP was found to be quite sensitive to the model geometry; for instance, spheres of

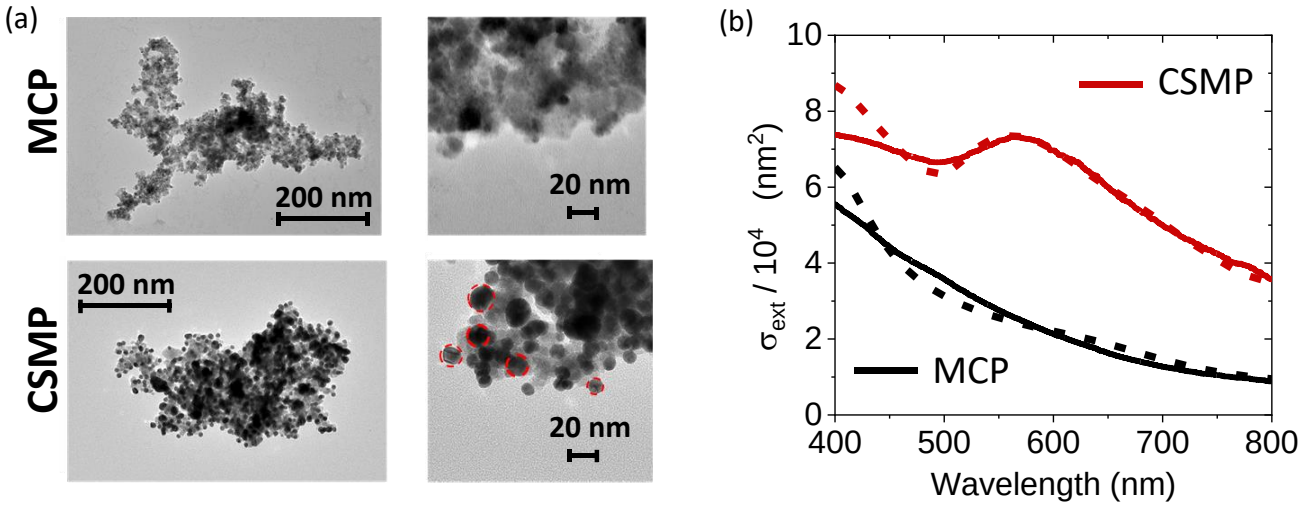

Figure 1.9. (a) TEM micrographs of bare MCPs and CSMPs at different magnifications. AuNPs are highlighted in red dashed circle. (a) Experimental (solid lines) and simulated (dashed lines) extinction spectra of MCPs and CSMPs, respectively. The extinction peak at 567 nm is due to LSPs of the AuNPs grafted onto the MCP. (From Ref.[16])

comparable diameters yielded significantly different spectra, confirming that an anisotropic shape was indeed necessary for modelling the MCP. Figure 1.9 shows the (unpolarized and orientation averaged) simulated extinction spectrum of the optimized model MCP as a dashed black line. The agreement with the experimental spectrum is very good, and the residual discrepancies ("wavy" features) are ascribed to interband transitions of the bulky Fe_3O_4 ellipsoid. It is likely that these discrepancies further reduce whenever an ellipsoid constituted by small Fe_3O_4 nanospheres is considered, so to better simulate the real substructure of MCPs. However, since the result was already satisfying, such a complex model was not investigated. For MCP simulations we chose the Fe_3O_4 dielectric function from Querry,[22] and a mesh size of 2 nm.

The model CSMP was then obtained by placing spherical AuNPs with diameter of 15 nm (suggested by the analysis of the TEM micrographs) randomly onto the surface of the model MCP, in such a way that their centre-to-centre distances were at least 15 nm (we used a Python code). Johnson and Christy[14] dataset for gold dielectric function was used, and a 2 nm mesh. The excellent agreement shown in Figure 1.9b (dashed black line) was achieved with a degree of covering of 85% (260 AuNPs). This final CSMP model is the scatterer depicted in Figure 1.8a. This result corroborated the claim that our CSMPs are made of MCPs coated by AuNPs with a high degree of covering, an ideal target for the magnetoresistive biosensor proposed by Campanile et al.[16]

In a subsequent work by Marra et al. (submitted) the CSMP synthesis protocol has been further modified to obtain sharper extinction LSPRs, making the CSMPs more suitable for applications in colorimetric biosensing. Figure 1.10a shows TEM micrographs of the as–synthesized CSMPs, whose meticulous analysis revealed bigger spheroidal AuNPs with normally distributed diameters $D = 28 \pm 4$ nm. As a consequence, the normalized experimental extinction spectrum (solid black line in Figure 1.10b) exhibited a significantly sharper LSPR, and slightly redshifted at 572 nm. The LSPR peak is higher than the extinction at 400 nm, whereas in the previous case it was the opposite.

In order to corroborate the experimental results, we simulated the optical response of the new CSMPs. Spherical AuNPs were now placed onto the model MCP surface according to the experimental Gaussian distribution of diameters ($D = 28 \pm 4$ nm). Instead, the centre–to–centre

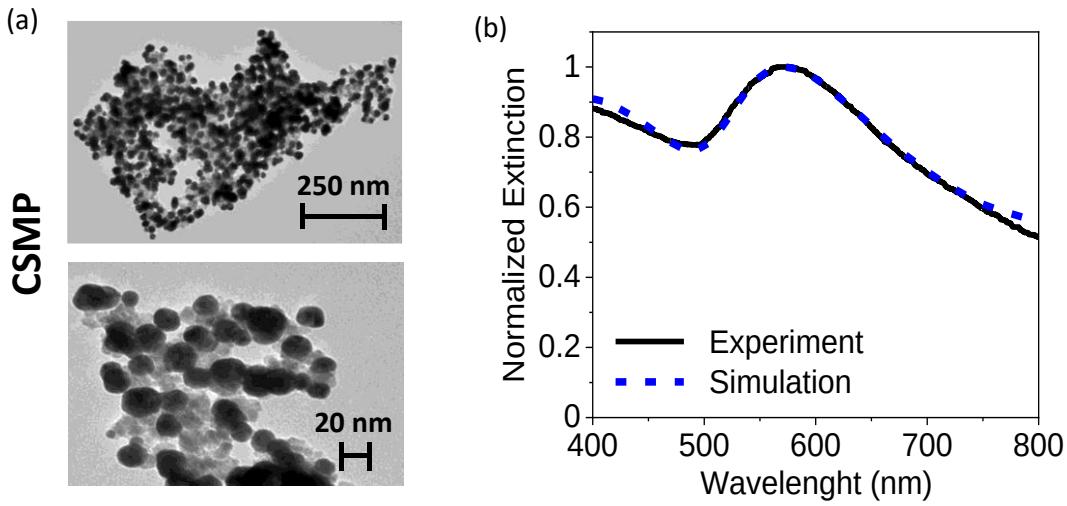

Figure 1.10. (a) TEM micrographs of CSMPs (optimized protocol) at different magnifications. (b) Experimental (solid black) and simulated (dashed blue) normalized extinction spectra of CSMPs (optimized protocol), respectively.

distances between AuNPs were optimized against the experimental spectrum, resulting in an optimal mean value of 29 nm. The degree of covering associated with all these parameters was approximately 100% (105 AuNPs), consistent with the high degree of covering shown by the TEM micrographs. It is worth noting that these parameters allowed to reproduce the observed overlap among AuNPs in the TEM micrographs, a feature resulting from the in–situ growth of pre–grafted gold seeds. The model CSMP used for these simulation is shown in Figure 1.12a (top–left).

These optimized CSMPs, functionalized by PIT,[18] served as active element of a colorimetric immunosensor for the rapid and sensitive detection of gliadin in gluten flour–based food products. The biosensor exhibited a high sensitivity in the range 5–50 ppm reaching a limit of detection (LOD) of 10 ppm for gliadin, which is below the legal threshold for labelling a product as gluten-free (20 ppm). Remarkably, the gliadin extraction protocol utilizes a non–toxic ethanol–water mixture, does not require trained personnel, and lasts only 20 min (total assay time: 30 min).

A peculiar feature of the proposed colorimetric biosensor is its disaggregation–based sensing scheme, rather than the usual aggregation–based scheme.[6] We found that a suitable concentration of the surfactant Tween–20 leads to the spontaneous formation of uniformly sized, stable, and weakly–bound clusters[23,24] of functionalized CSMPs (f-CSMP). The corresponding extinction spectrum is shown as a solid black line in Figure 1.11a (control experiment). This colloid, rich in surfactant–induced f-CSMP clusters, is responsive (exclusively) to gliadin, as a monotonic increase in the extinction is observed for increasing concentrations of gliadin (Figure 1.11a). When the extinction spectra are normalized with respect to the maxima, a monotonically decreasing trend is observed at long wavelengths for increasing gliadin concentrations, see Figure 1.11b. Therefore, the analysis of these two trends suggests that the monotonic increase of extinction for increasing gliadin concentration (Figure 1.11a) is due to the fragmentation of the initial surfactant–induced f-CSMP clusters (Figure 1.11b).

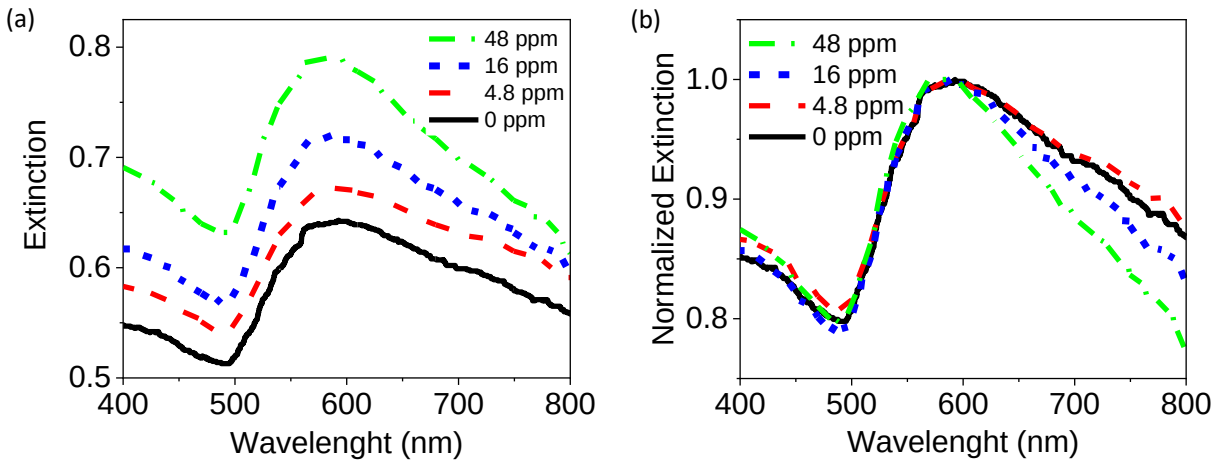

Figure 1.11. (a) Extinction spectra relative to gliadin detection, exhibiting a monotonically increasing trend for increasing gliadin concentrations and (b) corresponding normalized spectra, exhibiting a monotonically decreasing trend for increasing gliadin concentrations at long wavelengths. The two graphs suggested a mechanism of disaggregation of CSMP clusters due to gliadin detection.

In order to provide a theoretical support to our hypothesis, we investigated the optical response of CSMP clusters. To ensure manageable simulation times, we limited ourselves to consider only the

'reasonable' clusters shown in Figure 1.12a when their longitudinal axes were parallel to the external light polarization. For these simulations we used the Mie scattering workspace shown in Figure 1.8, and a mesh size of 2 nm.

The results are presented as the ratios:

$$R \equiv \frac{\sigma_{ext}^{cluster}}{n\,\sigma_{ext}^{sub-specie}}$$

between the σ_{ext} of a CSMP cluster and the σ_{ext} of one of the species potentially resulting from its complete fragmentation. Here, n just indicates the number of identical sub-species resulting from the complete fragmentation of the considered cluster. For instance, a 4-mer can be split into $n = 2$ dimer or $n = 4$ monomers. It is readily seen that $R < 1$ indicates that the fragmentation of the cluster results in the increase in extinction, while $R > 1$ a decrease in extinction.

We can see from Figure 1.12b that the complete fragmentation of a 2–mer of CSMPs into two single CSMPs (dashed black line) increases the extinction only in the range 400–600 nm, whereas the experimental spectra of Figure 1.11a show that the extinction increases across the entire optical range (compared to the control experiment). However, when a 4–mer of CSMPs splits into 2 2–mers (dotted magenta), or when an 8–mers is fragmented into 2 4–mers (solid red), 4 2–mers (solid green), and even 8 single CSMPs (solid blue), the extinction increases (as $R < 1$).

Therefore, these latter simulations theoretically supported the proposed mechanism. The effect is due to a decreased scattering contribution of a CSMP cluster compared to the sum of the scattering contributions of the corresponding sub-species, as clusters have inner surfaces shielded from the external electromagnetic radiation.

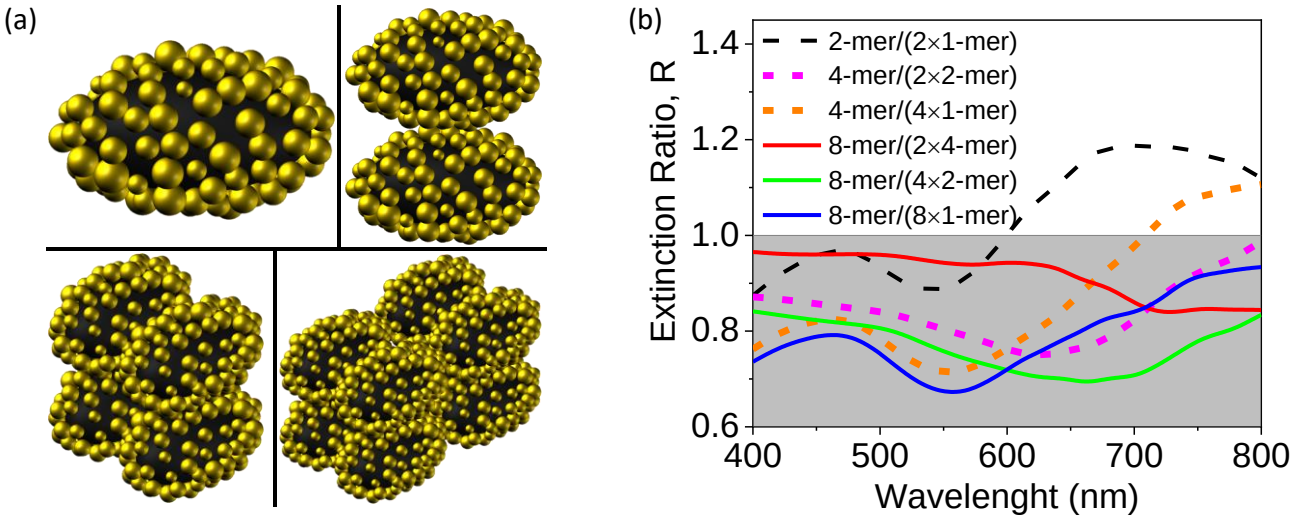

Figure 1.12. (a) Models of CSMP and CSMP clusters used for simulations: 1-mer (CSMP), 2-mer, 4-mer and 8-mer. (b) Ratios R between the simulated extinctions of 2-mer (black dashed), 4-mer (dotted), 8-mer (solid) and corresponding subspecies possibly resulting from their disaggregation. Since $R < 1$ indicates an increase of extinction due to cluster disaggregation, the proposed mechanism is theoretically supported.

Chapter 2. Nanofabrication

2.1 Turkevich's Inherent Seed–mediated Growth Dynamics

The most commonly used method for synthesizing colloidal AuNPs in aqueous solution is the reduction of tetrachloroauric acid ($HAuCl_4$) with trisodium citrate (Na_3Ct). The citrate method was first described in the textbook "Experiments in Colloid Chemistry" by Ernst A. Hauser and J. Edward Lynn, published in 1940.[25] However, it gained interest after Turkevich et al.[26] modified and deeply investigated the synthesis in 1951. Nowadays, "Turkevich's methods" has become a synonymous for citrate method. Sometimes it is called "Turkevich–Frens method", as Frens[27] (in 1973) provided specific Na_3Ct concentrations for synthesizing AuNPs with sizes up to 150 nm.

The protocol consists in adding Na_3Ct to an aqueous solution of $HAuCl_4$ at or near the boiling point, and waiting for a few minutes for NPs formation. This simplicity of the protocol actually hides a complex dynamics. Turkevich himself identified at least two stages: a first stage, which he called "nucleation"; and a second stage of growth. Remarkably, these two stages were found to be distinct. During the "nucleation" stage, small AuNPs with mean diameters $\overline{D} = 6$ nm and $\overline{D}_{min} = 3$ nm form (as confirmed by subsequent studies[28]). These particles, technically, are not "nuclei", a term which refers to the first thermodynamically stable clusters made of only few tens of atoms. Instead, they must be termed as *seeds* (made by $10^2 - 10^3$ atoms). Therefore, during the first stage, and only during this stage, gold seeds are formed (see Figure 2.0.1); subsequently, this fixed amount of seeds grow. For this reason, Turkevich's synthesis is actually characterized by an inherent seed–mediated growth dynamics.

Turkevich's seed mediated growth mechanism is a lucky coincidence created by a favourable interplay of different chemical processes. Figure 2.0.1 and 2.0.2, taken from Wuithschick et al.,[28] summarize the complex dynamics of a "standard" synthesis.[28] Before mixing, the $HAuCl_4$ solution contains a certain amount of $[AuCl_4]^-$ ions (pH 3.3). Upon addition of Na_3Ct, the buffer effect of Na_3Ct increases almost immediately (~ 1 s) the pH to ~6.5, and this new pH condition transforms the reactive $[AuCl_4]^-$ species into less reactive hydrolysed $[AuCl_{3-x}(OH)_{1+x}]^-$ species (see Figure 2.0.1). However, this fast process (~ 1 s) lasts enough to trigger the fast generation of a small but sufficient amount of Au^0 monomers from the reduction of $[AuCl_4]^-$. Au^0 monomers then form few (trillions of) small, stable seed particles (diameter $D > 3$ nm). The transformation of the reactive $[AuCl_4]^-$ into the less reactive $[AuCl_{3-x}(OH)_{1+x}]^-$ also blocks a further supply of Au^0 monomers in solution which could form more seeds or grow onto already existing seeds in uncontrolled way.

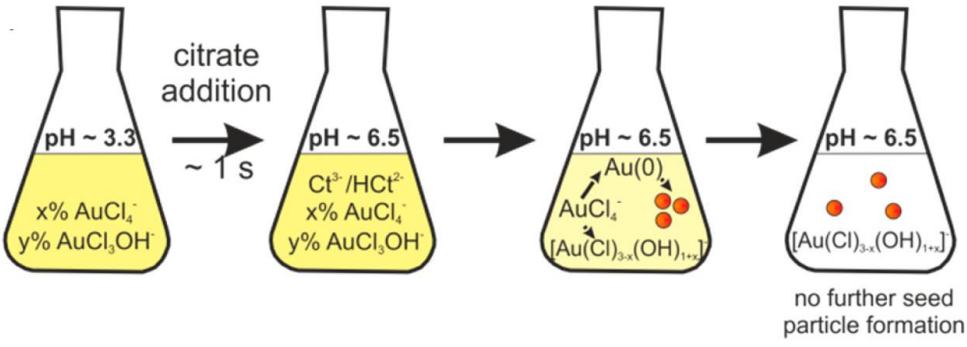

Figure 2.0.1. (c) Sketch of chemical processes during seed particle formation. See the text for details. (From Ref.[28])

The shift of the gold complexes equilibrium from $[AuCl_4]^-$ to $[AuCl_{3-x}(OH)_{1+x}]^-$ terminates the seed particle formation stage (~ 1 s after Na_3Ct addition), left panel of Figure 2.0.2. The resulting number of seeds is fixed (will not increase in later times, corresponds to the final AuNPs number).

It is worth mentioning that the kinetics of the hydrolysation of $[AuCl_4]^-$ into $[AuCl_{3-x}(OH)_{1+x}]^-$ and the kinetics of the reduction of $[AuCl_4]^-$ to Au^0 determine the amount of Au^0 monomers available for the seed particles formation. Both kinetics depend (non–trivially) on temperature and reagents concentrations. Seeds size defines how many seeds can be formed from the available $[AuCl_4]^-$ ions ($\leq 5\%$ of $HAuCl_4$ is reduced to Au^0). The resulting number of seeds determines the final size of the AuNPs: in fact, the residual gold ($\geq 95\%$), which is constituted by $[AuCl_{3-x}(OH)_{1+x}]^-$ species not reactive enough to be reduced to seeds, are attracted by the seeds, enrich the seed electronic double layer, and are reduced exclusively onto the seed surfaces, which then grow (right panel of Figure 2.0.2). Thus, more seeds means smaller AuNPs.

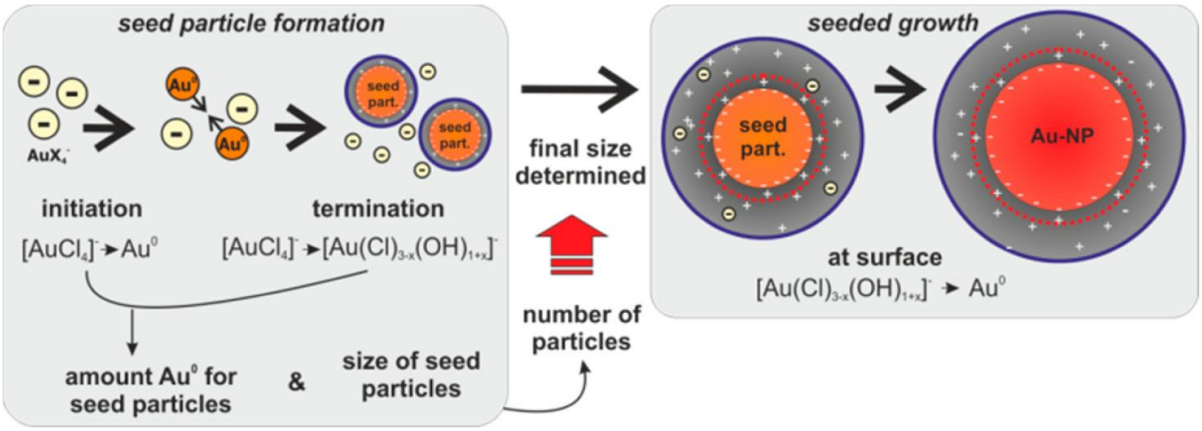

Figure 2.0.2. Summary of growth process and the underlying chemical processes of Turkevich synthesis. (From Ref.[28])

To be pragmatic, here follows the standard synthesis studied by Wuithschick et al.:[28] 199 mL of a 0.25 mM $HAuCl_4$ solution is warmed at specific temperatures under reflux for 15 min. Then, 1 mL of a 500 mM freshly prepared Na_3Ct solution is added quickly (final concentration $[Na_3Ct]$ = 2.5 mM). The solution is refluxed until ruby red. Figure 2.0.3 illustrate part of the study.

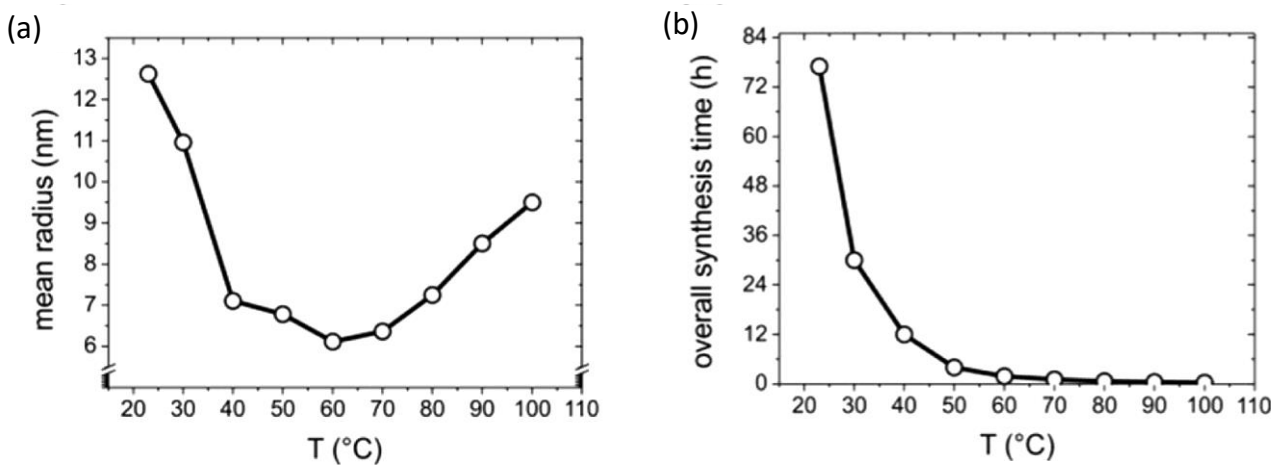

Figure 2.0.3. Results of temperature variation study. (a) Mean radii (polydispersity = 25% at 20 °C, 20% at 30 °C, rest 10%). (b) Overall synthesis time *versus* temperature determined by observing the color change of the reaction solution

From this perspective, the modern seed–mediated growth methods have rationalized the two fundamental stages (seed formation and seed growth), splitting them in separated reactions thanks to chemicals serving for each specific task.

2.2 Isotropic and Anisotropic AuNPs *via* Seed–mediated Methods

This section covers the synthesis and characterization of both isotropic (nanospheres) and anisotropic AuNPs obtained through seed–mediated growth methods. We embraced Mirkin's philosophy of renewed attention towards the quality of the NPs reactants ("seeds") to achieve unprecedented yields ($> 95\%$) and uniformity of the NPs products, all from a single source of monocrystalline seeds.[29] According to the method, single–crystal seeds are refined through a cyclical process of reductive growth and oxidative dissolution, which together narrow seeds size and shape distributions at each cycle, and soon yield spherical and monodisperse seeds, see Figure 2.1a. The dissolution step is at the core of Mirkin's method as it "chemically polishes" the seeds through the following redox reaction, first reported by Liz-Marzán:[30]

$$\mathrm{AuCl_4}^- + 2\ \mathrm{Au}^0 + 2\ \mathrm{Cl}^- \leftrightharpoons 3\ \mathrm{AuCl_2}^-.$$

$\mathrm{AuCl_4}^-$ and Cl^- result from the salt precursor $\mathrm{HAuCl_4}$ in water, and Au^0 are metal atoms of a AuNP. This reaction has equilibrium constant $K = 1.9 \times 10^{-8}$, i.e., it is highly unfavourable and the oxidation of AuNPs by gold chloride negligible. However, K increases by a factor $\geq 10^9$ in presence of the cationic surfactant cetyltrimethylammonium bromide (CTAB). Above the critical micelle concentration of ≈ 0.9 mM,[31] CTAB forms micelles, and both $\mathrm{AuCl_4}^-$ and $\mathrm{AuCl_2}^-$ electrostatically adsorb onto them creating $\mathrm{AuCl_4}^-/\mathrm{CTAB}$ and $\mathrm{AuCl_2}^-/\mathrm{CTAB}$ complexes. These complexations drastically change the reduction potential of gold chloride, allowing the oxidation process.

Oxidative dissolution was found to be irrespective of AuNPs shape while occurring preferentially at NP surface sites with lower radius of curvatures,[30] as in Figure 2.1b. However, the demand for large amounts of single-crystalline seeds led to the choice of gold nanorods (NRs) as the starting NP to be iteratively refined. AuNRs are indeed monocrystalline and can be synthesized in high yield (>95%), too.[32] Few iterations of reductive growth and oxidative dissolution over a batch of AuNRs result in the desired monocrystalline and monodisperse spherical seeds, as depicted in Figure 2.1a. Iterations were even unnecessary in our case, and the final seeds were obtained through just one dissolution step over the AuNRs, saving time and reagents.

The seeds produced through AuNRs refinement are capped by CTAB. However, the seed-mediated growth methods used for the synthesis of anisotropic NPs require the cationic surfactant cetylpyridinium chloride (CPC) both as capping agent of the single-crystalline seeds and for the growth solutions.[33] A surfactant exchange is therefore accomplished by multiple rounds of centrifugations and resuspensions by concentrated CPC solution. This step is paramount to avoid undesired dissolutions of the NPs products due to trace residues of gold and CTAB.

CPC properties as surfactant are finally used to synthesize anisotropic AuNPs. For our scopes, we limited to concave rhombic dodecahedra (CRD) and nanocubes (AuNCs), according to Niu's protocols with slight modifications.[29,33] Despite a little debate about the "true" geometry,[33–36] CPC certainly stabilizes energetically unfavoured crystallographic facets of gold. It is worth recalling that

the surface energy of the primary low-index crystallographic facets of gold increase in the order $E\{111\} < E\{100\} < E\{110\}$, meaning that {110} facets are the most energetically unstable. In the case CRD were perfect rhombic dodecahedra,[33] they would be bound by 12 rhombic {110} facets, indicating that CPC does adsorb to such facets, reduces their energy, and stabilize them. If CRD were trisoctahedra,[36] they would be bound by high-index facets {211}, and CPC action would hold *a fortiori*. According to his experiments, Niu[33] concluded that CPC alters the surface energy of the low-index gold facets ordering them as $\mathrm{E}\{111\} < \mathrm{E}\{110\} < \mathrm{E}\{100\}$, as gold nanocrystals bounded by {100} facets were not observed at all in the presence of CPC alone. Only when KBr was included in the growth solution were NCs (ideally bound by 6 {100} facets) synthesized, as the cooperative work of CPC and bromide ions actually serves to stabilize the {100} facets.

This is quite a general thing. Cationic surfactants based on quaternary ammonium cations do not adsorb directly onto a gold surface, rather via their halide counterions.[37,38] In principle, a bare gold surface can only have Au atoms from its crystal lattice, therefore it would be positively charged due to unsaturated sites occupied by Au^{+} and Au^{3+}. As a consequence, a cationic specie cannot electrostatically adsorb onto gold directly and an anionic layer is necessary as mediator. For CTAB–capped AuNRs, the anionic layer includes at least the counterion bromide Br^{-} of CTAB and, likely, other anions present in the growth solution,[39] and the CTA^{+} cations electrostatically adsorb onto the AuNRs *via* this anionic layer. For CPC–capped seeds, the anionic layer is provided by its chloride counterions. In our case, CTAB–capped seeds are converted in CPC-capped seeds by a surfactant exchange, which then serve to exchange both the mediator anion layers, Br^{-} with Cl^{-}, and the surfactants, CTA^{+} with CP^{+}.[33] Finally, in the synthesis of AuNCs from $(\mathrm{CP}^{+}/\mathrm{Cl}^{-})$–capped seeds, the addition of KBr to the growth solution realizes the exchange of Cl^{-} with Br^{-} since Br^{-} has a higher affinity for gold than Cl^{-}.[33] In a solution–phase synthesis, all adsorbates can interact selectively with the crystal facets changing their energies, thus determining the faith of the synthesis.[33]

Many researchers actually focused on reaction conditions (e.g., presence of trace metals, ligand affinity) to control "what happens on the gold surface". However, this is not sufficient to have full control over the NP products because the specific type of seeds is paramount, too. Niu's study of NCs provides a good example of this:[33] even using exactly the same reaction conditions, different types of seeds yielded different results, and AuNCs were effectively synthesized only when relatively big, monocrystalline, and $(\mathrm{CP}^{+}/\mathrm{Br}^{-})$–capped seeds were used. This stress once more the importance of seeds quality and refinement, i.e., the philosophy we embraced.

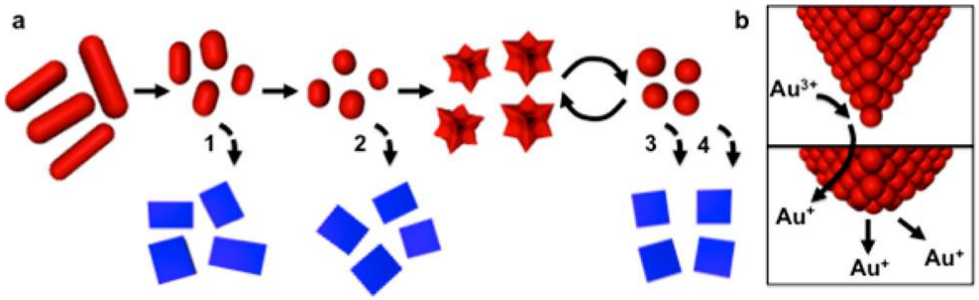

Figure 2.1. (a) Schematics of the process of reductive growth and oxidative dissolution used to refine the seeds. Single crystalline AuNRs are first etched into spheroidal seeds, then grown into CRD, and again etched into spherical seeds. The latter two steps can be reiterated to improve seed quality and, consequently, the quality of the AuNPs products (e.g., NCs). (b) Conceptualization of the oxidative dissolution process: CTAB micelles first carry $\mathrm{AuCl_4}^{-}$ (Au^{3+} in figure) towards a AuNP site with low radius of curvature (a sharp tip, in this case) and then sequester the oxidation product $\mathrm{AuCl_2}^{-}$ (Au^{+} in figure) from it, resulting in an overall smoothing of that NP site. (From Mirkin[29])

2.2.1 Synthesis of CPC–capped Gold Seeds

The initial CTAB-capped gold seeds and the AuNRs were obtained as detailed in Appendix A.1 and A.2, respectively, and their typical UV-Vis spectra are displayed in Figure 2.2a and b. A comparison with Mirkin's[29] NRs revealed that ours had the same transverse LSPR at ≈512 nm but a significantly blueshifted longitudinal LSPR (l-LSPR), at ≈700 nm rather than ≈760 nm. This indicates that our NRs had a lower aspect ratio (AR). As shown by El-Sayed,[32] AuNRs AR can be tuned depending on the $AgNO_3$ content, therefore a first possibility is that we used (freshly prepared) $AgNO_3$ of a different purity grade. Alternatively, AR can be controlled by the amount of seed solution added. Even using the same volumes, minor variations in seeds size and/or concentration may still alter the molar ratio between seeds and other reagents (e.g., $AgNO_3$) of the growth solution. Therefore, a second possibility is that our CTAB-capped seeds differed from Mirkin's, either due to the quality of $NaBH_4$ (reducing agent for the seeds) or a different way of preparing it (see Appendix A.1). However, the discrepancy between ours and Mirkin's AuNRs resulted to be advantageous, and merely demanded a study to figure out the proper concentration of gold to be used for their dissolution.

Small-volume test batches (0.5 mL AuNRs at OD 2) were then etched by a final $HAuCl_4$ concentration ranging over 60–95 μM, under gentle stirring for 4 h at 40°C. The resulting NPs exhibited the spectra displayed in Figure 2.2c. As gold concentration is increased, the aspect ratio of the AuNRs decreases until a spherelike geometry is reached. This is indicated by the transition from two well-separated LSPRs to only one at lower wavelengths (black to green lines). Slightly higher concentrations of gold further refine the spheroidal NPs into nearly spherical NPs, and both a further blueshift of the LSPR and a narrowing of the FWHM is observed (blue and orange lines). The optimal gold concentration is reached just before the FWHM starts to increase and the LSPR red-shift again.[29] Indeed, above the optimal gold concentration, the oxidative dissolution process competes with the reduction of liberated gold and results in a greater NPs size variation. In our case, no further LSPR blueshift nor its narrowing were observed at 90–95 μM $HAuCl_4$ (orange and magenta lines), whereas a lower yield was observed at 95 μM $HAuCl_4$. Therefore, we concluded that the optimal concentration for dissolution was 90 μM $HAuCl_4$ in our case, as in Mirkin's case.

The final CPC–capped gold seeds were then obtained by dissolution of AuNRs at 90 μM $HAuCl_4$ as detailed in Appendix A.3, and the typical UV-Vis spectrum of the colloid is displayed in Figure 2.2d. It is worth mentioning that Mirkin's procedure[29] prescribes at least one additional refinement of these seeds to improve their quality, e.g., to reduce polydispersion and increase circularity. The procedure would first let the seed growth to small CRD ("CRD6000" according to our terminology, see Appendix A.4) and then etch them back to spherical seeds. However, no improvements were observed after the additional refinement, as the UV-Vis spectrum of the refined seeds was perfectly overlapped to the spectrum of the starting seeds (Figure 2.2d). Remarkably, the lack of improvements could not be ascribed to a wrong implementation of the procedure, rather to the already higher quality of our seeds, as confirmed by a comparison of ours and Mirkin's seeds at the same stage (i.e., before the first refinement). We believe that our seeds had higher quality because our AuNRs were smaller than Mirkin's, therefore the (first) dissolution process was more effective in our case. Since the major improvements in seed quality occur after the first cycle of refinement,[29] we considered the NPs reported in Figure 2.2d as the final CPC–capped seeds.

The CPC–capped seeds could be used to synthesize many kinds of polyhedral NPs.[29] For our MEF study, we considered nanospheres (NSs) (obtained from the dissolution of concave rhombic

dodecahedra, CRD); and nanocubes (NCs). NSs will serve as reference; instead, the anisotropic cubic shape was chosen for the simultaneous abundance of sharp features entailing high field enhancements, and large flat facets for a strong and stable binding onto solid substrates.

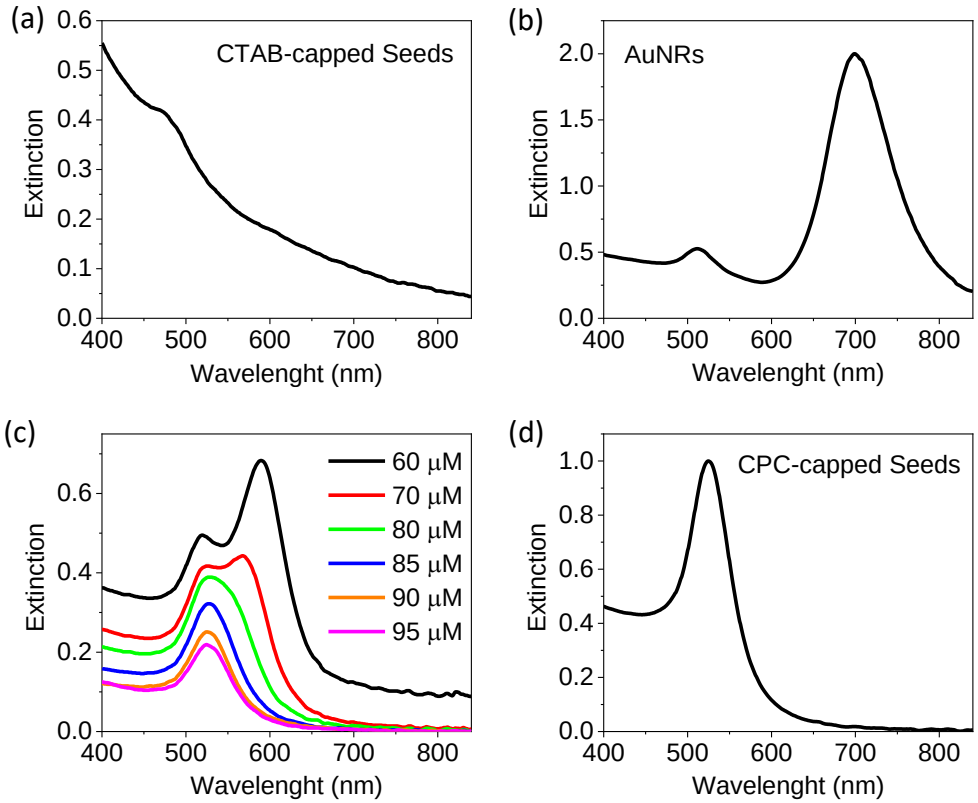

Figure 2.2. (a) Typical extinction spectrum of the initial CTAB–capped seeds for AuNRs synthesis. (b) Typical extinction spectrum of AuNRs at OD2 in 50 mM CTAB prior to the oxidative dissolution step. (c) Dissolution of AuNRs at various final concentrations of $HAuCl_4$. The optimal one was found to be 90 μM (orange line) since no further LSPR blueshift nor FWHM narrowing were observed at higher concentrations. (d) Final CPC–capped seeds at OD 1 in 100 mM CPC.

2.2.2 Synthesis of Gold Nanospheres (AuNSs)

Large (≈100 nm) AuNSs were obtained after a methodical study of both CRD growth and dissolution. In fact, according to the method,[29] the maximum dimension of the etched NP cannot exceed, roughly, the minimum dimension of the NP undergoing dissolution. Therefore, both steps must be performed and considered alongside each other.

CRD were synthesized as detailed in Appendix A.4, spanning from CRD500, i.e., CRD obtained from the growth of 500 μL of final seeds (at OD1 in 100 mM CPC), down to CRD100. Preliminary dissolutions identified the CRD200–CRD100 range as the interesting interval. Figure 2.3a displays the normalized extinction spectra of CRD200 (black), CRD180 (red), CRD140 (green), and CRD100 (blue). It is worth noting how the mean sizes could be finely tuned (increased) by slight variations (decreasing) in the amount of seeds, as indicated by their LSPR wavelengths: 630 nm for CRD200; 637 nm for CRD 180; 647 nm for CRD140; and 658 nm for CRD100. In order to determine the optimal dissolution conditions for such CRD, small-volume test batches of CRD200 were independently etched at final $HAuCl_4$ concentrations ranging from 0.1 to 100 μM, following the general procedure detailed in Appendix A.5. Figure 2.3b shows the relevant normalized extinction

spectra of the etched CRD200. A significant blueshift of ≈ 50 nm (w.r.t. CRD200) already occurred at the relatively low gold concentration (in the final volume) of 0.1 µM (red line), demonstrating that even trace amounts of gold can initiate the dissolution process of large NPs (whenever CTAB concentration is 50 mM). As mentioned earlier, this underscores the necessity for meticulous removal of excess reagents (especially CTAB and gold) through resuspension steps. A subsequent major blueshift of ≈ 17 nm (w.r.t. 0.1 µM) was then observed at 1 µM $HAuCl_4$ (green line), followed by minor relative blueshifts as the gold content was increased from 10 to 100 µM (cyan to black). The overall progression of the LSPR wavelengths was as follows: 630 nm for CRD200 before dissolution (black dotted); 581 nm at 0.1 µM $HAuCl_4$ (red); 564 nm at 1 µM (green); 561 nm at 10 µM and 20 µM (cyan and blue); 557 nm at 40 µM (orange); 555 nm at 100 µM (black solid). Since no changes were observed from 10 µM to 20 µM $HAuCl_4$, and further alterations were noted only after doubling this concentration, we concluded that 20 µM $HAuCl_4$ was an optimal choice for the dissolution of CRD200. Furthermore, according to Mirkin,[29] larger CRD generally require lower concentration for dissolutions. As a consequence, 20 µM was employed to etch all CRD, from CRD200 to CRD100, according to the protocol outlined in Appendix A.5. The corresponding normalized extinction spectra are displayed in Figure 2.3c. The concentration of surfactant CTAB is 50 mM for all. These NPs were termed as NSs200 (black), NSs180 (red), NSs140 (green), and NSs100 (blue) since electron micrographs did confirm their spherical shape. The corresponding LSPR wavelengths were: 560 nm for NSs200, 567 nm for NSs180, 581 nm for NSs140, and 584 nm for NSs100, respectively, confirming that virtually any size of NSs can be obtained by this method.

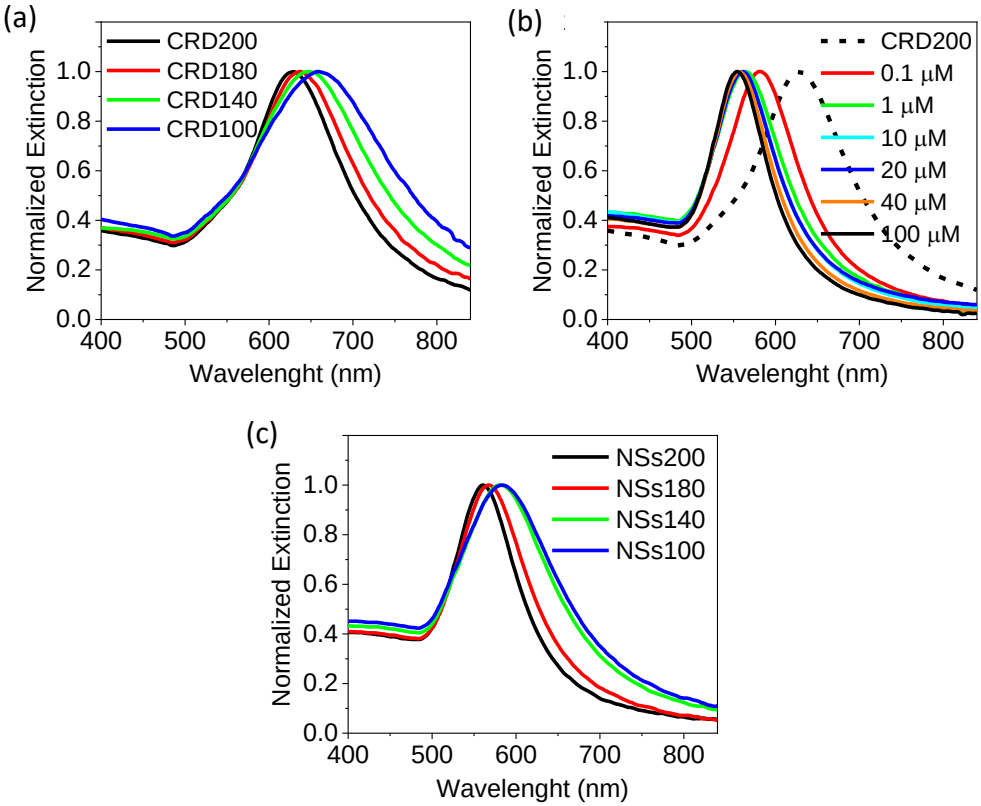

Figure 2.3. (a) Typical normalized extinction spectra of CRD200 (black), CRD180 (red), CRD140 (green), and CRD100 (blue). (b) Dissolution of CRD200 (dashed black) at $HAuCl_4$ concentrations ranging over 0.1—100 µM. The optimal concentration was considered to be 20 µM (blue). (c) AuNSs200 (black), AuNSs180 (red), AuNSs140 (green), and AuNSs100 (blue) obtained, respectively, from dissolution of CRD200, CRD180, CRD140, and CRD100 at 20 µM $HAuCl_4$.

For our MEF studies, our focus was on AuNSs140, which served as reference.

2.2.2.1 Morphological and Optical Analysis of AuNSs140

AuNSs140 were morphologically characterized by FEI Magellan scanning transmission electron microscopy (STEM) after immobilization onto a glass substrate (discussed in section 2.3). Prior to imaging, the samples underwent iridium sputtering (60 s, 25 mA). This sputtering produced an iridium layer with a nominal thickness of 6 nm, confirmed experimentally once and for all by a focused ion beam (FIB) cut shown in Appendix C.3. The analysis did consider this layer.

Figures 2.4a and b display typical top–view and tilted STEM micrographs at high magnification (250'000x) of AuNSs140, respectively. At first glance, they show large NPs (≈100 nm) with a spherical shape and no residual features of CRD. This demonstrates that the concentration of 20 µM $HAuCl_4$ chosen for the dissolution step guarantees a complete dissolution of the CRD140. In contrast, when $HAuCl_4$ concentration was too low, NPs did exhibit residual features of CRDs, as shown in Appendix F.1.

The quantitative analysis of shape and size was conducted on a top–view STEM micrograph at lower magnification (the one from Figure 2.15a of Section 2.3.2) to consider a sample of more than 550 NPs. Figure 2.4c and d show the corresponding distributions of aspect ratio (AR) and circularity (C), obtained directly by "Analyze particle" tool implemented in ImageJ (see Appendix C.1 for further details). Both distributions confirm the exceptional sphericity of the NPs, being the mean values $\overline{AR}$ = 1.05 ± 0.03 and $\bar{C}$ = 0.94 ± 0.02, respectively. We can then classify the AuNSs140 as spherical NPs and consider their diameter distribution. In this case, since diameter is crucial for simulations, we did consider the sputtering layer. The particles visible in the micrographs are, in fact, enclosed in a 6 nm thick iridium shell from the sputtering. Therefore, we first calculated the diameters $D^* = 2\sqrt{S/\pi}$ for the circular objects visible in the micrograph, where S is the area of each object as provided by the "Analize particle" tool. Subsequently, we determined the AuNSs140 diameters as $D = D^* - 12$ nm. The resulting distribution is presented in Figure 2.4e and is well-fitted by a Gaussian with mean diameter $\overline{D}$ = 104 nm and a remarkably narrow standard deviation $\sigma = 2$ nm. AuNSs140 are single-crystalline, spherical and monodisperse NPs.

These features are particularly suitable for simulations, as the simulated spectrum of a single nanosphere actually serves as a theoretical prediction for a perfectly monodisperse colloid (up to a normalization factor). Consequently, the extinction spectrum of a single gold sphere with diameter 104 nm was simulated and compared with the experimental spectrum of the AuNSs140 colloid. To closely mimic the real scenario, a series of technical adjustments were implemented. First, Olmon's dataset for single–crystalline gold was utilized,[40] our AuNSs being monocrystalline as per the synthesis method. Secondly, the AuNS was enclosed in a 3 nm thick CTAB shell of refractive index $n = 1.4350$,[41–43] replicating the well-known capping by a CTAB bilayer. The entire object was enclosed in a 0.8 nm mesh box. Finally, the background refractive index was set to $n = 1.3478$ to match the refractive index of a saturated CTAB solution,[44] as the experimental spectrum refers to a colloid at high CTAB concentration (50 mM). Together, these three adjustments resulted in a simulated spectrum that almost perfectly overlapped with the experimental one across the entire Vis range, as shown in Figure 2.5. Remarkably, when using other gold datasets such as Johnson and Christy[14] and CRC[45], the simulated spectra exhibited more pronounced discrepancies compared to

the experimental one. Furthermore, the simulated spectra exhibited LSPRs blueshifted up to 7 nm compared to the experimental one at 581 nm whenever the CTAB shell was not used, and the background index set to 1.333 (water). These additional simulations can be found in Appendix F.2. In particular, the spectrum of a AuNSs140 colloid at very low CTAB concentration (0.8 µM) was perfectly reproduced by a CTAB–capped 104 nm AuNS in pure water (see Appendix F.3). Therefore, our technical adjustments were effective in mimicking all the real scenarios. The excellent agreements also provide theoretical confirmation for the sputtering layer thickness being 6 nm (a sphere larger than 104 nm by 12 nm would have resulted in a redshifted spectrum, at least).

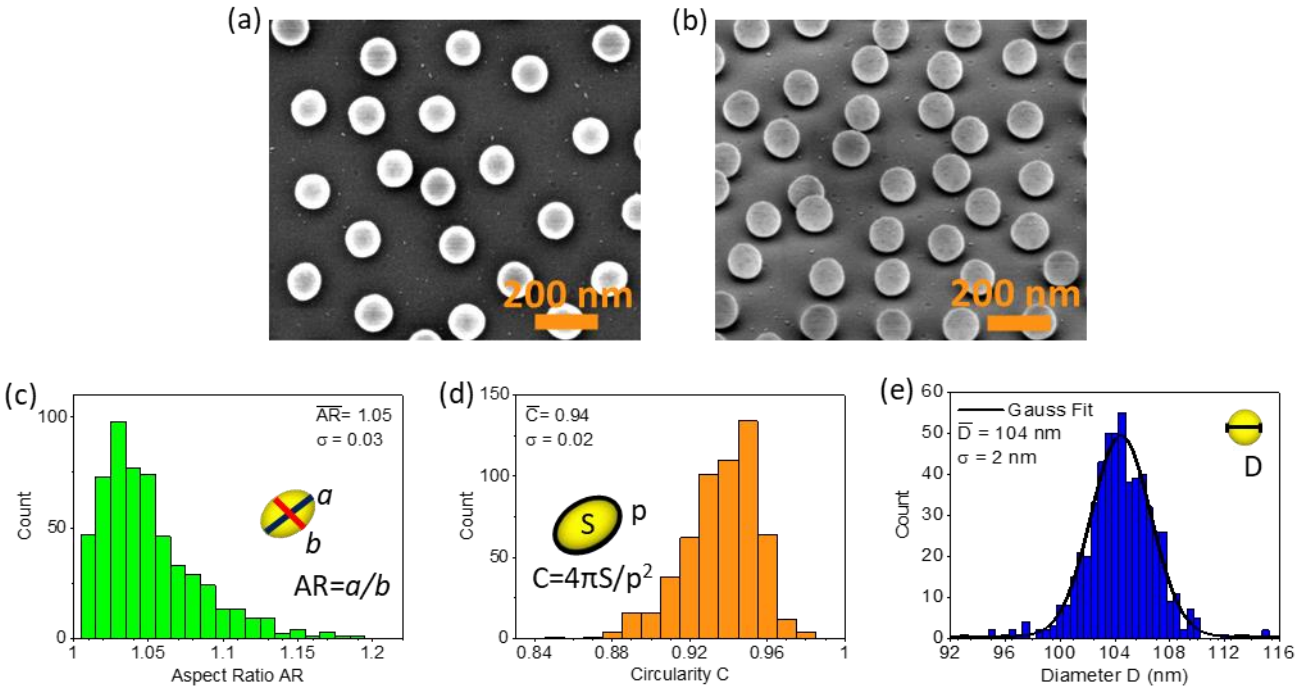

Figure 2.4. Morphological characterization of AuNSs140. (a) Top-view and (b) 52° tilted STEM micrographs at high magnification of AuNSs140 immobilized onto a glass substrate. (c) Histogram of AuNSs140 aspect ratio, with the inset representing the major (dark blue) and minor (red) axis of an idealized ellipsoidal nanoparticle. (d) Histogram of AuNSs140 circularity, with the inset showing an idealized ellipsoidal nanoparticle decomposed in perimeter (black line) and area (yellow filling). (e) Histogram of AuNSs140 diameter distribution and its Gaussian fit.

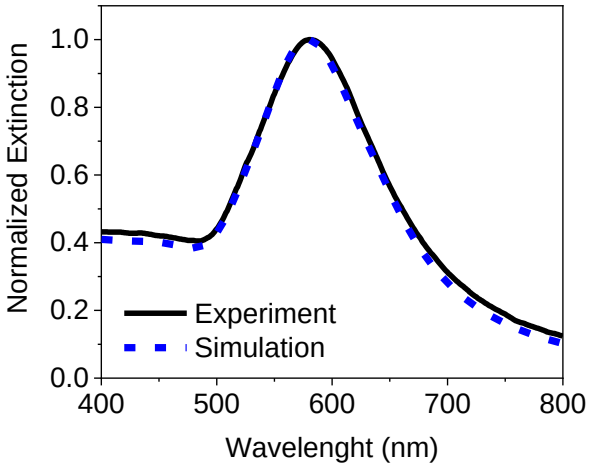

Figure 2.5. Experimental (black solid) and simulated (dashed blue) normalized extinction spectra for AuNSs140 colloid at 50 mM CTAB. A 104 nm AuNS with a 3 nm CTAB shell in a saturated CTAB solution was used for the simulation.

2.2.3 Synthesis of Gold Nanocubes (AuNCs60)

AuNCs were synthesized as detailed in Appendix A.6, spanning from NCs150, i.e., NCs obtained from the growth of 150 µL of final seeds (at OD1 and 100 mM CPC), down to NCs50. Figure 2.6 displays the normalized extinction spectra of NCs150 (black), NCs125 (red), NCs100 (green), NCs75 (blue), NCs60 (orange), NCs50 (dark yellow). The concentration of surfactant CPC is 1 mM for all. The mean NCs sizes could be finely tuned (increased) by slight variations (lowering) in the amount of seeds, as indicated by their LSPR wavelengths: 560 nm for NCs150; 566 nm for NCs125; 569 nm for NCs100; 580 nm for NCs75; 590 nm for NCs60; and 594 nm for NCs50.

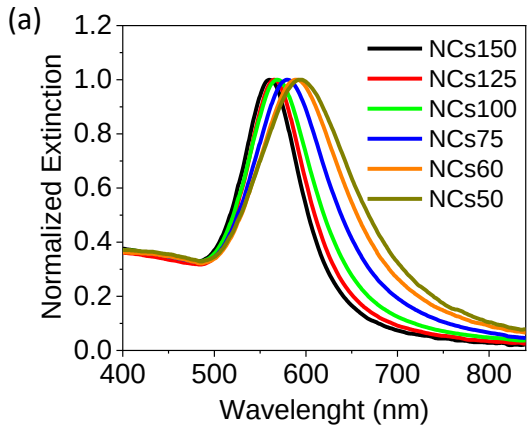

Figure 2.6. Normalized extinction spectra of AuNCs150 (black), AuNCs125 (red), AuNCs100 (green), AuNCs75 (blue), AuNCs60 (orange), AuNCs50 (dark yellow).

It is worth mentioning that the synthesis of AuNCs100–AuNCs50 typically resulted in bad-looking greyish solutions with extinction spectra exhibiting an almost horizontal line modulated by two short and wide plasmon peaks. Such peaks usually denote clusters of NPs, which in this context gradually formed in the late stages of the growth process because of the onset of surfactant–induced depletion forces.[46–48] However, such clusters were fully *reversible* and disrupted as soon as the CPC content was lowered at ≈ 1 mM after the first round of centrifugation and resuspension. Figure 2.7 displays this interesting phenomenon for a batch of AuNCs50.

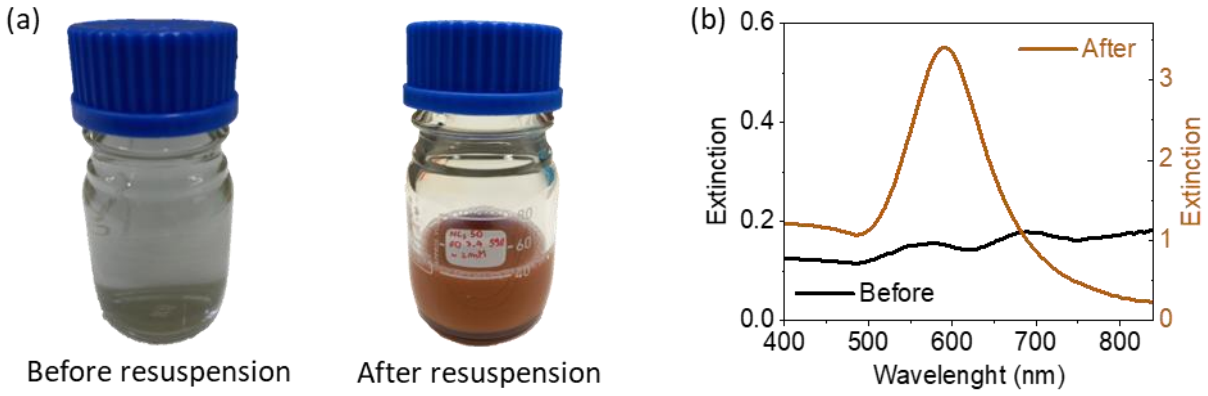

Figure 2.7. (a) Batch of AuNCs50 before and after the first resuspension. Greyish colour is due to (reversible) clusters of NCs fully disrupted after resuspension. (b) Associated extinction spectra before (black) and after (brown) resuspension. The two short peaks due to clusters disappear after resuspension, leaving a spectrum with a single peak at ≈590 nm.

For our MEF study, our focus was on AuNCs60, whose thorough characterization follows.

2.2.3.1 Morphological and Optical Analysis of AuNCs60

AuNCs60 were morphologically characterized by FEI Magellan STEM after immobilization onto a glass substrate (discussed in section 2.3). The samples were imaged after iridium sputtering (60 s, 25 mA) and the nominal 6 nm iridium layer (confirmed experimentally, see Appendix C.3) was considered in the analysis, as specified below.

Figures 2.8a and b display typical top-view STEM micrographs at high magnification (100'000 x and 250'000x, respectively). Together, they show large NPs with cubic or parallelepipedal shapes with seemingly flat facets. NPs having other shapes, e.g., circular/spherical, are almost absent and can be counted by eye. The shape yield was indeed found to be $\geq 95\%$ in all the micrographs, as expected from the synthesis methods we used.

The quantitative analysis of the rectangular shape and size was conducted on the top-view STEM of Figure 2.8a and another one at the same magnification, to consider a relatively large sample of 200 NPs without compromising the image resolution. The "Oriented Bounding Box" tool from "MorphoLibJ" plugin was employed to retrieve the lengths of both sides of the visible NPs. As detailed in Appendix C.2, this tool considers as "Length" and "Width" the major and minor sides of the oriented rectangle bounding a NP, respectively. Since this rectangle bounds an object from the outside, its dimensions are slight overestimations of the actual dimensions of the visible object. The overestimation was manually checked to be within 3 nm for the micrographs we considered (see Appendix C.2 for further details), and this value sums to the $6 + 6 = 12$ nm associated to the iridium sputtering. Therefore, we determined the actual NP Length (L) and Width (W) as $L = L^* - (3 + 12)$ nm and $W = W^* - (3 + 12)$ nm, respectively, where L^* and W^* are the corresponding values as provided by the ImageJ plugin. The two resulting distributions can be found in Appendix F.4, while the corresponding AR distribution is displayed in Figure 2.8c. It has a mean value $\overline{AR} = 1.12 \pm 0.10$, hence the majority of AuNCs60 are cubes or parallelepipeds slightly deviating from the cubic shape. Finally, Figure 2.8d displays the overall histogram of the AuNCs60 edges (no distinctions between L and W). A long but low tail can be noted on the right side, which is associated with a population of overgrown edges. Therefore, we fitted the histogram by two Gaussian curves, one for the edges grown in an ordinary way (solid green line) and the other for the overgrown edges (solid red line). Both the individual and cumulative bi-Gaussian (dashed black line) curves fit very well the histogram, with mean values $E_1 = 74 \pm 5$ nm and $E_2 = 92 \pm 7$ nm, respectively. The population of overgrown edges should not be attributed to our shorter seed refinement process (one cycle instead of the recommended two) but is rather typical. Indeed, not only the spectrum of our CPC–capped seeds but also the size dispersity and AR distributions of our NCs align with Mirkin's NCs. Therefore, the quality of our NCs is typical of Mirkin's double refinement process but, notably, resulting from a single iteration. While further refinements could have further improved the seed quality and, consequently, NCs quality, the results were already highly satisfying. We chose to adopt a simpler and shorter procedure rather than a longer, more tedious one, which would have resulted in only minor improvements.

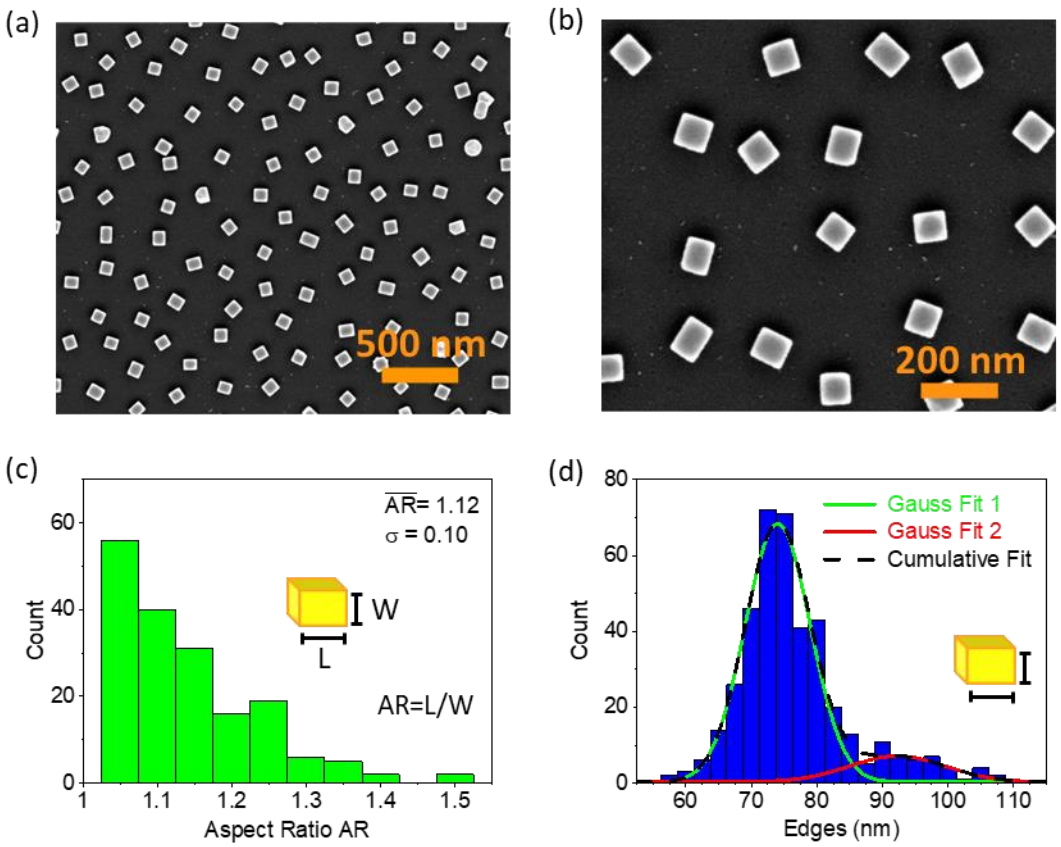

Figure 2.8. Morphological characterization of AuNCs60. (a)-(b) Top-view STEM micrographs at high magnification of AuNCs60 immobilized onto a glass substrate. (c) Histogram of AuNCs60 aspect ratio, with the inset representing major and minor edges of the visible face of an idealized parallelepiped. (d) Histogram of AuNCs60 visible edges with Gaussian Fits for fractions of ordinarily grown edges (green), overgrown edges (red) and entire sample (black dashed). Histograms refer to a sample of NCs from micrograph (a) and another at the same magnification.

Furthermore, 52° tilted STEM micrographs, as in Figure 2.9b, offered a 3D perspective of the NCs showcasing their entire crystallographic profile, i.e., flat {100} facets delimited by rounded {110} edges and truncated {111} vertices, as reported in literature.[49] While the perfect cubic shape is simply impossible to achieve, it is of paramount importance to quantify the actual sharpness of edges and vertices, as the plasmonic properties of any nanoparticle are drastically different whether it has sharp features or not.

Therefore, a careful analysis was conducted by ImageJ to estimate the mean radius of curvature $\overline{R_{curv}}$ for the visible corners of AuNCs60. The top–view STEM micrograph at high magnification (250'000x) of Figure 2.9c was analyzed at this scope, counting a sample of 68 corners from 19 NCs (few corners are outside the image). The "Curvature" plugin was employed to list the radius of curvature $R_{curv}(x,y)$ of each point (x,y) from the NPs outlines, with each local minimum corresponding to a corner. All points in the neighbourhood of a local minimum were considered till a discontinuity $\gtrsim 5$ nm in R_{curv} was encountered (excluding such discontinuous points). For each corner, the selected range was averaged, obtaining the mean radius of curvature ${R_{curv}}^{i}$ of that specific corner. Finally, we assumed all the corners as independent, and obtained $\overline{R_{curv}} = 12$ nm with standard deviation $\sigma = 2$ nm. Figure 2.9d displays a graphical representation of the raw data provided by the "Curvature" plugin. The graph is superimposed to the corresponding micrograph of Figure 2.9c and, for a better readability, points with $R_{curv} > 16$ nm are not represented (they

mostly lie beyond the corner regions). It can be noted that the dominating colours at the corners are green and yellow, corresponding to points with R_{curv} from 8 to 16 nm.

It is worth to stress that $\overline{R_{curv}} = 12 \pm 2$ nm refers to visible edges strictly, as a top-view micrograph cannot give information about the 3D curvature of vertices (which are truncated). However, since our analysis attributes the same $\overline{R_{curv}}$ to each of the three independent pairs of edges associated to a vertex, it seems reasonable assuming $\overline{R_{curv}}$ as the radius of curvature of the entire corner, at least as a first approximation. The result $\overline{R_{curv}} = 12 \pm 2$ nm indicates that the corners of our AuNCs60 are sharp, even though not super sharp. In fact, radius of curvatures as small as 8.27 ± 0.39 were estimated (by ImageJ) from TEM micrographs of 72 nm AuNCs synthesized by a different protocol with optimized bromide concentration,[49] even though the authors do not describe how.

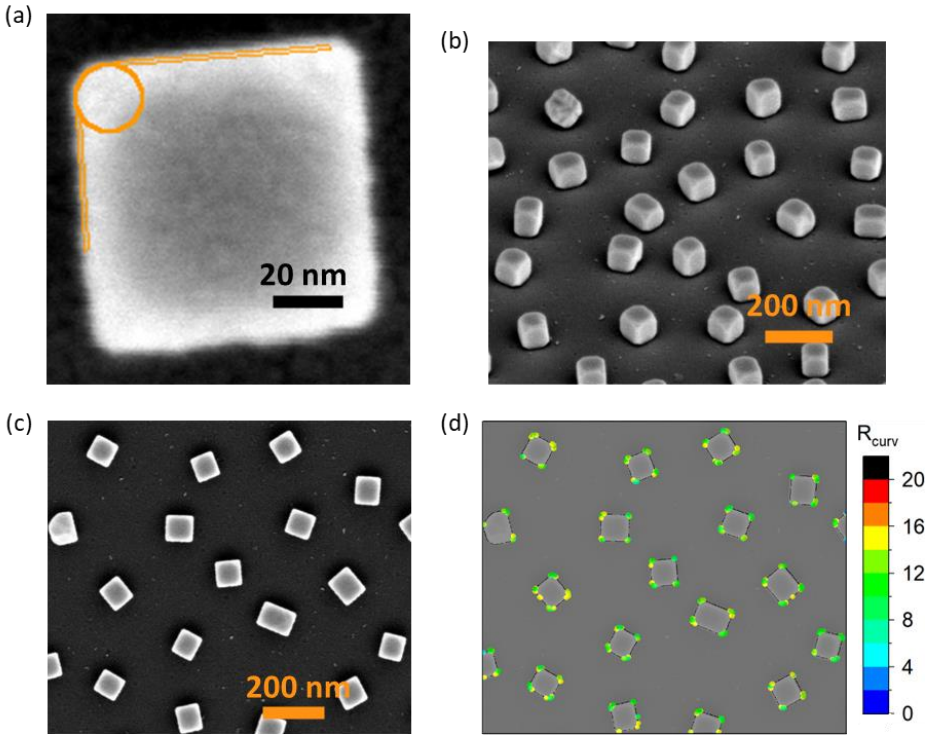

Figure 2.9. Characterization and analysis of AuNCs60 edges curvatures. (a) Top-view STEM micrograph at high magnification (500'000x) showing one NC. The orange circle has a radius of 10 nm, as resulting from the analysis of this specific corner. (b) 52° tilted STEM micrograph at high magnification of AuNCs60 on glass substrate, showcasing flat {100} facets, rounded {110} edges, and truncated {111} vertices. (c)-(d) Top-view STEM micrograph at high magnification (250'000) of immobilized AuNCs60 together with the graphical representation of NCs edges R_{curv}. The graph is superimposed on the micrograph. For better readability, only coloured dots corresponding to R_{curv} in the range]0, 16[(blue to yellow) are displayed. Points with higher R_{curv} mostly lie beyond the corner regions.

The morphological analysis conducted so far enables the modelling of the average AuNC60 as a 74 ± 5 nm nanocube with all edges and vertices rounded by $\overline{R_{curv}} = 12 \pm 2$ nm. To theoretically validate this model, its extinction spectrum was simulated and compared to the experimental spectrum of the AuNCs60 colloid. The "all rounded quadrilateral" from Lumerical's object library — a parallelepiped with all edges and corners rounded by suitable cylinders and spheres, respectively — was found to precisely match with our model and was adopted as the final geometry for simulations. To mimic the real scenario, the rounded nanocube was enclosed in a 3 nm thick dielectric shell, replicating the CPC bilayer capping,[50] and embedded in a dielectric medium to

replicate a saturated CPC aqueous solution. Reliable values for the associated refractive indexes were not found in literature, and we adopted the same values as those for CTAB ($n = 1.4350$ [41–43] for the dielectric shell and $n = 1.3478$ [44] for the background medium). While the actual parameters for CPC may differ from those of CTAB, our assumptions at least account for an organic layer capping a NP that is further embedded in a highly concentrated surfactant solution (1 mM, as the colloid). Finally, Olmon's dataset for single crystalline gold was utilized,[40] our AuNCs being monocrystalline as per the synthesis methods. When using other gold datasets (such as Johnson and Christy[14], CRC[45]), discrepancies were observed in the shape of the simulated spectrum when compared to the experimental one. The entire object was enclosed in a 0.5 nm mesh box for a precise and accurate discretization of the rounded edges and vertices.

We run simulations with the wave vector of the incident light being orthogonal to a NC facet, and the polarization parallel to an edge. Such simulations already provided the unpolarized optical response of that specific nanocube orientation, thanks to the invariance of a square under 90° rotations. For simplicity, further orientations were not considered. They would contribute in a negligible way thanks to the cube invariance under any (3D) rotation by 90°. We constrained the rounded nanocube edges to be 74 nm but varied R_{curv} (the same for both edges and vertices) in the range 0—37 nm, i.e., covering the entire transition from a perfect cube to a perfect sphere. R_{curv} significantly influenced the LSPR wavelength, blue-shifting from $\lambda_{LSPR} \approx 650$ nm for $R_{curv} = 0$ (perfect cube) to $\lambda_{LSPR} \approx 550$ nm for $R_{curv} = 37$ nm (perfect sphere). The satisfactory agreement with the experimental spectrum shown in Figure 2.10 was achieved with $R_{curv} = 14$ nm, a value consistent with our morphological analysis. The narrower FWHM compared to the experimental spectrum can be safely ascribed to the perfect monodispersion of the simulated object (a single particle) versus the polydispersion of the AuNCs60 colloid (mean edge 74 ± 5 nm).

We conclude that a 74 nm NC with all edges and vertices rounded by cylinders and spheres with radii 14 nm is an accurate model for the average AuNC60, both experimentally and theoretically.

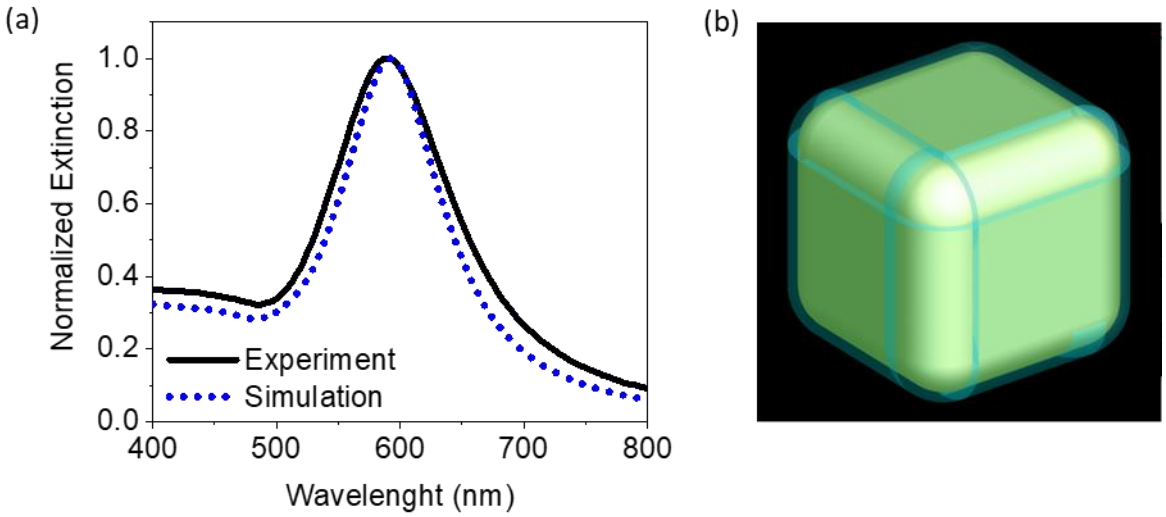

Figure 2.10. (a) Experimental (black solid) and simulated (blue dotted) normalized extinction spectra for AuNCs60 colloid at high concentration of CPC (as synthesized nanoparticles). (b) Model geometry used for simulations as from Lumerical workspace, i.e., a 74 nm nanocube with all edges and vertices rounded by cylinders and spheres of radii 14 nm, respectively. The object is enclosed in a 3 nm thick dielectric shell, replicating the surfactant bilayer.

2.3 Electrostatic Self-assembly of AuNPs on Glass

The electrostatic self-assembly technique allows the fabrication of 2D self–assembled monolayers (SAMs) of NPs randomly distributed over a substrate. This method relies on the spontaneous adsorption of pre-made NPs onto a substrate, driven by electrostatic interactions. The successful implementation of this process necessitates opposite charges on substrate and NPs. Therefore, the technique is not suitable for systems that do not possess significant (opposite) surface charges as the stability and reproducibility of the resulting nanostructure would not be guaranteed. The formation of the SAM is also influenced and limited by the physicochemical properties of the NP colloid, e.g., pH and solvent compatibility, as well as the physicochemical and mechanical properties of the substrate. Furthermore, the technique cannot realize ordered arrays by concept. Many of these issues can be overcome, for example, by colloidal lithography (CL), which offers a high level of stability and reproducibility when compared to just NPs deposition and, at the same time, the possibility to fabricate ordered arrays.[51] However, in CL, the array shapes are constrained to those complementary to the mask (a SAM of polystyrene nanospheres), such as triangular NPs, dots, holes, disks, bowls, cups, hollow sphere/shell, with more unusual shapes obtained only in combination with other techniques (etching, photolithography). In contrast, once electrostatics is well–suited, the electrostatic self–assembly technique gives the freedom to fabricate random arrays of pre–made NPs of any shape. In fact, the aforementioned issues can be partially or totally overcome. Chemical modifications are routinely applied to the substrate interfaces to suit the NPs electric charges, overcoming the limited material compatibility. Even the NPs themselves can be modified by ligand exchanges processes which, however, demand meticulous attention to prevent irreversible NPs aggregations.[52] Furthermore, oxygen plasma treatments can be used to improve the array stability if necessary.[53] The conceptual simplicity, versatility, scalability over large areas (dm^2), and minimal equipment requirements make electrostatic self-assembly technique ideal for practical applications. We focused on such nanofabrication technique in our endeavours.

The substrates used thorough this work were borosilicate glass of hydrolytic class 1. Type 1 glasses are made of 65–72% SiO_2, therefore their interfaces are rich in silanol (Si-OH) bonds which are negatively charged as long as they are in contact with electrolyte solutions at $\mathrm{pH} \gtrsim 4$.[54] As the electrolyte pH increases, the interface becomes more and more negatively charged,[54] and this is why glass is highly hydrophilic. A common practice is to expose the pristine glass to a low–pressure oxygen plasma to fully oxidize the SiO_2 at the interface, thereby increasing the number of silanol bonds. This treatment, known as "activation", enhances the surface charge of the pristine glass (at a given pH of the electrolyte solution) and ensures a uniform charge distribution.

At this stage, the activated glass substrate can be chemically modified to suit the physicochemical properties of both NPs and buffer/electrolyte solution; or, vice versa, the physicochemical properties of NPs and buffer/electrolyte solution can be modified to suit the properties of the substrate. We are going to show both the cases, focusing on the latter.

2.3.1 Case 1: SAMs of Negatively Charged AuNPs

Turkevich's AuNPs are citrate-capped NPs stabilized in aqueous Trisodium citrate buffer.[26] This buffer solution is generally alkaline ($\mathrm{pH} > 7$), and the NPs carry a negative charge. Given that type

1 glass interfaces retain a negative charge at pH≳4 conditions, Turkevich's AuNPs are consequently repelled by pristine glass and cannot undergo electrostatic adsorption. Therefore, a chemical modification of either the glass interface or the AuNPs is essential.

Glass substrates were subjected to a silanization process using the amino-terminated silane 3-aminopropyltriethoxysilane (APTES) to impart the desired positive charge. In presence of water molecules, APTES is first hydrolysed and then binds covalently to the glass as its organosilyl terminations react with glass silanols bonds forming –Si–O–Si– bonds.[55] In this bond, one Si atom is sourced from the glass, and the other comes from an APTES molecule. APTES amino terminations are easily protonated to $-NH_3^+$ in aqueous solution. Consequently, APTES-functionalized substrates carry a positive charge if put in contact with our AuNPs colloids, maintaining the positive charge over a broad pH range.[54] The electrostatic SAM of Turkevich's AuNPs onto APTES-functionalized glass interfaces can thus occur. The AuNPs surface density can be easily tuned, for instance, by changing the AuNPs concentration and the incubation time.

It is worthwhile to mention that APTES is prone to polymerization leading to multilayers formation and to a non-homogeneous coating of the substrate, generally. The deviations from the ideal APTES monolayer give rise to regions (from nm^2 up to μm^2) with a higher local density of amino terminations. Once in contact with aqueous solutions, these regions locally carry a higher positive charge density that may trigger aggregations and/or formation of clusters of negatively charged NPs. In order to achieve the ideal APTES monolayer, vapour phase deposition and specific curing steps are often employed;[56] however, this demands specific equipment (e.g., a glovebox) and trained personnel as well as up to overnight ageing or thermal annealing. Furthermore, the APTES monolayer is not essential in many applications like ours, where a sufficiently homogeneous coating, capable of preventing substantial AuNPs aggregations, is satisfactory. For these reasons, we chose the simpler aqueous solution–phase deposition, a method frequently employed in literature with great success especially when APTES was used in relatively low concentrations.[56,57] We followed one of such silanization protocols[57] together with a final oxygen plasma cleaning (Figure 2.11e) to remove all residue of APTES which could have degraded during later times affecting the array stability. The employed method guaranteed good stability and reproducibility, as the oxygen plasma cleaning leaves bare AuNPs strongly bound to glass.[53]

Nanostructure fabrication generally counted five steps, detailed in Appendix B.1, and schematically shown in Figure 2.11: a) glass substrate cleaning; b) substrate activation by low-pressure oxygen plasma; c) silanization by APTES (aqueous solution–phase deposition); d) immobilization of Turkevich's AuNPs; e) final cleaning by low-pressure oxygen plasma.

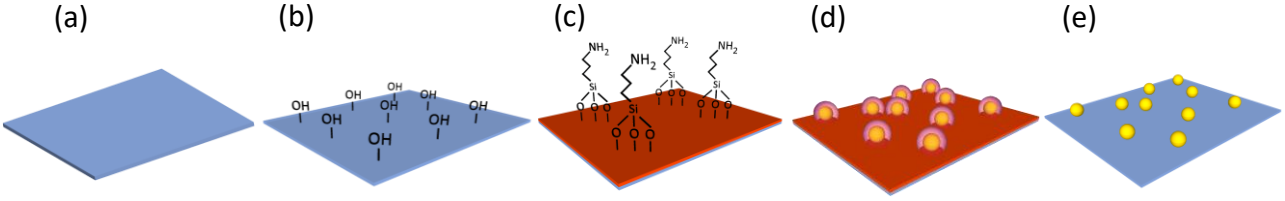

Figure 2.11. Fabrication of 2D SAM of randomly positioned AuNPs on glass through electrostatic self-assembly technique. (a) Substrate cleaning. (b) Surface activation by oxygen plasma. (c) Surface silanization by APTES. (d) Citrate-capped AuNPs immobilization. (e) Citrate and silane layer etching by oxygen plasma.

2.3.1.1 Morphological and Optical Characterizations

The as-fabricated nanostructures were morphologically characterized by FEI Nova NanoSEM 450 scanning electron microscopy (SEM) after gold/palladium sputtering (30 s, 25 mA). A typical micrograph at low magnification shows spheroidal NPs randomly distributed over the substrate as both single NPs and clusters (Figure 2.12a), the latter ascribed to APTES multilayer spots formed during silanization. However, AuNP clusters are not an issue, and the SAM is quite homogeneous, indicating that the specific aqueous solution-phase deposition method we adopted for silanization resulted in a nearly homogeneous APTES coating. Appendices C.1 and C.2 report the detailed analysis of the SEM micrograph by ImageJ software. Thanks to our optimized protocol, a high AuNPs surface density of ≈ 380 AuNPs/μm^2 was reached, which is suitable for biosensing applications demanding for abundancy of binding sites for bioreceptors. Figure 2.12b and c show the aspect ratio (AR) and circularity (C) distributions of the AuNPs, respectively. The mean values $\overline{AR}$ = 1.25 ± 0.19 and $\bar{C}$ = 0.82 ± 0.06 convey a relatively high regularity in nanoparticle roundness and also reflect their spheroidal (rather than perfectly spherical) shape, as expected from Turkevich's synthesis. However, such spheroidal AuNPs can be considered as spheres in a first approximation, and a gaussian distribution for their diameters with mean value $\overline{D}$ = 30 nm and σ = 5 nm (Figure 2.12d) is readily obtained. Finally, Figure 2.12e shows the histogram of the nearest-neighbour centre-to-centre distances (NND) whose distribution has mean value $\overline{NND}$ = 35 nm and σ = 9 nm. On the one hand, $\overline{NND}$ = 35 nm is very close to $\overline{D}$ = 30 nm, indicating a high surface density of AuNPs; on the other hand, the broader standard deviation (9 nm) simply reflects that the AuNPs are randomly distributed over the glass, a consequence of the electrostatic self-assembly technique.

The nanostructures were optically characterized through UV-Vis spectroscopy by measuring the extinction spectrum. Figure 2.13a shows the experimental extinction spectrum of the array (solid black line), showing a plasmon resonance at 526 nm and a "shoulder" in the range 600-800 nm. The former is associated both to single AuNPs that are far enough from their nearest neighbours (NND>3/2 D)[58] to be considered as isolated, and AuNPs that are close enough (NND≲3/2 D) to interact to each other. Instead, the shoulder is associated with AuNPs in close proximity, forming clusters that interact with longer wavelengths because of their huge overall size.[59]

A 500 nm × 500 nm ROI (Figure 2.13b) was selected from the top-left quarter of the SEM micrograph of Figure 2.12a and used for running FDTD simulations by Lumerical software (see Appendix C.2 for details on the modelling). This specific ROI was chosen in an "educated" manner to include clusters manageable by ImageJ. More intricate clusters cannot be properly processed (segmented) by ImageJ and, therefore, cannot be imported into the simulation software. The simulated extinction spectrum associated with the selected ROI (solid blue line in Figure 2.13a) agreed well to the experimental extinction spectrum (solid black line) as soon as the Johnson and Christy[14] dataset was chosen for gold. Remarkably, not only was the plasmon resonance at 526 nm recovered, but the shoulder associated with AuNPs clusters was also accurately reproduced. Consequently, the selected sub-micrometric ROI serves as representative morphology at the macroscopic level too (the experimental extinction spectrum is relative to ≈7 mm^2 of nanostructure). In other words, the morphology holding at both the sub-micrometric scale and the macroscopic scale are highly consistent, which conveys the uniformity of the nanostructures (visible to the naked eye through its uniform light pink colour).

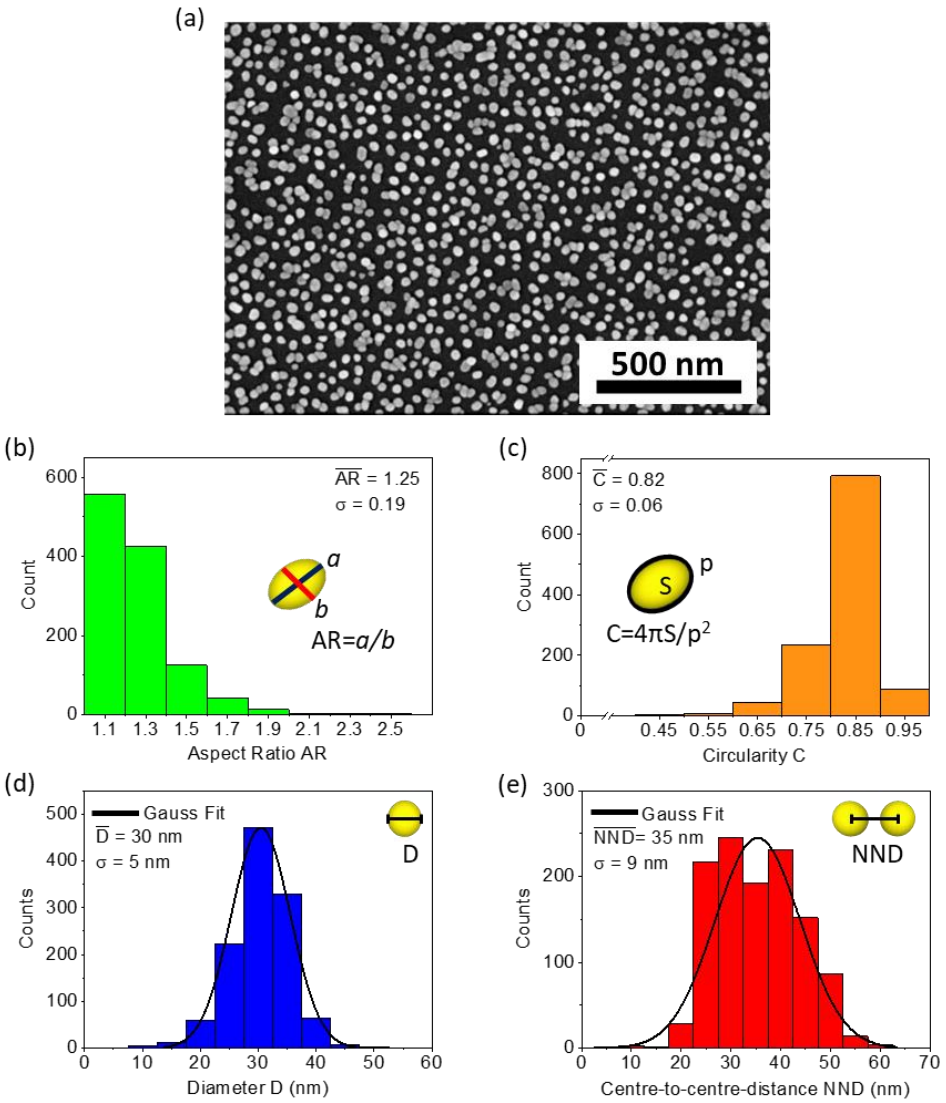

Figure 2.12. Morphological characterization of the nanostructured substrate. (a) Top view SEM micrograph of the 2D SAM of AuNPs. (b) Histogram of AuNPs aspect ratio, with the inset representing the major (dark blue) and minor (red) axis of an idealized ellipsoidal nanoparticle. (c) Histogram of AuNPs circularity, with the inset showing an idealized ellipsoidal nanoparticle decomposed in perimeter (black line) and area (yellow filling). (d) Nanoparticle diameter distribution. (e) Nearest neighbour Centre-to centre distance (NND) distribution.

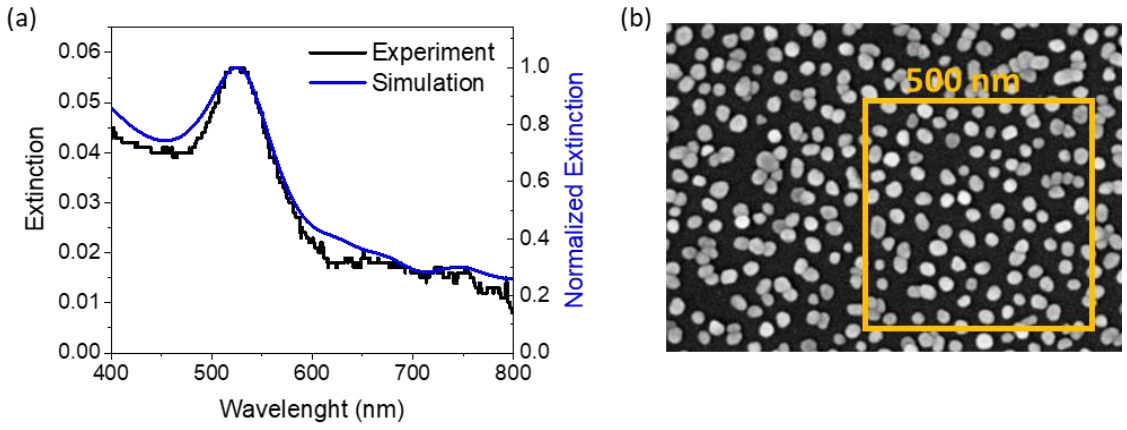

Figure 2.13. (a) Experimental (black) and simulated (blue) extinction spectra of the array. (b) Top-left quarter of the SEM micrograph of Figure 2.12a including the 500 nm ROI (highlighted in dark yellow) chosen to run the simulation.

2.3.2 Case 2: SAMs of Positively Charged AuNSs and AuNCs

The seed–mediated methods described in Section 2.2 were used to synthesize CTAB–capped AuNSs (stabilized in CTAB buffer) and CPC–capped AuNCs (stabilized in CPC buffer). These aqueous buffer solutions were found to be mildly acidic or alkaline according to the specific concentration of surfactant. For instance, a pH of 5.4 was measured for CPC solutions at ≥100 μM (in ultrapure water), and a pH of 7.4 was measured for a 1 μM CPC solution, 7.4 being the pH of the ultrapure water, too. Nearly the same values were measured for the pH of corresponding CTAB solutions, in accordance with literature. [60] Therefore, CTAB and CPC aqueous solutions generally have a pH≳4, a condition at which type 1 glass interfaces retain a negative charge. On the other hand, both CTAB and CPC are cationic surfactants which make the AuNSs and AuNCs positively charged. These circumstances pave the way to the exciting possibility of an electrostatic self-assembly of AuNPs with no need for chemical modifications of either the substrate or the NPs, since both would already have the right electric charges. However, this scenario is slightly oversimplified, as surfactants like CTAB or CPC can themselves adsorb electrostatically onto negatively charged (hydrophilic) surfaces, given their cationic nature.[61] This phenomenon gradually shifts the charge of the negatively charged substrate towards positive values, hindering the electrostatic adsorption of positively charged AuNPs.

According to this reasoning, our glass substrate would retain sufficient negative charge for the adsorption of CTAB–stabilized or CPC–stabilized AuNPs only when a negligible adsorption of CTAB or CPC molecules occur during the incubation with the colloids. As a matter of fact, no NP adsorption was observed for those colloids with surfactant concentrations in the range ≈ 100 mM (as–synthesized AuNPs) to ≈ 1 μM.

However, the process was successful as soon as the surfactant concentration was reduced to $\lesssim 1$ μM, with the concentration of 0.25 μM serving as lower threshold: below this concentration, irreversible NP aggregations spoiled the colloids, likely caused by an insufficient number of ligands around the NPs. The electrostatic adsorption of AuNPs was then successful only at very low concentrations of surfactants, and within a range as narrow as 0.25–1 μM. This range of concentrations was notably 5 orders of magnitude lower than the concentrations of surfactants used for the synthesis, i.e., 50 mM CTAB for the AuNSs and 100 mM CPC for the AuNCs. A minimum of 3 rounds of centrifugations and resuspensions were necessary to bridge this significant gap, and the exact number depended also upon the specific instrument used (Eppendorf MiniSpin® or Heraeus Megafuge 1.0 R). It was paramount to centrifuge and resuspend the NPs colloids each time using solutions at known concentrations of CTAB or CPC, since the working range as narrow as 0.25–1 μM demanded a very strict and meticulous control over the concentrations of surfactants.

The synthesis methods we adopted allowed for the fine tuning of AuNPs sizes. AuNSs140 and AuNSs180 as well as AuNCs60 and AuNCs125 were used to fabricate electrostatic SAMs over glass substrates. The fabrication generally counted six steps, detailed in Appendix B.2, and here summarized: a) preliminary preparation of AuNPs at OD 5 and 0.8 μM CTAB (AuNSs) or 0.5 μM CPC (AuNCs); b) glass substrate cleaning; c) glass activation by low–pressure oxygen plasma; d) immobilization of AuNPs; e) nanostructure rinsing by ultrapure water, solvent exchange, and drying; f) final cleaning by a low–pressure oxygen plasma.

The as-fabricated nanostructures exhibited an exceptional uniformity at the naked eye already, as conveyed by their bright colours (in air), see Figure 2.14.

Figure 2.14. Top-view picture of few as-fabricated nanostructures on a white background.

We primarily worked with AuNSs140 and AuNCs60 nanostructures in the upcoming MEF study. Therefore, we focus here on these two types of nanostructures.

2.3.2.1 Morphological and Optical Analysis of AuNSs140 and AuNCs60 Arrays

The nanostructures were morphologically characterized by STEM after iridium sputtering (60 s, 25 mA). An iridium layer with a nominal thickness of 6 nm was considered for the analysis, as previously done. Figures 2.15a and b, and 2.16a and b, display typical top-view and tilted STEM micrographs at low magnifications for AuNS140 and AuNCs60, respectively. In both cases, the NPs are randomly distributed over the substrate as individual NPs, exhibiting exceptional uniformity over large areas (≥30 μm^2). Almost no clusters were observed. We were looking forward to these features, which were expected from both the uniform plasma activation of the glass substrate and, more importantly, the absence of its chemical modification. As discussed in a previous section, an intermediate, potentially non-uniform layer (e.g., APTES) can be a source of NPs aggregation. In contrast, in our case, clusters may only arise from either pre-existing NP aggregates in the colloids (due to the low concentration of surfactants) or the drying process (due to capillary forces). Our nanofabrication methods successfully avoided or mitigated all these issues.

In the case of AuNSs140 nanostructures, it is noteworthy that small areas (≈ 1 μm^2) occasionally exhibited a quasi-hexagonal lattice, i.e., the maximum packing configuration for spheres. This feature arose from the relatively high surface density $\Sigma_1 \approx 19$ NSs/μm^2 achieved for AuNSs140 of diameter as large as 104 ± 2 nm (see Figure 2.15c). The NND histogram in Figure 2.15d reinforces this evidence of high coverage. Excluding the first two bins related to a few clusters, the Gaussian fit yielded a $\overline{NND} = 192\ \mathrm{nm}$ with σ = 22 nm, which implies that each NS has at least one

neighbour approximatively 88 ± 22 nm far from it (interparticle gap). Consequently, there is often insufficient space for another NS to be positioned in between.

The same does not apply to the AuNCs60 nanostructures. The NND histogram in Figure 2.16d has $\overline{NND}$ = 223 nm and σ = 33 nm, while $\bar{E} = 74 \pm 5$ nm (excluding the small population of overgrown edges, see Figure 2.16c). It follows that there is typically enough space for another NC to be situated in between two neighbouring NCs. This NND distribution is a result of a lower surface density, which for AuNCs60 nanostructure is $\Sigma_2 \approx 14$ NCs/μm^2.

A geometric parameter relevant to the upcoming MEF study is the "3D effective surface" of nanostructure per unit substrate, Σ_{eff}, representing the 3D array surface exposed to the local environment per unit substrate. For simplicity, we modelled the AuNSs as perfect spheres with $\bar{D}$ = 104 nm, and the AuNCs60 as perfect cubes with $\bar{E}$ = 74 nm, respectively. According to this modelling, the entire surface of a sphere is exposed to the local environment while only 5/6 of the total cube surface is exposed (one face is entirely in contact with the substrate). It easily follows that $\Sigma_{eff} = 4\pi(\bar{D}/2)^2\Sigma_1 = 0.64\ \mu m^2/\mu m^2$ for AuNSs140 nanostructures, while $\Sigma_{eff} = 5\bar{E}^2\Sigma_2 = 0.38\ \mu m^2/\mu m^2$ for AuNCs60 nanostructures. These parameters will serve as geometrical renormalization factors for the fluorescence intensities attained by these arrays in the context of a MEF study, cancelling the differences in both the single particle surfaces and their densities over the substrate. In other words, the renormalized fluorescence intensities will roughly refer to the same 3D effective surface of both arrays, and can be compared.

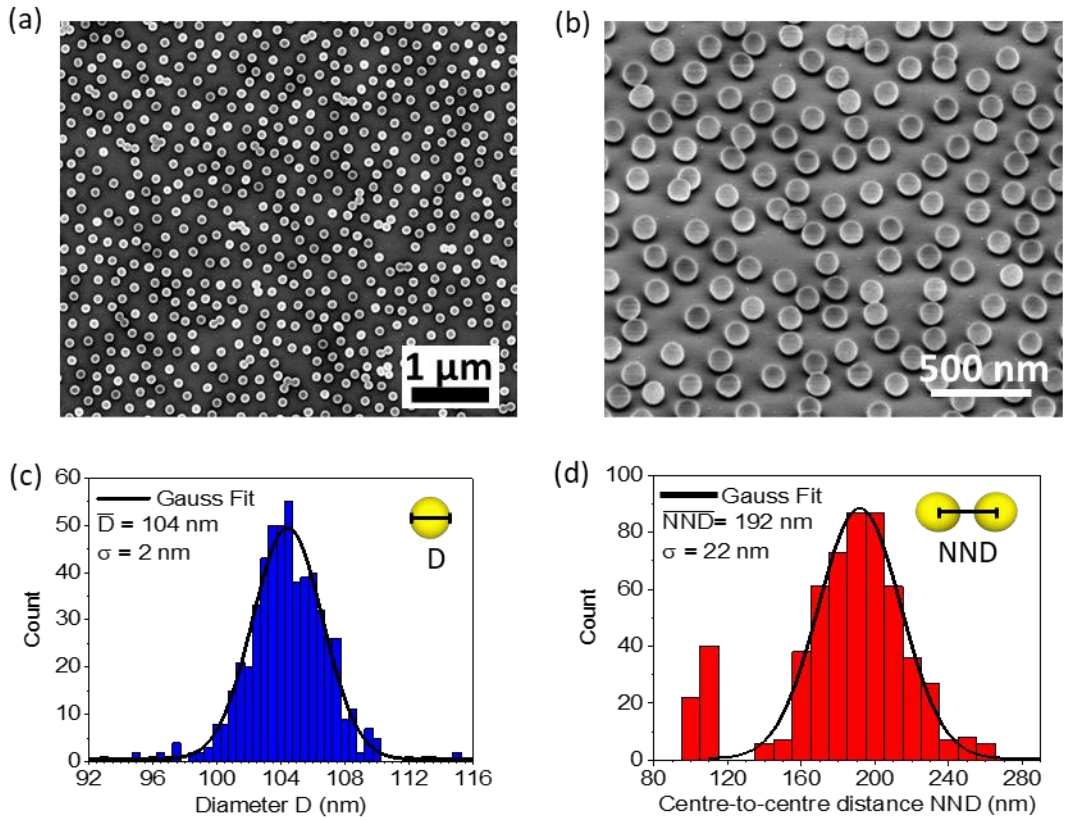

Figure 2.15. Morphological characterization of AuNSs140 nanostructures. (a) Top-view and (b) 52° tilted STEM micrographs at low magnifications of the SAM. (c) Diameter and (d) NND distributions as resulting from analysis of (a).

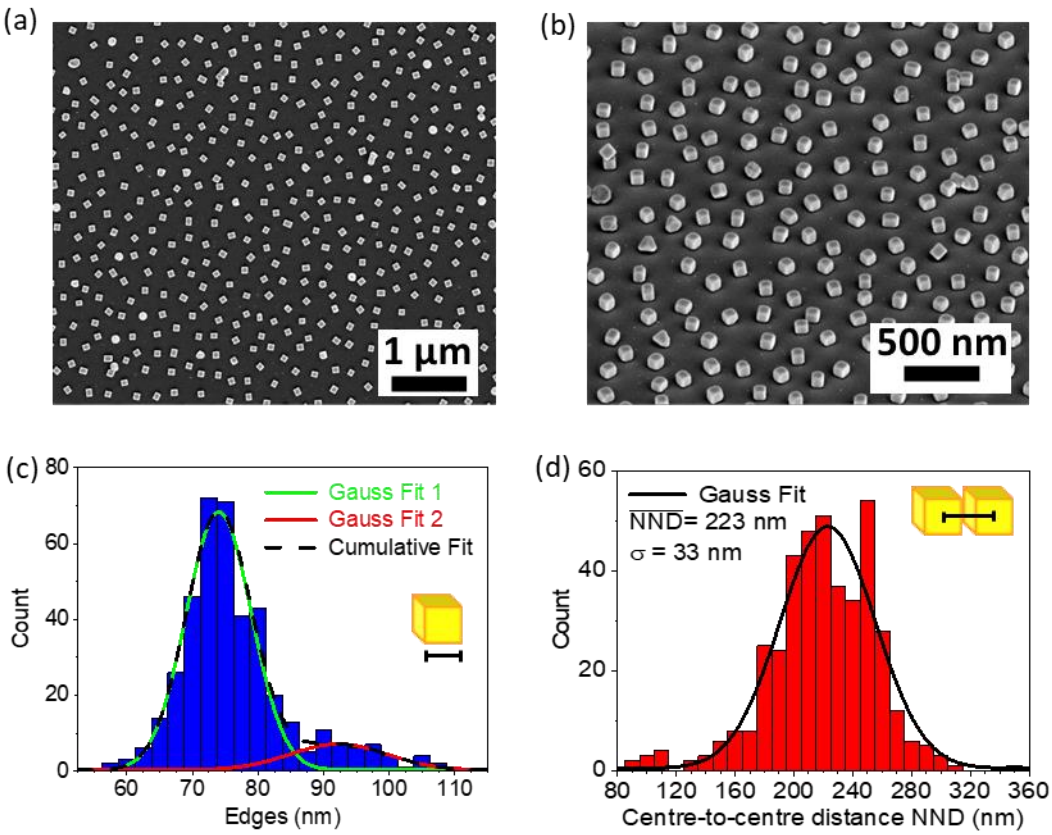

Figure 2.16. Morphological characterization of AuNCs60 nanostructures. (a) Top-view and (b) 52° tilted STEM micrographs at low magnifications of the SAM. (c) Diameter distribution (already shown in Figure 2.8a) and (d) NND distributions as resulting from analysis of (a).

The nanostructures were optically characterized through UV-Vis spectroscopy by measuring their extinction spectrum both in dry (air) and wet (water) conditions. The experimental spectra are shown as solid black lines in Figure 2.17: in particular, Figure 2.17a and b refer to the AuNSs140 array in air and water, respectively; analogously, Figure 2.17c and d refer to the AuNCs60 array in air and water, respectively.

The experimental extinction spectrum of the AuNSs140 nanostructure in air (solid black line in Figure 2.17a) exhibits a LSPR peak at 515 nm with FWHM of 35 nm, and no secondary LSPRs nor shoulders at longer wavelengths. This would suggest that the NSs140 constituting the array do not interact with each other and can be considered as isolated, consistently with the condition $\overline{NND} > 3/2\ \overline{D}$ holding for such array.[58] In contrast, simulations of a single 104 nm AuNS over glass in air showed that a single–particle model is not sufficient to optically describe the nanostructure, as its extinction spectrum (dashed green line in Figure 2.17a) exhibits mismatches throughout the Vis range, notably, a redshifted LSPR peaked at 524 nm with a wider FWHM of 43 nm. Typically, LSPRs undergo redshift and broadening when NPs couple with each other; instead, our simulations yielded the opposite result, i.e., the NSs140 constituting the array are interacting in such a way that the LSPR of the nanoparticle ensemble is both blueshifted and narrower compared to an isolated AuNS140 on glass. Remarkably, the same circumstance was found in water, even more pronounced, as well as in the case of AuNCs60 array. The redundancy of such result led us to hypothesize the rise of unusual collective plasmon phenomena, which we now investigate deeper by simulations along with the optical characterizations.

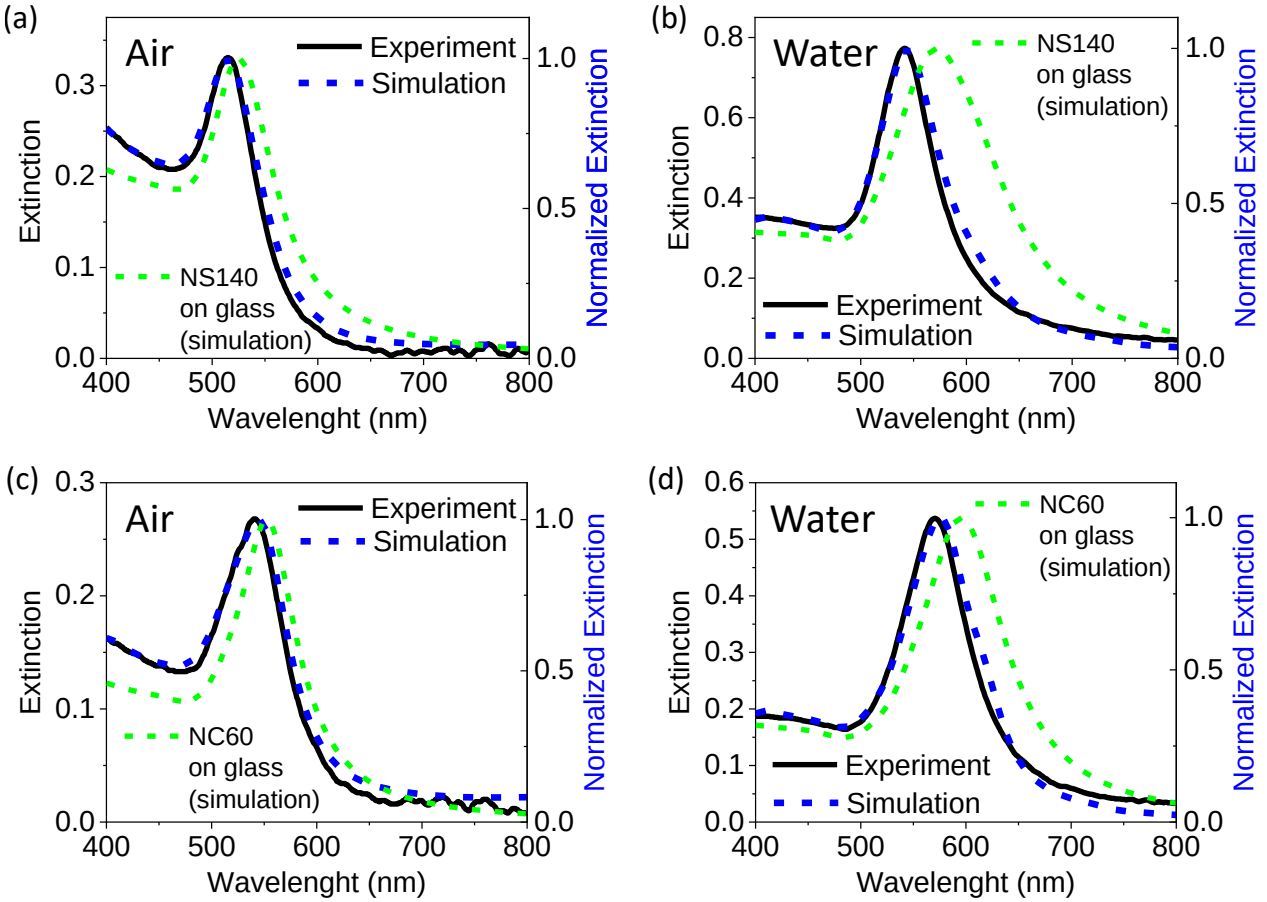

Figure 2.17. (a) Experimental (solid black) and simulated (dashed blue) extinction spectra of the AuNSs140 nanostructure in air. The simulated extinction spectrum of a single AuNS140 on glass in air is reported as dashed green line. (b) Corresponding spectra in water. (c) Experimental (black solid) and simulated (dashed blue) extinction spectra of the NCs60 nanostructure in air. The simulated extinction spectrum of a single AuNC60 on glass in air is reported as dashed green line. (d) Corresponding spectra in water. Due to long-range dipolar coupling among the NP constituting the arrays, the LSPR of the arrays is both blueshifted and narrower than the LSPR of the single particle on glass.

2.3.2.2 Investigation of Unusual Collective Plasmon Phenomena

To investigate the hypothesis of an unusual collective plasmon phenomenon, a many–body simulation was set up for the AuNS140 array. In particular, we simulated the unpolarized extinction spectrum of the STEM micrograph of Figure 2.4a, after processing and importing its morphology in Lumerical workspace (considering the 6 nm sputtering layer). That micrograph covers an area of ≈ 1 μm^2 counting 20 AuNSs140 with diameters ranging between 101 and 108 nm and a mean diameter 104 ± 1 nm . It is important to note that the experimental spectrum is associated to ≈ 7 mm^2 of nanostructure, which is essentially infinite in the context of nanophotonic simulations. To mimic the extended nature of the nanostructure, periodic boundary conditions were applied along the x and y axes of the simulation workspace. Consequently, we simulated the unpolarized extinction spectrum of an infinite array, with the chosen STEM micrograph serving as the unit cell. Similar to the simulations of colloids, we adopted Olmon's dataset for single-crystalline gold,[40] but no CTAB capping was added to NSs, as it should be negligible after the final oxygen plasma cleaning. We set $n_{glass} = 1.52$, the background index to 1 (vacuum), and a 2 nm mesh overriding the NSs to run the simulation within a reasonable time. Given that NSs140 have diameters of ≈ 100 nm, a 2 nm mesh is already considered highly accurate. The as–simulated (normalized and

unpolarized) extinction spectrum is depicted as a dotted blue line in Figure 2.17a and, notably, it perfectly aligns with the experimental one. Therefore, the above–mentioned hypothesis of an unusual collective plasmon phenomenon seems to be confirmed. Moreover, the perfect agreement theoretically demonstrates that the nanostructure is uniform over macroscopic scales (at least cm^2), while being locally described by the STEM micrograph of Figure 2.4a.

The outcome of any simulation may be affected by artifacts, and the simulated spectrum (dashed green line) of Figure 2.17a can, in principle, suffer this issue. Therefore, the aforementioned study was replicated under wet conditions (AuNS140 array in contact with water) to double check the physical nature of the phenomenon. On one hand, the presence of a dielectric medium (water) is expected to enhance plasmon phenomena. On the other hand, the nanostructure spectrum (ensemble spectrum) in water could be directly compared with the experimental spectrum of the AuNSs140 colloid (single–particle spectrum), whenever a AuNS140 in colloidal solution was optically equivalent to a single AuNS140 on glass in water.

Figure 2.17b displays the experimental extinction spectrum of the NSs140 nanostructure in water (solid black line), obtained by placing a small slice of nanostructure in a cuvette subsequently filled by ultrapure water. The spectrum exhibits a LSPR peaked at 542 nm with a FWHM of 49 nm, and no secondary LSPRs nor shoulders at longer wavelengths. The many–body simulation (dotted blue line) perfectly aligns with the experimental spectrum, while the single–particle simulation (dashed green line) once again produced a significantly redshifted and broader LSPR, peaked at 572 nm with a FWHM of 87 nm. Both simulations were run as in the previous case, but with background refractive index adjusted to 1.333 (water). Note that a single AuNS140 over glass in water resemble a colloidal AuNS140, as the local dielectric environments are roughly the same in both cases. Consequently, the reliability of the simulated spectrum (dashed green line) is confirmed by its nearly–perfect agreement with the experimental extinction spectrum of the AuNSs140 colloid at low CTAB concentration (as shown in Appendix F.5). Vice versa, it demonstrates that a AuNS140 in colloidal solution is optically equivalent to a single AuNS140 over glass in water. Consequently, it is legitimate to directly compare the experimental spectra of nanostructure and colloid, leading to the conclusion that the LSPR of our array of AuNSs140 is (significantly) blueshifted and narrower than the LSPR of the AuNSs140 colloid due to unusual collective plasmon phenomena.

Similar phenomena were observed in a situation entirely comparable to ours by Jenkins et al.,[62] who demonstrated (through simulations) that these effects arise from far–field dipolar interactions among *large* neighbouring NPs whose centre-to-centre NND distances are *larger* than their (*large*) diameter. In other words, the dipolar components of the scattering of our large AuNSs140 coherently interacts in the far–field zone, and both a blueshift and a narrowing of the LSPR of the nanoparticle array result from such long–range interactions. The calculated NND distance–dependence of the LSPR wavelength for Jenkins' 120 nm AuNS array (comparable to our AuNSs140) is reported in Appendix F.6. Interestingly, the curve has a local minimum, and the following picture holds: when the NPs constituting the (random) array are very far from each other (e.g., 10 times their diameter), the LSPR of the array coincides with the single–particle LSPR; as the NND distance decreases, the nanostructure LSPR blueshifts until reaching a local minimum; finally, for smaller NND distances, the array LSPR starts redshift. For a 120 nm AuNS, the local minimum is at $\mathrm{NND} \approx 180$ nm. Since our AuNS140 have a comparable $\overline{D} = 104 \pm 2$ nm, and a $\overline{NND} = 192 \pm 22\ \mathrm{nm}$, the blueshift and narrowing of the LSPR of our AuNSs140 array would be nearly maximal.

Indeed, in water, we observed a substantial blueshift of 30 nm and a narrowing of the LSPR linewidth by 38 nm compared to a single AuNS140 on glass (in water).

The blueshift and narrowing of the LSPR were also observed for the AuNCs60 nanostructures. Figure 2.17c shows the experimental extinction spectra of the array in air (solid black line), the simulated extinction spectrum of a single AuNC60 (the model AuNC60 discussed in section 2.2.3.1) (dashed green lines), and the simulated extinction spectrum of a periodic array having the STEM micrograph of Figure 2.9c as the unit cell. Figure 2.17d shows the corresponding spectra in water. The single–particle simulations were run by using a 0.5 nm mesh overriding the NC for optimal fidelity of vertices and edges curvatures; while for the many–body simulations it was set to 1.5 nm according to our computational resources. Moreover, since the chosen STEM micrograph exhibited 3 overgrown AuNCs60 over a sample of 17 AuNCs60 (which is more than the fraction of overgrown edges in the much larger sample previously analyzed, see Figure 2.8d), we replaced them with our model AuNC60. The resulting many–body simulations perfectly match the experimental extinction spectra of the nanostructures in both air and water. In contrast, the single–particle simulations exhibited a significant LSPR redshifted and broadening. In air, the array LSPR is peaked at 541 nm with a FWHM of 48 nm, while a single AuNC60 over glass has a (simulated) LSPR peaked at 552 nm with FWHM of 50 nm. In water, the array LSPR is peaked at 571 nm with a FWHM of 60 nm, while a single AuNC60 over glass has a (simulated) LSPR peaked at 595 nm with FWHM of 79 nm. It is worth noting that these LSPR blueshifts and broadening are smaller than the case of AuNSs140 array, compatibly with the larger centre-to-centre NND distance of AuNCs60 array compared to AuNSs60 array. However, the phenomenon was clearly observed, therefore we can affirm that the AuNSs60 constituting the array do interact with each other via the aforementioned far–field dipolar interactions among neighbouring NCs.

It is worth noting that the presence of a dielectric medium (water) greatly enhanced the physical phenomenon discussed so far. In fact, the LSPRs of the arrays in water are as pronounced as the LSPRs of the corresponding single particle on glass (solid black and dashed green lines in Figures 2.17b and d); and, at the same time, much narrower, almost like the LSPRs of the arrays in air. Note that sharp resonances are usually observed in ordered lattices fabricated by more sophisticated techniques.[7] In contrast, we obtained sharp resonances from random arrays of NPs fabricated by the simple self–assembly technique as a result of unexpected far–field dipolar coupling between large NPs. Furthermore, the LSPRs can be finely tuned over a wide spectral range by varying the surface density of the same kind of (large) NP, which can be easily achieved, e.g., by changing the concentration of the NPs used for the incubation step. Simplicity, versatility, and sharp, tuneable LSPRs are highly desirable features in many kinds of applications. In particular, we studied the distance–dependent metal enhanced fluorescence (MEF) performance of our arrays for a future application as MEF–based optical biosensor.

Chapter 3. Metal–enhanced Fluorescence (MEF)

This chapter follows the analytical treatments reported in the series of papers[63–66], and papers[67,68].

3.1 Enhancement of the Optical Absorption

The optical absorption of N_a molecules having absorption cross section σ_a placed close to a (Drude) metal nanosphere of radius a embedded in a dielectric medium ε_D can be described as a two–step process in the presence of the LSPs modes supported by the sphere. The process is schematically shown in Figure 3.1. In the specific case of a sphere, because of the spherical symmetry, the higher–order LSPs modes ($l \geq 2$) have a zero dipole moment $p_l = 0$, hence they cannot couple with the incident light (nonradiative modes). Therefore, the energy from free–space modes contained (within the far–field solid angle Ω) in the external radiation of frequency ω_{ex} gets coupled exclusively into the dipole LSP mode ($l = 1$, resonant frequency $\omega_1 = \omega_{dp}$), with an in–coupling coefficient K_{in}^{Ω}. Subsequently, the energy "stored" in the dipole mode gets absorbed at the rate γ_{abs} by the N_a molecules with absorption cross section (probability) σ_a located at distance d from the sphere.

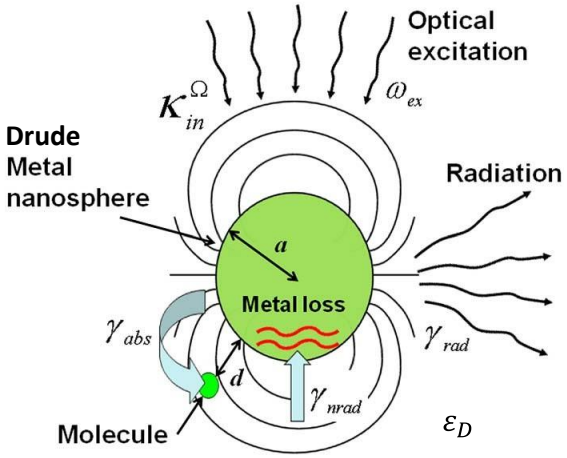

Figure 3.1. Process of enhancement of the optical absorption of a molecule placed at distance *d* from a metal sphere of radius *a*. The NP dipole is assumed to be parallel to the external radiation. (From Ref.[63])

The nonradiative decay rate γ_{abs} of the sphere dipole mode due to absorption by molecules, is

$$\gamma_{abs} = \gamma_{abs}^{free} \frac{1}{V_{\text{eff},dp}} \left(\frac{1}{1+d/a}\right)^6 = \frac{c}{n_D} \frac{N_a \sigma_a}{V_{\text{eff},dp}} \left(\frac{1}{1+d/a}\right)^6, \tag{3.1}$$

which is enhanced compared to the case of molecules in "free space" ($\gamma_{abs}^{free} = \frac{c}{n_D} N_a \sigma_a$) thanks to the Forster resonance energy transfer (FRET) from the NP dipole LSP mode towards the molecules. Here, c is speed of light in vacuum and n_D is the refractive index of the dielectric medium in which molecules (and sphere) are embedded. Instead, $V_{\text{eff},dp}$ is the effective volume of the sphere dipole mode ($l = 1$). Generally, $V_{\text{eff},l}$ is a parameter introduced by Khurgin and Sun[63] to describe the "effective volume" containing the energy U_l of l-th mode of the sphere:

$$U_l = \frac{1}{4}\varepsilon_0\varepsilon_D E_{max,l}^2 V_{\text{eff},l}$$

$$V_{\text{eff},l} \equiv \frac{8\pi a^3}{(l+1)(2l+1)}\left[1+\frac{l}{\varepsilon_D(l+1)}\right], \qquad V_{\text{eff},dp} \equiv V_{\text{eff},1} = \frac{4}{3}\pi a^3\left(1+\frac{1}{2\varepsilon_D}\right) \tag{3.2}$$

Note that we are referring to the subscript $l = 1$ for the dipole mode as '*dp*'.

The molecules absorption enhancement factor EF_{abs} is defined as the ratio of the absorption rate of the dipole energy $B_{dp} \equiv \gamma_{abs}U_{dp}$ (the power absorbed by molecules in presence of the metal nanosphere) to their rate of absorption B_{free} of the incident light in absence of the metal sphere (molecules "free space", or natural, absorption). Assuming $\boldsymbol{p}_{dp} \,//\, \boldsymbol{E_{ex}}$

$$B_{dp} \equiv \gamma_{abs}U_{dp} = \frac{c}{n_D}N_a\sigma_a\left(\frac{1}{4}\varepsilon_0\varepsilon_D E_{max,dp}^2\right)\left(\frac{1}{1+d/a}\right)^6 \tag{3.3}$$

$$B_{free} \equiv \gamma_{abs}^{free}U_{ex}^{free} = \left(\frac{c}{n_D}N_a\sigma_a\right)\left(\frac{1}{2}\varepsilon_0\varepsilon_D E_{ex}^2\right) \tag{3.4}$$

and the molecules absorption enhancement factor $EF_{abs}(\omega_{ex})$ is:[63]

$$EF_{abs}(\omega_{ex}) \equiv \frac{B_{dp}}{B_{free}} = \frac{1}{2}\frac{E_{max,dp}^2}{E_{ex}^2}\left(\frac{1}{1+d/a}\right)^6 = \\ = \frac{9\varepsilon_D}{4}\left(\frac{\omega_{dp}}{\omega_{ex}}\right)^2\frac{1}{\delta_{ex}^2+(Q_{rad}^{-1}+Q_{nrad}^{-1}+Q_{abs}^{-1})^2}\left(\frac{1}{1+d/a}\right)^6 \tag{3.5}$$

where:

$$\gamma_{dp} \equiv \gamma_{rad}+\gamma_{nrad}+\gamma_{abs}\ , \qquad \delta_{ex} \equiv (1+2\varepsilon_D)\frac{|\omega_{ex}-\omega_{dp}|}{\omega_{dp}}$$

$$Q_{rad} \equiv \frac{2\,\omega_{dp}}{(1+2\varepsilon_D)}\frac{1}{\gamma_{rad}} = \chi^{-3}, \qquad \gamma_{rad} = \frac{2\,\omega_{dp}}{(1+2\varepsilon_D)}\chi^3\,, \qquad \chi \equiv \frac{2\pi a}{\lambda_{dp}}, \qquad \chi_d \equiv \frac{2\pi d}{\lambda_{dp}} \tag{3.6}$$

$$Q_{nrad} \equiv \frac{2\,\omega_{dp}}{(1+2\varepsilon_D)}\frac{1}{\gamma_{nrad}} \approx \frac{2\,\omega_{dp}}{(1+2\varepsilon_D)}\frac{1}{\gamma}\,, \qquad \gamma \equiv \gamma_{Drude}$$

$$Q_{abs} \equiv \frac{2\,\omega_{dp}}{(1+2\varepsilon_D)}\frac{1}{\gamma_{abs}} = \frac{\lambda_{dp}^2}{3\pi\varepsilon_D}\frac{1}{N_a\sigma_a}(1+d/a)^6\chi^3$$

Here, γ_{dp} is the total decay rate of the sphere dipole mode, which is the sum over the three contributions of radiative decay γ_{rad}, nonradiative decay γ_{nrad} due to metal losses, and nonradiative decay γ_{abs} due to energy transfer to the molecules. The parameter δ_{ex} is the normalized excitation detuning, which accounts for mismatches between the frequency of the external excitation radiation and the dipole mode frequency. Finally, Q_{rad} is a Q factor for the radiative decay γ_{rad} of the dipole mode; χ is a normalized NP radius; Q_{nrad} is a Q factor for the

nonradiative decay γ_{nrad} of the dipole mode due to metal losses ($\gamma_{nrad} \approx \gamma$ for a Drude metal described by the dielectric function $\varepsilon(\omega) = 1 - \omega_p^2/(\omega^2 + i\gamma\omega)$); Q_{abs} is a Q factor for the nonradiative decay of the dipole mode due to absorption by molecules.

The equation for $EF_{abs}(\omega_{ex})$ can be optimized in many ways. For instance, at $\omega_{ex} = \omega_{dp}$ and $N_a\sigma_a \approx 0$ (i.e., $\delta_{ex} \approx 0$ and $Q_{abs}^{-1} \approx 0$), the max EF_{abs} at a given NP–molecules distance d is:

$$\begin{cases} \omega_{ex} = \omega_{dp} \\ \\ N_a\sigma_a \approx 0 \end{cases} \Rightarrow \quad EF_{abs}^{MAX} = \frac{9/4 \;\; \varepsilon_D Q_{nrad}^2}{\left(1 + \chi_d^{3/4} \, Q_{nrad}^{1/4}\right)^8} \quad \text{at} \quad a_{MAX} = \left(\frac{\lambda_{dp}}{2\pi}\right)^{\frac{3}{4}} \left(\frac{d}{Q_{nrad}}\right)^{\frac{1}{4}} \tag{3.7}$$

While optimization at resonance $\omega_{ex} = \omega_{dp}$ for small $d \approx 0$ but arbitrary $N_a\sigma_a$ gives:

$$\begin{cases} \omega_{ex} = \omega_{dp} \\ \\ d \approx 0 \end{cases} \Rightarrow EF_{abs}^{MAX} = \frac{9\varepsilon_D Q_{nrad}^2}{4} \left[2Q_{nrad} \left(\frac{3\pi\varepsilon_D N_a\sigma_a}{\lambda_{dp}^2} \right)^{\frac{1}{2}} + 1 \right]^{-2} \quad \text{at } \chi_{MAX} = \left(\frac{3\pi\varepsilon_D N_a\sigma_a}{\lambda_{dp}^2} \right)^{\frac{1}{6}} \tag{3.8}$$

Whenever $N_a\sigma_a \geq \lambda_{dp}^2/(12\,\pi\varepsilon_D Q_{nrad}^2)$, the total absorption of the molecules $N_a\sigma_a$ starts to play a significant role in determining the upper limit of EF_{abs}^{MAX}. For the Ag/GaN system of Khurgin and Sun[63], constituted by a Ag nanosphere embedded in GaN ($\hbar\omega_{dp} = 2.35$, $\varepsilon_D = 5.8$), it follows that $N_a\sigma_a \geq \lambda_{dp}^2/(12\,\pi\varepsilon_D Q_{nrad}^2) \approx 7$ nm^2, and above this threshold the EF_{abs}^{MAX} experimented by the molecules is limited by their own presence. For instance, fluorescent molecules (fluorophores) usually have $\sigma_a \lesssim 0.1$ nm^2 (being 0.1 nm^2 the σ_a of the large Rhodamine 6G[63]). It follows that a small number of fluorophores (few tens) play no role in determining the upper limit of EF_{abs}^{MAX}; but a hundred of fluorophores do limit EF_{abs}^{MAX} since the surplus of energy provided by NP has to be divided among many molecules, hence each of them has less energy at his disposal.

In the case of the Ag/GaN system of Khurgin and Sun,[63] some overall trends can be visualized in Figure 3.2. In Figure 3.2a the significant impact of the absorbing molecules on EF_{abs} is evident: for instance, EF_{abs} decreases from ≈ 34 to ≈ 8.5 when $N_a\sigma_a$ increases from 1 nm^2 to 100 nm^2, for $a = 15$ nm ($d = 5$ nm, $\omega_{ex} = \omega_{dp}$). It is also worthwhile to note that the local maximum in EF_{abs} is due to the opposite trend of $Q_{rad}^{-1} \propto a^3$ (or, equivalently, $\gamma_{rad} \propto a^3$) and $Q_{abs}^{-1} \propto a^{-3}$ (or, equivalently, $\gamma_{abs} \propto a^{-3}$) with increasing AgNP radius (Q_{nrad}^{-1} is constant). When the AgNP is too large, most of the energy stored into the dipole mode is radiated to the far–field and, therefore, little energy can be transferred non–radiatively (by FRET) to the molecules. Consequently, EF_{abs} decreases. Conversely, if a is too small, FRET mechanism is inefficient, and the molecules scarcely absorb. Figure 3.2b shows a 2D plot of EF_{abs}^{MAX} at resonance as a function of $(d, N_a\sigma_a)$, and in which it is maximized with respect to the AgNP radius a. Along each line, the AgNP radius a varies to maximize $EF_{abs}(d, N_a\sigma_a)$. The optimized EF_{abs}^{MAX} clearly indicate that the strongest EF_{abs} is attainable for a small number of weakly absorbing molecules placed close to the Ag nanosphere, while for a large number of strong absorbers the EF_{abs} is considerably lower if present at all.

We conclude that metal nanospheres can dramatically improve the performance of optical sensors in which the analyte molecules are few and their original absorption is low. At the same time, when the original absorption is already significant, the enhancement is weak or non–existent.

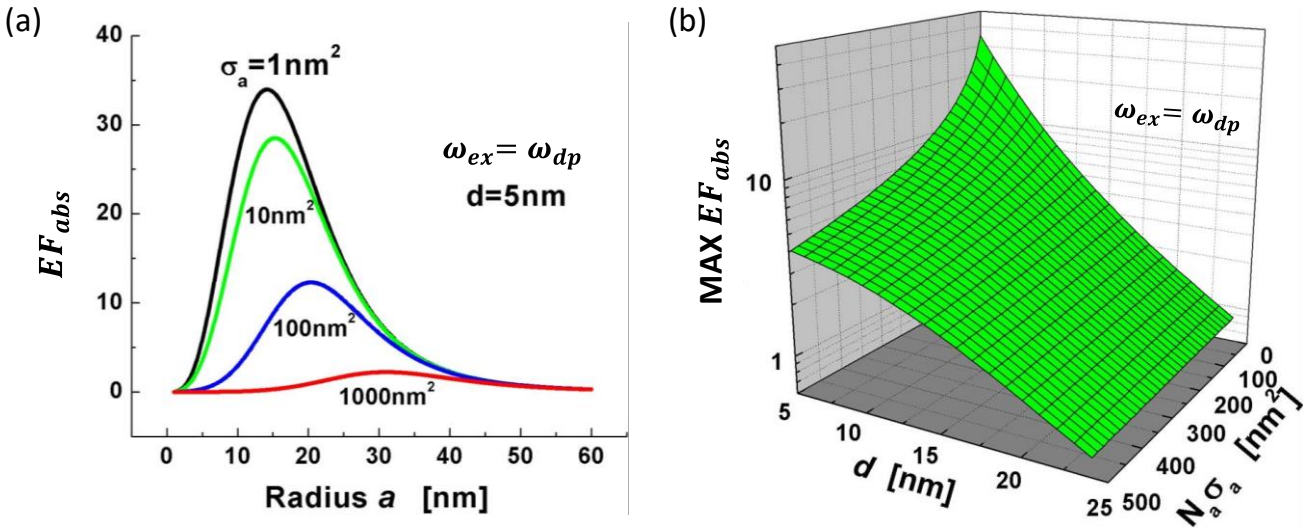

Figure 3.2. EF_{abs} for the Ag/GaN system of Khurgin and Sun.[63] (a) EF_{abs} at the dipole resonance ω_{dp} as a function of the Ag nanosphere radius *a* at various values of the total absorption cross section $N_a\sigma_a$ of absorbing molecules placed at $d = 5$ nm from the Ag sphere. (b) EF_{abs}^{MAX} for optimized sphere radii at ω_{dp} for absorbing molecules with total absorption cross section $N_a\sigma_a$ placed at distance *d* from the Ag nanosphere. (Adapted from Ref.[63])

3.2 Enhancement of the Optical Emission

The electroluminescence emission by an excited molecule can be treated as a two-step process, as shown in Figure 3.3. First, the electrically excited molecule with original radiative decay rate τ_{rad}^{-1} relaxes by emitting energy of frequency ω_{em} into all LSP modes associated with the metal nanosphere at the rate of $F_{p,l}\tau_{rad}^{-1}$ for the l–th mode, enhanced by the Purcell factor $F_{p,l}$. In the specific case of a sphere, because of the spherical symmetry, only the dipole LSP mode $l = 1$ has a non–zero dipole moment and will subsequently couple–out to external radiation by decaying radiatively at the rate γ_{rad} (it will also decay nonradiatively at the rate γ_{nrad}). All higher–order LSP modes $l \geq 2$, having $p_l = 0$, do not couple with the external radiation and will exclusively dissipate nonradiatively into the metal at the rate γ_{nrad}. Simultaneously, the molecule itself also internally relaxes nonradiatively at its original nonradiative rate τ_{nrad}^{-1}.

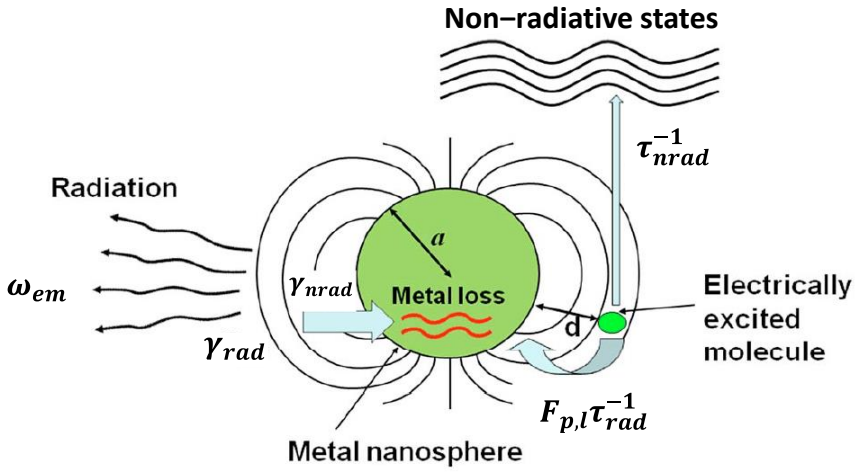

Figure 3.3. Process of enhancement of the electroluminescence emission by a molecule placed at distance *d* from a metal sphere of radius *a*. The NP dipole is assumed to be parallel to the external radiation (From Ref.[63])

The Purcell factor $F_{p,l}$ can be estimated as a ratio of the effective density of the l–th mode $\rho_l(\omega_{em}, d)$ to the effective density of the radiation continuum $\rho_{rad}(\omega_{em})$ associated with an electroluminescence emission wavelength λ_{em} in the dielectric whose polarization is lined up with the LSP dipole. Therefore, being:

$$\rho_l(\omega_{em}, d) = \frac{L_l(\omega_{em})}{V_{\text{eff},l}}\left(1 + \frac{d}{a}\right)^{-2l-4} \tag{3.9}$$

$$\rho_{rad}(\omega_{em}) = \frac{1}{3\pi^2}\left(\frac{2\pi}{\lambda_{em}}\right)^3 \frac{1}{\omega_{em}} \tag{3.10}$$

with $L_l(\omega)$ is the normalized Lorentzian linewidth factor of the l–th mode,

$$L_l(\omega) = \frac{\gamma_l/2\pi}{(\omega_{em} - \omega_l)^2 + \gamma_l^2/4}, \qquad \gamma_l \equiv \begin{cases} \gamma_{rad} + \gamma_{nrad}, & l = 1 \\ \gamma_{nrad}, & l \geq 2 \end{cases} \tag{3.11}$$

the Purcell Factor is:

$$F_{p,l}(\omega_{em}) = \frac{\rho_l(\omega_{em}, d)}{\rho_{rad}(\omega_{em})} = \frac{3\pi\varepsilon_D\omega_{em}L_l(\omega_{em})}{8\chi_{em}^3}\frac{(2l+1)(l+1)^2}{\varepsilon_D(l+1)+l}\left(\frac{1}{1+d/a}\right)^{2l+4} \tag{3.12}$$

where $\chi_{em} = 2\pi a/\lambda_{em}$.

Let us discuss the Purcell factors at resonance $\omega_{em} = \omega_{dp}$, i.e., when the molecules emit energy resonantly with the dipole mode frequency. The Purcell factors at $\omega_{em} = \omega_{dp}$, i.e., $F_{p,l}(\omega_{dp})$, clearly demonstrate the physical origin of luminescence quenching (see Figure 3.4): as the separation d decreases, progressively larger fraction of energy stored in the excited molecule gets coupled into the higher–order modes ($l \geq 2$), where it gets subsequently dissipated into the metal (the higher–order modes decay only nonradiatively in the case of a sphere). Figure 3.4 showcases $F_{p,l}(\omega_{dp})$ at few distances d from a Au nanosphere of radius $a = 30$ nm in GaN dielectric.

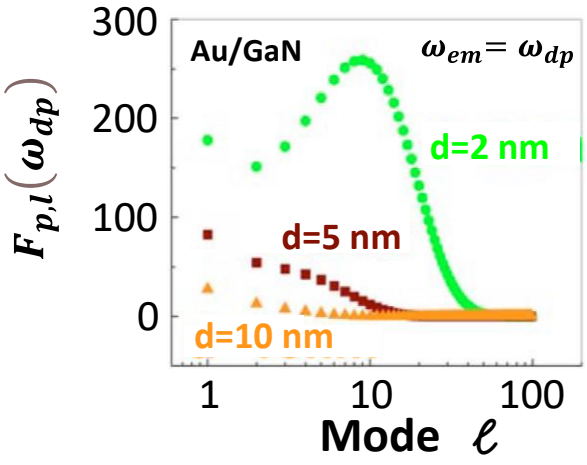

Figure 3.4. Purcell factors at the dipole resonance ω_{dp} associated with various LSP modes for a molecule placed at $d = 2, 5, 10$ nm from a Au nanosphere of radius $a = 30\ nm$ embedded in GaN dielectric. (Adapted from Ref.[64])

This phenomenon is better illustrated through the cumulative effect of the higher–order modes, known as "luminescence quenching ratio" f_q and defined as:

(Exact) Quenching Ratio

$$f_q(\omega_{dp}) \equiv \frac{\sum_{l=2}^{\infty} F_{p,l}(\omega_{dp})}{F_{p,1}(\omega_{dp})} = \sum_{l=2}^{\infty} \frac{\pi \gamma_{dp} L_l(\omega_{dp})(2\varepsilon_D + 1)}{24(1 + d/a)^{2l-2}} \frac{(2l+1)(l+1)^2}{\varepsilon_D(l+1) + l} \tag{3.13}$$

An analytical estimation of $f_q(\omega_{dp})$ can be obtained using some average mode frequency $\bar{\omega}_{l\geq 2}$ of the nonradiative modes in the Lorentzian $L_l(\omega_{dp})$ and also assuming $2\varepsilon_D \gg 1$:

Approximated Quenching Ratio

$$f_q(\omega_{dp}) \approx \frac{1}{12} \frac{\gamma_{dp}\, \gamma_{nrad}}{(\bar{\omega}_{l\geq 2} - \omega_{dp})^2 + \gamma_{nrad}^2/4} \sum_{l=2}^{\infty} \frac{(2l+1)(l+1)}{(1 + d/a)^{2l-2}} \approx$$

$$\approx \frac{1}{6}(1 + Q_{nrad}\, \chi^3) \frac{1}{1 + \delta_{l\geq 2}^2} \left(\frac{a}{d}\right)^3 \tag{3.14}$$

where the average detuning $\delta_{l\geq 2}$ is defined as

$$\delta_{l\geq 2} \equiv \frac{2(\bar{\omega}_{l\geq 2} - \omega_{dp})}{\gamma_{nrad}} = \frac{2(\bar{\omega}_{l\geq 2} - \omega_{dp})}{\gamma_{Drude}} \,. \tag{3.15}$$

The d^{-3} dependence of Eq. (3.14) is the same luminescence–quenching dependence that can be obtained using the simple model of a dipole close to a flat metal surface by the method of image charges; but here this rate also shows a strong frequency dependence due to $\delta_{l\geq 2}^2$ (which, in turn, strongly depends on the metal).

Figure 3.5 compares the exact and approximated results for $f_q(\omega_{dp})$ for a Au nanosphere of radius 30 nm embedded in GaN ($\varepsilon_D = 5.8$). In a Drude model, the Au/GaN system parameters are: $\hbar\omega_{dp} = 1.97$ eV; $\hbar\omega_\infty = 2.26$ eV; $\hbar(\bar{\omega}_{l\geq 2} - \omega_{dp}) = 0.28$ eV; $\hbar\gamma_{Drude} \approx 0.2$ eV; $Q_{nrad} = 1.55$; $\delta_{l\geq 2} = 2.82$. The d^{-3} approximation is accurate for $d \leq 5$ but significantly underestimates the quenching effect of the high–order modes for $d \geq 10$ nm. Considering a $10 - 20\%$ of quenching as negligible, then a molecule should be placed at $d \geq 50\ \text{nm} \approx 2a$ far from the AuNP (of radius $a = 30$ nm) in order to have a negligible quenching of its emission.

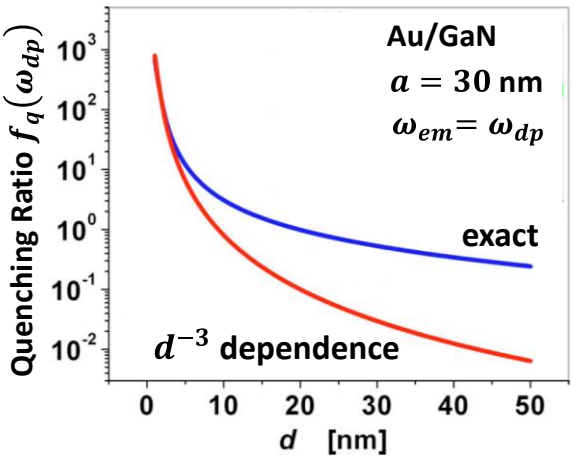

Figure 3.5. Quenching ratios at ω_{dp} obtained exactly by Eq. (3.13) and approximately by Eq. (3.14) as a function of the molecule distance *d* from an Au sphere of radius $a = 30$ nm embedded in GaN ($\delta_{l\geq 2} = 2.82$). (Adapted from Ref.[64])

Generally, considering a $10-20\%$ of quenching as negligible, the approximate d^{-3} dependence would suggest placing a molecule at a minimum distance

$$d^{-3}\ \text{approximation} \implies d \geq d_{min} \approx \left[(1+Q_{nrad}\,\chi^3)\frac{1}{1+\delta_{l\geq 2}^2}\right]^{\frac{1}{3}} a\ . \tag{3.16}$$

For the considered Au/GaN system (see relevant parameters above) the approximate d^{-3} dependence would suggest $d_{min} \approx 15$ nm, which is significantly underestimated (see Figure 3.5).

For the Ag/GaN system, instead, the approximate d^{-3} dependence would suggest $d_{min} \approx 5$ nm which is sufficiently small to match with the exact prediction. Therefore, the quenching effect of the higher–order modes is negligible for an emitter placed at $d \geq 5$ nm far from a Ag nanosphere of radius $a = 30$ nm embedded in GaN. Recall that at these small separation distances EF_{abs} is close to its maximum, hence the high gain in absorption is, at least, not quenched off. The relevant parameters for the Ag/GaN system (in a Drude model) are: $\hbar\omega_{dp} = 2.35$ eV; $\hbar\omega_{\infty} = 3.19$ eV; $\hbar(\overline{\omega}_{l\geq 2} - \omega_{dp}) \approx 0.8$ eV; $\hbar\gamma_{Drude} \approx 0.067$ eV; $Q_{nrad} = 5.54$; $\delta_{l\geq 2} = 23.88$.

It is worth noting that the $\delta_{l\geq 2}$ value for the Ag/GaN system is 8.5 times higher than Au/GaN. Such a huge difference is due to both the higher average energy detuning of the AgNP dipole mode with respect to the higher–order modes ($\hbar(\overline{\omega}_{l\geq 2} - \omega_{dp}) = 0.8$ eV for the Ag/GaN versus 0.28 eV for the Au/GaN) and the lower metal losses ($\hbar\gamma_{Drude} = 0.067$ eV for Ag/GaN versus 0.2 for Au/GaN). In other words, the energy emitted by a molecule gets efficiently coupled to the higher–order modes of the AuNP since their energies are similar to the energy of the dipole mode, an energy subsequently lost in the metal. Conversely, the energy emitted by a molecule gets inefficiently coupled to the higher–order modes of the AgNP as the average energy difference between the dipole mode and the higher–order modes is significant, hence a much smaller fraction of the emitted energy can be lost in the metal. This concept is well quantified by $\hbar(\omega_{\infty} - \omega_{dp})$, which is equal to 0.29 eV for the Au/GaN system and 0.84 eV for the Ag/GaN system.

Let us now continue from Eq. (3.12). We consider again a generic ω_{em}.
Let us explicitly write $F_{p,1}(\omega_{em})$:

$$F_{p,1}(\omega_{em}) = \frac{9\varepsilon_D}{2\chi_{em}^3}\left(\frac{\omega_{em}}{\omega_{dp}}\right)\frac{\chi^3 + Q_{nrad}^{-1}}{\delta_{em}^2 + (\chi^3 + Q_{nrad}^{-1})^2}\left(\frac{1}{1+d/a}\right)^6 \tag{3.17}$$

where $\delta_{em} \equiv (1+2\varepsilon_D)|\omega_{em} - \omega_{dp}|/\omega_{dp}$. Let us remember that the excited molecule relaxes its energy into all nanosphere electromagnetic modes and only the dipole mode couples–out to the external radiation. Therefore, this Purcell factor $F_{p,1}(\omega_{em})$ is the one that directly contributes to the enhancement of the optical emission of the excited molecule, while all the other Purcell factors boost the losses. As shown in Figure 3.6 at the dipole resonance for Ag/GaN, $F_{p,1}$ exhibits a strong dependence on both the molecule distance and the NP size: $F_{p,1}$ diminishes very quickly with the separation distance d between NP and emitter; for a fixed d, it rapidly increases with the sphere size a, reaches a local maximum, and then decreases in a relatively mild way as the normalized sphere volume χ^3 increases.

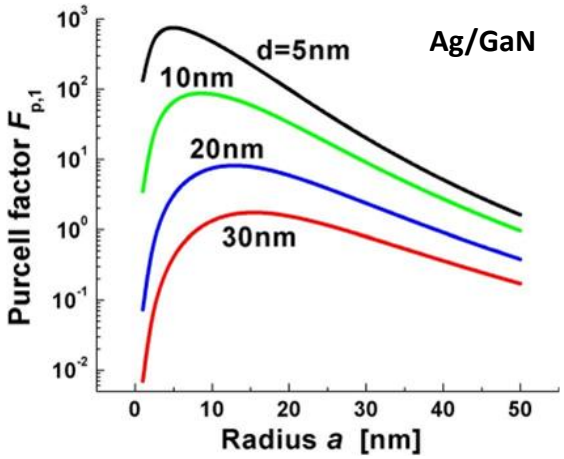

Figure 3.6. Purcell factor $F_{p,1}(\omega_{dp})$ of Ag/GaN system as a function of the sphere radius a for NP–molecule separation $d = 5, 10, 20, 30$ nm. The exact positions of the maxima are not relevant. (From Ref.[63])

However, the trend for $F_{p,1}$ is not relevant per se, as the radiative emission gain introduced by $F_{p,1}$ is partially or totally attenuated by the nonradiative emission gains introduced by all the other $F_{p,l\geq 2}$, since in the case of a sphere all the higher–order modes do not couple to external radiation.

Let us then introduce the original, "free space" radiative efficiency η_{rad}^{free} of the molecule together with its corresponding radiative efficiency in the presence of the metal nanosphere η_{rad}^{M}:

$$\eta_{rad}^{free} \equiv \frac{\tau_{rad}^{-1}}{\tau_{rad}^{-1} + \tau_{nrad}^{-1}} \tag{3.18}$$

$$\eta_{rad}^{M} \equiv \frac{\tau_{rad}^{-1} + F_{p,1}\tau_{rad}^{-1}\,\xi_{rad,1}}{\tau_{rad}^{-1} + \sum_{l=1}^{\infty} F_{p,l}\,\tau_{rad}^{-1} + \tau_{nrad}^{-1}} = \frac{\tau_{rad}^{-1} + \xi_{rad,1}\,F_{p,1}\tau_{rad}^{-1}}{\tau_{rad}^{-1}(1 + F_{p,1} + F_{p,1}\,f_q) + \tau_{nrad}^{-1}} \tag{3.19}$$

where

$$\xi_{rad,1} \equiv \frac{\gamma_{rad,1}}{\gamma_{rad,1} + \gamma_{nrad,1}} = \frac{Q_{nrad}\chi^3}{1 + Q_{nrad}\chi^3} \tag{3.20}$$

is the radiative coupling efficiency of the nanosphere dipole mode into the radiation continuum. Note that $\xi_{rad,1}$ is higher for larger NPs ($Q_{nrad}\chi^3 \gg 1$), while for smaller NPs the nonradiative decay of the dipole mode dominates ($Q_{nrad}\chi^3 \ll 1$). Recall that, for a nanosphere, the dipole mode is the only one decaying both radiatively and nonradiatively, i.e., $\gamma_1 = \gamma_{dp} = \gamma_{rad} + \gamma_{nrad}$. We also used formulae (3.6).

It follows that the molecule emission efficiency enhancement factor EF_{QY} is the ratio:

$$EF_{QY} \equiv \frac{\eta_{rad}^{M}}{\eta_{rad}^{free}} = \frac{1 + \xi_{rad,1}\,F_{p,1}}{1 + F_{p,1}\big(1 + f_q\big)\,\eta_{rad}^{free}} \tag{3.21}$$

where the subscript "QY" stands for "quantum yield", a synonymous for emission efficiency. We clearly see the presence of the quenching ratio f_q at the denominator, meaning that the effect of the higher–order electromagnetic modes of a sphere on the molecule emission is a quenching effect. In order to have $EF_{QY} > 1$, it must be $\xi_{rad,1} > \big(1 + f_q\big)\,\eta_{rad}^{free}$, i.e., the radiative coupling

efficiency of the nanosphere dipole mode into the radiation continuum must be greater than the free space radiative efficiency of the molecule for a factor $(1 + f_q)$ depending on the quenching. It is evident that when $\eta_{rad}^{free} \ll 1$ is very easy to have $EF_{QY} > 1$, while it is progressively harder when $\eta_{rad}^{free} \longrightarrow 1$. Even for the ideal case $f_q \approx 0$, it must be $\xi_{rad,1} > \eta_{rad}^{free}$ to have $EF_{QY} > 1$.

To analyse EF_{QY}, let us first consider the ideal case $f_q \approx 0$ of negligible quenching.

This ideal case is very pregnant, since it clearly shows that the emission enhancement is the highest for very low–quality emitters ($\eta_{rad}^{free} \ll 1$). In fact, at resonance:

$$\begin{cases} f_q \approx 0 \\ \eta_{rad}^{free} \ll 1 \\ \omega_{em} = \omega_{dp} \end{cases} \quad \Longrightarrow \quad EF_{QY} \approx 1 + \xi_{rad,1}\, F_{p,1} = 1 + \frac{9\varepsilon_D Q_{nrad}^2}{2(1 + Q_{nrad}\chi^3)^2}\left(\frac{1}{1 + d/a}\right)^6 \tag{3.22}$$

As we saw in Figure 3.6, $F_{p,1}$ is greatly enhanced for small nanospheres at small distances, whereas $\xi_{rad,1}$ decreases for small nanospheres. Therefore, in this case we easily predict a sharp local maximum for relatively small NPs and small separation distances. In fact, in the case of a molecule with original radiative efficiency $\eta_{rad}^{free} \ll 1$, the matter of most concern is the transfer of energy from the excited molecule into the nanosphere dipole mode before the molecule "wastes" its energy via internal nonradiative decay (being $\eta_{nrad}^{free} \approx 1$). The energy transfer to the nanosphere dipole mode depends on $F_{p,1}$, and favours small nanoparticle size (see Figure 3.6) for its small effective mode volume; on the other hand, a small volume also leads to small radiative coupling efficiency $\xi_{rad,1}$ of the dipole mode into the radiation continuum. As a result, the increase of EF_{QY} with the reduction of the nanoparticle volume quickly saturates when $\eta_{rad}^{free} \ll 1$.

When $f_q \approx 0$ but η_{rad}^{free} is finite,

$$\begin{cases} f_q \approx 0 \\ \eta_{rad}^{free} \text{ finite} \end{cases} \quad \Longrightarrow \quad EF_{QY} \approx \frac{1 + \xi_{rad,1}\, F_{p,1}}{1 + F_{p,1}\, \eta_{rad}^{free}} \tag{3.23}$$

i.e., EF_{QY} is still higher for smaller η_{rad}^{free} but now the dependence on the nanosphere size is more complicated since the size dependence appears also at the denominator through $F_{p,1}$.

The Ag/GaN system well represents the ideal case $f_q \approx 0$ whenever the emitter is placed at distances $d > d_{min} \approx 5$ nm, as previously showed. Figure 3.7a shows the EF_{QY} for such a system as a function of the Ag nanosphere radius for emitters of various η_{rad}^{free} placed at $d = 10$ nm, where $f_q \approx 0$. We can see that EF_{QY} exhibits strong dependence upon the nanosphere dimensions with the peak occurring when the radius is small enough to yield smaller effective mode volume for an enhanced Purcell factor $F_{p,1}$, yet is still sufficiently large to assure strong radiative coupling of the dipole mode $\xi_{rad,1}$. As expected, the higher the original radiative efficiency η_{rad}^{free}, the less critical becomes the concern of transferring energy from the emitter into the dipole mode, and, accordingly, the more important becomes the concern for the efficient energy transfer from the dipole mode into free–space radiation modes. This situation favours larger nanoparticles that can emit the dipole mode energy into the free space modes before it get lost in the metal. Finally, Figure 3.7b shows the maximum EF_{QY} attainable by Ag spheres whose size is optimized for each molecule position *d* and original radiative efficiency η_{rad}^{free}. It is evident

that as η_{rad}^{free} increases (in particular, when $\eta_{rad}^{free} \geq 0.05$) all the EF_{QY} rapidly decreases and point to 1, as the emission of a molecule with $\eta_{rad}^{free} \approx 1$ cannot be further enhanced by definition.

Considering both the graphs, it can be concluded that the EF_{QY} is higher for those molecules with smaller original radiative efficiency η_{rad}^{free} and gets reduced rather quickly as $\eta_{rad}^{free} \longrightarrow 1$ as well as it is placed further away from the metal nanoparticle. For distances $d < d_{min} \approx 5$ nm, quenching effects always dominates and yield significant reduction of the emission (for this reason they were omitted from Figure 3.7b)

To conclude the discussion of the simplest, ideal case $f_q \approx 0$, let us also consider the final emission efficiencies in the presence of a metal, η_{rad}^{M}. From Figure 3.7a we see that when $\eta_{rad}^{free} = 0.001$, $EF_{QY}^{MAX} \approx 20$, implying that $\eta_{rad}^{M} \approx 0.02$ at max; when $\eta_{rad}^{free} = 0.01$, $EF_{QY}^{MAX} \approx 15$, implying that $\eta_{rad}^{M} \approx 0.15$ at max; when $\eta_{rad}^{free} = 0.1$, $EF_{QY}^{MAX} \approx 5$, implying that $\eta_{rad}^{M} = 0.5$. Therefore, the emission efficiency of low–quality fluorophores can be sensibly increased but not so much to surpass the emission of already high–quality emitters. For applications requiring high emissions, like optical biosensing, it is more convenient using higher quality fluorophores (whose emission cannot be further enhanced) rather than lower quality fluorophores (whose emission can be enhanced but cannot surpass the emission of the higher quality ones).

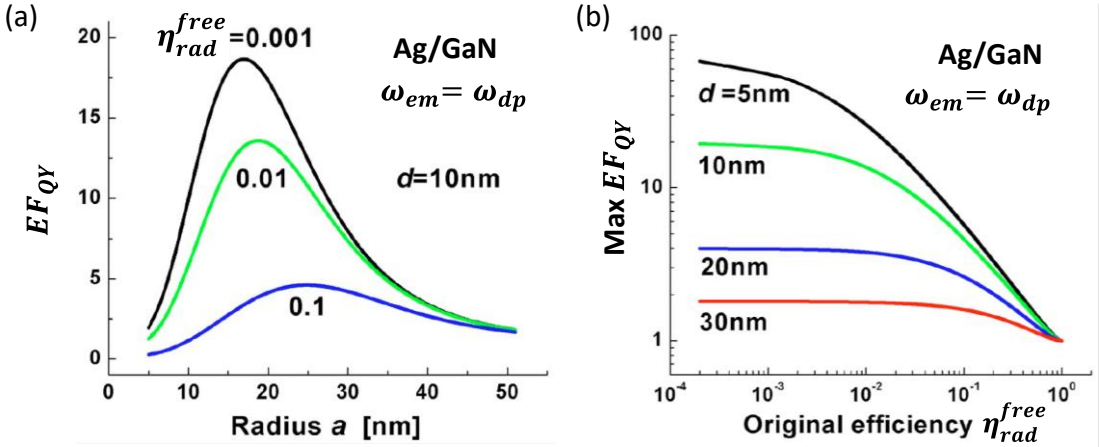

Figure 3.7. (a) EF_{QY} at resonance attainable by an Ag nanosphere embedded in GaN as a function of sphere radius a for few original η_{rad}^{free} of molecules placed at $d = 10$ nm (f_q is negligible at such distance).(b) Maximum EF_{QY} attainable by size-optimized Ag nanosphere embedded in GaN as a function of the η_{rad}^{free} of molecules at distance d from the metal sphere (f_q is negligible at such distances). Along each line the AgNP size varies. (Adapted from Ref.[63])

Let us now discuss the case of non–negligible f_q.

The Au/GaN system provides a good example since f_q cannot be neglected neither for small nor for large molecule–AuNP separation distances (see Figure 3.5).

Figure 3.8a shows the calculated 2D plot for the EF_{QY} of the Au/GaN system as a function of both the Au nanosphere radius and the molecule–sphere distance for a molecule with original $\eta_{rad}^{free} = 0.01$. As in the ideal case of no quenching, the optimal nanosphere size a_{opt} is some radius which is small enough to yield small effective mode volume for an enhanced Purcell factor $F_{p,1}$, yet is still sufficiently large to assure strong radiative out–coupling $\xi_{rad,1}$ of the dipole mode. However, in contrast to the ideal case —where is always better to have molecules positioned as close as possible to the metal sphere in order to take advantage of the large Purcell factor of the dipole

mode $F_{p,1}$— in this case EF_{QY} has a local maximum at some intermediate value of $d = d_{opt}$. In fact, the energy of the excited molecules placed too close to the metal sphere gets coupled into the higher–order, nonradiative (or "dark") modes, and dissipates as metal loss. As a result, the optimized separation d_{opt} is the one allowing for significant coupling into the dipole mode while adequately attenuating the luminescence quenching due to the high–order modes. In the specific case considered, the molecule with original $\eta_{rad}^{free} = 0.01$ experiments an $EF_{QY}^{MAX} \approx 4$ when placed at $d_{opt} \approx 10$ nm far from a Au nanosphere of $a_{opt} \approx 25$ nm embedded in GaN. This EF_{QY}^{MAX} is ≈ 3 times lower than the one obtained in the Ag/GaN system (green line in Figure 3.7a) with the same parameters ($a_{opt} \approx 25$ nm, $d = 10$ nm, $\eta_{rad}^{free} = 0.01$).

The optimized EF_{QY}^{MAX} for a wide range of original radiative efficiencies η_{rad}^{free} obtained at the corresponding a_{opt} and d_{opt} is shown in Fig. 3.8b.

For molecules with low η_{rad}^{free} the matter of most concern is to compete with their own high nonradiative decay rate τ_{nrad}^{-1} by transferring energy into the dipole mode even at the expense of simultaneous coupling into high–order modes. This case favours small NPs and small d.

For higher η_{rad}^{free}, the concern of energy transfer from the molecule to the dipole mode becomes less critical; rather, acquire importance both the energy transfer from the dipole mode to free–space radiation and the energy loss in the metal caused by coupling into the higher–order modes. Obviously, this situation prefers larger nanospheres, as they are characterized by higher γ_{rad} (hence higher $\xi_{rad,1}$), and larger separations distances, which reduce the energy coupling into the high–order modes (i.e., reduce f_q, see blue line in Figure 3.5).

As a general conclusion, EF_{QY} can be quite strong for weak emitters, even with metal nanospheres with high losses (as gold). Instead, for efficient emitters ($\eta_{rad}^{free} > 0.05$), EF_{QY} is much limited, even for metal nanospheres with low losses (as silver).

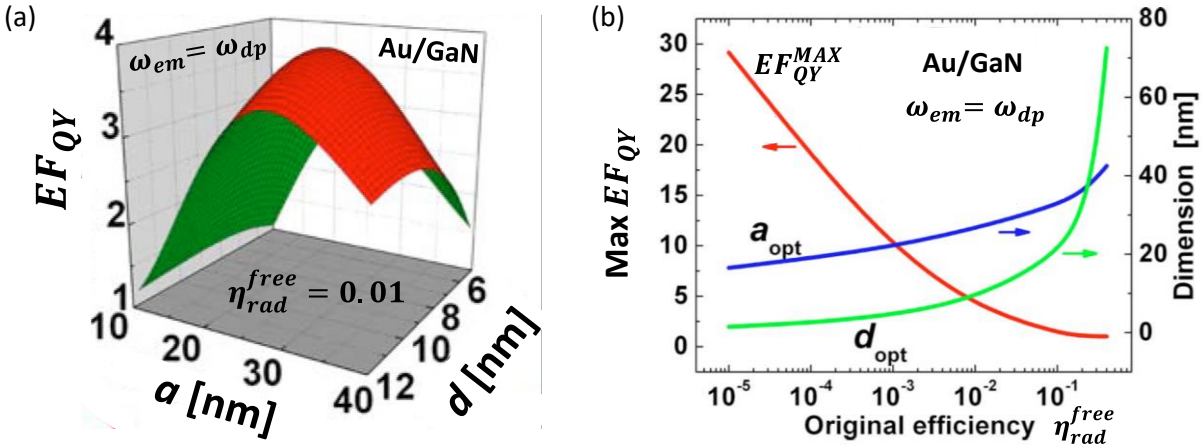

Figure 3.8. (a) EF_{QY} at resonance attainable by Au nanospheres embedded in GaN as a function of both the AuNP radius and the molecule-sphere distance for a molecule with original $\eta_{rad}^{free} = 0.01$. (b) Optimized EF_{QY}, Au nanosphere radius, and molecule-sphere separation over a range of original radiative efficiency. (Adapted from Ref.[64])

3.3 Enhancement of the Photoluminescence

Figure 3.9 illustrates the enhancement of the complete photoluminescence process, which is the combination of optical absorption and optical emission processes illustrated in Figs. 3.1 and 3.3 respectively. Optical excitation at the frequency of ω_{ex} is focused into the region where a metal nanosphere and a molecule separated by distance *d* are located. The excitation beam couples only into the dipole mode confined around the metal sphere with an in-coupling coefficient K_{in}^{Ω}. Energy stored into the sphere dipole mode is then absorbed at the rate γ_{abs} by the active molecules with total absorption cross section $N_a\sigma_a$. This absorption process competes with radiative and nonradiative decays of the dipole mode with decay rates of γ_{rad} and $\gamma_{nrad} = \gamma_{Drude}$, respectively. The optically excited molecule with the original radiative decay rate τ_{rad}^{-1} subsequently relaxes by emitting energy at the frequency ω_{em} into all the LSP modes associated with the metal nanosphere at the rate of $F_{p,l}\tau_{rad}^{-1}$ for the l–th mode, enhanced by the Purcell factor $F_{p,l}$. All the energy stored in the higher–order modes ($l \geq 2$) is subsequently lost in the metal nanosphere at the rate γ_{nrad}. The energy emitted by the molecule at the frequency ω_{em} into the dipole mode at the rate of $F_{p,1}\tau_{rad}^{-1}$ is, instead, partially available for out–coupling. Simultaneously, the molecule itself also internally relaxes nonradiatively at its original nonradiative rate τ_{nrad}^{-1}.

The observed final photoluminescence power depends on the out–coupling efficiency $\xi_{rad,1}$ of the dipole mode into the free space external radiation modes. In the ideal case, it is clear that strong photoluminescence enhancement occurs when the frequencies of both optical excitation and emission are close to the dipole mode resonance ω_{dp}.

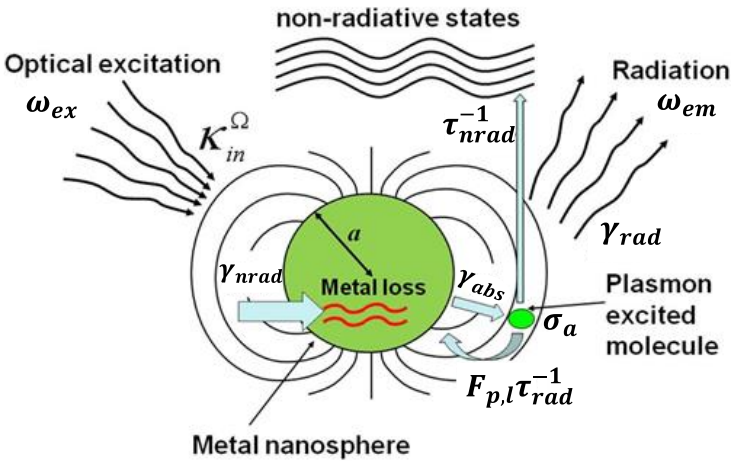

Figure 3.9. Enhancement of a photoluminescence process by the in–coupling of the external optical excitation into the dipole mode surrounding a metal nanosphere and by the out–coupling of the dipole mode into the radiative modes. (Adapted from Ref.[63])

Combining the two sequential enhancement processes given by Eqs. (3.5) and (3.21) we arrive at the total photoluminescence (PL) enhancement factor:

$$EF_{PL}(\omega_{ex}, \omega_{em}) = EF_{abs}(\omega_{ex})\, EF_{QY}(\omega_{em}) \tag{3.24}$$

that exhibits a complicated dependence on the size of the nanosphere (the only adjustable parameter for a sphere). This dependence can be ascribed to the fact that NPs play two mutually exclusive roles, i.e., that of antenna for efficient in– and out–coupling of energy; and that of a

nanocavity for energy concentration. An efficient antenna requires a large dipole, while a high concentration of energy calls for a small nanocavity. Therefore, for each combination of d, $N_a\sigma_a$, η_{rad}^{free} there exists an optimum nanosphere radius a that maximizes EF_{PL}.

The largest EF_{PL} is achieved by a small number of molecules with small absorption cross section, $Q_{abs} \gg Q_{nrad}$, having a small original quantum yield, $\eta_{rad}^{free} \ll 1$, placed close to the metal sphere, $a \gg d \geq d_{min}$, when both excitation and emission frequencies are close to the dipole resonance, $\omega_{ex}, \omega_{em} \approx \omega_{dp}$. It is understood that the theoretical maximum is achieved by a single molecule ($\sigma_a \leq 1$ nm^2 for fluorophores).

In the ideal case $f_q \approx 0$, under the above–mentioned ideal conditions, $EF_{PL}^{MAX,theo} \approx 10\varepsilon_D^2 Q_{nrad}^4$ for a small nanosphere $Q_{nrad}\,\chi^3 \ll 1$ (the small size is the optimum for the ideal case $f_q \approx 0$). For the Ag/GaN system $EF_{PL}^{MAX} \approx 3 \times 10^5$. This huge enhancement is in line with what has been observed in SERS,[69] which is actually a photoluminescence process with both $\sigma_a, \eta_{rad}^{free} \longrightarrow 0$ (for this reason, the EF_{Raman} are usually significantly larger than EF_{PL}, being $EF_{Raman} \sim EF_{PL}^{MAX,theo}$). On the other hand, for molecules with finite $N_a\sigma_a$ and η_{rad}^{free}, EF_{PL} is much less significant.

Let us consider once again the Ag/GaN system, which approximates well the ideal case $f_q \approx 0$ of no quenching for $d \geq 5$ nm. Figure 3.10a compares the three enhancements factors for molecules with $N_a\sigma_a = 1$ nm^2 and original $\eta_{rad}^{free} = 0.01$ placed at $d = 5$ nm from an Ag nanosphere embedded in GaN, at the resonant condition $\omega_{ex}, \omega_{em} \approx \omega_{dp}$. With this specific kind of molecules (weak absorber and inefficient emitter), the two contributions EF_{abs} and EF_{QY} are of the same order of magnitude and the $EF_{PL} = EF_{abs}EF_{QY}$ shows a maximum value of ≈ 800 for $a \approx 17$ nm. Note that such value is much lower than the above theoretical maximum ($\approx 3 \times 10^5$) because $N_a\sigma_a$, η_{rad}^{free}, γ_{nrad}, f_q (and so on) are small but not infinitesimal. Figure 3.10b shows the optimized PL enhancement factor (AgNP radius optimized) as a function of the detuning of optical excitation ω_{ex} and emission ω_{em} frequencies to that of LSP dipole mode $\omega_{dp}$for the same example. It clearly indicates that it is critical to have $\omega_{ex}, \omega_{em} \approx \omega_{dp}$ in the ideal case.

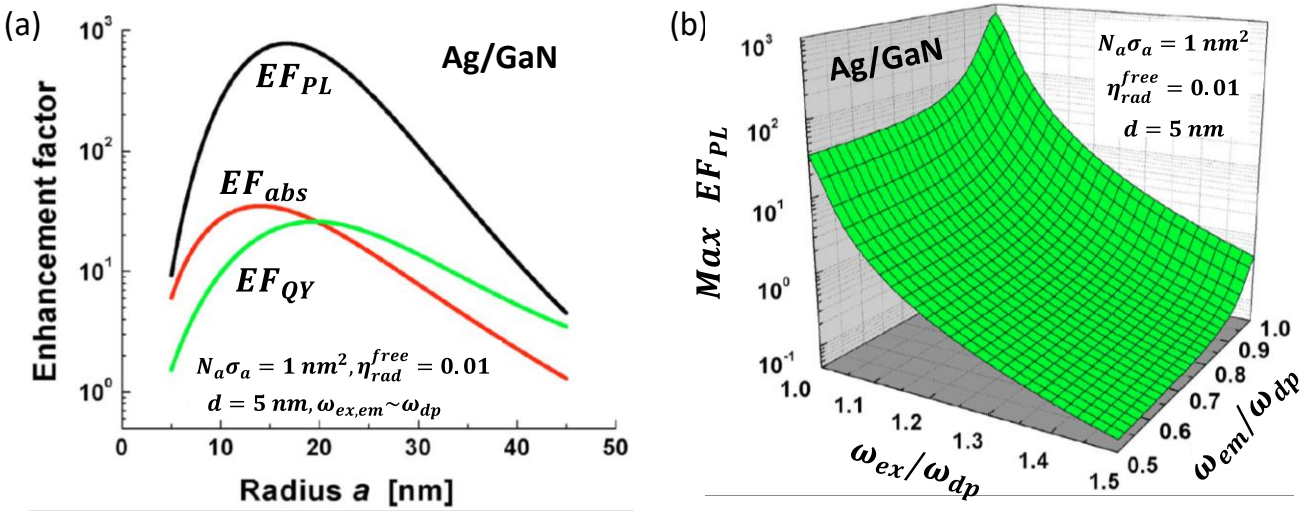

Figure 3.10. (a) EF_{abs} , EF_{QY} , and EF_{PL} attainable by an Ag nanosphere embedded in GaN as a function of AgNP radius for a molecule with $N_a\sigma_a = 1$ nm^2 and original $\eta_{rad}^{free} = 0.01$ placed at $d = 5$ nm from the AgNP, at $\omega_{ex}, \omega_{em} \approx \omega_{dp}$. (b) 2D plot of the EF_{PL}^{MAX} attainable by the same system at optimized radius of the AgNP as a function of the frequency detuning ratios of optical absorption ω_{ex}/ω_{dp} and emission ω_{em}/ω_{dp}. (Adapted from Ref.[63])

Therefore, the frequency relationship $\omega_{ex} \geq \omega_{dp} \geq \omega_{em}$ (or $\lambda_{ex} \leq \lambda_{dp} \leq \lambda_{em}$) is the optimum for PL measurements in the ideal conditions $f_q, N_a\sigma_a, \eta_{rad}^{free}, \gamma_{nrad} \approx 0$.

For metals with not negligible losses ($f_q \not\approx 0$), like Au, it was demonstrated that EF_{PL} could be maximized for a λ_{ex} red–detuned from the LSP dipole mode, i.e., for $\lambda_{dp} \leq \lambda_{ex}$.[67] Figure 3.11a shows this case by comparing the calculated spectral dependences of the EF_{MEF} of a single fluorophore with $\eta_{rad}^{free} = 1$ placed at a distance $z = 10$ nm from a Ag nanosphere (blue line) and a Au nanosphere (red line) of diameters $D = 80$ nm in vacuum. For the calculations, it was assumed $\lambda_{em} = \lambda_{ex} = \lambda$. While in the Ag/vacuum system EF_{MEF}^{MAX} is reached at $\lambda_{ex} \approx \lambda_{dp} \approx 360$ nm, in the Au/vacuum system EF_{MEF}^{MAX} is reached when the ideal fluorophore is excited at $\lambda_{ex} = 650$ nm, being $\lambda_{dp} \approx 520$ nm. The increase in EF_{MEF} is significant as $EF_{MEF}(\lambda_{dp}) \approx 2$ while $EF_{MEF}(\lambda_{ex}) \approx 3.5$. This circumstance was attributed to metal losses: in fact, the inspection of the imaginary part of the dielectric function of gold $\mathrm{Im}\{\varepsilon_{Au}\}$ as reported by Johnson and Christy[14] reveals that $\mathrm{Im}\{\varepsilon_{Au}\}$ monotonically decreases from $\mathrm{Im}\{\varepsilon_{Au}\} \approx 2.58$ at $\lambda = 520$ nm to $\mathrm{Im}\{\varepsilon_{Au}\} \approx 1.03$ at $\lambda = 650$, which is actually a local minimum for $\mathrm{Im}\{\varepsilon_{Au}\}$.Therefore, the metal (Ohmic) loss, encoded into the non–radiative decay rate γ_{nrad}, are significantly higher at $\lambda = 520$ nm than at $\lambda = 650$ nm. Recall that γ_{nrad} appears both in EF_{abs} and EF_{QY}, with the latter crucially depending on γ_{nrad} via the Purcell factors (which contain the Lorentzian linewidth): an increase in γ_{nrad} entails an increase in the quenching ratio f_q. Therefore, in the Au/vacuum system, the decreases in EF_{abs} and EF_{QY} associated to the red–detuning is surpassed by the more significant increase due to the reduction in γ_{nrad}. Figure 3.11b also shows the distance–dependent EF_{MEF} at $\lambda_{ex} = \lambda_{em} = 488$ nm for both systems. Not only this wavelength is blueshifted from the AuNP resonance but $\mathrm{Im}\{\varepsilon_{Au}\}$ is now even higher (≈ 4.1) and the losses are so significant that EF_{MEF} is either lower than 1 (PL quenching) or barely higher than 1 for the Au nanosphere.

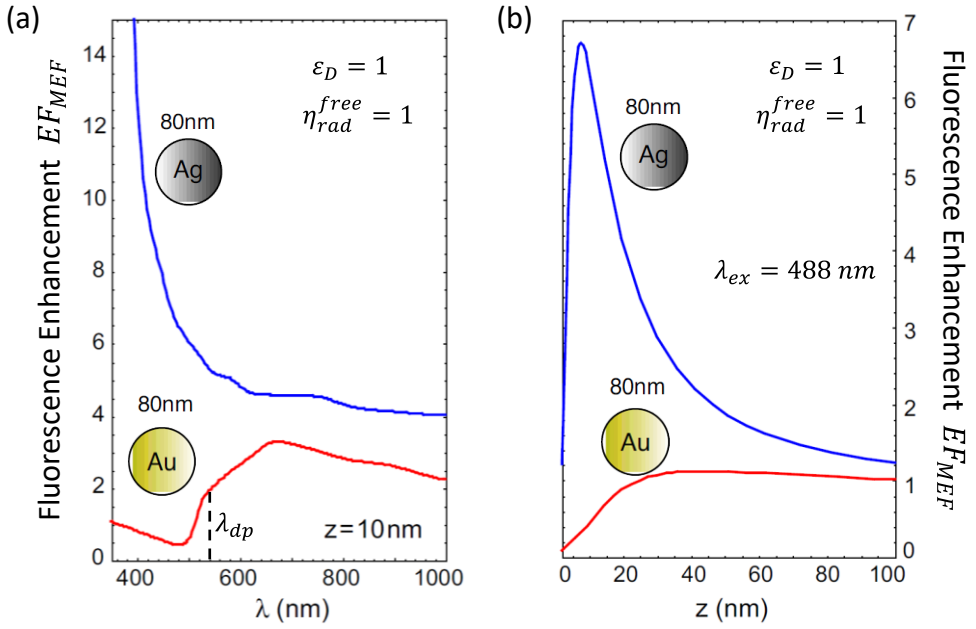

Figure 3.11. (a) Calculated spectral dependence for EF_{MEF} of a single, ideal fluorophore ($\eta_{rad}^{free} = 1$) placed at a distance $z = 10$ nm from a Au nanosphere (solid red) and a Ag nanosphere (solid blue) of diameter $D = 80$ nm. The dashed vertical line marks the resonant wavelength $\lambda_{dp} \approx 520$ nm for the AuNP (in vacuum), which is blueshifted with respect to $\lambda_{max} \approx 650$ nm. The corresponding resonance for the AgNP is at ≈ 360 nm. (b) Calculated distance–dependent EF_{MEF} at $\lambda_{ex} = \lambda_{em} = 488$ nm. (Adapted from Ref.[67])

The key conclusion is that photoluminescence enhancement effect is significant only for small quantities of molecules having both an originally low absorption cross section (weak absorbers) and an originally low emission efficiency (weak emitters), and that are placed in close proximity to the metal nanoparticles. While for metals with low losses the effect is maximized when $\lambda_{ex} \leq \lambda_{dp} \leq \lambda_{em}$), for metal with losses it could be maximized for $\lambda_{dp} \leq \lambda_{ex} \leq \lambda_{em}$, i.e., when λ_{ex} is red–detuned from the LSP dipole mode.

3.4 The Special Case of $\eta_{rad}^{free} = 1$

The examples shown in Figure 3.11 dealt with the special case of a single, ideal fluorophore, i.e., one having $\eta_{rad}^{free} = 1$. This special case is not purely theoretical, but many high–quality fluorophores having $\eta_{rad}^{free} \approx 1$ are actually available nowadays, e.g., Alexa Fluor or ATTO series fluorophores. For many applications in biosensing where the fluorescence intensity is the sensing parameter, such high–quality (high original QY) fluorophores are preferred for their higher brightness (implying higher fluorescence signals). Therefore, this case deserves special attention.

Since the energy emitted by a molecule couples with all modes of a sphere, and all the energy transferred to the higher modes is lost in the metal, it is readily seen that EF_{QY} can only be $EF_{QY} < 1$ whenever $\eta_{rad}^{free} = 1$. For this reason, the EF_{MEF} of high–quality fluorophores essentially loses one factor, becoming $EF_{MEF} \leq EF_{abs}$, implying significant lower enhancements with respect to the case $\eta_{rad}^{free} \ll 1$, but still significantly higher fluorescence intensities

Figure 3.12a shows the calculated distance–dependent EF_{abs} (solid red) and EF_{QY} (solid blue) for a single, ideal fluorophore ($\eta_{rad}^{free} = 1$) excited by a 60 nm Au nanosphere in vacuum irradiated with $\lambda_{ex} = \lambda_{max} \approx 650$ nm. [67,68] The calculations were performed by the multiple multipole method (MMP) (solid lines) or an approximation (dashed lines), and $\lambda_{em} = \lambda_{ex}$ was set for simplicity.

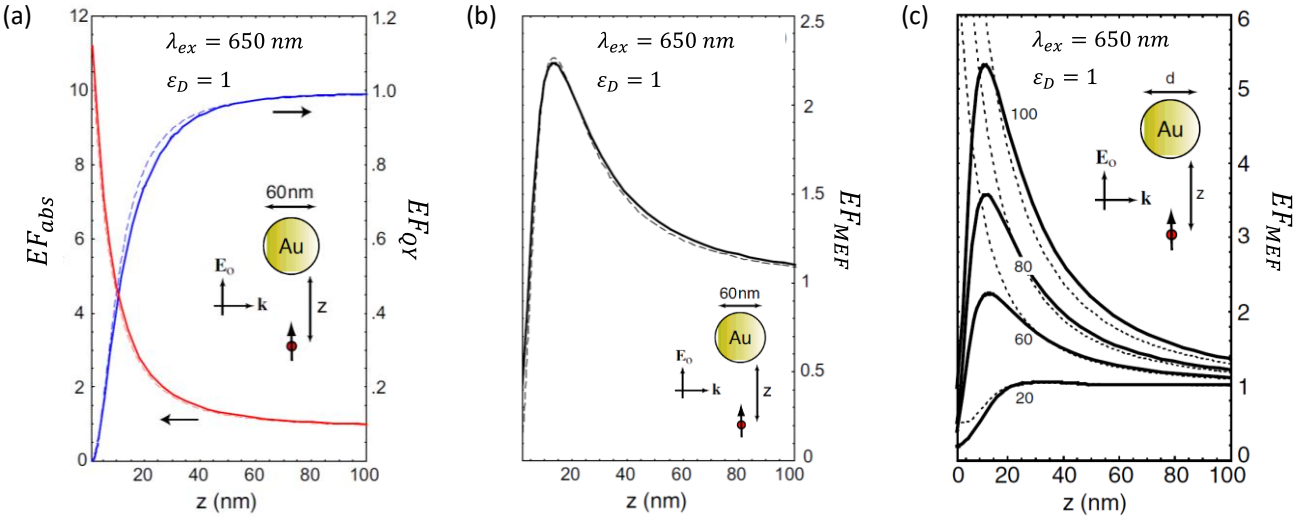

Figure 3.12. (a) Calculated EF_{abs} (red) and EF_{QY} (blue) for a single, ideal fluorophore of original $\eta_{rad}^{free} = 1$ excited at $\lambda_{ex} = \lambda_{max} \approx 650$ nm as a function of the distance from a 60 nm Au nanosphere in vacuum. (b) Corresponding EF_{MEF}. (c) Calculated EF_{MEF} in the same conditions for Au nanospheres with diameters of 20, 60, 80, and 100 nm. All solid curves are exact results based on the MMP method, dashed curves are approximations. (Adapted from Refs.[67,68])

While the trend for EF_{abs} is the usual one already seen for $N_a\sigma_a \longrightarrow 0$ in Figure 3.2b, the trend for EF_{QY} does not show any local maximum as it did when $\eta_{rad}^{free} \ll 1$ (see Figure 3.8a): it monotonically decreases for decreasing fluorophore–NP distances. This trend is general, and holds true for any metal nanosphere whenever the molecule has $\eta_{rad}^{free} = 1$. The corresponding EF_{MEF} is reported in Figure 3.12b. It can be noted a charactheristic shape with a local maximum due to the two competing effects of enhancement of the absorption and quenching of the emission. For this specific system, the (calculated) local maximum is $EF_{MEF}^{MAX} \approx 2.2$ at $d \approx 13$ nm. Finally, Figure 3.12c shows the calculated distance–dependent EF_{MEF} in the same conditions (in particular, $\lambda_{ex} = 650$ nm) for Au nanospheres with diameters of 20, 60, 80, and 100 nm. The PL of a single, ideal fluorophore is everywhere quenched in the case of the smallest 20 nm Au nanospheres. The first significant enhancement (a factor of 2) begins only with the 60 nm Au nanosphere. Note that EF_{MEF} monotonically increases with the size of the Au nanospheres, and the EF_{MEF}^{MAX} are always reached when $d \in [10, 15]$ nm. The increase in EF_{MEF} with the NP size can be attributed to the corresponding increase of the dipole mode, which entails an increase of both γ_{rad} and γ_{abs}, with a consequent increase of both EF_{abs} and EF_{QY}.

The prediction showed in Figures 3.12 and 3.11 were tested experimentally in the case of 80 nm Ag and Au nanospheres, with results shown in Figure 3.13a and b respectively. In the former case, a single Alexa488 fluorophore (exc./em. 499/520 nm, $\eta_{rad}^{free} = 0.92$ in H_2O) was excited by a 80 nm Ag nanosphere irradiated with $\lambda_{ex} = 488$ nm; in the latter case, a single Nile Blue fluorophore (exc./em. 631/660 nm, $\eta_{rad}^{free} = 0.27$ in EtOH) was excited by a 80 nm Au nanosphere irradiated with $\lambda_{ex} = 637$ nm. The single fluorophores samples were prepared by spincoating the molecules on a glass coverslip and then again spincoating a thin layer (< 5 nm) of polymer (PMMA, $n_D = 1.49$) on top. The NP were raster–scanned over the polymer surface at variable heights *z*, and the results are shown in Figure 3.13a and b, respectively. It is worth noting that the local dielectric environment "seen" by the NPs is not everywhere air (like in the previous calculations) as the fluorophores are embedded in the polymer. Therefore, the nanospheres are actually placed at the interface air/PMMA. The presence of dielectric increases the plasmon activity and, as a result, the

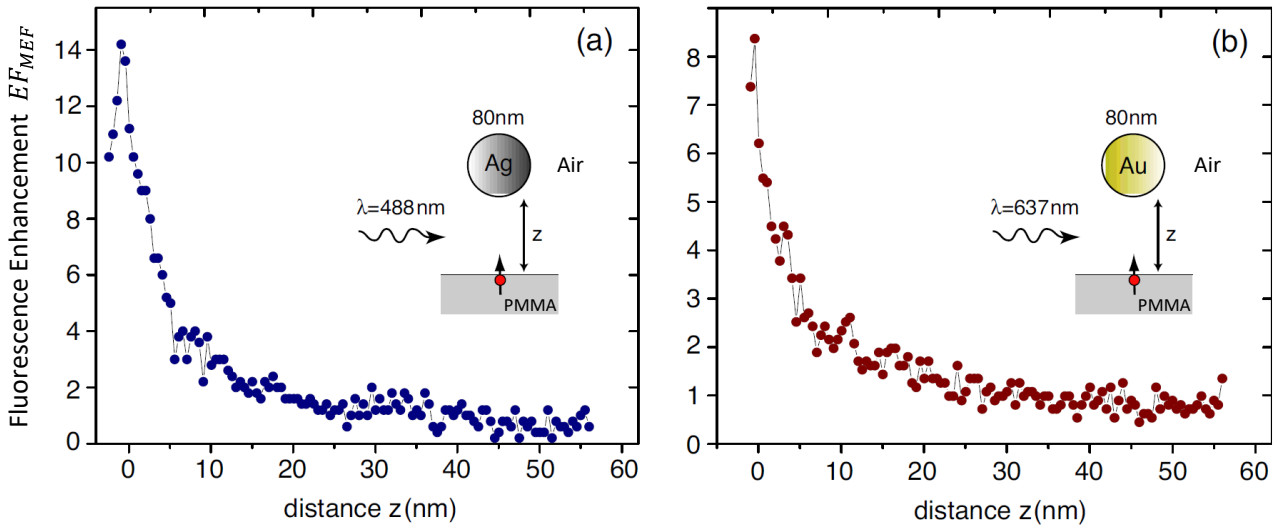

Figure 3.13. (a) Experimental distance–dependent EF_{MEF} for a single Alexa488 fluorophore ($\eta_{rad}^{free} = 0.92$ in H_2O) excited by a 80 nm Ag nanosphere irradiated with $\lambda_{ex} = 488$ nm. (b) Experimental distance–dependent EF_{MEF} for a single Nile Blue fluorophore ($\eta_{rad}^{free} = 0.27$ in EtOH) excited by a 80 nm Au nanosphere irradiated with $\lambda_{ex} = 637$ nm. Both curves show a decrease at short distances due to fluorescence quenching, which is not total at z=0 since the fluorophores are spin–coated by a PMMA layer (of thickness ≤ 5 nm). (Adapted from Ref.[67])

measured values are 2–3 times higher than those predicted in vacuum (compare with Figures 3.11b and 3.12c). However, once the calculation takes into account the actual local environment, theory and experiments match (graph shown in Ref.[68]). Furthermore, the presence of the dielectric entails a redshift of the λ_{dp}. In the case of an Ag nanosphere fully embedded into PMMA, $\lambda_{dp} \approx 500$ nm, hence the choice of Alexa488 and the excitation at 488 nm are optimal. In the case of an Au nanosphere fully embedded into PMMA, $\lambda_{dp} \approx 580$ nm: since $\lambda_{dp} < \lambda_{max} \approx 650$ nm, it is still convenient irradiating the Au nanosphere at 650 nm to have lower losses. Finally, because of the thickness (< 5 nm) of the PMMA layer, $z = 0$ do not correspond to a zero fluorophore–NP distance, but it is still ≈ 5 nm. For this reason, the experimental curves do not fall to 0 for $z = 0$, and the total quenching of fluorescence could not be observed. However, both curves exhibits the predicted local maximum and the decreasing trend on its left due to quenching. Taking into account the actual "horizontal offset" the local maximum is located at an actual fluorophore–NP distance of at least 5 nm, as also confirmed by the similar graph reported by in Ref.[68]

3.5 Symmetry Breaking: Towards Anisotropic Nanoparticles

All that has been said so far holds for a single metal nanosphere.

In the specific case of single sphere, we saw that there is an upper limit to the energy that can be transferred by FRET to a nearby molecule, i.e., only the energy "stored" into the dipole mode of the sphere. Analogously, there is an upper limit to the energy that can be actually emitted to the far–field, i.e., only the energy transferred by the molecule to the dipole mode of the sphere.

Both the limitations are due to the fact that the higher–order LSPs modes ($l \geq 2$) of a sphere have a zero dipole moment $p_l = 0$ and, hence, they cannot in–couple or out–couple radiatively with the external radiation. The higher–order modes of a sphere only decay nonradiatively into the sphere (e.g., into phonons, electron pairs, etc), so that the energy "stored" into the higher–order modes of a sphere are absorbed by the sphere, giving rise to Ohmic loss.

Ultimately, $p_l = 0 \; \forall l \geq 2$ in the case of a sphere because of the spherical symmetry itself, namely, the spherical symmetry of the Legendre polynomials describing the electromagnetic modes of a sphere (solutions of the Laplace equation $\nabla^2 \Phi = 0$, with Φ the electric potential).

Whenever the spherical symmetry is lost, the higher–order electromagnetic modes can acquire a dipole moment $p_l > 0$ and then contribute positively to the PL process. One could ideally write

$$\textit{Spherical Symmetry Breaking} \quad \Longrightarrow \quad p_l > 0 \;\; \forall l \quad \Longrightarrow \quad \gamma_l = \gamma_{l,rad} + \gamma_{l,nrad} \;\; \forall l$$

which implies that not only the LSP dipole mode $l = 1$ but also the LSP higher–order modes $l \geq 2$ can in–couple and out–couple radiatively with the external radiation, at least partially. As a consequence, both EF_{abs} and EF_{QY} (hence EF_{PL}), could be higher compared to the case of spherical symmetry.

The spherical symmetry can be broken in many ways. For instance, it is sufficient to place two nanospheres close to each other, forming a dimer, as in this way the system acquires a preferential direction given by the dimer axis. In fact, it was demonstrated that an emitter placed in the gap of

a nanosphere dimer undergoes a reduced quenching effect, which becomes significant only very close to the metal surface (< 2 nm).[70–72] Figure 3.14 shows the different behaviour of EF_{QY} calculated for a single, ideal fluorophore (original $\eta_{rad}^{free} = 1$) in presence of a single 90 nm Ag nanosphere (black curve), the corresponding dimer configuration (blue curve), and a linear chain (red curve). In both cases, the spherical symmetry is broken because of a preferential direction was introduced (dimer axis or chain axis, respectively). As a consequence of the symmetry breaking, the molecule emission is quenched less than the single particle case.

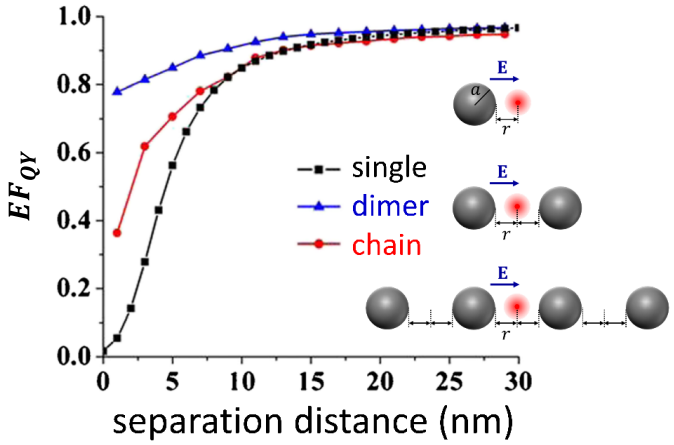

Figure 3.14. Calculated $\boldsymbol{EF_{QY}}$ of a single, ideal fluorophore ($\eta_{rad}^{free} = 1$) emitting at 480 nm near a single 90 nm Ag nanosphere (black curve), in the gap of two Ag nanospheres (blue curve), and in the middle of an AgNP chain (red curve) as a function of the separation distance from the nanoparticle surface. (From Ref. [71])

It is worth noting that, in the case of a dimer, or a chain, the coupling among the LSPs also entails an enhancement of the local electromagnetic field in the gap (where the molecule is placed), as showed in the previous Figure 1.5 in chapter 1. Consequently, EF_{abs} increases, too. Therefore, in the above mentioned cases of dimer and linear chain, both EF_{abs} and EF_{QY}, hence EF_{MEF}, are higher if compared to the single particle case of a nanosphere.

A direct way to break the spherical symmetry is considering nanoparticles with non–spherical shapes. On the one hand, the non–spherical metal NPs could offer reduced degrees of quenching (then, higher EF_{QY}); on the other hand, they could offer stronger local electromagnetic fields near some sharp corner, edge, or tip than a uniformly curved sphere (then, higher EF_{abs}). This consideration introduce our experimental study of the distance–dependent EF_{MEF} on both large Au nanosphere (which offer higher performance than smaller one) and, more importantly, large anisotropic nanoparticles like Au nanocubes.

Chapter 4. A Comparative Study on Nanostructures MEF performance with dsDNA as Spacers

4.1 Preliminaries: dsDNA Spacer and High Quality Fluorophore

The study of distance–dependent metal enhanced fluorescence (MEF) by AuNSs140 and AuNCs60 nanostructures was approached from a biosensing perspective. This viewpoint guided our specific choices regarding both the dielectric material serving as nanometric "spacer" and the fluorescent dye label. A variety of spacers have been reported to date, both inorganic (e.g., silica) and organic (e.g., polyelectrolytes);[73] however, neither the former nor the latter is superior, as each has its pros and cons.[74] Similarly, many fluorophores are available nowadays. In this case, the choice of the fluorescent molecule has a direct impact on the MEF enhancement factor ($\mathrm{EF_{MEF}}$), which is fluorophore–dependent even for fluorophores with identical spectral features due to different quantum yields (QY).

In our study, we utilized (di-thiolated) double strand DNAs (dsDNA) as spacers. DNA length can be finely tuned with sub–nanometric resolution ($3\ \mathrm{bp} \approx 1\ \mathrm{nm}$) by simply changing the sequence. Within the range $0{-}50$ nm (or $0{-}150$ bp), DNA can be considered as a stiff rod, given its persistence length $\gtrsim 50$ nm in typical ionic strength conditions.[75] Additionally, DNA can be covalently tethered to gold through thiol groups. Drawbacks are the strict experimental conditions. In particular, parameters including buffer ionic strength, (oligonucleotide) concentration, (oligonucleotide) length, and substrate curvature, can affect the surface density of end–tethered oligonucleotides as well as their actual tilt angle from the surface normal. [76–79] For instance, the latter implies that the actual height of the distal label from the surface is lower than the linear length of the dsDNA.[76,77] Considering these potential issues, a preparatory distance–dependent MEF study of our nanostructures using dsDNA spacers is relevant for their future utilization as transducers in a MEF–based optical biosensor[80] for nucleic acids detection.

It is important to stress that the typical sensing parameter of a MEF–based optical biosensor is fluorescence intensity, which is thus the actual quantity to be maximized rather than $\mathrm{EF_{MEF}}$. Since $\mathrm{EF_{MEF}} = \mathrm{EF_{abs}} \cdot \mathrm{EF_{QY}}$, MEF may result in very high $\mathrm{EF_{MEF}}$ ($> 10^3$) whenever low–quality fluorophores ($\mathrm{QY} < 0.1$) are used.[81,82] Nevertheless, the resulting (enhanced) fluorescence intensity might be still surpassed by the "free-space" (not enhanced) fluorescence intensity of a fluorophore with sufficiently higher QY and equal absorption cross section. Hence, from a biosensing perspective, opting for a high–quality fluorophore with superior QY and brightness seems more appropriate than using one with lower QY to be hopefully enhanced via MEF. New generations of fluorophores with very high QY and brightness are currently available (even to label nucleic acids), and a current challenge in MEF is the enhancement of such high–quality fluorophores.[83] Compatibly with dsDNA, we selected a fluorophore from the ATTO series having superior QY, which we anticipate being 0.9 in PBS 1X (pH 7.4), as later detailed.

Both the QY and exc./em. spectra of any fluorophore depend on the buffer solution, and can dramatically vary upon buffer variations. To maintain the nominal specifications of the fluorophore,

we opted not to alter its natural environment. This choice involved working under wet conditions, meaning that at every stage of MEF experiment, the fluorophores were kept in their buffer solution (PBS). Consequently, the nanostructures were always kept in the same buffer, and their spectra in water were considered for spectral matching with the fluorophores exc./em. (nanostructures extinction spectra exhibited no variations in PBS 1X compared to water)

4.2 Spectral Matchings: Plasmons vs Fluorophore vs Filters Bandpass

The choice of a fluorophore with a $\mathrm{QY} = 0.9$ simplified the spectral matching between nanostructure and fluorophore spectra. Since QY cannot exceed 1, the enhancement of a QY of 0.9 by Purcell effect is indeed negligible, making the FRET mechanism the primary consideration in our case. According to Li,[84] FRET occurs when the excitation spectrum of the fluorophore matches well with the absorption LSPR ($\mathrm{LSPR_{abs}}$). Consequently, it is crucial to decompose the extinction spectra of our nanostructures (in water or, equivalently, PBS 1X) in the absorption and scattering components in view of the final choice of the specific fluorophore.

Absorption and scattering contributions were obtained by simulations. We limited ourselves to run again the same simulations used for the extinction spectra (Figure 4.1a and Figure 4.2a) after enclosing the arrays in a transmission box, whose direct outcome is the array absorbance. The scattering contribution was obtained by subtracting the absorbance from the extinction. These simulated spectra are reported in Figure 4.1b for the AuNSs140 array and Figure 4.2b for the AuNCs60 array. In both cases, absorption (red line) and scattering (grey line) spectra are blueshifted and redshifted, respectively, compared to the extinction spectrum (blue line). For the array of AuNSs140 (Figure 4.1b), the (simulated) $\mathrm{LSPR_{abs}}$ is peaked at 534 nm with FWHM of 50 nm, scattering LSPR ($\mathrm{LSPR_{scat}}$) at 546 nm with FWHM of 56 nm, and extinction LSPR ($\mathrm{LSPR_{ext}}$) at 544 nm with FWHM of 54 nm. Absorption and scattering contributions to the $\mathrm{LSPR_{ext}}$ peak are 38% and 62%, respectively, indicating that the two contributions are comparable, but the scattering contributes more. In fact, the entire $\mathrm{LSPR_{ext}}$ (range: 472–600 nm) resembles much more the $\mathrm{LSPR_{scat}}$ than $\mathrm{LSPR_{abs}}$; therefore, scattering provides the main contribution to the simulated (and to the experimental) extinction spectrum in the relevant range.

Similar considerations hold for the array of AuNCs60 (Figure 4.2b): $\mathrm{LSPR_{abs}}$ is peaked at 572 nm, $\mathrm{LSPR_{scat}}$ at 578 nm, $\mathrm{LSPR_{ext}}$ at 576 nm, all with a FWHM of 65 nm. However, in this case, absorption contribution is higher than scattering over the entire Vis range, in particular its contribution to the $\mathrm{LSPR_{ext}}$ peak is 54% against the 46% of scattering. It can be noted that the $\mathrm{LSPR_{abs}}$ of AuNCs60 array is sharper than the $\mathrm{LSPR_{abs}}$ of AuNSs140 array, while $\mathrm{LSPR_{scat}}$ is less pronounced. Moreover, both $\mathrm{LSPR_{scat}}$ and $\mathrm{LSPR_{abs}}$ are sharp and almost equally contribute to the sharp $\mathrm{LSPR_{ext}}$. The differences in absorption and scattering spectra between the two arrays can be attributed to their geometry. In fact, AuNSs140 are larger than AuNCs60 (104 nm against 74 nm, on average) as well as more packed (NND is 192 nm for the NS array while 223 nm for the NCs array, on average). Larger NPs generally scatter more, and a higher surface density sustain the long–range (scattering) dipolar coupling better, as discussed in the previous chapter.

It is worth noting that, as the $\mathrm{LSPR_{scat}}$ of both arrays are pronounced and sharp (especially for AuNSs140 array), the emission of a fluorophore with very low QY could be highly enhanced

through Purcell effect upon matching its emission spectrum with the $\mathrm{LSPR}_{\mathrm{scat}}$. In other words, our arrays are good candidates for reaching high $\mathrm{EF}_{\mathrm{MEF}}$ ($\geq 10^3$). However, our biosensing viewpoint led us to prefer a high–quality fluorophore ($\mathrm{QY} = 0.9$) whose emission efficiency is already at its maximum, eliminating the need for further enhancement. In this way, one of the two tasks of MEF, i.e., fluorophore emission efficiency enhancement, was accomplished through the choice of a high–quality fluorophore. Only the fluorophore excitation rate needs for enhancements. As mentioned earlier, this can be obtained by FRET upon matching fluorophore's excitation spectrum with the $\mathrm{LSPR}_{\mathrm{abs}}$. The above analysis showed that both nanostructures exhibit prominent $\mathrm{LSPR}_{\mathrm{abs}}$, comparable with the $\mathrm{LSPR}_{\mathrm{scat}}$. Consequently, a high $\mathrm{EF}_{\mathrm{abs}}$ is expected. In particular, we expect the AuNCs60 array to provide a higher $\mathrm{EF}_{\mathrm{abs}}$ than the AuNSs140 array as its $\mathrm{LSPR}_{\mathrm{abs}}$ contributes more to the extinction if compared to AuNSs140 array (54% against 38%) and is sharper.

For simplicity, we opted for a single type of fluorophore to be used with both nanostructures. Optimal matching of the same fluorophore with the two arrays was challenging as their $\mathrm{LSPR}_{\mathrm{abs}}$ had maxima separated by 40 nm. We prioritized the matching with the AuNCs60 nanostructure as it is our interesting case. The quality of matching will be considered and discussed during the result analysis. Eventually, ATTO 565 fluorophore was selected for the fine matching of its excitation spectrum with AuNCs60 array $\mathrm{LSPR}_{\mathrm{abs}}$ as well as a satisfying matching with the AuNSs140 array $\mathrm{LSPR}_{\mathrm{abs}}$, as shown in Figures 4.1c and 4.2c (dotted green line). In particular, it has exc./em. maxima at 563/589 nm, $\mathrm{QY} = 0.9$, molar extinction coefficient $\varepsilon = 1.2 \cdot 10^5\ \mathrm{M^{-1}cm^{-1}}$ and brightness $\beta \equiv \varepsilon \cdot \mathrm{QY} = 108 \times 10^4\ \mathrm{M^{-1}cm^{-1}}$ (data available on ATTO–TEC website). Its excitation spectrum matches with the right portion of $\mathrm{LSPR}_{\mathrm{abs}}$ of AuNSs140 array, but its maximum does not overlap with $\mathrm{LSPR}_{\mathrm{abs}}$ peak; instead, its excitation spectrum perfectly aligns with AuNCs60 array $\mathrm{LSPR}_{\mathrm{abs}}$ peak, slightly to its left. Figures 4.1d and 4.2d also display the matching of ATTO565 spectra (magenta/purple) with the scattering spectra (grey) of the two arrays. Both excitation and emission of ATTO 565 are very well matched with the $\mathrm{LSPR}_{\mathrm{scat}}$ of the AuNCs60 array, while only the excitation is well matched with the $\mathrm{LSPR}_{\mathrm{scat}}$ of AuNSs140 array. However, the quality of these matchings is not relevant since ATTO 565 has QY of 90%, therefore its emission efficiency cannot be further enhanced by Purcell effect upon spectral matching with $\mathrm{LSPR}_{\mathrm{scat}}$.

The above discussion is still uncomplete, as the excitation and emission bandpass filters play a pivotal role as well. In absence of the plasmonic nanostructure, fluorophores have to be properly excited, and their emission properly collected. Therefore, exc./em. bandpass filters have to match the fluorophores exc./em. spectra to guarantee high fluorescence signal collection. When a plasmonic nanostructures is introduced, particularly the exc. bandpass (or the excitation light, generally) has to further match with the nanostructure $\mathrm{LSPR}_{\mathrm{abs}}$ to guarantee a proper excitation of plasmons. Figures 4.1c and d, and Figure 4.2c and d display the ex./em. bandpass in our specific case. In particular, the exc. bandpass (green band) is 538–563 nm, or 550 ± 12.5 nm namely; while the em. bandpass (orange-red band) is 570–640 nm, or 605 ± 35 nm namely. ATTO 565 excitation ranges from 40% to 100% within the excitation bandpass, with a 30% of overall spectral overlap. The spectral overlap of ATTO 565 emission with the emission bandpass is 76%. The excitation bandpass matches well the $\mathrm{LSPR}_{\mathrm{abs}}$ of both the arrays. Therefore, ATTO 565 is properly excited, and its emission properly collected. On the other hand, plasmons are effectively excited for both the arrays, and are expected to enhance the absorption rate of ATTO 565.

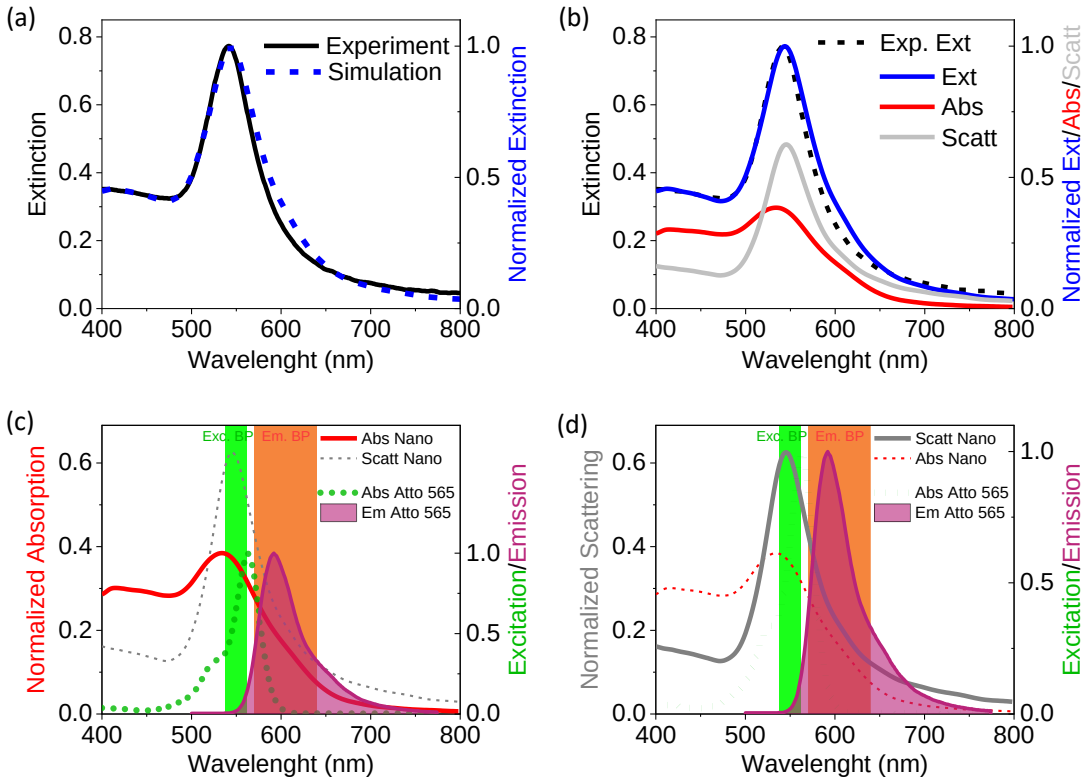

Figure 4.1. (a)-(b) Decomposition of the simulated extinction spectrum of AuNSs140 nanostructure (dashed blue) into absorption (red) and scattering (grey) contributions. (c)-(d) Overlap of absorption and scattering contributions with excitation (dotted green) and emission (filled purple) spectra of ATTO565 fluorophore as well as excitation (green band) and emission (orange band) bandpass filters.

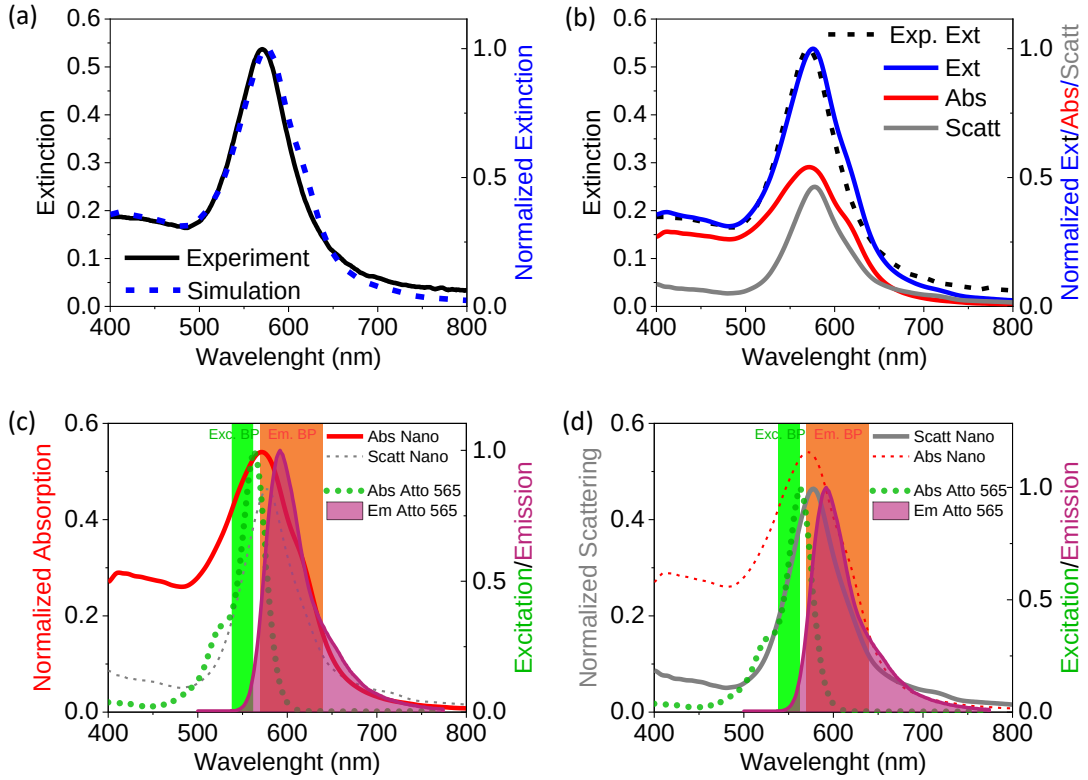

Figure 4.2. (a)-(b) Decomposition of the simulated extinction spectrum of AuNCs60 nanostructure (dashed blue) into absorption (red) and scattering (grey) contributions. (c)-(d) Overlap of absorption and scattering contributions with excitation (dotted green) and emission (filled purple) spectra of ATTO565 fluorophore as well as excitation (green band) and emission (orange band) bandpass filters.

4.3 Experimental Results

Three dsDNAs, i.e., a 21-mer (dsDNA21), a 50-mer (dsDNA50), and a 100-mer (dsDNA100), were selected for the distance–dependent MEF study by AuNSs140 and AuNCs60 arrays. Since $3\ \mathrm{bp} \approx 1\ \mathrm{nm}$, the corresponding linear lengths are 7, 17, and 33 nm, respectively, covering a range relevant for aptasensing as well as immunosensing based on the "sandwich" working-scheme. Duplex sequences and experimental procedures are detailed in Appendix D and E, respectively.

In our group, electrochemical electrodes are routinely functionalized by single strand DNAs (ssDNAs) at concentrations of 50–5000 nM in buffers at high ionic strength, i.e., high salt content. Therefore, we first conducted experiments at the intermediate/high concentration of 500 nM dsDNA-ATTO565 in PBS 1X at both low salt (LS) and high salt (HS) content. In the former case, PBS 1X was used with no further addition of salts; in the latter case, PBS 1X was brought to final concentrations of 1 M NaCl and 1 mM $MgCl_2$. As expected, the HS conditions generally resulted in higher fluorescence intensities (≈ 4 times), hence all the subsequent experiments at lower concentrations of dsDNAs always employed PBS 1X HS as buffer. In particular, the experiments at 2.5 nM and 1 nM dsDNAs in PBS 1X HS resulted in fluorescent signals slightly above the control experiment signals, representing a low–concentration regime.

All fluorescent images (at any concentration of any dsDNA) showcased a strikingly uniform signal all over the samples, not only when using the Zeiss Plan-Apochromat 10x/0.45 Ph1 M27 (FWD = 2.1 mm) objective, but also at higher magnifications. This evidence is compatible, and confirms once more, the extraordinary uniformity of the nanostructures. Examples of processed fluorescence images attained by AuNSs140 and AuNCs60 arrays at relevant concentrations of dsDNA21–ATTO565 (in PBS 1X HS) are reported in Figure 4.3a and b, respectively. Showing ROIs with scratches, and/or ROIs acquired at the sample boundary, is an intentional choice aiming at displaying images with "defects". Obviously, the images considered for the analysis did not contain such defects but are homogenous images (except for, e.g., grains of dust) with varying intensities.

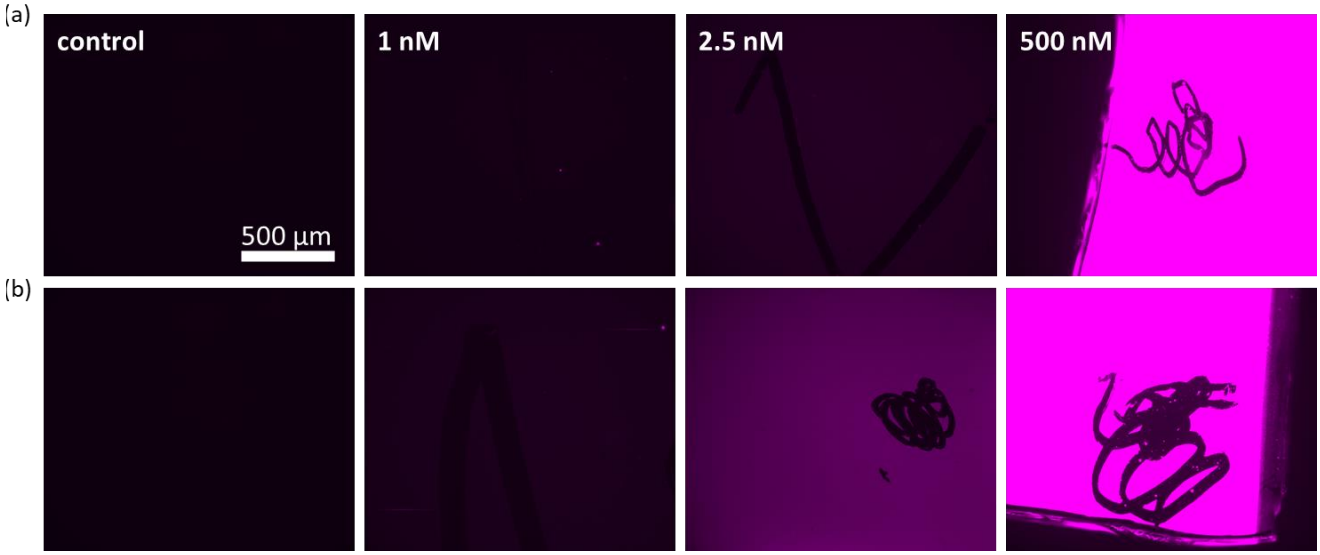

Figure 4.3. Examples of fluorescence images at relevant concentrations of dsDNA21-ATTO565 at HS conditions attained by (a) AuNSs140 array and (b) AuNCs60 array. Scratches are intentional. The images at 500 nM were recorded towards nanostructures edges. For graphical purposes, black pixel intensity was set to 0 while white (magenta) to 5000, and for this reason the images at 500 nM look saturated.

It is worth mentioning that the images displayed in Figure 4.3 were processed (by ImageJ) for graphical purposes. Indeed, the pco.edge 5.5 sCMOS photodetector mounted on our microscope provides black/white 16–bit images. Therefore, white was changed to magenta to roughly match the emission colour of the dye; and the intensities of black and white (magenta) were everywhere set to 0 and 5000, respectively, to better visualize the images at low concentration. Consequently, the images at 500 nM look saturated as the pixel max intensity of the raw image is ≈15000.

Each $\approx 0.5 \times 0.5\ \mathrm{cm}^2$ sample was entirely mapped as 9 not–overlapping $1664 \times 1404\ \mu\mathrm{m}^2$ ROIs (typically). ImageJ function "RawIntDen" was utilized to retrieve the overall intensity (sum of the intensities of all the pixels constituting the image) of each ROI, whose average provided the mean RawIntDen I_i associated to each sample. At each dsDNA concentration, 4 independent replicates were considered, obtaining $\mathrm{I(dsDNA)} = \mathrm{mean(I_1, \dots, I_4)}$ together with the associated standard deviation (of the mean). When applied to the control experiments, i.e., nanostructures incubated by PBS 1X LS or HS, $\mathrm{I(control)} = (1.745 \pm 0.011) \times 10^9$ was obtained for AuNSs140 array and $\mathrm{I(control)} = (1.662 \pm 0.004) \times 10^9$ for AuNCs60 array. Finally, the renormalized total fluorescence intensity, I_{ren}, was calculated as:

$$\mathrm{I_{ren}(dsDNA)} = [\mathrm{I(dsDNA)} - \mathrm{I(control)}] \,/\, \Sigma_{\mathrm{eff}}\,,$$

where Σ_{eff} is the geometric parameter introduced in Section 2.3.2 accounting for the "3D effective surface" of nanostructure per unit substrate. $\Sigma_{eff} = 0.64$ for AuNSs140 array and $\Sigma_{eff} = 0.38$ for AuNCs60 array. After renormalization, the fluorescent intensities attained by the two arrays can be compared as associated to the same 3D effective array surface.

Table 1 summarizes the I_{ren} for the relevant cases of 500 nM dsDNAs in PBS 1X LS (top-left) and HS (top-right), 2.5 nM dsDNAs in PBS 1X HS (bottom-left), and 1 nM dsDNAs in PBS 1X HS (bottom-right), together with the relative distance-dependent $\mathrm{EF_{MEF}}$ calculated as $\mathrm{EF_{MEF}(ds21)} = I_{ren}(\mathrm{ds21})/I_{ren}(\mathrm{ds100})$ and $\mathrm{EF_{MEF}(ds21)} = I_{ren}(\mathrm{ds50})/I_{ren}(\mathrm{ds100})$. The last column reports $G = I_{ren}^{NCs}/I_{ren}^{NSs}$, which is the gain of the AuNCs60 array compared to the AuNSs140 array. Note that the renormalization affects the gains G but not the relative distance–dependent $\mathrm{EF_{MEF}}$.

Table 1. Summary of the Results

500 nM dsDNA-ATTO565, Low Salt			
	AuNSs140	AuNCs60	G
	$I_{ren}/10^9$ (&**EF**)	$I_{ren}/10^9$ (&**EF**)	
ds21	33.5 ± 0.4 (**0.9**)	74 ± 2 (**2**)	2.2
ds50	34.1 ± 0.1 (**0.9**)	42.1 ± 0.2 (**1.1**)	1.2
ds100	36.8 ± 0.5 (**1**)	37.5 ± 0.6 (**1**)	1

500 nM dsDNA-ATTO565, High Salt			
	AuNSs140	AuNCs60	G
	$I_{ren}/10^9$ (&**EF**)	$I_{ren}/10^9$ (&**EF**)	
ds21	111.4 ± 0.2 (**1**)	227 ± 2 (**1.8**)	2
ds50	110 ± 1 (**1**)	144 ± 2 (**1.2**)	1.3
ds100	111 ± 1 (**1**)	124 ± 1 (**1**)	1.1

2.5 nM dsDNA-ATTO565, High Salt			
	AuNSs140	AuNCs60	G
	$I_{ren}/10^9$ (&**EF**)	$I_{ren}/10^9$ (&**EF**)	
ds21	5.2 ± 0.4 (**33**)	17.3 ± 1.3 (**7**)	3.3 ± 0.4
ds50	0.50 ± 0.05 (**3**)	4.2 ± 0.3 (**1.7**)	8 ± 1
ds100	0.16 ± 0.01 (**1**)	2.5 ± 0.2 (**1**)	16 ± 2

1 nM dsDNA-ATTO565, High Salt			
	AuNSs140	AuNCs60	G
	$I_{ren}/10^9$ (&**EF**)	$I_{ren}/10^9$ (&**EF**)	
ds21	1.04 ± 0.03	3.42 ± 0.04 (**20**)	3.3
ds50	0.00 ± 0.01	0.63 ± 0.04 (**3.7**)	n. a.
ds100	-0.07 ± 0.01	0.17 ± 0.01 (**1**)	n. a.

The same results for I_{ren} are also graphically represented in Figure 4.4 as a function of the linear length of the three dsDNAs, red squares for data attained byAuNSs140 array and blue circles for those attained by AuNCs60 array. Error bars are generally too small to be visualized. Datapoints were connected by exponential fit curves for a better readability.

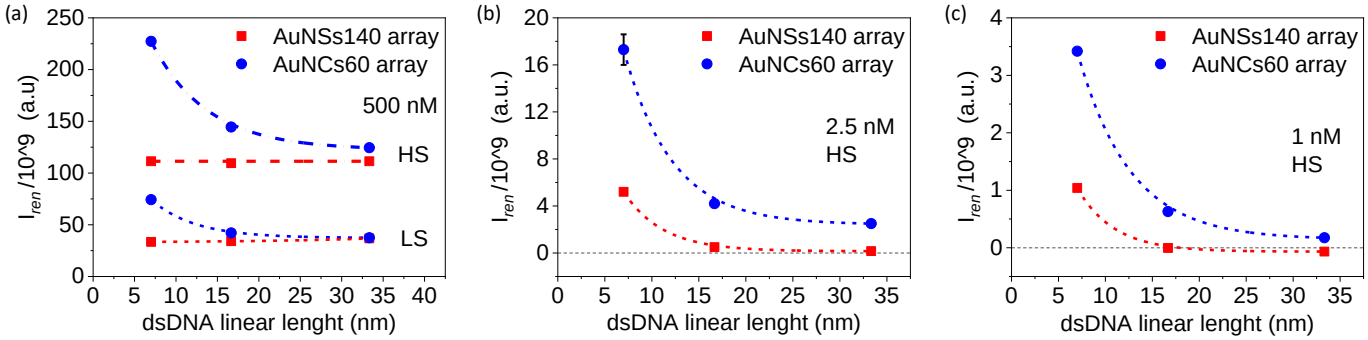

Figure 4.4. Graphical representation of the results from Table 1, attained by AuNSs140 array (red squares) and AuNCs60 array (blue circles) at (a) 500 nM dsDNA–ATTO565 in PBS 1X LS and HS, (b) 2.5 nM dsDNA–ATTO565 in PBS 1X HS, and (c) 1 nM dsDNA–ATTO565 in PBS 1X HS. Each dataset of 3 points is connected by exponential curves for readability.

At the relatively high concentration of 500 nM dsDNA, the use of PBS 1X HS generally entailed a ≈ 4–fold increase of I_{ren} compared to the LS condition. The significant increase in I_{ren} is ascribed to the improved screening of the dsDNA negative charges generally occurring at higher ionic strength, which allowed a higher number of dsDNA to surpass the potential barrier and tether onto NPs surfaces. The general nature of this effect is confirmed by the fact that the 4–fold improvement was observed for all three dsDNAs on both arrays. As a further general consideration, it can be noted that the exponential curves connecting each dataset, see Figure 4.4a, point towards the same asymptotic value, and in LS conditions the values of $I_{ren}(ds100)$ for both arrays already coincide. Such shared asymptotic values of I_{ren} could represent the natural (free-space) fluorescence intensity resulting from the *same* number of fluorophores. Indeed, fluorophores 33 nm far from the NPs surfaces would experience a relatively small plasmonic enhancement (see below); on the other hand, the nanostructures would be fully saturated by fluorophores at the high concentration of 500 nM and, At saturation, the total number of fluorophores would depend only on the 3D effective surface, which was effectively equalized by Σ_{eff}.

Apart these general considerations, the distance-dependent $\mathrm{EF_{MEF}}$ (of each array separately) as well as the fluorescence intensity gain factor G of the AuNCs60array vs AuNSs140 array agree at 500 nM dsDNA in both HS and LS conditions. While no relative $\mathrm{EF_{MEF}}$ was observed for AuNSs140 array, a relative $\mathrm{EF_{MEF}}$ up to 2 was observed for the AuNCs60 array in the case of the shortest dsDNA21. The same can be said about G. Therefore, at high dsDNA concentrations, AuNCs60 array generally offered both higher $\mathrm{EF_{MEF}}$ and higher fluorescence intensities I_{ren} compared to the AuNSs140 array. However, the obtained $\mathrm{EF_{MEF}}$ are unexpectedly low, and no distance–dependent $\mathrm{EF_{MEF}}$ at all was observed for AuNSs140 array.

At low dsDNA concentrations (HS condition), the scenario drastically changed. At 2.5 nM, the $\mathrm{EF_{MEF}}$ are much higher and, surprisingly, the $\mathrm{EF_{MEF}}$ of AuNSs140 array are higher than AuNCs60 array, in contrast to the previous case. Furthermore, the $\mathrm{EF_{MEF}}$ of AuNSs140 array increases at a much faster rate than AuNCs60 array, being $\mathrm{EF_{MEF}(ds50)} = 3$ and $\mathrm{EF_{MEF}(ds21)} = 33$ for

AuNSs140 array, while $\mathrm{EF_{MEF}(ds50)} = 1.7$ and $\mathrm{EF_{MEF}(ds50)} = 7$ for AuNCs60 array. As a consequence, while AuNCs60 array continues to offer higher I_{ren} than AuNSs140 array, now G is highest for the longest dsDNA100 and progressively decreases for the shorter dsDNAs, being $G(\mathrm{ds100}) = 16 \pm 2$, $G(\mathrm{ds50}) = 8 \pm 1$, and $G(\mathrm{ds21}) = 3.3 \pm 0.4$.

Finally, at the lowest concentration of 1 nM dsDNA, the I_{ren} attained by AuNSs140 array was not detectable (i.e., compatible with the control experiment signal) for both ds100 and ds50, and measurable only for the shortest ds21. Therefore, no relative $\mathrm{EF_{MEF}}$ are available for AuNSs140 array. Instead, I_{ren} was detectable for AuNCs60 array with all dsDNAs at 1 nM, with values very close to those attained by AuNSs140 array at the higher concentration of 2.5 nM. This confirms its superior performance at low concentrations, too. Interestingly, the relative $\mathrm{EF_{MEF}}$ of AuNCs60 array resulted to be significantly higher than those at 2.5 nM, being $\mathrm{EF_{MEF}(ds50)} = 3.7$ and $\mathrm{EF_{MEF}(ds21)} = 20$. The only available gain G, $\mathrm{G(ds21)} = 3.3$, is compatible with the corresponding gain at 2.5 nM (the other G are virtually infinite)

We conclude that AuNCs60 array generally offered superior performance compared to AuNSs140 array, both at high and low concentrations. In particular, at the lowest concentration of 1 nM, no fluorescence signal at all was attained by AuNS140 array when using ds50 and ds100, which corresponds to an "infinite" gain. Instead, thanks to higher $\mathrm{EF_{MEF}}$, fluorescence signals from all the dsDNAs were attained by AuNCs60 array at 1 nM, with values comparable with those attained by AuNS140array at the higher concentration of 2.5 nM. From a biosensing perspective, this would allow AuNCs60 array to reach lower LODs than AuNS140 array. Note that the highest measurable gains (at the same concentration) were found at 2.5 nM: up to 3.3 times in the case of the 7 nm long dsDNA21; up to 8 times in the case of the 17 nm long dsDNA50; and up to 16 times in the case of the 33 nm long dsDNA100. This unexpected trend, which increases with increasing dsDNA lengths, suggests that the use of AuNCs60 array (rather than AuNS140) is particularly convenient for the detection of long oligonucleotides at low concentrations, as lower LODs could be reached as a result of much higher (at least 1 order of magnitude higher) fluorescent signals.

The above mentioned trend for the gains G at 2.5 nM was unexpected, as well as the abrupt increase from $\mathrm{EF_{MEF}(ds50)} = 3$ to $\mathrm{EF_{MEF}(ds21)} = 33$ for AuNS140 array. Moreover, if we consider the three trends for $\mathrm{EF_{MEF}}$ attained by AuNCs60 array at high and low concentrations, as well as the two available trends for $\mathrm{EF_{MEF}}$ attained by AuNSs140, we can note that they do not agree with each other. Rather, it seems that the low concentration regime unlocked the actual MEF potentialities of the arrays, which were hidden/damped at high concentration. In fact, MEF seems to be totally absent for AuNSs140 array, and very limited ($\mathrm{EF_{MEF}} \leq 2$) for AuNCs60 array, at high concentrations.

In an effort to assess these open issues, here follows a theoretical interpretation of the results, based on simulations and few reports available in literature.

4.4 Discussion and Analysis

To gain a deeper insight into the experimental findings, we simulated the electromagnetic EF $\mathrm{EF_{e.m.}} = |\mathbf{E}/\mathbf{E_0}|^2$ in the surroundings of a target AuNS140 and AuNC60. The simulations used for the extinction spectra (with the morphology of the STEM micrographs of Figure 2.4a and 2.9c,

respectively) were rerun after introducing frequency–domain field profile monitors in sub-ROIs with a NS140 or a NC60 at the centre, surrounded by all its first neighbours. Therefore, these target NPs effectively represent a generic NS140 or a generic NC60 within the array.

Two main considerations follow, regarding the excitation wavelength λ_{exc} and the position of the monitors, as both highly impact the results of any $\mathrm{EF}_{\mathrm{e.m.}}$ profile.

Firstly, according to our simulations, the max $\mathrm{EF}_{\mathrm{e.m.}}$ monotonically increase until a local maximum at $\lambda_{exc} > 570$ nm for both arrays. However, the excitation filter of our microscope has exc. bp limited to the range 538–563 nm, and beyond this range plasmons could not be excited by our equipment. Therefore, we considered the $\mathrm{EF}_{\mathrm{e.m.}}$ profiles at the maximum excitation wavelength $\lambda_{exc} = 563$ nm allowed by our filter.

Secondly, as shown by the $\mathrm{EF}_{\mathrm{e.m.}}$ xz-profile of a single 104 nm AuNS on glass displayed in Figure F.7a in Appendix F.7, the spatial distribution of $\mathrm{EF}_{\mathrm{e.m.}}$ is not purely dipolar for our large AuNSs140 at 563 nm. The electric field $\mathbf{E}$ "wraps" around the NS according to the direction of the incident light: if the (plane wave) source is located below the NS and the incident light hits the NS "from the bottom" (the case shown), then $\mathbf{E}$ "wraps" around the NS slightly above the equator; conversely, if the source is located above the NS and the incident light hits the NS "from the top", then $\mathbf{E}$ "wraps" around the NS slightly below the equator. Similar considerations apply to the AuNCs60, as shown by the $\mathrm{EF}_{\mathrm{e.m.}}$ xz-profile of a single AuNC60 on glass displayed in Figure F.7b in Appendix F.7. Here, the xz-monitor intersects the NC60 at the corner region, where the $\mathrm{EF}_{\mathrm{e.m.}}$ is at its maximum. $\mathrm{EF}_{\mathrm{e.m.}}$ is more intense at the top facet corners when external radiation hits the cube from the bottom, and, vice versa, at the bottom facet corners when external radiation hits the cube from the top. The configuration we considered in our simulations is with light incident "from the bottom", as the microscope we used is an inverted microscope. The frequency–domain field profile monitors were placed in suitable positions accommodating the actual spatial $\mathrm{EF}_{\mathrm{e.m.}}$ profiles; essentially, where $\mathrm{EF}_{\mathrm{e.m.}}$ is maximized.

The (unpolarized) $\mathrm{EF}_{\mathrm{e.m.}}$ profiles at $\lambda_{exc} = 563$ nm of the entire sub-ROIs (at specific xy-monitor heights) with light incident "from the bottom" are displayed in Figure F.8 in Appendix F.7. Instead, Figure 4.5 shows the (unpolarized) $\mathrm{EF}_{\mathrm{e.m.}}$ profile of the target AuNS140 ($D = 103$ nm) along a xy-plane located 10 nm above the equatorial plane (Figure 4.5a); and the (unpolarized) $\mathrm{EF}_{\mathrm{e.m.}}$ profile of the target AuNC60 (edge lengths $E \approx 72$ nm) along a xy-plane located 5 nm below its top facet (Figure 4.5b), both with $\lambda_{exc} = 563$ nm incident "from the bottom". For a better visualization of the decaying fields, thresholds for $\mathrm{EF}_{\mathrm{e.m.}}$ were set at 30 and 100 for the AuNS140 and the AuNC60, respectively, and points with higher $\mathrm{EF}_{\mathrm{e.m.}}$ values are all represented as white. In the case of AuNS140, where a 1 nm mesh was set, the threshold at 30 stress some (mesh) artifacts at the gold/water boundary. Instead, for the AuNC60, the threshold highlights relatively large regions around the corners (up to 5 nm far from the corner) with $\mathrm{EF}_{\mathrm{e.m.}} \geq 100$. Values up to 170 were recorded at the (top-right) corner surface (partially due to mesh artifacts). However, since our shortest dsDNA21 has linear length of 7 nm, we are interested in the $\mathrm{EF}_{\mathrm{e.m.}}$ from points ≥ 5 nm far from the NPs surfaces. Both meshes are fine enough to avoid artifacts in the interesting regions. Note that the $\mathrm{EF}_{\mathrm{e.m.}}$ profiles around both NPs are not symmetric due to plasmonic coupling with the neighbours NPs (beyond the frames shown here, but shown in Figure F.8 in Appendix F.7).

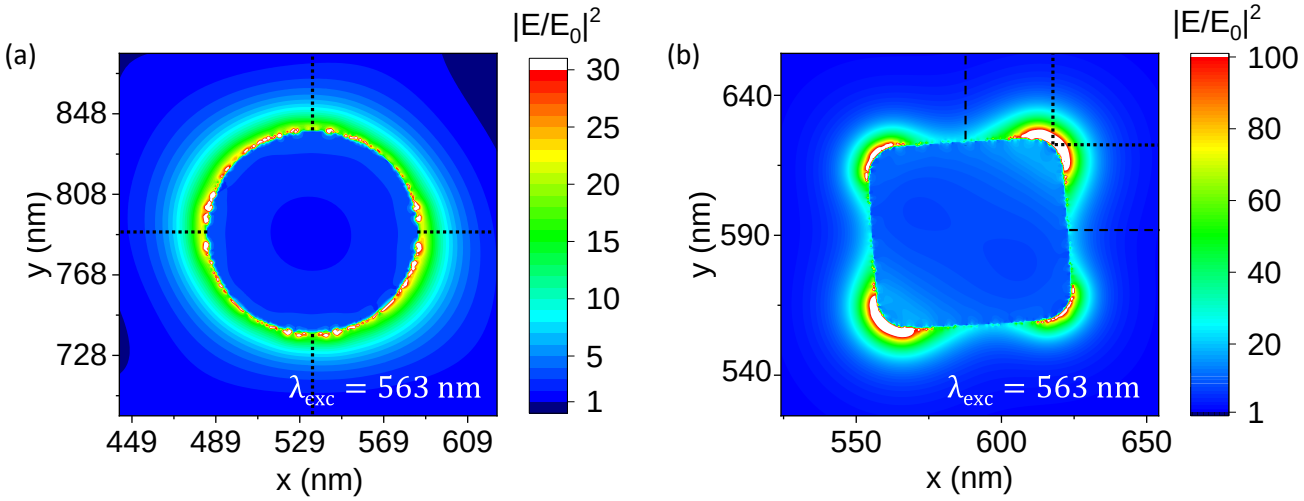

Figure 4.5. Unpolarized $\mathrm{EF_{e.m.}}$ profiles at 563 nm for (a) AuNS140 and (b) AuNC60. For graphical purposes, points with $\mathrm{EF_{e.m.}} \geq 30$ and $\mathrm{EF_{e.m.}} \geq 100$ for AuNS140 and AuNC60, respectively, are all indicated as white. Dotted and dashed black lines include directions along which $\mathrm{EF_{e.m.}}$ was recorded and analyzed (not all directions shown for AuNCs60).

The $\mathrm{EF_{e.m.}}$ for the target AuNS140 were recorded (and averaged) along the four directions denoted by dotted black lines in Figure 4.5a. Analogously, the $\mathrm{EF_{e.m.}}$ for the target AuNC60 were recorded (and averaged) along the x- and y-directions at each corner (dotted black lines in Figure 4.5b) as well as along the normal to each edge midpoint (dashed black lines in Figure 4.5b). For graphical purposes, Figure 4.5b displays the considered direction only for one corner and two edges.

Table 2 summarizes the simulated distance–dependent mean $\mathrm{EF_{e.m.}}$ profiles resulting from our analysis, together with the corresponding relative $\mathrm{EF_{e.m.}}$ profiles calculated with respect to the 33 nm long dsDNA100 (in round brackets).

Table 2. Summary of the simulated $\mathrm{EF_{e.m.}}$ profiles for the target AuNS140 and AuNC60 along with the relative $\mathrm{EF_{e.m.}}$ (assuming the 33 nm long dsDNA100 as reference).

Distance (nm)	Target AuNS	
	$\mathrm{EF_{e.m.}}$	(&**EF**)
5	15.8	(**7.5**)
7	13	(**6.2**)
10	9.9	(**4.7**)
15	6.7	(**3.2**)
17	5.7	(**2.7**)
20	4.7	(**2.2**)
25	3.4	(**1.6**)
30	2.5	(**1.2**)
33	2.1	(**1**)
35	1.9	

Distance (nm)	Target AuNC, Corners		Target AuNC, Edge midpoints	
	$\mathrm{EF_{e.m.}}$	(&**EF**)	$\mathrm{EF_{e.m.}}$	(&**EF**)
5	65	(**25**)	14	(**7.8**)
7	43	(**16.5**)	11	(**6.1**)
10	26	(**10**)	8.4	(**4.7**)
15	12.5	(**4.8**)	5.5	(**3**)
17	10	(**3.8**)	4.8	(**2.7**)
20	7	(**2.7**)	3.8	(**2.1**)
25	4.5	(**1.7**)	2.7	(**1.5**)
30	3	(**1.2**)	2	(**1.1**)
33	2.6	(**1**)	1.8	(**1**)
35	2.3		1.6	

The values of the relative $\mathrm{EF}_{\mathrm{e.m.}}$, shown in round brackets, are the ones to be compared with the experimental $\mathrm{EF}_{\mathrm{MEF}}$ reported in Table 1, since both are calculated taking the longest (33 nm long) dsDNA100 as reference.

4.4.1 Low Concentration Regime: 1 nM HS dsDNAs

We can readily see that the relative (mean) $\mathrm{EF}_{\mathrm{e.m.}}$ around the AuNC60 top facet corners totally agree with the experimental relative $\mathrm{EF}_{\mathrm{MEF}}$ found for the AuNC60 array at the lowest concentration of 1 nM (bottom-right panel of Table 1). Indeed, at 1 nM, $\mathrm{EF}_{\mathrm{MEF}}(\mathrm{ds50}) = 3.7$ and $\mathrm{EF}_{\mathrm{MEF}}(\mathrm{ds21}) = 20$, which have to be compared with the simulated relative $\mathrm{EF}_{\mathrm{e.m.}}(17\ \mathrm{nm}) = 3.8$ and $\mathrm{EF}_{\mathrm{e.m.}}(7\ \mathrm{nm}) = 16.5$, respectively. The former perfectly matches the experimental result, and the latter is in well agreement with the corresponding experimental result. Note that $\mathrm{EF}_{\mathrm{e.m.}}(5\ \mathrm{nm}) = 25$, and the average between $\mathrm{EF}_{\mathrm{e.m.}}(7\ \mathrm{nm})$ and $\mathrm{EF}_{\mathrm{e.m.}}(5\ \mathrm{nm})$ is $\approx$ 21. Considering the $\mathrm{EF}_{\mathrm{e.m.}}(5\ \mathrm{nm})$ is reasonable since dsDNA can have some minor tilt from the normal to the surface.[77] Therefore, the simulated $\mathrm{EF}_{\mathrm{e.m.}}$ profiles for the AuNC60 (top facet) corners totally align with the experimental result at 1 nM. Remarkably, this circumstance suggests that dsDNAs preferentially bind to the AuNCs60 (top facet) corners at the lowest concentration of 1 nM.

A comparison between the experimental $\mathrm{EF}_{\mathrm{MEF}}$ at 1 nM and simulated $\mathrm{EF}_{\mathrm{e.m.}}$ cannot be done for the AuNS140 array, as no experimental $\mathrm{EF}_{\mathrm{MEF}}$ are available at 1 nM (the fluorescence signal for ds100 and ds50 are, essentially, zero).

Finally, at 1 nM, we can discuss about the fluorescence gain G of the AuNC60 array versus the AuNS140 array for the dsDNA21. It is worth recalling that $G = I_{ren}^{NCs}/I_{ren}^{NSs}$, i.e., it is a ratio between fluorescence intensities. Therefore, not only G depends on the enhancement factors but also on the number of fluorophores bound to the arrays (but does not depend on the array surface, which is equalized by the geometric parameter Σ_{eff}). Let us assume that the same number of fluorophores are bound to AuNS140 and AuNC60 array. Furthermore, let us assume that the fluorophores are preferentially located at the NCs corners (as suggested by the previous analysis) and at the north NSs hemisphere (where the monitor is placed). Under these two assumptions, the experimental G would now reduce to the ratio between the two experimental $\mathrm{EF}_{\mathrm{MEF}}$ offered by the arrays, and can be compared with the corresponding ratio of the simulated (absolute) $\mathrm{EF}_{\mathrm{e.m.}}$. Since $\mathrm{EF}_{\mathrm{e.m.}}(7\ \mathrm{nm}) = 43$ for the AuNC60 corner and $\mathrm{EF}_{\mathrm{e.m.}}(7\ \mathrm{nm}) = 13$ for AuNS140, their ratio $43/13 = 3.3$ would be the theoretical prediction for G under the above-mentioned assumptions. Remarkably, this theoretical prediction is equal to the experimental gain. This circumstance supports our assumptions, i.e., that an equal number of fluorophores are bound to AuNSs140 and AuNCs60 array at 1 nM; and that, in the case of AuNCs60, they are concentrated towards the four top facet corners, while they are evenly distributed over the entire north hemisphere of the AuNSs140. It is worth stressing that this gain would be purely plasmonic, and due to the sharp AuNC60 corners, which exhibits a 3.3 times more intense **E** than AuNS140 (at a distance of 7 nm).

4.4.2 Low Concentration Regime: 2.5 nM HS dsDNAs

The experimental relative $\mathrm{EF_{MEF}}$ for the AuNC60 array are $\mathrm{EF_{MEF}(ds50)} = 1.7$ and $\mathrm{EF_{MEF}(ds21)} = 7$, see Table 1 (bottom-left panel). A satisfying agreement was found with the simulated $\mathrm{EF_{e.m.}}$ profile along directions orthogonal to the top facet edge midpoints (see Figure XX), being the corresponding relative $\mathrm{EF_{e.m.}}(17\ \mathrm{nm}) = 2.7$ and $\mathrm{EF_{e.m.}}(7\ \mathrm{nm}) = 6.1$. Note that the relative $\mathrm{EF_{e.m.}}(5\ \mathrm{nm}) = 7.8$, and the average between $\mathrm{EF_{e.m.}}(7\ \mathrm{nm})$ and $\mathrm{EF_{e.m.}}(5\ \mathrm{nm})$ is exactly equal to 7, i.e., the experimental value for ds21. Instead, $\mathrm{EF_{e.m.}}(17\ \mathrm{nm}) = 2.7$ is higher than 1.7 and there is no reasonable way to better match this simulated value (along the normal to the top edge midpoints) with the experimental value.

However, the following picture easily emerge. At 2.5 nM, the four top corners have not enough space to house all the dsDNAs, therefore the "surplus" of dsDNA (compared to 1 nM) start to bind along the edges, at least. The shortest dsDNA21 would follow this dynamics strictly; instead, the longer dsDNA50 could have access not only to the top corners and edges, but also to the side facets and edges. In fact, the longer dsDNA50 carries a negative charge higher than dsDNA21, consequently it would naturally spread over a surface more than the shorter dsDNA21 to minimize repulsions. Since the $\mathrm{EF_{e.m.}}$ profiles of the side facets and edges are less intense than the top edges, a fraction of dsDNA50 would experience a $\mathrm{EF_{e.m.}}$ lower than 2.7 at a distance of 17 nm from the surface, and the mean $\mathrm{EF_{e.m.}}$ would eventually match the experimental value of 1.7.

The experimental relative $\mathrm{EF_{MEF}}$ for the AuNS140 array at 2.5 nM dsDNA are $\mathrm{EF_{MEF}(ds50)} = 3$ and $\mathrm{EF_{MEF}(ds21)} = 33$, see Table 1 (bottom-left panel). Considering a minor tilt of the dsDNA, the simulated values to be considered are, respectively, the relative $\mathrm{EF_{e.m.}}(17\ \mathrm{nm}) = 2.7$ and the relative $\mathrm{EF_{e.m.}}(15\ \mathrm{nm}) = 3.2$, whose mean is 3; and the relative $\mathrm{EF_{e.m.}}(7\ \mathrm{nm}) = 6.2$ and the relative $\mathrm{EF_{e.m.}}(5\ \mathrm{nm}) = 7.5$, whose mean is 6.8. While the theoretical prediction of 3 totally agrees with the experimental result for the dsDNA50, there is a huge discrepancy between simulation and experiment in the case of dsDNA21, as the experimental $\mathrm{EF_{MEF}(ds21)}$ is 5 times higher than the theoretical prediction of 6.8.

It is worth noting that $\mathrm{EF_{e.m.}}$ profile displayed in Table 1 is already maximal, since the frequency–domain field profile monitor is already placed at an optimized height (10 nm above the equatorial plane) at the optimized $\lambda_{exc} = 563$ (the max excitation wavelength allowed by our experimental equipment). Therefore, the plasmonic enhancement alone cannot explain the experimental result, and the missing factor has to be attributed to non-plasmonic effects. The most obvious effect to take into consideration is the steric effect. In fact, an intrinsic variable of our experiment is represented by the linear lengths of the dsDNAs, i.e., 7 nm for the 21-mer, 17 nm for the 50-mer, and 33 nm for the 100-mer). Notably, the ratio between the number of base pairs of the 100-mer and the 21-mer is exactly the missing factor of 5. Therefore, we hypothesize that the number of dsDNA21 binding to the AuNS140 array is 5 times higher than the number of dsDNA100 at 2.5 nM due to steric effects (while no steric effects would take place in the case of dsDNA50, which is "just" 2 times longer than dsDNA100). This would mean that, at low concentrations, the surface density of dsDNA on AuNS140 strongly depends on the linear length of the dsDNAs themselves, due to steric effect. The rapid decrease in surface coverage with increase in dsDNA length is actually reported in literature. [78] Therefore, our hypothesis is legitimate.

Finally, let us discuss the fluorescence intensity gains G of the AuNCs60 array compared to AuNSs140 array. The experimental gains are $\mathrm{G(ds21)} = 3.3 \pm 0.4$, $\mathrm{G(ds50)} = 8 \pm 1$, and $\mathrm{G(ds100)} = 16 \pm 2$. The theoretical predictions for G, calculated as the ratio of the absolute AuNC60 $\mathrm{EF_{e.m.}}$ along the normal to the edge midpoint and the corresponding absolute AuNS140 $\mathrm{EF_{e.m.}}$, are $\mathrm{G} \leq 1$ at any distance, surprisingly. The theoretical predictions would not agree with the experimental trend even considering the absolute $\mathrm{EF_{e.m.}}$ around the AuNCs60 corners, as the theoretical gain would be 3.3 for the 7 nm long dsDNA21, 1.8 for the 17 nm long dsDNA50, and 1.2 for the 33 nm long dsDNA100. Therefore, our simulations cannot explain the experimental results.

Apart from the specific values, the experimental trend resembles an exponential growth, since $3.3 \approx 4 = 2^2$, $8 = 2^2$, and $16 = 2^4$. The only way to account for this experimental trend by plasmonics would be a AuNC60 $\mathrm{EF_{e.m.}}$ profile decaying (exponentially) much more slowly than the exponential decay of AuNS140 $\mathrm{EF_{e.m.}}$, i.e., constant compared to the AuNS140. At the same time, this constant value should be very high. For instance, if the $\mathrm{EF_{e.m.}}$ of AuNC60 was 43 everywhere, and the AuNS140 $\mathrm{EF_{e.m.}}$ was the one reported in Table 2, a fair agreement could be obtained. But such a scenario is not physical, and would contradict not only our simulations for the AuNCs60 but also the experimental $\mathrm{EF_{MEF}}$ for AuNCs60 (which matches very well with the simulated $\mathrm{EF_{e.m.}}$profile along the normal to the edge midpoints). Therefore, plasmonics alone cannot explain the observed experimental trend for G.

Instead, a combination of steric effect due to the increasing lengths of the dsDNA as well as nanoparticle curvature effect could qualitatively account for the observed trend. As experimentally demonstrated by Mirkin and coworkers, [79] smaller spherical AuNPs (smaller radius of curvature) exhibits higher surface densities than larger NPs (higher radius of curvature) when saturated by thiolated ssDNA with 25 bp. For smaller AuNPs (smaller radius of curvature), the deflection angle between neighbour ssDNAs orthogonally attached to the AuNP surface increases, allowing each ssDNA to stay more and more distant from its neighbours as moving radially out from the AuNP surface. This curvature-related effect naturally decreases the steric interactions (electrostatic repulsion) between the ssDNA, allowing more ssDNA to be attached to highly curved surfaces (with smaller radius of curvature) than to the larger flatter surfaces. Defining the footprint as the average area each ssDNA occupies on the nanoparticle, they found that the footprint of their ssDNA (at saturation) was 4.9 $\mathrm{nm^2}$ on a AuNP with diameter of 10 nm (calculated deflection angle of 29°), 7 $\mathrm{nm^2}$ on a 20 nm AuNP (deflection angle: 17°), 11 $\mathrm{nm^2}$ on a 30 nm AuNP (deflection angle: 14°), 14 $\mathrm{nm^2}$ for a 100 nm nanoparticle (deflection angle: 4.9°), and 18 $\mathrm{nm^2}$ for planar gold (deflection angle: 0°). In particular, the deflection angle exponentially decreases as a function of the AuNP diameter. We cannot directly compare our results with Mirkin's as we have dsDNAs (rather than ssDNA) as well as we are in a low concentration regime (rather than at saturation), and we did not find similar reports for dsDNA in literature. However, since dsDNA carries a double negative charge compared to ssDNA, the curvature related effect on dsDNA should be even more significant than the case of ssDNA. Furthermore, steric effect should be even greater at low concentrations.

By analogy with the above-mentioned Mirkin's findings, we speculate here that the AuNCs60 are much more efficient than the (≈ 100 nm) AuNS140 in housing the longer dsDNAs thanks to their rounded edges and corners, which have radius of curvature of 14 nm according to our modelling (while 12 ± 2 nm experimentally). Since the theoretical gain $\mathrm{G} \leq 1$ at any distance, we speculate

that the experimental gains are purely steric at least for ds50 and ds100, and that this steric gains increase exponentially with the length of the dsDNA. For instance, the surface density of dsDNA onto the AuNCs60 could mildly depend on the dsDNA length (since the highly curved edges and corner well accommodate the dsDNAs) while the surface density of dsDNA onto the large AuNS140 could rapidly (exponentially) decrease with the length of the dsDNA, as it resembles the planar gold case. [78] At the best of our knowledge, the dependence of dsDNA surface density on the length of dsDNA at varying AuNPs size is not yet reported in literature.

4.4.3 High concentration Regime: 500 nM HS dsDNAs

Let us finally discuss the results at 500 nM HS. The LS case is analogous except for a 4-fold decrease in I_{ren}, due to the different ionic strength of the buffer, as already mentioned.

The experimental relative $\mathrm{EF_{MEF}}$ for the AuNC60 array are $\mathrm{EF_{MEF}(ds50)} = 1.1$ and $\mathrm{EF_{MEF}(ds21)} = 2$, while $\mathrm{EF_{MEF}(ds50)} = \mathrm{EF_{MEF}(ds21)} = 0.9$ for the AuNS140 array, see Table 1 (top-left panel). In other words, $\mathrm{EF_{MEF}}$ showed only a 2–fold increase in the case of AuNC60 array, while $\mathrm{EF_{MEF}}$ is nearly 1 (no enhancement) for AuNSs140 array. Not only these experimental results totally disagree with any simulated $\mathrm{EF_{e.m.}}$, but also disagree with the experimental $\mathrm{EF_{MEF}}$ at low concentrations. Moreover, the same trends were observed at LS conditions as well.

The redundancy of these experimental results led us to the hypothesis that MEF mechanisms itself is operating differently at this high concentration regime. In fact, any $\mathrm{EF_{e.m.}}$ profile refers to the local electromagnetic field **E** resulting from the interplay between the external source radiation and the nanostructure, but it does not consider the interplay of the fluorescent molecules with the nanostructure. In other words, any simulated $\mathrm{EF_{e.m.}}$ profile strictly refers to the case of a negligible number of fluorophores located in the neighbourhood of the plasmonic nanostructures, i.e., a low-concentration regime. While $\mathrm{EF_{e.m.}} = \mathrm{EF_{abs}}$ at low concentrations (as obtained at 1 nM for the AuNCs60), $\mathrm{EF_{e.m.}} > \mathrm{EF_{abs}}$ at high concentrations, where the interplay between fluorophores and plasmons becomes relevant.

The work by Khurgin and Sun[63] provides a theoretical support to our hypothesis. In the case of a spherical NP, they obtained an analytical expression for $\mathrm{EF_{abs}}$ (see their formula 38) which also contain a $(N_a\sigma_a)^{-1}$ dependence, with N_a the number of fluorophores, each having absorption cross section σ_a. Therefore, MEF mechanisms and, in particular, $\mathrm{EF_{abs}}$, crucially depend on the total absorption cross sections $N_a\sigma_a$ of the fluorescent molecules located in the neighbourhood of nanostructure. To be specific, $N_a\sigma_a$ becomes an important factor when it approaches the loss in the metal.[63] For instance, in Khurgin and Sun[63] specific case, the presence of 10^3 Rhodamine G molecules ($\sigma_a = 0.1$ nm^2) [63] with a total absorption cross section $N_a\sigma_a = 100$ nm^2 placed 5 nm far from a 20 nm AgNP embedded in GaN was estimated to cause a decrease of $\mathrm{EF_{abs}}$ of 3.5 times.

Obviously, our system is different from theirs. However, it is interesting to quantify the relevant variables in our case. Using the previous work by Mirkin,[79] we can easily estimate $N_a\sigma_a$(ATTO565) for our 104 nm AuNS140 saturated by dsDNA21 (whose length is comparable to the ssDNA used by Mirkin). Assuming our dsDNA21 has double the footprint of Mirkin's ssDNA on a 100 nm sphere, i.e., 28 nm^2, and considering that our 104 nm sphere has area $A = 4\pi r^2 \approx 34 \times 10^3$ nm^2, it follows that ≈ 1200 dsDNA21 could be tethered onto a AuNSs140 at saturation. Using the

formula[85] $\sigma = \varepsilon \ln(10)\, 10^3/N_A \approx 3.82\, \varepsilon \times 10^{-21}$ (in unity of cm^2) with N_A Avogadro's number and $\varepsilon = 1.2 \cdot 10^5\ \mathrm{M^{-1}cm^{-1}}$, it follows $\sigma(\mathrm{ATTO565}) = 0.05$ nm^2. Therefore, under our assumptions, $N_a\sigma_a(\mathrm{ATTO565}) = 60$ nm^2 for a AuNS140 saturated by dsDNA21. According to Khurgin and Sun,[63] this value is high enough to cause a drastic decrease of $\mathrm{EF_{abs}}$.

It is worth recalling that for AuNS140 (see Table 2) our simulations predicted relative $\mathrm{EF_{e.m.}}$ of 2.7 and 6.2 for ds50 and ds21, respectively, whereas experimentally $\mathrm{EF_{MEF}(ds50) = EF_{MEF}(ds21)} \approx 1$. To match the experimental values, we need a length-dependent damping factor. The most obvious length-dependent parameter are the following relative steric parameters

$$\xi_{21} = \frac{\mathrm{dsDNA(21)}}{\mathrm{dsDNA(100)}} = 1/5\,, \qquad \xi_{50} = \frac{\mathrm{dsDNA(50)}}{\mathrm{dsDNA(100)}} = 1/2\,, \qquad \xi_{100} = \frac{\mathrm{dsDNA(100)}}{\mathrm{dsDNA(100)}} = 1$$

i.e., the ratio between the number of base pairs of each dsDNA with respect to the longest dsDNA100. Introducing the relative damped $\mathrm{EF}_{e.m.}^{damp}$ as

$$\mathrm{EF}_{e.m.}^{damp} \equiv \xi\, \mathrm{EF_{e.m.}},$$

we readily obtain:

$$\mathrm{EF}_{e.m.}^{damp}(ds21) = \frac{6.2}{5} = 1.24 \qquad \mathrm{EF}_{e.m.}^{damp}(ds50) = \frac{2.7}{2} = 1.35 \qquad \mathrm{EF}_{e.m.}^{damp}(ds50) = \frac{1}{1} = 1$$

i.e., a nearly constant trend close to 1, which well matches with the experimental $\mathrm{EF_{MEF}}$. Moreover, as mentioned above, [78] the number of dsDNAs tethered onto a flat surface (and a 100 nm sphere is nearly flat) depends on the length of dsDNAs. Therefore, our length-dependent $\mathrm{EF}_{e.m.}^{damp}$ can be seen as a function of N_a. In other words, the expected dependence on $(N_a\sigma_a)^{-1}$ is roughly retrieved.

The same principles can be applied to AuNC60, even though the geometry of such particle is more complex. With the help of our nanoparticle model, i.e., a 74 nm nanocube with edges and corners rounded by spheres and cylinders with radii of 14 nm, we can provide few numerical estimations.

Neglecting the bottom cube facet together with its rounded corners and edged (not available to dsDNA because bound to the glass), as well the top facet corners (for simplicity), then we can re-think our NC60 as made by 4 rounded vertical edges, each described by a 1/4 slice of a 74 nm long cylinder; 4 rounded edges connecting the previous vertical edges at the top facet, each described by a 1/4 slice of 46 nm long cylinder; and 5 remaining rectangular flat facets of 46 nm. Respectively, they have areas 6.5×10^3 nm^2, 8×10^3 nm^2, and 10.6×10^3 nm^2. In particular, the sum of the first two rounded areas is 10.5×10^3 nm^2 while the total flat area is 10.6×10^3 nm^2, i.e., they are essentially equal. Let us now recall that, according to Mirkin, the footprint of (its) ssDNA over a planar gold was 18 nm^2 while on a 30 nm AuNP it was a 11 nm^2. The flat portion of our cube are analogous to planar gold, and we can assume a footprint of 36 nm^2 for our dsDNA21. The rounded portions of our cube have nearly the same radius of curvature of a 30 nm AuNP (the radius of curvature of the rounded portions of our model is 14 nm), and we can assume a footprint of 22 nm^2. At saturation, $N_a = (10.6/36 + 10.5/22) \times 10^3 \approx 800$ and $N_a\sigma_a(\mathrm{ATTO565}) = 40$ nm^2.

Therefore, nearly the same damping effect occurring for AuNS140 should be observed over a AuNC60 at saturation, slightly less pronounced. In this case, an estimation of $\mathrm{EF}_{e.m.}^{damp}$ is harder, since a nanocube is highly anisotropic and different portions have different $\mathrm{EF}_{\mathrm{e.m.}}$ profiles, as shown in Table 2. However, if we use the relative $\mathrm{EF}_{\mathrm{e.m.}}$ profile normal to the edge midpoint (see Table 2), we obtain

$$\mathrm{EF}_{e.m.}^{damp}(ds21) = \frac{6.1}{5} = 1.22\,, \qquad \mathrm{EF}_{e.m.}^{damp}(ds50) = \frac{2.7}{2} = 1.35\,, \qquad \mathrm{EF}_{e.m.}^{damp}(ds50) = \frac{1}{1} = 1\,,$$

i.e., a constant trend; instead, if we use the relative $\mathrm{EF}_{\mathrm{e.m.}}$ profile around the corner (see Table 2), we obtain:

$$\mathrm{EF}_{e.m.}^{damp}(ds21) = \frac{16.5}{5} = 3.3\,, \qquad \mathrm{EF}_{e.m.}^{damp}(ds50) = \frac{3.8}{2} = 1.9\,, \qquad \mathrm{EF}_{e.m.}^{damp}(ds50) = \frac{1}{1} = 1\,,$$

i.e., an increasing trend (as the experimental trend). Therefore, we expect that a proper volume averaged $\mathrm{EF}_{\mathrm{e.m.}}$ could yield the observed experimental trend. For instance, if we simply average the two previous results, we obtain $\mathrm{EF}_{e.m.}^{damp}(ds21) = 2.26$ and $\mathrm{EF}_{e.m.}^{damp}(ds21) = 1.63$ and the former value, remarkably, matches with the corresponding experimental result.

Conclusions

The use of seed–mediated methods embracing Mirkin's meticulous attention to the quality of the seeds allowed for the synthesis of high–quality AuNSs and AuNCs with exceptional yield (>95%).[29] Compared to Mirkin's procedures, we found that the cyclical seed refinement was unnecessary in our case. This allowed us to simplify the synthesis of the final CPC–capped seeds while maintaining the same high quality. The improvement can be attributed to the higher yield in the initial synthesis of CTAB–capped seeds, achieved thanks to a meticulous attention to subtle technical details (see Appendix A.1). This higher yield resulted in AuNRs with lower AR, which facilitated their dissolution to spherical seeds. Further optimization of CPC–capped seed fabrication could be easily predicted by using larger amounts of initial CTAB–capped seeds for AuNRs synthesis. This would lead to a greater number of AuNRs with even lower AR, thereby facilitating their dissolution further. This, in turn, would optimize the subsequent synthesis of CRD, AuNSs, and AuNCs as the seeds would be even more spherical.

As expected, AuNSs were found to be perfectly spherical in shape as a result of the CTAB–mediated dissolution reaction first studied by Liz-Marzán.[30] Instead, AuNCs are best described as cubes with rounded edges and corners ($R_{curv} = 14$ nm), due to crystallographic limitations (energy of the crystallographic facets). The understanding of "what happens on the gold surface" is paramount for optimizing the synthesis protocols and achieving the sharpest features. In fact, the desired high local electromagnetic fields facilitating the MEF phenomena largely depend on the sharpness. In this regards, the MEF performance of the AuNCs60 array could be improved optimizing the AuNCs protocols for bromide concentrations, e.g., adopting the optimized protocol found in Ref.[49], where the authors obtained $R_{curv} \approx 8$ nm for the corners of AuNCs of size comparable to our AuNCs60.

The actual, physically achievable sharpness of anisotropic NPs is a crucial consideration for any plasmon–related phenomena. In these regards, FDTD as well as other type of simulations are invaluable tools. They enable not only the study of the optical properties of NPs with ideal geometry but also the determination of the best optical model to describe actual NP morphology. Simulations based on these realistic models, rather than ideal ones, are key for designing experiments, predicting outcomes, and guiding research effectively.

The synthesis of positively charged AuNPs (due to their natural cationic surfactant cappings) allowed for their immobilization onto standard, pristine glass substrates with no need for chemical modifications. A routinary plasma activation of the glass and a specific concentration of surfactant in the colloids were the only necessary things. The absence of an intermediate and potentially non-uniform layer (e.g., APTES) contributed to the extraordinary uniformity over macroscopic scale (tens of cm^2) of the fabricated nanostructures, which candidate them to large scale production. Moreover, the very high uniformity of the nanostructures was also indirectly confirmed by the fluorescence measurements, which are indeed affected by negligible errors. This high uniformity could result in very accurate and reproducible results in a future biosensing application.

The large sizes of our AuNPs triggered unusual collective plasmon effects, reported by Jenkins,[62] due to long–range dipolar interactions. FDTD simulations were paramount to be aware of this

effects, which entailed blueshifted, narrower, and sharper LSPR compared to the corresponding colloidal NPs. Notably, sharp resonances are usually obtained in ordered lattices fabricated by more sophisticated techniques.[7] In contrast, we obtained sharp resonances from random arrays fabricated by the simple self–assembly technique. Furthermore, such LSPRs are tuneable over a wide spectral range by varying the NND itself, which can be achieved by changing the concentration of NPs used for the incubation, or by varying the NP size, which can be easily achieved during synthesis.

Finally, our distance-dependent MEF study on AuNSs140 and AuNCs60 arrays exhibited an unexpected $\mathrm{EF_{MEF}}$ trend at high concentration (500 nM dsDNA). In contrast to all our simulations, no fluorescence enhancement at all was attained by the AuNSs140 array, and only a 2–fold enhancement was attained by the AuNCs60 array. This experimental evidence was explained by an inherent yet subtle MEF mechanism, described by Khurgin and Sun,[63] according to which the $\mathrm{EF_{abs}}$ does depend on the number of fluorophores placed in the nanostructure surroundings and can be much limited whenever their total absorption cross section is too high, as seen in chapter 3. This is the main reason why the highest $\mathrm{EF_{MEF}}$ reported in literature are always found in single–molecule experiments. On the other hand, this also means that MEF is a technology intrinsically optimized for single–molecule detection.

The comparative study on AuNSs140 and AuNCs60 arrays clearly showed that the latter generally offer superior performance, especially in the low concentration regime. Therefore, the use of a AuNCs60 nanostructure is generally recommended against the use of a AuNSs140 nanostructure in view of its future application as transducer of a MEF–based biosensor. In fact, a gain up to 16 times was observed at 2.5 nM of dsDNA100.

While the experimental results are clear, their explanation was not easy to address, and can be still debatable. Our FDTD simulations suggested that the above–mentioned gain (as well as few others) cannot be explained by plasmonics alone. According to another work by Mirkin and coworkers[79] (on the role radius of curvature plays in thiolated oligonucleotide loading on spheroidal AuNPs) as well as a work by Huang[78] (which also deals with the role the dsDNA length plays in thiolated oligonucleotide loading onto a flat gold surface), we speculated that the observed gain has to be attributed to the simultaneous dependence of dsDNA surface density on both the AuNPs local curvature *and* the dsDNA linear length. At the best of our knowledge, such a simultaneous dependence is not yet reported in literature and is, possibly, an original contribution of this work. If we were right, this would mean that the AuNCs60 nanostructure, which always offers superior performance when compared to the AuNS140 nanostructure, would offer the best performance when detecting longer nucleic acids, since these would be better accommodated by the sharp features of the cubes.

Finally, it is worthwhile to note that the nanostructure fabrication method we developed is based on electrostatics, therefore it can be extended to any kind of positively charged NP and negatively charged substrate. In fact, three different kinds of positively charged AuNPs (AuNSs, AuNCs, and CRD, too) capped by two different types of cationic surfactants (CTAB and CPC) were effectively immobilized onto the same type of glass substrate according to this method. The choice of glass substrate was merely due to the past “history” of our group, and an exciting perspective would be the application of the developed method for the fabrication of similar nanostructures on a

polystyrene substrate, since petri dishes and multiwell microplates are made of polystyrene. This would open up the panorama of high–throughput bioanalytical applications.

Appendix A. Seed–mediated Growth Synthesis

A.1 Initial CTAB-capped Gold Seeds

The initial CTAB-capped seeds for AuNRs were synthesized according to Mirkin's paper[29], with integrations from El-Sayed's seminal paper.[32] Firstly, 5 mL of 100 mM CTAB was warmed at 28°C under gentle stirring till complete solubilization (solution colour: transparent), 100 mM being the maximum solubility of CTAB in water at 20°C. Afterwards, 125 µL of 10 mM $HAuCl_4 \cdot 3H_2O$ were added and thoroughly mixed for 2 min under vigorous stirring. At this stage, the solution colour turned from transparent to a characteristic dark yellow due to the $AuCl_4^-$ adsorption to CTAB micelles.[30] Finally, 300 µL of freshly prepared ice-cold 10 mM $NaBH_4$ was rapidly injected and vigorously stirred for 2 min. Then, stirring was stopped, magnetic rod removed, and solution kept at 25 °C (to avoid CTAB crystallization) until NRs synthesis. It is indeed recommended to age the seed solution for 2-6 h prior to use to allow for complete hydrolysis of unreacted $NaBH_4$.[86] Seed solution was not stored nor used beyond this time spot since it degrades during time: its initial light yellow-brown colour slowly turned to light pink over a week, signalling the formation of larger AuNPs. It is also worth stressing that $NaBH_4$ powder should be freshly prepared for every synthesis, dissolved in ice-cold ultrapure water (rather than in room-temperature water to be refrigerated afterwards), and used as soon as possible. In fact, $NaBH_4$ separates into Na^+ and BH_4^- once in water, and BH_4^- soon starts to hydrolyse (with release of H_2 pressurizing the vial). Since BH_4^- is the actual reducing specie for the seeds formation, its hydrolysis is un unwanted process to be limited as mentioned above.

A.2 Gold Nanorods (AuNRs)

AuNRs were synthesized following Mirkin's paper,[29] with integrations from El-Sayed's seminal paper.[32] Firstly, 130 mL of 100 mM CTAB was warmed at 28°C under gentle stirring till complete solubilization. Afterwards, 6.5 mL of 10 mM $HAuCl_4 \cdot 3H_2O$ were added and thoroughly mixed for 2 min under vigorous stirring. At this stage, the solution colour turned from transparent to a characteristic dark yellow due to the $AuCl_4^-$ adsorption to CTAB micelles.[30] Then, 1.17 mL of freshly prepared 10 mM $AgNO_3$ and 741 µL of freshly prepared 100 mM L-ascorbic acid were added in succession and stirred for 2 min each. Addition of L-ascorbic acid changed the solution colour from dark yellow to transparent, as Au^{3+} is reduced to Au^+. The as-obtained solution served as growth solution for AuNRs. Indeed, 156 µL of freshly-prepared initial gold seeds (see previous protocol above) were finally added to the growth solution (at 28 °C) and thoroughly mixed under vigorous stirring for 2 min. Subsequently, stirring was stopped, magnetic rod removed, and the solution left untouched in the 28°C water bath for 2 h (to let the AuNRs grow). At this time, AuNRs usually exhibited OD 1.3 ± 0.1 at the l-LSPR of 700 ± 5 nm. Growth process was stopped, and excess of reagents removed, by 2 rounds of centrifugations and resuspensions by 50 mM CTAB each time. The parameters used for centrifugation were (4300 g, 15 min, RT) at Eppendorf MiniSpin® (max rotor radius: 6 cm), or (6300 g, 30 min, RT) at Heraeus Megafuge 1.0 R (max rotor radius: 15.5 cm). In view of the next step, AuNRs concentration was brought to OD 2 by adding 50 mM CTAB as well.

A.3 Final CPC-capped Gold Seeds (From AuNRs Dissolution)

The final CPC-capped gold seeds were obtained from the AuNRs oxidative dissolution first reported by Liz-Marzán.[30] We followed both Liz-Marzán's and Mirkin's papers.[29,30] A desired amount of AuNRs at OD 2 in 50 mM CTAB was brought to a final concentration of 90 µM $HAuCl_4$ by adding a suitable volume of 10 mM $HAuCl_4 \cdot 3H_2O$, keeping the solution under gentle stirring for 4 h at 40°C. At this point, the etched NPs usually exhibited OD 0.25 ± 0.05 at the LSPR of 524 ± 1 nm. Dissolution process was stopped, and excess of reagents removed, by (at least) 3 rounds of centrifugations and resuspensions by 100 mM CPC each time. This step was essential to remove residues of CTAB and gold leading to unwanted dissolutions in the next steps. Roughly, CTAB content was dropped down to nM level. The parameters used for centrifugation were (8100 g, 30 min, RT) at Eppendorf MiniSpin® (max rotor radius: 6 cm). In view of the next synthesis, the concentration of the colloidal solution was brought to OD 1 by adding 100 mM CPC. The colloid was stored at room temperature until use up to 4 weeks. No measurable changes in UV-Vis spectrum were observed over this time period.

A.4 Gold Concave Rhombic Dodecahedra (CRD)

CRD were synthesized according to the works of Niu[33] and Mirkin[29]. 20 mL of 10 mM CPC was warmed at 25°C under gentle stirring. Then, 350 µL of 10 mM $HAuCl_4 \cdot 3H_2O$ and 4.5 mL of freshly prepared 100 mM L-ascorbic acid were added in succession and thoroughly stirred for 2 min each. Addition of gold turned the solution colour from transparent to dark yellow while the subsequent addition of L-ascorbic acid turned the colour back to transparent. The as-obtained solution served as growth solution for the CRD. A desired amount of seeds adjusted to yield a desired CRD size (typically, 100 - 200 µL of seeds at OD 1 and 100 mM CPC) was then injected in the growth solution and thoroughly mixed under vigorous stirring for 1 min. Subsequently, stirring was stopped, magnetic rod removed, and the solution left untouched in the 25°C water bath for 30 min (to let the CRD grow). Growth process was stopped, and excess of reagents removed, by 3 rounds of centrifugations and resuspensions. In particular, ultrapure water was used as buffer for the first resuspension while 50 mM CTAB for each of the remaining two resuspensions. The initial use of ultrapure pure (rather than CTAB) avoids undesired CRD dissolutions at this stage, due to residues of unreacted gold in the growth solution (even ≤0.1 µM gold triggers dissolution in presence of 50 mM CTAB). The parameters used for centrifugations were (150 g, 15 min, RT) at Eppendorf MiniSpin® (max rotor radius: 6 cm), or (500 g, 30 min, RT) at Heraeus Megafuge 1.0 R (max rotor radius: 15.5 cm). In view of the subsequent dissolution to NSs, CRD concentration was brought to OD 1 by adding 50 mM CTAB as well. The above protocol was found to be scalable up to a factor 10 in volume, at least. Many sizes of CRD were synthesized according to this protocol and termed as the amount of seeds: for instance, CRD180 were obtained by addition of 180 µL of seeds (at OD 1 and 100 mM CPC) to the growth solution; CRD140 by 140 µL of seeds; and so on. The lower the amount of seeds, the larger the size of CRD.

A.5 Gold Nanospheres (AuNSs) (From CRD Dissolution)

AuNSs were obtained from oxidative dissolution of CRD.[29,30] The desired amount of CRD at OD 1 in 50 mM CTAB was brought to a final concentration of 20 µM $HAuCl_4$ by adding a suitable volume of 10 mM $HAuCl_4 \cdot 3H_2O$, keeping the solution under gentle stirring for 4 h at 40°C. Dissolution process was stopped, and excess of reagents removed, by 2-3 rounds of centrifugations and resuspensions by 0.5 mM CTAB each time. The parameters used for centrifugation were (150-250 g, 20 min, RT) at Eppendorf MiniSpin® (max rotor radius: 6 cm) and (500 g, 30 min, RT) at Heraeus Megafuge 1.0 R (max rotor radius: 15.5 cm). It is worth noting that CTAB concentration of 0.5 mM is lower than its critical micelle concentration of 0.9 mM,[31] hence no further dissolutions may take place during storing. Generally, AuNSs were termed according to the corresponding CRD: AuNSs180 resulted from the dissolution of CRD180; AuNSs140 from the dissolution of CRD140, and so on.

A.6 Gold Nanocubes (AuNCs)

Gold nanocubes (AuNCs) were synthesized according to the works of Niu[33] and Mirkin.[29] 5 mL of 100 mM CPC were warmed at 30°C under gentle stirring. Then, 500 µL of 100 mM KBr, 100 µL of 10 mM $HAuCl_4 \cdot 3H_2O$, and 150 µL of 100 mM L-ascorbic acid were added in succession and thoroughly mixed under vigorous stirring for 1 min each. The as-obtained solution served as growth solution for the NCs. A desired amount of seeds adjusted to yield a desired NCs size (typically, 50 - 150 µL of seeds at OD 1 and 100 mM CPC) was then injected in the growth solution and thoroughly mixed under vigorous stirring for 1 min. Subsequently, stirring was stopped, magnetic rod removed, and the solution left untouched in the 30°C water bath for 1 h (to let the AuNCs grow). Growth process was stopped, and excess of reagents removed, by 1–2 rounds of centrifugations and resuspensions by 1 mM CPC. The parameters used for centrifugations were (200–400 g, 15 min, RT) at Eppendorf MiniSpin® (max rotor radius: 6 cm), or (600–1000 g, 30 min, RT) at Heraeus Megafuge 1.0 R (max rotor radius: 15.5 cm). The above protocol was found to be scalable and reproducible up to a factor 20 in volume, at least. AuNCs were termed as the amount of seeds: for instance, AuNCs125 were obtained by addition of 125 µL of seeds (at OD 1 and 100 mM CPC) to the growth solution; AuNCs60 by 60 µL of seeds; and so on. The lower the amount of seeds, the larger the size of the NCs. It is worth mentioning that surfactant-related depletion forces[46–48] induced *reversible* aggregations of the AuNCs obtained by ≤100 µL seeds during the synthesis itself. This process gradually turned the solution colour to grey during synthesis, with the corresponding extinction spectrum exhibiting an almost horizontal line modulated by wide plasmon peaks. However, the aggregates are *reversible* and fully disrupted as soon as the CPC concentration was lowered at 1 mM after the first round of centrifugation and resuspension.

Appendix B. Fabrication of Electrostatic SAMs of AuNPs on Glass

B.1 SAM of Negatively Charged (Turkevich's) AuNPs on Glass

This fabrication generally counted five steps:

a) 24×60 mm type 1 glass coverslips (Knittel Glass, no.1) were cleaned in an ultrasonic bath for 5 min by pure 2-propanol and ultrapure water sequentially. Afterwards, the substrates were extensively rinsed by ultrapure water and dried by a gentle stream of nitrogen.
b) The cleaned substrates were activated by a low-pressure oxygen plasma (1.4 mbar, 200 W, 2') at Gambetti Colibrì Multipurpose Plasma System, to increase the silanol bonds serving as bonding sites for the APTES molecules.
c) The activated substrates were incubated by 0.5% APTES (v:v) in ultrapure water for 45 min for the silanization process. Afterwards, they were extensively rinsed by ultrapure water to remove unbound molecules and dried under a gentle stream of nitrogen.
d) The amino-functionalized substrates were incubated for 4 h at room temperature by 2 mL of citrate-capped AuNPs at OD 2 (after a dilution by ultrapure water of AuNPs synthesized by Pollitt's modification[87] of Turkevich's method). Afterwards, the nanostructured substrates were extensively rinsed by ultrapure water to remove the unbound AuNPs and finally dried under a vigorous stream of nitrogen.
e) The nanostructured substrates were cleaned from citrate ligands and silane layer by a low-pressure oxygen plasma treatment (0.8 mbar, 200 W, 30') at Gambetti Colibrì Multipurpose Plasma System, leaving the bare AuNPs anchored to the bare glass substrate.

B.2 SAM of Positively Charged AuNSs and AuNCs on Glass

This fabrication generally counted six steps:

a) Freshly synthesized AuNSs (AuNSs140, AuNSs180) and AuNCs (AuNCs60, AuNCs125) were centrifuged and resuspended at least three times using 0.8 μM CTAB and 0.5 μM CPC buffer solutions, respectively. The colloids were then brought to a final OD 5 by further diluting with the same buffers. For centrifugations at Eppendorf MiniSpin® (max rotor radius: 6 cm), AuNSs were centrifuged by (≈150 g, 15', RT) while AuNCs by (≈220 g, 15', RT). At Heraeus Megafuge 1.0 R (max rotor radius: 15.5 cm), both AuNSs and AuNCs (≤20 mL in 50 mL tubes) were centrifuged by (≈700 g, 30', 25°C).
b) 24×60 mm or 24×32 mm type 1 glass coverslips (Menzel Gläser, no.1) were cleaned in an ultrasonic bath for 5 min by pure 2-propanol and ultrapure water sequentially. Afterwards, the substrates were rinsed by ultrapure water and dried by a gentle stream of nitrogen.
c) The cleaned substrates were activated by a low-pressure oxygen plasma (0.8 mbar, 200 W, 5') at Diener Electronic PICO low-pressure plasma system, to increase the silanol bonds serving as bonding sites for the CTAB-capped AuNSs or the CPC-capped AuNCs.
d) The activated substrates were incubated for 4 h at room temperature by 2 mL of AuNSs or AuNCs at OD 5 and 0.8 μM CTAB or 0.5 μM CPC, respectively (prepared as in a)). Specifically, AuNSs140, AuNSs180, AuNCs60 and AuNCs125 colloids were used.
e) After 4 h, ultrapure water was used to thoroughly rinse the substrate and remove unbound NPs. The substrates were left in ultrapure water for a few minutes, then ultrapure water was slowly exchanged by a 10% (v:v) 2-propanol aqueous solution. Finally, the samples were rapidly dried by a vigorous stream of nitrogen (≈3 bar). Solvent exchange and fast, vigorous drying minimized capillary forces, preventing morphological changes in the arrays (particle movements) during drying.
f) The nanostructured substrates were cleaned from CTAB or CPC ligands through a low-pressure oxygen plasma treatment at Diener Electronic PICO low-pressure plasma system, leaving the bare AuNPs anchored to the bare glass substrate. CTAB-capped AuNSs were treated by (0.8 mbar, 200 W, 30'); instead, CPC-capped AuNCs by (0.8 mbar, 200 W, 3') to prevent plasma-induced modifications of the cubic shape.

Appendix C. Morphological Analysis

C.1 General Processing of SEM/STEM Micrographs

Both nanoparticles and nanostructures were morphologically characterized by Fei Nova NanoSEM 450 or by FEI Magellan STEM. Top-view SEM/STEM micrographs were processed by ImageJ software to retrieve information about NPs shapes, sizes, and nearest-neighbour centre-to-centre distances (NNDs). The process involved few common steps, depicted in Figure C.1 for a complex SEM micrograph of a SAM of negatively charged AuNPs.

Initially, any raw image (Figure C.1a) was thresholded to isolate the NPs from the background and binarized using the “Make Binary” command to create a mask template, in which the object pixel value was set equal to 1 and the background to 0 (Figure C.1b). Subsequently, the “Watershed” command was applied to segment adjacent objects, i.e., clusters of NPs (Figure C.1c). It is noteworthy that the "Make Binary" tool may occasionally merge intricate NP clusters into a single connected object and, as a consequence, the subsequent segmentation fails. This circumstance mainly occurred in the case of SAMs of citrate-capped AuNP (due to both the exceptionally high surface density and the silanization step).

Various NPs parameters including perimeter p, area S, centroid coordinates, and shape descriptors (circularity $C = 4\pi S/p^2$ and aspect ratio $AR = a/b$, with a and b being the major and minor axes of the ellipsoid best fitting an object) were obtained by the “Analyze Particles” tool. For spheroidal or spherical NPs, the diameters were estimated as $D = 2\sqrt{S/\pi}$. Instead, the edge lengths of AuNCs were estimated by the “Oriented Bounding Box” tool included in the “MorphoLibJ” plugin. Moreover, the mean curvatures of the AuNCs (rounded) corners were estimated by the “Curvature” Plugin, which generally calculates the curvature of each point belonging to the perimeter of an object. The NNDs were obtained using the ImageJ Plugin “Nnd”, which calculate (for each NP) the distance between its centroid and the centroid of the nearest neighbour NP.

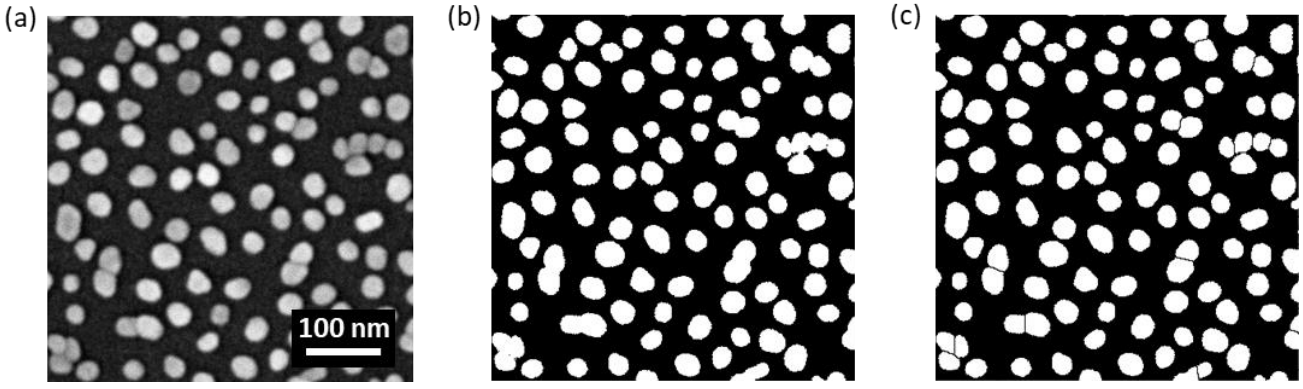

Figure C.1. Example of micrograph processing. (a) Top-view (raw) SEM micrograph at high magnification. (b) Corresponding thresholded and binarized image. (c) Thresholded, binarized, and segmented image.

C.2 Coding of the Simulation Model

Extinction spectra and electromagnetic EF profiles of the actual nanostructures morphologies were simulated after processing, modelling, and importing micrometric regions of SEM/STEM micrographs in Lumerical workspace. For clarity, SAMs of spheroidal/spherical and cuboidal/cubic AuNPs are treated separately.

Case 1: SAM of spheroidal/spherical AuNPs

After the initial binarization and segmentation, the "Analyze Particles" command was used to extract centroid coordinates ($X_{n,c}$, $Y_{n,c}$) and the area S_n of each *n*-th NP within the chosen ROI. Each NP was then modelled as a perfect sphere of radius $r_n = \sqrt{S_n/\pi}$. Finally, the $Z_{n,c}$ coordinate of each centroid was calculated as $Z_{n,c} = r_n + h$ with respect to the substrate level h set as $h = -\max(r_1, \dots, r_n, \dots)$. The vectors $\boldsymbol{V_n} = (X_{n,c}, Y_{n,c}, Z_{n,c}, r_n)$ associated to each NP of the ROI were sufficient to model its morphology and could be imported in Lumerical workspace via a script. Figure C.2b shows the top-view of the model corresponding to the processed ROI of Figure C.2a. The actual ROI morphology is reproduced with exceptional precision (Figure C.2c).

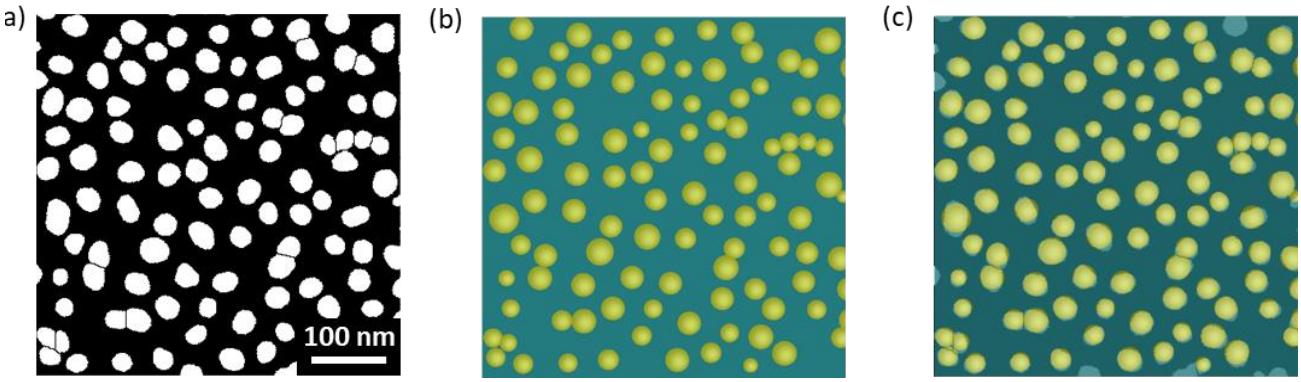

Figure C.2. Processing and modelling of a SEM micrograph of a SAM of spheroidal AuNPs. (a) Processed SEM micrograph at high magnification. (b) Corresponding model in Lumerical workspace, where AuNPs are modelled as perfect spheres (yellow) over a glass substrate (light blue). (c) Overlap of (a) and (b), to emphasize the faithful reproduction of the actual ROI morphology by the model. All three images are 500 nm × 500 nm squares.

Case 2: SAM of AuNCs

After the initial binarization and segmentation, the "Oriented Bounding Box" tool from "MorphoLibJ" plugin was used to extract centre coordinates ($X_{n,c}$, $Y_{n,c}$), length L_n, width W_n, and orientation α_n of the box bounding each *n*-th NP within the chosen ROI. By default, L_n always represents the longest side of the box, that is $L_n > W_n$, and the box orientation α_n is the angle between x-axis and L_n. Regarding the third dimension, i.e., the heights H_n, they are unknown due to the 2D nature of STEM/SEM micrographs. However, tilted STEM micrographs showed AuNCs having randomly distributed heights (as expected) rather than being at the same level. To capture this general feature, we set the heights as $H_n = (L_n + W_n)/2$. The $Z_{n,c}$ coordinate of each box centre was then calculated as $Z_{n,c} = H_n/2 + h$ with respect to the substrate level h set as $h = -\max(H_1/2, \dots, H_n/2, \dots)$. It is worth to note that our AuNCs are not ideal cubes/parallelepipeds; rather, their edges and corners have a mean radius of curvature $\bar{R} = 12 \pm 2$ nm. Therefore, each

AuNC was modelled as the "all-rounded quadrilateral" object from Lumerical's object library — a parallelepiped with all edges and corners rounded by suitable cylinders and spheres, respectively. The vectors $\boldsymbol{V_n} = \left(X_{n,c}, Y_{n,c}, Z_{n,c}, L_n, W_n, H_n, \alpha_n, \bar{R}\right)$ associated to each NP of the ROI were sufficient to model its morphology and could be imported in Lumerical workspace via a script. Figure C.3b displays the top-view of the model corresponding to the already processed ROI of Figure C.3a, except for the radii of curvatures, which are not considered for simplicity. The actual ROI morphology is reproduced with exceptional precision (Figure C.3c). It is worth mentioning that the "oriented bounding box" outcomes L_n, W_n are slight overestimations of length and width of a rectangular object. In fact, the bounding box includes *all* the pixels of an object; in particular, it includes all the pixels along the object outline, which is typically not entirely smooth because of, e.g., finite resolution of a micrograph, processing steps, etc. . It follows that L_n, W_n are upper limits for length and width of an object. The overestimation can be easily evaluated (and corrected) after comparison with "manual" measurements. In the case of the STEM of Figure C.3a (magnification: 250'000x, 0.865 pixel/nm), the overestimation of L_n, W_n was found to be within 3 nm (1-3 pixels).

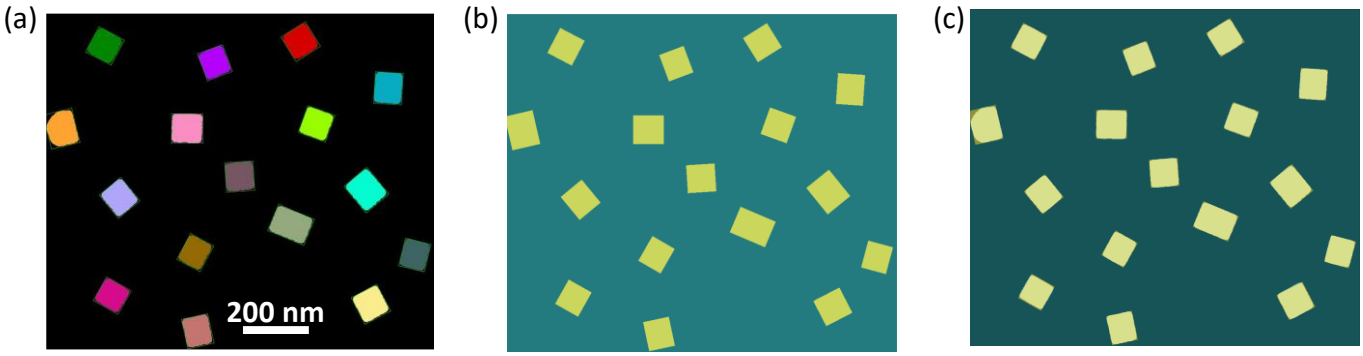

Figure C.3. Processing and modelling of a STEM micrograph of a SAM of AuNCs60. (a) Processed STEM micrograph at high magnification. Each NP is enclosed into an oriented bounding box as a result of the "oriented bounding box" plugin. (b) Top-view of the corresponding model in Lumerical workspace. For mere graphical reasons, AuNCs are modelled as ideal parallelepipeds rather than all-rounded parallelepipeds (yellow) over a glass substrate (light blue). (c) Overlap of (a) and (b), to emphasize the faithful reproduction of the actual ROI morphology by the modelling.

C.3 Iridium Sputtering Layer

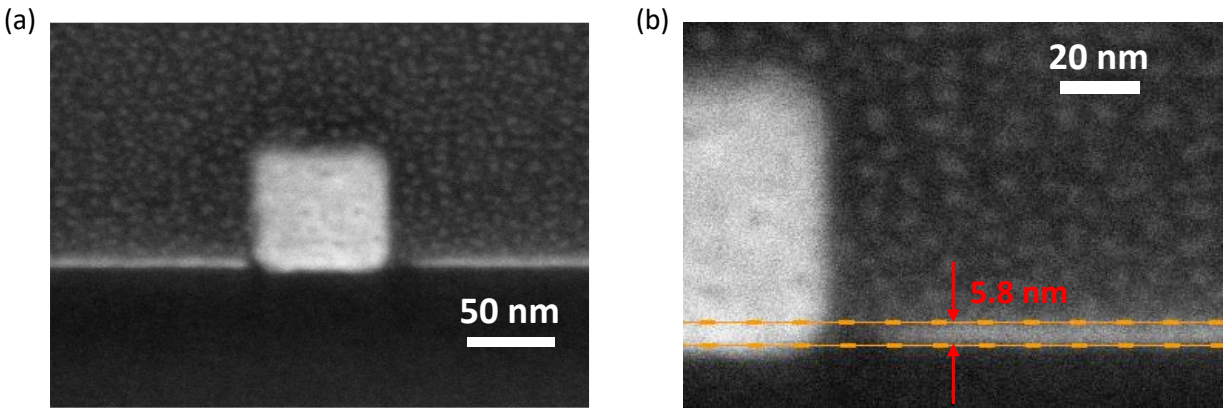

Figure C.4. STEM micrographs of a Focused Ion Beam (FIB) cut of a NCs array on glass, showing one NC and the iridium sputtering layer resulting from the (60 s, 25 mA) sputtering process. (a) Overall image, exhibiting a uniform iridium layer. (b) Right side of the previous image, reporting the measurement of the iridium layer thickness by ImageJ.

Appendix D. dsDNA Sequences

Three (modified) dsDNAs were purchased from Integrated DNA Technologies (IDT), already purified (HPLC purification), and annealed. The 5'–ends carried a dithiol group (indicated as "5DTPA"), and an ATTO™ 565 (NHS Ester) fluorophore (indicated as "5ATTO565N"), respectively. Here are the sequences:

dsDNA21[77]

5'- /5DTPA/GAA TTC GAG CTC GGT ACC CGG -3' (Sense)

5'- /5ATTO565N/CCG GGT ACC GAG CTC GAA TTC -3' (Antisense)

dsDNA50[77]

5'- /5DTPA/GAA TTC GAG CTC GGT ACC CGG GGA TCC TCT AGA GTC GAC CTG CAG GCA TG -3'

5'- /5ATTO565N/CAT GCC TGC AGG TCG ACT CTA GAG GAT CCC CGG GTA CCG AGC TCG AAT TC -3'

dsDNA100[88]

5'- /5DTPA/CCA CCA AAC GTT TCG GCG AGA AGC AGG CCA TTA TCG CCG GCA TGG CGG CCG ACG CGC TGG GCT ACG TCT TGC TGG CGT TCG CGA CGC GAG GCT GGA TGG T -3'

5'- /5ATTO565N/ACC ATC CAG CCT CGC GTC GCG AAC GCC AGC AAG ACG TAG CCC AGC GCG TCG GCC GCC ATG CCG GCG ATA ATG GCC TGC TTC TCG CCG AAA CGT TTG GTG G -3'

Appendix E. Procedures for MEF Experiments

E.1 Use and Quantification of dsDNAs

Lyophilized dsDNAs (from IDT) were initially resuspended in PBS1X pH 7.4 (Gibco) making 5 µL aliquots at high concentration (87 µM dsDNA21, 140 µM dsDNA50, and 83 µM dsDNA100), stored at -20 °C until use (within 4 weeks). The PBS 1X pH 7.4 (Gibco) will be now referred to as PBS 1X LS (as done in the main), to stress that no salts were added to it.

For use, a starting (5 µL) aliquot was pre-diluted at 20 µL by adding PBS 1X LS. This 20 µL dsDNA aliquot (in PBS 1X LS) was mixed with 20 µL of freshly prepared TCEP (in ultrapure water) according to a molar ratio $\mathrm{dsDNA:TCEP} = 1:500$, for the activation of dithiol groups. After 1 h, the activated dsDNA solution (40 µL) was brought to a (known) concentration of ≈ 1 µM by adding PBS 1X LS or PBS1X HS (i.e., PBS 1X at 1M NaCl and 1 mM $MgCl_2$). The concentration of ≈ 1 µM is associated to an extinction (at 260 nm) which is still clearly measurable. The final (activated) dsDNAs aliquots at 500 nM, 2.5 nM, and 1 nM were eventually obtained through serial dilutions by PBS 1X LS or PBS 1X HS of the previous, intermediate aliquots (at the known concentration of ≈ 1 µM). All the procedures were done in dark conditions to preserve the fluorophores.

It is worth noting that IDT does not provide the molar extinction coefficient ε for the dsDNAs, but only for the two individual strands. We calculated $\varepsilon(\mathrm{dsDNA})$ according to the formula[89]

$$\varepsilon(\mathrm{dsDNA}) = (\varepsilon_{S1} + \varepsilon_{S2}) \times (1 - h)\ ,$$

where the subscripts S1 and S2 stand for “strand 1” and “strand 2”, i.e., the two complementary strands of the duplex, and h is the hypochromicity factor (at 260 nm), defined as

$$h = 0.059 \times f_{GC} + 0.287 \times f_{AT}\ ,$$

with f_{GC} and f_{AT} the fractions of GC and AT bases of the individual strands. For our dsDNAs, the hypochromicity factors are $h(ds21) = 0.146$, $h(ds50) = 0.150$, and $h(ds100) = 0.137$. Therefore, $\varepsilon(\mathrm{dsDNA})$ deviations from $(\varepsilon_{S1} + \varepsilon_{S2})$ are relatively small, but we considered them, obtaining: $\varepsilon(\mathrm{ds21}) = 365 \times 10^3\ M^{-1}cm^{-1}$, $\varepsilon(\mathrm{ds50}) = 828 \times 10^3\ M^{-1}cm^{-1}$, $\varepsilon(\mathrm{ds100}) = 1617 \times 10^3\ M^{-1}cm^{-1}$.

E.2 Samples Preparation

AuNS140 and AuNCs60 nanostructures were cut as 5 mm × 5 mm chips by a diamond tip. The chips were cleaned from residual surfactant cappings (and made more hydrophilic) by a short oxygen plasma treatment (200 W, 0.8 mbar, 2') at Diener Pico plasma oven. Afterwards, they were incubated overnight (16 h) in dark conditions at 4 °C by 30 µL dsDNAs at the desired concentration (in PBS 1X LS or PBS 1X HS, prepared as described above). The volume of 30 µL was (more than) enough to fully cover the chips with a bulky drop of dsDNA solution. After incubation, the samples were thoroughly rinsed by PBS1X LS to remove unbound dsDNA and let soaked in PBS 1X LS (in dark conditions) till imaging (from few minutes till few hours). For imaging, the samples were transferred in a glass bottom dish filled by PBS 1X LS as well. During all the procedures, including imaging, nanostructures were never dried to not alter the natural environment of ATTO565, i.e., a PBS 1X solution. Dark conditions were always guaranteed.

E.3 Instrumentation for Fluorescence Imaging

Fluorescence images were recorded by Zeiss Axio Observer Z1 inverted phase contrast fluorescence microscope equipped by Zeiss Colibri.2 LED light source (module 555/30, green), Zeiss Plan-Apochromat 10x/0.45 Ph1 M27 (FWD = 2.1 mm) objective, Zeiss 43 HE filter (excitation 538–563 nm; emission 570–640 nm), and pco.edge 5.5 sCMOS photodetector (scaling 0.650 µm × 0.650 µm per pixel, image size 2560 × 2160 pixels, scaled image size 1664 × 1404 μm^2, 16 bit dynamic range). LED power was set at 90% and exposure time at 2 s, for each image.

Appendix F. Supplementary Material

F.1 Dissolution of CRD200 at Low Concentration (0.1 µM) of $HAuCl_4$

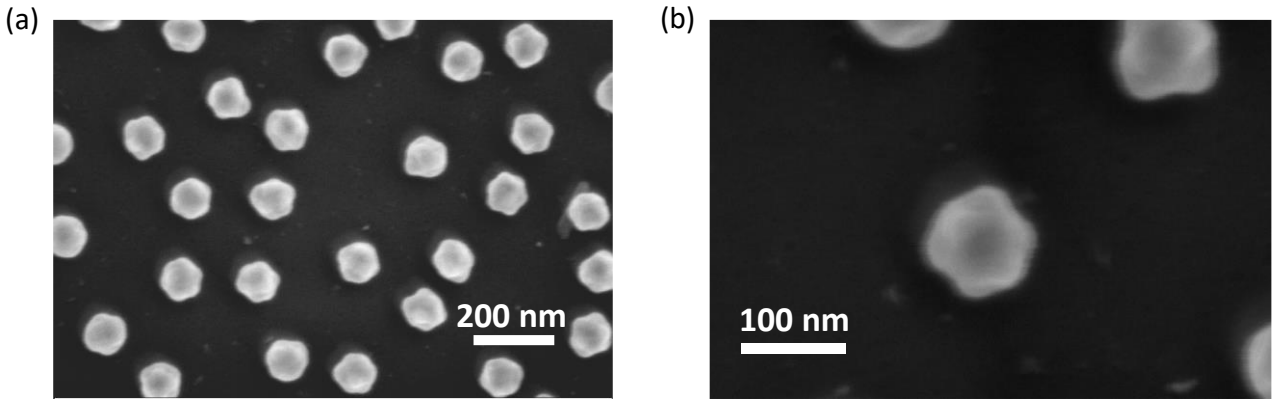

Figure F.1. STEM micrographs of CRD200 etched by 0.1 µM $HAuCl_4$. Nanoparticles exhibit residual features of CRDs after dissolution at such low concentration of gold. (a) Micrograph at high magnification of the array. (b) Micrograph at very high magnification, showing few etched CRD200 with residual features of the polyhedral geometry of a CRD.

F.2 Simulated Spectra for AuNS140 at Increasing CTAB Content

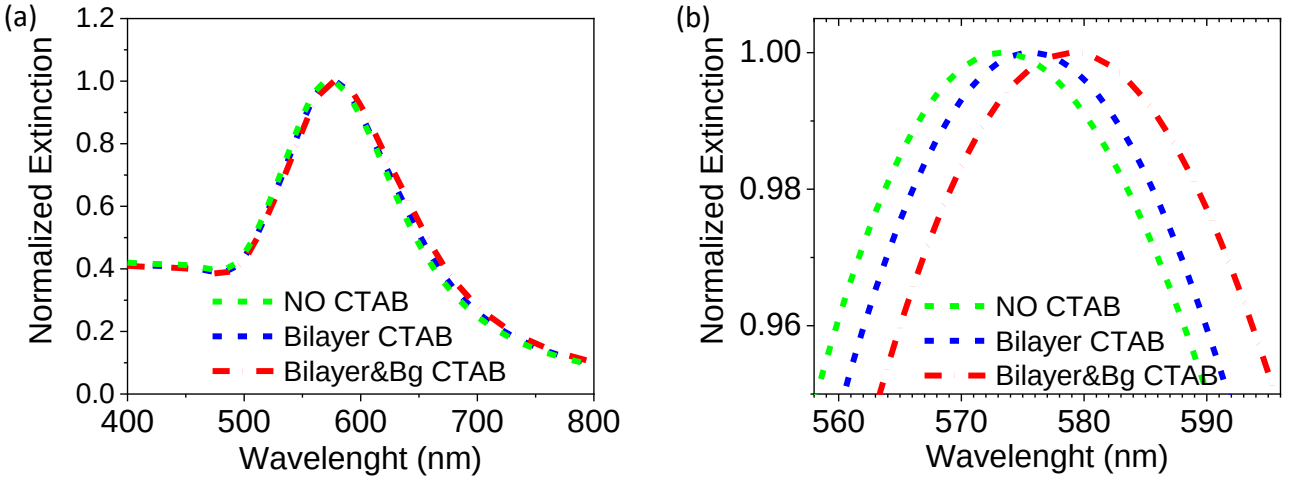

Figure F.2. (a) Simulated normalized extinction spectra for: a 104 nm AuNS in water (n=1.333) (dashed green), a CTAB-capped (n=1.4350) 104 nm AuNS in water (dashed blue), and a CTAB-capped 104 nm AuNS in a saturated CTAB solution (n=1.3478) (dash dotted red). (b) Focus on the LSPR peaks, to appreciate the minor redshifts as CTAB-capping and saturated CTAB solution were considered

F.3 AuNSs140 at low concentration of CTAB, Exp. Vs Sim.

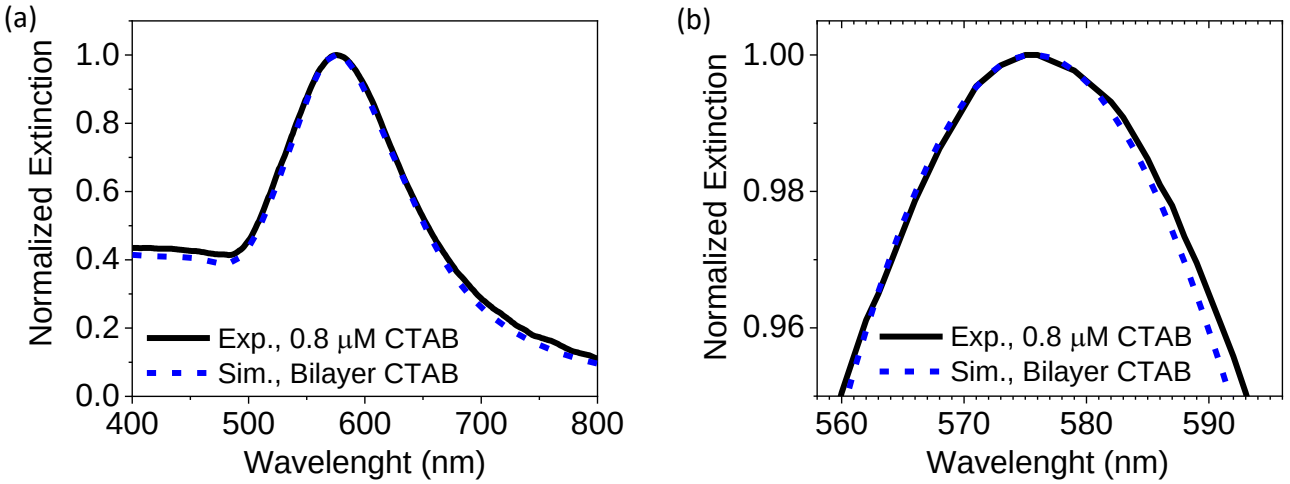

Figure F.3. (a) Experimental (solid black) and simulated (dashed blue) normalized extinction spectra of a AuNSs140 colloid at low concentration of CTAB (0.8 μM). The simulated spectrum corresponds to a CTAB-capped 104 nm AuNS in water (n=1.333). (d) Focus on the LSPR peak, to appreciate the perfect agreement between experimental and simulated spectra.

F.4 Length and Width Distributions of AuNCs60

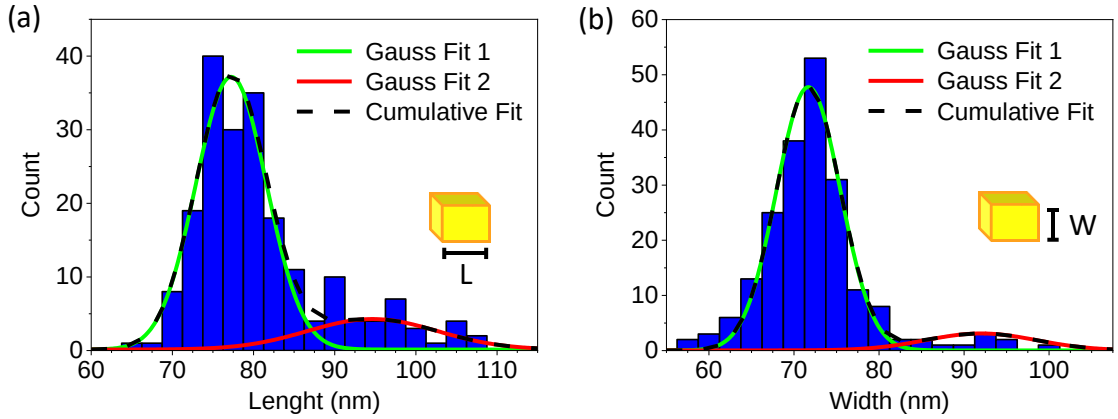

Figure F.4. (a) AuNCs60 major edge and (b) minor edge distributions retrieved by the "Oriented Bounding Box" tool from "MorphoLibJ" plugin. Each histogram was fitted by two Gaussian curves, one for edges grown in an ordinary way (solid green) and the other for overgrown edges (solid red), resulting in the overall bi-gaussian fit (dashed black).

F.5 AuNSs140 at 0.8 µM CTAB vs single AuNS140 on glass in water

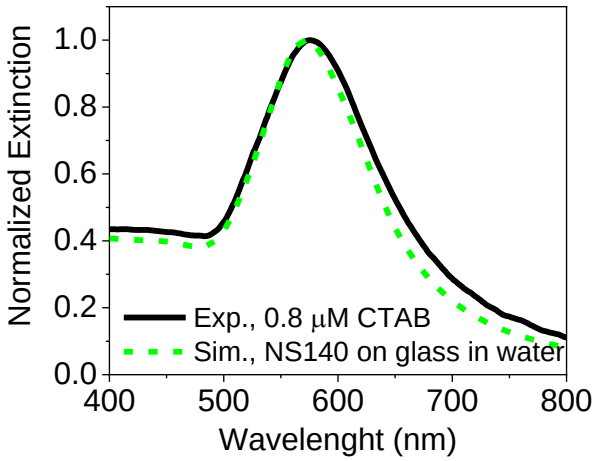

Figure F.5. Experimental (normalized) extinction spectra of AuNSs140 colloidal solution at low concentration of CTAB (0.8 µM) (solid black) and simulated (normalized) extinction spectrum of a single 104 nm AuNS on glass in water (dashed green). The nearly perfect agreement validates the reliability of the simulation and, vice versa, proves that a colloidal AuNSs140 is (almost) optically equivalent to a AuNS140 on glass in water.

F.6 λ_{LSPR} for a 120 nm AuNSs random array at varying NND

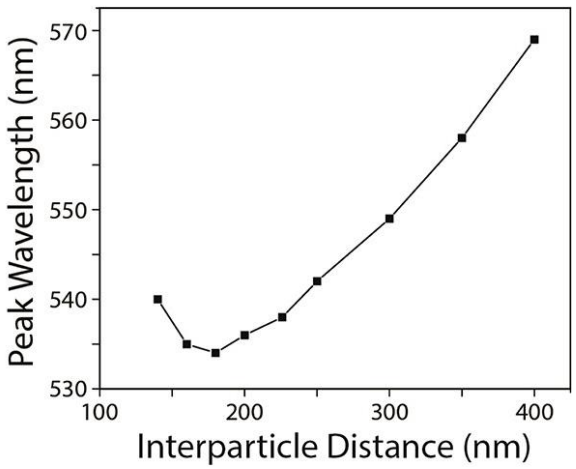

Figure F.6 Simulated extinction spectra λ_{LSPR} for a 120 nm AuNSs random array while varying the centre-to-centre NND interparticle distance. λ_{LSPR} blue shifts as the interparticle distance decreases from 400 to 180 nm until a local minimum at $\mathrm{NND} = 180$ nm, then it starts to redshift as the interparticle distance further decreases. (From Jenkins [62])

F.7 Supplementary $EF_{e.m.}$ Field Profiles

F.7.1 Single AuNS140 and AuNC60 on Glass in Water

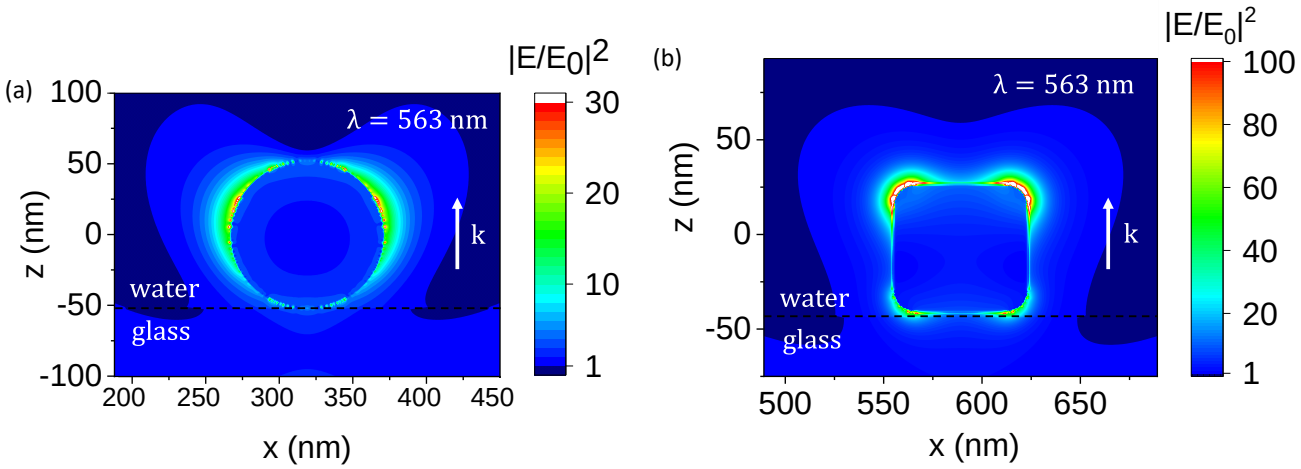

Figure F.7. Unpolarized $EF_{e.m.}$ xz-profiles at 563 nm for (a) a single AuNS140 on glass (b) a single AuNC60 on glass, both with external radiation incident from the bottom. The xz-monitors intersect the NS through its centre and the NC through the corners (this is why the NC seems not to touch the glass). Non-dipolar effects cause **E** to "wrap" towards the upper portions of the NPs, according to the direction of **k** (light incident from the bottom). For graphical purposes, points with $EF_{e.m.} \geq 30$ and $EF_{e.m.} \geq 100$ for AuNS140 and AuNC60, respectively, are all indicated as white.

F.7.2 Selected ROIs from AuNSs140 and AuNCs60 Arrays in Water

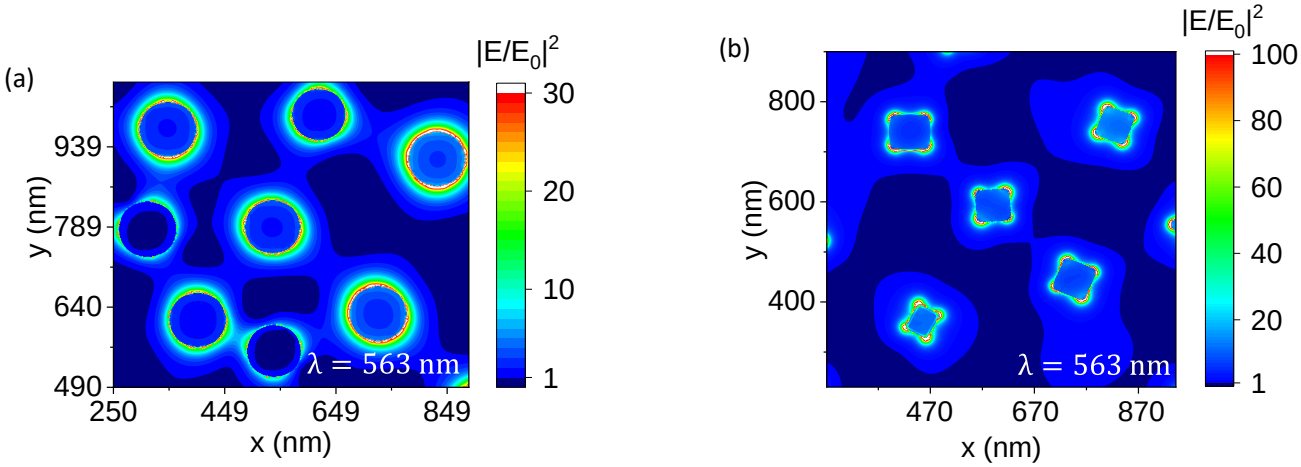

Figure F.8. Unpolarized $EF_{e.m.}$ xy-profiles (in water) at 563 nm for (a) selected sub-ROI from the STEM micrograph of Figure 2.4a for AuNS140 array, and (b) selected sub-ROI from the STEM micrograph of Figure 2.9c for AuNC60 array. Both sub-ROIs are constituted by a target NP (at the centre) surrounded by its first neighbours. The xy-monitors are located, respectively, at z=10 nm (i.e., 10 nm above the equatorial plane of the target NS140), and z=24 nm (i.e., 5 nm below the top facet of the target NC60). External radiation is incident from the bottom. For graphical purposes, points with $EF_{e.m.} \geq 30$ and $EF_{e.m.} \geq 100$ for AuNS140 and AuNC60, respectively, are all indicated as white.

References

(1) Pines, D. *Elementary Excitations in Solids*; CRC Press, 2018.

(2) Madelung, O. *Introduction to Solid-State Theory*; Springer Science & Business Media, 2012; Vol. 2.

(3) Maier, S. A. *Plasmonics: Fundamentals and Applications*; Springer US: New York, NY, 2007. https://doi.org/10.1007/0-387-37825-1.

(4) Mie, G. Beiträge Zur Optik Trüber Medien, Speziell Kolloidaler Metallösungen. *Ann. Phys.* **1908**, *330* (3), 377–445. https://doi.org/10.1002/andp.19083300302.

(5) Klimov, V. *Nanoplasmonics*; 2013. https://doi.org/10.4032/9789814267427.

(6) Acunzo, A.; Scardapane, E.; De Luca, M.; Marra, D.; Velotta, R.; Minopoli, A. Plasmonic Nanomaterials for Colorimetric Biosensing: A Review. *Chemosensors* **2022**, *10* (4), 136. https://doi.org/10.3390/chemosensors10040136.

(7) Minopoli, A.; Acunzo, A.; Della Ventura, B.; Velotta, R. Nanostructured Surfaces as Plasmonic Biosensors: A Review. *Adv. Mater. Interfaces* **2022**, *9* (2), 2101133. https://doi.org/10.1002/admi.202101133.

(8) Haes, A. J.; Van Duyne, R. P. Nanoscale Optical Biosensors Based on Localized Surface Plasmon Resonance Spectroscopy. In *Plasmonics: Metallic Nanostructures and Their Optical Properties*; Halas, N. J., Ed.; SPIE, 2003; Vol. 5221, p 47. https://doi.org/10.1117/12.508308.

(9) Hammond, J. L.; Bhalla, N.; Rafiee, S. D.; Estrela, P. Localized Surface Plasmon Resonance as a Biosensing Platform for Developing Countries. *Biosensors* **2014**, *4* (2), 172–188. https://doi.org/10.3390/bios4020172.

(10) Jung, L. S.; Campbell, C. T.; Chinowsky, T. M.; Mar, M. N.; Yee, S. S. Quantitative Interpretation of the Response of Surface Plasmon Resonance Sensors to Adsorbed Films. *Langmuir* **1998**, *14* (19), 5636–5648. https://doi.org/10.1021/la971228b.

(11) Jackson, J. D. *Classical Electrodynamics, 3rd Edition*; John Wiley & Sons Inc, Ed.; 1998.

(12) Mayer, K. M.; Hafner, J. H. Localized Surface Plasmon Resonance Sensors. *Chem. Rev.* **2011**, *111* (6), 3828–3857. https://doi.org/10.1021/cr100313v.

(13) Trügler, A. *Optical Properties of Metallic Nanoparticles : Basic Principles and Simulation*; 2016.

(14) Johnson, P. B.; Christy, R. W. Optical Constants of the Noble Metals. *Phys. Rev. B* **1972**, *6* (12), 4370–4379. https://doi.org/10.1103/PhysRevB.6.4370.

(15) Shafiqa, A. R.; Abdul Aziz, A.; Mehrdel, B. Nanoparticle Optical Properties: Size Dependence of a Single Gold Spherical Nanoparticle. *J. Phys. Conf. Ser.* **2018**, *1083* (1), 012040. https://doi.org/10.1088/1742-6596/1083/1/012040.

(16) Campanile, R.; Acunzo, A.; Scardapane, E.; Minopoli, A.; Martins, V. C.; Di Girolamo, R.; Cardoso, S.; Velotta, R.; Della Ventura, B.; Iannotti, V. Multifunctional Core@Satellite Magnetic Particles for Magnetoresistive Biosensors. *ACS Omega* **2022**, *7* (41), 36543–36550. https://doi.org/10.1021/acsomega.2c04442.

(17) Minopoli, A.; Della Ventura, B.; Lenyk, B.; Gentile, F.; Tanner, J. A.; Offenhäusser, A.; Mayer, D.; Velotta, R. Ultrasensitive Antibody-Aptamer Plasmonic Biosensor for Malaria Biomarker Detection in Whole Blood. *Nat. Commun.* **2020**, *11* (1), 6134. https://doi.org/10.1038/s41467-020-19755-0.

(18) Della Ventura, B.; Banchelli, M.; Funari, R.; Illiano, A.; De Angelis, M.; Taroni, P.; Amoresano, A.; Matteini, P.; Velotta, R. Biosensor Surface Functionalization by a Simple Photochemical Immobilization of Antibodies: Experimental Characterization by Mass Spectrometry and Surface Enhanced Raman Spectroscopy. *Analyst* **2019**, *144* (23), 6871–6880. https://doi.org/10.1039/C9AN00443B.

(19) Moraes Silva, S.; Tavallaie, R.; Sandiford, L.; Tilley, R. D.; Gooding, J. J. Gold Coated Magnetic Nanoparticles: From Preparation to Surface Modification for Analytical and Biomedical Applications. *Chem. Commun.* **2016**, *52* (48), 7528–7540. https://doi.org/10.1039/C6CC03225G.

(20) Tóth, I. Y.; Nesztor, D.; Novák, L.; Illés, E.; Szekeres, M.; Szabó, T.; Tombácz, E. Clustering of Carboxylated Magnetite Nanoparticles through Polyethylenimine: Covalent versus Electrostatic Approach. *J. Magn. Magn. Mater.* **2017**, *427*, 280–288. https://doi.org/10.1016/j.jmmm.2016.11.011.

(21) Saikia, K.; Sen, D.; Mazumder, S.; Deb, P. Reassembling Nanometric Magnetic Subunits into Secondary Nanostructures with Controlled Interparticle Spacing. *RSC Adv.* **2015**, *5* (1), 694–705. https://doi.org/10.1039/c4ra12115e.

(22) Spiller, E. Optical Constants. In *Soft X-Ray Optics*; SPIE: 1000 20th Street, Bellingham, WA 98227-0010 USA, 2010; Vol. CR-85034, pp 5–22. https://doi.org/10.1117/3.176482.ch2.

(23) Varón, M.; Peña, L.; Balcells, L.; Skumryev, V.; Martinez, B.; Puntes, V. Dipolar Driven Spontaneous Self Assembly of Superparamagnetic CO Nanoparticles into Micrometric Rice-Grain like Structures. *Langmuir* **2010**, *26* (1), 109–116. https://doi.org/10.1021/la902169s.

(24) Huang, Y.; Zhang, B.; Xie, S.; Yang, B.; Xu, Q.; Tan, J. Superparamagnetic Iron Oxide Nanoparticles Modified with Tween 80 Pass through the Intact Blood-Brain Barrier in Rats under Magnetic Field. *ACS Appl. Mater. Interfaces* **2016**, *8* (18), 11336–11341. https://doi.org/10.1021/acsami.6b02838.

(25) Hauser, E. A.; Lynn, J. E. *Experiments in Colloid Chemistry*; McGraw-Hill: New York, 1940.

(26) Turkevich, J.; Stevenson, P. C.; Hillier, J. A Study of the Nucleation and Growth Processes in the Synthesis of Colloidal Gold. *Discuss. Faraday Soc.* **1951**, *11* (c), 55. https://doi.org/10.1039/df9511100055.

(27) FRENS, G. Controlled Nucleation for the Regulation of the Particle Size in Monodisperse Gold Suspensions. *Nat. Phys. Sci.* **1973**, *241* (105), 20–22. https://doi.org/10.1038/physci241020a0.

(28) Wuithschick, M.; Birnbaum, A.; Witte, S.; Sztucki, M.; Vainio, U.; Pinna, N.; Rademann, K.; Emmerling, F.; Kraehnert, R.; Polte, J. Turkevich in New Robes: Key Questions Answered for the Most Common Gold Nanoparticle Synthesis. *ACS Nano* **2015**, *9* (7), 7052–7071. https://doi.org/10.1021/acsnano.5b01579.

(29) O'Brien, M. N.; Jones, M. R.; Brown, K. A.; Mirkin, C. A. Universal Noble Metal Nanoparticle

Seeds Realized Through Iterative Reductive Growth and Oxidative Dissolution Reactions. *J. Am. Chem. Soc.* **2014**, *136* (21), 7603–7606. https://doi.org/10.1021/ja503509k.

(30) Rodríguez-Fernández, J.; Pérez-Juste, J.; Mulvaney, P.; Liz-Marzán, L. M. Spatially-Directed Oxidation of Gold Nanoparticles by Au(III)−CTAB Complexes. *J. Phys. Chem. B* **2005**, *109* (30), 14257–14261. https://doi.org/10.1021/jp052516g.

(31) Li, W.; Zhang, M.; Zhang, J.; Han, Y. Self-Assembly of Cetyl Trimethylammonium Bromide in Ethanol-Water Mixtures. *Front. Chem. China* **2006**, *1* (4), 438–442. https://doi.org/10.1007/s11458-006-0069-y.

(32) Nikoobakht, B.; El-Sayed, M. A. Preparation and Growth Mechanism of Gold Nanorods (NRs) Using Seed-Mediated Growth Method. *Chem. Mater.* **2003**, *15* (10), 1957–1962. https://doi.org/10.1021/cm020732l.

(33) Niu, W.; Zheng, S.; Wang, D.; Liu, X.; Li, H.; Han, S.; Chen, J.; Tang, Z.; Xu, G. Selective Synthesis of Single-Crystalline Rhombic Dodecahedral, Octahedral, and Cubic Gold Nanocrystals. *J. Am. Chem. Soc.* **2009**, *131* (2), 697–703. https://doi.org/10.1021/ja804115r.

(34) Langille, M. R.; Personick, M. L.; Zhang, J.; Mirkin, C. A. Defining Rules for the Shape Evolution of Gold Nanoparticles. *J. Am. Chem. Soc.* **2012**, *134* (35), 14542–14554. https://doi.org/10.1021/ja305245g.

(35) Hong, J. W.; Lee, S.-U.; Lee, Y. W.; Han, S. W. Hexoctahedral Au Nanocrystals with High-Index Facets and Their Optical and Surface-Enhanced Raman Scattering Properties. *J. Am. Chem. Soc.* **2012**, *134* (10), 4565–4568. https://doi.org/10.1021/ja300598u.

(36) Yu, Y.; Zhang, Q.; Lu, X.; Lee, J. Y. Seed-Mediated Synthesis of Monodisperse Concave Trisoctahedral Gold Nanocrystals with Controllable Sizes. *J. Phys. Chem. C* **2010**, *114* (25), 11119–11126. https://doi.org/10.1021/jp103840k.

(37) Ha, T. H.; Koo, H.-J.; Chung, B. H. Shape-Controlled Syntheses of Gold Nanoprisms and Nanorods Influenced by Specific Adsorption of Halide Ions. *J. Phys. Chem. C* **2007**, *111* (3), 1123–1130. https://doi.org/10.1021/jp066454l.

(38) Langille, M. R.; Personick, M. L.; Zhang, J.; Mirkin, C. A. Defining Rules for the Shape Evolution of Gold Nanoparticles. *J. Am. Chem. Soc.* **2012**, *134* (35), 14542–14554. https://doi.org/10.1021/ja305245g.

(39) Murphy, C. J.; Thompson, L. B.; Alkilany, A. M.; Sisco, P. N.; Boulos, S. P.; Sivapalan, S. T.; Yang, J. A.; Chernak, D. J.; Huang, J. The Many Faces of Gold Nanorods. *J. Phys. Chem. Lett.* **2010**, *1* (19), 2867–2875. https://doi.org/10.1021/jz100992x.

(40) Olmon, R. L.; Slovick, B.; Johnson, T. W.; Shelton, D.; Oh, S.-H.; Boreman, G. D.; Raschke, M. B. Optical Dielectric Function of Gold. *Phys. Rev. B* **2012**, *86* (23), 235147. https://doi.org/10.1103/PhysRevB.86.235147.

(41) Kékicheff, P.; Spalla, O. Refractive Index of Thin Aqueous Films Confined between Two Hydrophobic Surfaces. *Langmuir* **1994**, *10* (5), 1584–1591. https://doi.org/10.1021/la00017a043.

(42) Szabó, G.; Albert, E.; Both, J.; Kócs, L.; Sáfrán, G.; Szöke, A.; Hórvölgyi, Z.; Mureşan, L. M. Influence of Embedded Inhibitors on the Corrosion Resistance of Zinc Coated with Mesoporous Silica Layers. *Surfaces and Interfaces* **2019**, *15* (March), 216–223.

https://doi.org/10.1016/j.surfin.2019.03.007.

(43) Gómez-Graña, S.; Hubert, F.; Testard, F.; Guerrero-Martínez, A.; Grillo, I.; Liz-Marzán, L. M.; Spalla, O. Surfactant (Bi)Layers on Gold Nanorods. *Langmuir* **2012**, *28* (2), 1453–1459. https://doi.org/10.1021/la203451p.

(44) Cieśla, J.; Koczańska, M.; Narkiewicz-Michałek, J.; Szymula, M.; Bieganowski, A. The Physicochemical Properties of CTAB Solutions in the Presence of α-Tocopherol. *J. Mol. Liq.* **2016**, *222*, 463–470. https://doi.org/10.1016/j.molliq.2016.07.058.

(45) Haynes, W. M. *CRC Handbook of Chemistry and Physics*; CRC Press, 2016.

(46) Park, K.; Koerner, H.; Vaia, R. A. Depletion-Induced Shape and Size Selection of Gold Nanoparticles. *Nano Lett.* **2010**, *10* (4), 1433–1439. https://doi.org/10.1021/nl100345u.

(47) Wang, C.; Siu, C.; Zhang, J.; Fang, J. Understanding the Forces Acting in Self-Assembly and the Implications for Constructing Three-Dimensional (3D) Supercrystals. *Nano Res.* **2015**, *8* (8), 2445–2466. https://doi.org/10.1007/s12274-015-0767-1.

(48) Schupp, D. J.; Angst, J.; Schaefer, E. A.; Schupp, S. M.; Cölfen, H. Controlling Oriented Attachment of Gold Nanoparticles by Size and Shape. *J. Phys. Chem. C* **2021**, *125* (37), 20343–20350. https://doi.org/10.1021/acs.jpcc.1c05937.

(49) Huang, C.-J.; Chiu, P.-H.; Wang, Y.-H.; Chen, W. R.; Meen, T. H. Synthesis of the Gold Nanocubes by Electrochemical Technique. *J. Electrochem. Soc.* **2006**, *153* (8), D129. https://doi.org/10.1149/1.2203931.

(50) Meleshyn, A. Cetylpyridinium Chloride at the Mica−Water Interface: Incomplete Monolayer and Bilayer Structures. *Langmuir* **2009**, *25* (2), 881–890. https://doi.org/10.1021/la802450q.

(51) Wang, Y.; Zhang, M.; Lai, Y.; Chi, L. Advanced Colloidal Lithography: From Patterning to Applications. *Nano Today* **2018**, *22*, 36–61. https://doi.org/10.1016/j.nantod.2018.08.010.

(52) Stewart, A.; Murray, S.; Bell, S. E. J. Simple Preparation of Positively Charged Silver Nanoparticles for Detection of Anions by Surface-Enhanced Raman Spectroscopy. *Analyst* **2015**, *140* (9), 2988–2994. https://doi.org/10.1039/C4AN02305F.

(53) Tran, A. Q.; Kaulen, C.; Simon, U.; Offenhäusser, A.; Mayer, D. Surface Coupling Strength of Gold Nanoparticles Affects Cytotoxicity towards Neurons. *Biomater. Sci.* **2017**, *5* (5), 1051–1060. https://doi.org/10.1039/C7BM00054E.

(54) Greben, K.; Li, P.; Mayer, D.; Offenhäusser, A.; Wördenweber, R. Immobilization and Surface Functionalization of Gold Nanoparticles Monitored via Streaming Current/Potential Measurements. *J. Phys. Chem. B* **2015**, *119* (19), 5988–5994. https://doi.org/10.1021/acs.jpcb.5b02615.

(55) Howarter, J. A.; Youngblood, J. P. Optimization of Silica Silanization by 3-Aminopropyltriethoxysilane. *Langmuir* **2006**, *22* (26), 11142–11147. https://doi.org/10.1021/la061240g.

(56) Yadav, A. R.; Sriram, R.; Carter, J. A.; Miller, B. L. Comparative Study of Solution–Phase and Vapor–Phase Deposition of Aminosilanes on Silicon Dioxide Surfaces. *Mater. Sci. Eng. C* **2014**, *35* (1), 283–290. https://doi.org/10.1016/j.msec.2013.11.017.

(57) Oh, S. Y.; Heo, N. S.; Bajpai, V. K.; Jang, S.-C.; Ok, G.; Cho, Y.; Huh, Y. S. Development of a

Cuvette-Based LSPR Sensor Chip Using a Plasmonically Active Transparent Strip. *Front. Bioeng. Biotechnol.* **2019**, *7* (November), 1–11. https://doi.org/10.3389/fbioe.2019.00299.

(58) Ghosh, S. K.; Pal, T. Interparticle Coupling Effect on the Surface Plasmon Resonance of Gold Nanoparticles: From Theory to Applications. *Chem. Rev.* **2007**, *107* (11), 4797–4862. https://doi.org/10.1021/cr0680282.

(59) Jiang, C.; Markutsya, S.; Tsukruk, V. V. Collective and Individual Plasmon Resonances in Nanoparticle Films Obtained by Spin-Assisted Layer-by-Layer Assembly. *Langmuir* **2004**, *20* (3), 882–890. https://doi.org/10.1021/la0355085.

(60) Liu, Y.; Tourbin, M.; Lachaize, S.; Guiraud, P. Silica Nanoparticles Separation from Water: Aggregation by Cetyltrimethylammonium Bromide (CTAB). *Chemosphere* **2013**, *92* (6), 681–687. https://doi.org/10.1016/j.chemosphere.2013.03.048.

(61) Tyrode, E.; Rutland, M. W.; Bain, C. D. Adsorption of CTAB on Hydrophilic Silica Studied by Linear and Nonlinear Optical Spectroscopy. *J. Am. Chem. Soc.* **2008**, *130* (51), 17434–17445. https://doi.org/10.1021/ja805169z.

(62) Jenkins, J. A.; Zhou, Y.; Thota, S.; Tian, X.; Zhao, X.; Zou, S.; Zhao, J. Blue-Shifted Narrow Localized Surface Plasmon Resonance from Dipole Coupling in Gold Nanoparticle Random Arrays. *J. Phys. Chem. C* **2014**, *118* (45), 26276–26283. https://doi.org/10.1021/jp508181g.

(63) Khurgin, J. B.; Sun, G. Enhancement of Optical Properties of Nanoscaled Objects by Metal Nanoparticles. *J. Opt. Soc. Am. B* **2009**, *26* (12), B83. https://doi.org/10.1364/JOSAB.26.000B83.

(64) Sun, G.; Khurgin, J. B.; Yang, C. C. Impact of High-Order Surface Plasmon Modes of Metal Nanoparticles on Enhancement of Optical Emission. *Appl. Phys. Lett.* **2009**, *95* (17). https://doi.org/10.1063/1.3250160.

(65) Khurgin, J. B.; Sun, G.; Soref, R. A. Practical Limits of Absorption Enhancement near Metal Nanoparticles. *Appl. Phys. Lett.* **2009**, *94* (7), 1–4. https://doi.org/10.1063/1.3081631.

(66) Khurgin, J. B.; Sun, G.; Soref, R. A. Electroluminescence Efficiency Enhancement Using Metal Nanoparticles. *Appl. Phys. Lett.* **2008**, *93* (2), 93–96. https://doi.org/10.1063/1.2957989.

(67) Bharadwaj, P.; Novotny, L. Spectral Dependence of Single Molecule Fluorescence Enhancement. *Opt. Express* **2007**, *15* (21), 14266. https://doi.org/10.1364/OE.15.014266.

(68) Anger, P.; Bharadwaj, P.; Novotny, L. Enhancement and Quenching of Single-Molecule Fluorescence. *Phys. Rev. Lett.* **2006**, *96* (11), 113002. https://doi.org/10.1103/PhysRevLett.96.113002.

(69) Nie, S.; Emory, S. R. Probing Single Molecules and Single Nanoparticles by Surface-Enhanced Raman Scattering. *Science (80-.).* **1997**, *275* (5303), 1102–1106. https://doi.org/10.1126/science.275.5303.1102.

(70) Polemi, A.; Shuford, K. L. Distance Dependent Quenching Effect in Nanoparticle Dimers. *J. Chem. Phys.* **2012**, *136* (18), 184703. https://doi.org/10.1063/1.4711759.

(71) Le, K. Q. Nanoplasmonic Enhancement of Molecular Fluorescence: Theory and Numerical Modeling. *Plasmonics* **2015**, *10* (2), 475–482. https://doi.org/10.1007/s11468-014-9830-0.

(72) Klimov, V. V; Guzatov, D. V. Optical Properties of an Atom in the Presence of a Two-

Nanosphere Cluster. *Quantum Electron.* **2007**, *37* (3), 209–230. https://doi.org/10.1070/qe2007v037n03abeh013322.

(73) Jeong, Y.; Kook, Y.-M.; Lee, K.; Koh, W.-G. Metal Enhanced Fluorescence (MEF) for Biosensors: General Approaches and a Review of Recent Developments. *Biosens. Bioelectron.* **2018**, *111* (January), 102–116. https://doi.org/10.1016/j.bios.2018.04.007.

(74) Cui, Q.; He, F.; Li, L.; Möhwald, H. Controllable Metal-Enhanced Fluorescence in Organized Films and Colloidal System. *Adv. Colloid Interface Sci.* **2014**, *207* (1), 164–177. https://doi.org/10.1016/j.cis.2013.10.011.

(75) Guilbaud, S.; Salomé, L.; Destainville, N.; Manghi, M.; Tardin, C. Dependence of DNA Persistence Length on Ionic Strength and Ion Type. *Phys. Rev. Lett.* **2019**, *122* (2), 1–6. https://doi.org/10.1103/PhysRevLett.122.028102.

(76) Kaiser, W.; Rant, U. Conformations of End-Tethered DNA Molecules on Gold Surfaces: Influences of Applied Electric Potential, Electrolyte Screening, and Temperature. *J. Am. Chem. Soc.* **2010**, *132* (23), 7935–7945. https://doi.org/10.1021/ja908727d.

(77) Moiseev, L.; Ünlü, M. S.; Swan, A. K.; Goldberg, B. B.; Cantor, C. R. DNA Conformation on Surfaces Measured by Fluorescence Self-Interference. *Proc. Natl. Acad. Sci.* **2006**, *103* (8), 2623–2628. https://doi.org/10.1073/pnas.0511214103.

(78) Huang, L.; Seker, E.; Landers, J. P.; Begley, M. R.; Utz, M. Molecular Interactions in Surface-Assembled Monolayers of Short Double-Stranded DNA. *Langmuir* **2010**, *26* (13), 11574–11580. https://doi.org/10.1021/la100860d.

(79) Hill, H. D.; Millstone, J. E.; Banholzer, M. J.; Mirkin, C. A. The Role Radius of Curvature Plays in Thiolated Oligonucleotide Loading on Gold Nanoparticles. *ACS Nano* **2009**, *3* (2), 418–424. https://doi.org/10.1021/nn800726e.

(80) Minopoli, A.; Acunzo, A.; Della Ventura, B.; Velotta, R. Nanostructured Surfaces as Plasmonic Biosensors: A Review. *Adv. Mater. Interfaces* **2021**, *2101133*, 2101133. https://doi.org/10.1002/admi.202101133.

(81) Kinkhabwala, A.; Yu, Z.; Fan, S.; Avlasevich, Y.; Müllen, K.; Moerner, W. E. Large Single-Molecule Fluorescence Enhancements Produced by a Bowtie Nanoantenna. *Nat. Photonics* **2009**, *3* (11), 654–657. https://doi.org/10.1038/nphoton.2009.187.

(82) Hoang, T. B.; Akselrod, G. M.; Argyropoulos, C.; Huang, J.; Smith, D. R.; Mikkelsen, M. H. Ultrafast Spontaneous Emission Source Using Plasmonic Nanoantennas. *Nat. Commun.* **2015**, *6* (1), 7788. https://doi.org/10.1038/ncomms8788.

(83) Rasskazov, I. L.; Moroz, A.; Carney, P. S. Extraordinary Fluorescence Enhancement in Metal-Dielectric Core–Shell Nanoparticles. *J. Phys. Chem. Lett.* **2021**, *12* (27), 6425–6430. https://doi.org/10.1021/acs.jpclett.1c01368.

(84) Li, M.; Cushing, S. K.; Wu, N. Plasmon-Enhanced Optical Sensors: A Review. *Analyst* **2015**, *140* (2), 386–406. https://doi.org/10.1039/C4AN01079E.

(85) Lakowicz, J. R. *Principles of Fluorescence Spectroscopy*; Lakowicz, J. R., Ed.; Springer US: Boston, MA, 2006. https://doi.org/10.1007/978-0-387-46312-4.

(86) Millstone, J. E.; Wei, W.; Jones, M. R.; Yoo, H.; Mirkin, C. A. Iodide Ions Control Seed-

Mediated Growth of Anisotropic Gold Nanoparticles. *Nano Lett.* **2008**, *8* (8), 2526–2529. https://doi.org/10.1021/nl8016253.

(87) Pollitt, M. J.; Buckton, G.; Piper, R.; Brocchini, S. Measuring Antibody Coatings on Gold Nanoparticles by Optical Spectroscopy. *RSC Adv.* **2015**, *5* (31), 24521–24527. https://doi.org/10.1039/C4RA15661G.

(88) Papadakis, G.; Tsortos, A.; Bender, F.; Ferapontova, E. E.; Gizeli, E. Direct Detection of DNA Conformation in Hybridization Processes. *Anal. Chem.* **2012**, *84* (4), 1854–1861. https://doi.org/10.1021/ac202515p.

(89) Tataurov, A. V.; You, Y.; Owczarzy, R. Predicting Ultraviolet Spectrum of Single Stranded and Double Stranded Deoxyribonucleic Acids. *Biophys. Chem.* **2008**, *133* (1–3), 66–70. https://doi.org/10.1016/j.bpc.2007.12.004.